Axisymmetric simulation codes for Hall effect thrusters and plasma plumes

by

Adrián Domínguez Vázquez

in partial fulfillment of the requirements for the degree of Doctor in

Mecánica de Fluidos Programa Interuniversitario

Universidad Carlos III de Madrid

Advisor 1:
Pablo Fajardo Peña

Advisor 2:
Eduardo Ahedo Galilea

Tutor:
Eduardo Ahedo Galilea

May 2019

Actitud para reconocer,
disciplina para trabajar,
voluntad para aprender.

A mis padres y a mi hermano.

Acknowledgments

En primer lugar quisiera agradecer a mis padres su apoyo incondicional durante estos cuatro años de doctorado. Sé que el comienzo de este período, tras mudarme a Madrid, no fue fácil tampoco para vosotros. Sabed, sin embargo, que vivís en mi corazón. Sois Casa para mí. Gracias también a vosotros tengo la inmensa suerte de tener al mejor hermano del mundo, quien me ha acompañado durante estos años “en múltiples peligros”, y de quien no puedo sentirme más orgulloso. Me reconforta saber que podrás llegar todo lo lejos que tú mismo te propongas.

Quiero agradecer especialmente a mis directores Eduardo y Pablo su constante guía, dedicación, ayuda y consejo durante el completo desarrollo de la Tesis. Vine a Madrid para aprender y lo he conseguido gracias a vosotros. Agradezco también a Mario todo el apoyo prestado durante estos años.

Also, I would like to thank Professor Francesco Taccogna for his kind support during my stay in Bari. I learnt a lot and I really enjoyed that great and unforgettable experience, which definitely improved my PhD.

Por supuesto, no puedo olvidarme de mis amigos, la familia que uno elige. Sin duda, estos cuatro años y este trabajo de investigación habrían sido mucho peores sin la inestimable ayuda de mi gran amigo Filippo, de quien sigo aprendiendo cada día. Gracias por las infinitas discusiones de ciencia, propias de enfermos sin remedio, aunque siempre enriquecedoras, que espero sigamos manteniendo en el futuro. Gracias también a mi buen amigo Álvaro, genial investigador, mejor persona, e infinitamente mejor jugador de baloncesto que un servidor, por razones obvias. A los dos: aquí (y en mi Málaga, muy especialmente en feria con un “Cartojáh”) tenéis un amigo “pa’ lo que sea”. No puedo olvidarme de mi gran amiga Marta, fundamental e incondicional durante estos años. Gracias por enseñarme Madrid, por tantas y tantas aventuras perroflauteras, por alcoholizarme durante una buena temporada y, en definitiva, por quedarte en mi vida. Eres muy grande. Tampoco me olvido de mi buena (y loca) amiga Monica. Desde luego, mi estancia en Bari no habría sido lo mismo sin ti. Aún recuerdo aquel riso patate e cozze de tu mami. Ti voglio bene!

Finalmente, dedico estas últimas lineas a agradecer al resto de profesores y compañeros de doctorado todos los momentos compartidos durante estos años. En particular, agradezco a Dani el desarrollo del módulo de electrones y el intenso trabajo conjunto en el código, y a mi buen compañero de despacho, Jiewei, su ayuda con el código de electrones durante estos últimos meses de trabajo.

Published and submitted content

Article 1

A. Domínguez-Vázquez and F. Cichocki and M. Merino and P. Fajardo and E. Ahedo. Axisymmetric plasma plume characterization with 2D and 3D particle codes. *Plasma Sources Sciences and Technology*, 27(10):104009, 2018. DOI: 10.1088/1361-6595/aae702.

Article published in the peer-reviewed journal Plasma Sources Science and Technology. The author of this Thesis has contributed up to the 50% to the contents of the article, including all the 2D particle code results and the shared results discussion with F. Cichocki, responsible for the remaining 50% of the article contents, aside from the revisions of the advisors M. Merino, P. Fajardo and E. Ahedo. The contents are wholly included in the Chapter 3 of this Thesis. Whenever material from this source is included in this Thesis, it is singled out with typographic means and explicit reference.

Article 2

A. Domínguez-Vázquez, F. Taccogna and E. Ahedo. Particle modeling of radial electron dynamics in a controlled discharge on a Hall thruster. *Plasma Sources Sciences and Technology*, 27(6):064006, 2018. DOI: 10.1088/1361-6595/aac968.

Article published in the peer-reviewed journal Plasma Sources Science and Technology. Aside from the revisions of the advisors F. Taccogna and E. Ahedo, the author of this Thesis has contributed to the 100% of the contents of the article. The contents are wholly included in the Chapter 5 of this Thesis. Whenever material from this source is included in this Thesis, it is singled out with typographic means and explicit reference.

Article 3

F. Cichocki, A. Domínguez-Vázquez, M. Merino, and E. Ahedo. Hybrid 3D model for the interaction of plasma thruster plumes with nearby objects. *Plasma Sources Sciences and Technology*, 26(12):125008, 2017. DOI: 10.1088/1361-6595/aa986e.

Article published in the peer-reviewed journal Plasma Sources Science and Technology. The author of this Thesis has contributed up to the 20-30% to the article contents, mainly concerning the particle-in-cell models and algorithms described. The contents are partly included in the Chapter 2 of this Thesis. Whenever material from this source is included in this Thesis, it is singled out with typographic means and explicit reference.

Article 4

A. Domínguez-Vázquez, F. Taccogna, P. Fajardo and E. Ahedo. Influence of relevant parameters on the radial particle simulation of a Hall thruster discharge. Submitted to *Journal of Physics D: Applied Physics.*

Article submitted to the peer-reviewed journal Journal of Physics D: Applied Physics. Apart from the revisions of the advisors F. Taccogna, P. Fajardo and E. Ahedo, the author of this Thesis has contributed to the 100% of the contents of the article. The contents are partially included in the Chapter 6 of this Thesis. Whenever material from this source is included in this Thesis, it is singled out with typographic means and explicit reference. This article is an extension of the conference proceeding 1 shown below.

Conference proceeding 1

A. Domínguez-Vázquez, F. Taccogna, P. Fajardo and E. Ahedo. Influence of relevant parameters on the radial PIC simulation of a Hall effect thruster discharge. In *Space Propulsion Conference*, paper SP2018-288, Sevilla, Spain, May 14-18, 2018. 3AF, https://www.3af.fr/.

Conference paper published in Space Propulsion Conference 2018. Aside from the revisions of the advisors F. Taccogna, P. Fajardo, and E. Ahedo, the author of this Thesis has contributed to the 100% of the contents of the article. The contents are wholly included in the Chapter 6 of this Thesis. Whenever material from this source is included in this Thesis, it is singled out with typographic means and explicit reference.

Conference proceeding 2

A. Domínguez-Vázquez, F. Cichocki, M. Merino, P. Fajardo and E. Ahedo. 2D and 3D hybrid PIC-fluid modeling of electric thruster plumes. In *35th International Electric Propulsion Conference*, paper IEPC 2017-209, Atlanta, GA, USA, October 8-12, 2017. Electric Rocket Propulsion Society, https://erps.spacegrant.org.

Conference paper published in 35th International Electric Propulsion Conference 2017. The author of this Thesis has contributed up to the 50% to the contents of the paper, including all the 2D particle code results and the shared results discussion with F. Cichocki, responsible for the remaining 50% of the paper contents, aside from the revisions of the supervisors M. Merino, P. Fajardo and E. Ahedo. The contents are partly included in the Chapter 2 of this Thesis. Whenever material from this source is included in this Thesis, it is singled out with typographic means and explicit reference.

Conference proceeding 3

D. Pérez-Grande, J. Zhou, A. Domínguez-Vázquez, P. Fajardo and E. Ahedo. Development updates for a two-dimensional axisymmetric hybrid code for plasma thruster discharges. In *35th International Electric Propulsion Conference*, paper IEPC 2017-201, Atlanta, GA, USA, October 8-12, 2017. Electric Rocket Propulsion Society, https://erps.spacegrant.org.

Conference paper published in 35th International Electric Propulsion Conference 2017. The author of this Thesis has contributed up to the 20-30% to the article contents, being the responsible for the development of the heavy species module used for obtaining the results. The contents are partly included in the Chapter 2 of this Thesis. Whenever material from this source is included in this Thesis, it is singled out with typographic means and explicit reference.

Conference proceeding 4

A. Domínguez-Vázquez, D. Pérez-Grande, P. Fajardo, and E. Ahedo. NOMADS: development of a versatile plasma discharge simulation platform for electric propulsion. In *Space Propulsion Conference*, paper SP2016-3124869, Rome, Italy, May 2–6, 2016. 3AF, https://www.3af.fr/.

Conference paper published in Space Propulsion Conference 2016. The author of this Thesis has contributed up to the 70% to the contents of the paper, including the general code structure and architecture and the heavy species model description. The contents are partly included in the Chapter 2 of this Thesis. Whenever material from this source is included in this Thesis, it is singled out with typographic means and explicit reference.

Other research merits

Additional conference proceedings contributions of this Thesis:

- J. Zhou, A. Domínguez-Vázquez, D. Pérez-Grande, P. Fajardo and E. Ahedo. An axisymmetric hybrid model for the plasma transport in a Helicon plasma thruster. In *Space Propulsion Conference*, paper SP2018-308, Sevilla, Spain, May 14-18, 2018. 3AF, https://www.3af.fr/.
- F. Cichocki, A. Domínguez-Vázquez, M. Merino, and E. Ahedo. A 3D hybrid code to study electric thruster plumes. In *Space Propulsion Conference*, paper SP2016-3124968, Rome, Italy, May 2–6, 2016. 3AF, https://www.3af.fr/.

Poster sessions, workshops and scientific communications in the frame of this Thesis:

- A. Domínguez-Vázquez, P. Fajardo, E. Ahedo and F. Taccogna. Non-Maxwellian electron VDF features in a Hall thruster chamber. In *Princeton ExB Plasma Workshop*, Princeton University, Princeton, NJ, USA, November 1-2, 2018. Princeton Plasma Physics Laboratory, https://htx.pppl.gov/exb2018about.html.
- A. Domínguez-Vázquez, D. Pérez-Grande, F. Cichocki, M. Merino, P. Fajardo and E. Ahedo. Hybrid PIC-fluid codes for plasma discharge simulations. Invited talk by Máster Interuniversitario de Hidráulica Ambiental, at Escuela de Ingenierías Indistriales, Universidad de Málaga, May 2, 2018.
- F. Cichocki, A. Domínguez-Vázquez, D. Pérez-Grande, M. Merino, E. Ahedo, and P. Fajardo. Hybrid particle codes for electric propulsion. Poster session at *14th Spacecraft Charging Technology Conference*, ESTEC, Noordwijk, The Netherlands, April 4–8, 2016.

Abstract

The development of reliable and versatile plasma discharges simulation codes is becoming of central importance, given the rapidly evolving electric propulsion landscape. These tools are essential for facilitating and complementing the design of new prototypes, significantly reducing development time and costs. Moreover, they can provide a deeper insight on already proven technologies, revealing optimization opportunities so as to improve the thruster performance and lifetime, and predicting the operational parameters at different regimes of interest.

This Thesis is devoted to the numerical study of different plasma discharges and, in particular, the Hall effect thruster (HET) discharge. With special focus on particle-based modeling, two simulation codes have been developed. The first one, named HYPHEN, is a new two-dimensional axisymmetric hybrid, particle-in-cell (PIC)/fluid multi-thruster simulation platform. Its versatile PIC-based module for heavy species supports the simulation of inner active surfaces, mixed specular-diffuse neutral-wall reflection, and charge-exchange (CEX) collisions, thus extending the code capabilities and enabling the simulation of axisymmetric plasma plumes. Moreover, it features a new population control which monitors independently every heavy species and limits the statistical noise at a low computational cost. Furthermore, an improved version of the HET electron-fluid module for the isotropic electron pressure case is presented. Three major studies have been carried out with this code. First, the simulation of an ion thruster plasma plume has permitted to benchmark HYPHEN against the 3D plasma plume code EP2PLUS. Second, an investigation on the neutral-wall interaction effects on an unmagnetized plasma discharge in a surface-dominated cylindrical channel with isothermal electrons has been performed. The discharge ignition requires different propellant injection mass flows in the diffuse and specular neutral-wall reflection cases. Third, preliminary simulations of a SPT-100 HET have been carried out to demonstrate the code capabilities and reveal its limitations. Consistent results have been obtained for different cathode locations in the near plume region and various electron turbulent transport parameter profiles.

The second code corresponds to a new version of the one-dimensional radial particle model of a HET discharge, originally developed by F. Taccogna. The major improvements are an ionization controlled discharge algorithm, which enables sustaining a steady-state discharge, and an extended volumetric weighting algorithm which provides a more accurate macroscopic description of the low populated species, such as the wall-emitted secondary electrons. The radial dynamics of both the primary and secondary electron populations have been analyzed in detail, assessing the temperature anisotropy ratio of their velocity distribution functions and the asymmetries introduced by cylindrical geometry effects in the macroscopic laws of interest, thus aiming at a future improvement of the plasma-wall interaction module implemented in HYPHEN.

Resumen

El desarrollo de códigos fiables y versátiles para la simulación de descargas de plasma es cada vez más importante dada la rápida evolución de la propulsión espacial eléctrica. Estas herramientas son esenciales para facilitar y complementar el diseño de nuevos prototipos, reduciendo significativamente los tiempos y costes de desarrollo. Además, pueden ampliar la comprensión de las tecnologías ya establecidas, revelar vías de optimización del propulsor que permitan mejorar su rendimiento y vida útil, y predecir los parámetros de operación del mismo en diferentes regímenes de interés.

Esta Tesis está dedicada al estudio numérico de diferentes descargas de plasma y, en particular, de descargas HET. Se han desarrollado dos códigos de simulación, con especial énfasis en los modelos de partículas. El primero de ellos, llamado HYPHEN, es una nueva plataforma de simulación multi-propulsor, híbrida PIC/fluida y axisimétrica. Su módulo PIC para especies pesadas permite la simulación de superficies activas inmersas en el plasma, procesos de reflexión especular-difuso de neutros en pared y colisiones CEX, extendiendo por tanto las capacidades del código y permitiendo la simulación de plumas de plasma axisimétricas. Además, incluye un nuevo control de población que monitoriza a cada especie pesada por separado limitando el ruido estadístico y el coste computacional. Por otra parte, se presenta una versión mejorada del modelo fluido de electrones isótropos para HET. Tres estudios principales se han llevado a cabo con este código. En primer lugar, la simulación de la pluma de plasma de un motor iónico ha permitido validar HYPHEN con el código de plumas 3D EP2PLUS. Por otro lado, se ha investigado el efecto de la interación del gas neutro con la pared en una descarga no magnetizada con electrones isotermos en un canal cilíndrico esbelto. La ignición de la descarga requiere inyectar diferentes gastos másicos de propulsante en los casos de reflexión difusa y especular. En tercer lugar, se han realizado simulaciones preliminares de un motor HET de tipo SPT-100 con el objeto de demostrar las capacidades del código y revelar sus limitaciones, obteniendo resultados consistentes para diferentes posiciones del cátodo en la región de la pluma cercana, y perfiles del parámetro de turbulencia de electrones.

El segundo código representa una nueva versión del modelo radial de partículas de una descarga HET desarrollado originalmente por F. Taccogna. Las principales mejoras consisten en un algoritmo de control de la descarga a través de la ionización, que permite obtener una descarga estacionaria, y un algoritmo de pesado volumétrico extendido, que proporciona una descripción macroscópica más precisa de las especies poco pobladas, como los electrones secundarios emitidos desde las paredes del motor. Para posibilitar una futura mejora del módulo de HYPHEN de interacción plasma-pared, se han analizado en detalle la dinámica radial de los electrones primarios y secundarios, la anisotropía de temperatura de sus funciones de distribución de velocidad, y las asimetrías cilíndricas en las leyes macroscópicas de interés.

Contents

List of Figures

List of Tables

Glossary

List of Symbols

α_B	Magnetic angle.
α_t	Electron turbulent parameter acting in both the momentum and energy equation considered in the HET simulations of this Thesis (see Chapter 4).
α_W	Wall accommodation coefficient
α_{te}	Electron turbulent parameter acting in the electron energy equation.
α_{tm}	Electron turbulent parameter acting in the electron momentum equation.
α_{tq}	Electron turbulent parameter acting in the electron heat flux equation.
$\mathbf{1}$	Unit vector.
$\boldsymbol{\xi}$	2D computational position vector.
$\boldsymbol{B}$	Magnetic field vector.
$\boldsymbol{c}$	Thermal velocity vector.
$\boldsymbol{E}$	Electric field vector.
$\boldsymbol{F}$	Force vector in the electron momentum equation gathering the inertial force $\boldsymbol{F}_I$ and the turbulent force $\boldsymbol{F}_t$.
$\boldsymbol{g}$	Particle flux vector.
$\boldsymbol{j}$	Current density vector.
$\boldsymbol{j}_c$	Heavy species equivalent collisional current density.
$\boldsymbol{M}$	Collisional momentum transfer term.
$\boldsymbol{n}$	Normal versor to a given MFAM face.
$\boldsymbol{q}$	Heat flux vector.
$\boldsymbol{Q}_t$	Turbulent contribution term in the electron heat flux equation.
$\boldsymbol{r}$	2D axisymmetric position vector.
$\boldsymbol{u}$	Drift velocity vector.
$\boldsymbol{v}$	Particle velocity vector.
$\boldsymbol{x}$	3D cartesian position vector.
$\boldsymbol{Y}$	Vector term in the electron heat flux equation grouping both the electron heat flux and momentum inertial contributions.

$\boldsymbol{Y}_q$	Complete inertial vector term in the electron heat flux equation.
χ	Hall parameter.
Δi	Grid size along the i coordinate, with $i = x, y, z, r$.
Δm	Amount of mass of a given heavy species to be generated, eliminated or injected, depending on the context.
ΔS	Area of a given PIC mesh surface element.
Δt	Timestep.
δt	Time sub-interval.
ΔV	Nodal weighting volume associated to a given PIC mesh node.
ΔZ	Atom charge number jump in a given ionization collision.
δ	Dirac function or secondary electron emission yield, depending on the context.
$\Delta\phi$	Electric potential correction introduced by the Kinetic Bohm Forcing algorithm, sheath potential drop, or simply a given potential drop, depending on the context.
$\dot{\boldsymbol{p}}$	Particle momentum flux vector.
$\dot{m}_A$	Propellant mass flow injected through the anode (or injection surface) into the simulation domain.
ϵ	Relative error (depending on the context).
ϵ_0	Vacuum permittivity.
η_e	Electron resistivity.
η_{cur}	Current efficiency.
η_{div}	Divergence efficiency.
η_{prod}	Production efficiency.
η_{thr}	Thrust efficiency.
η_u	Utilization efficiency.
γ	Polytropic coefficient.
λ	Magnetic stream function.
λ_c	Mean free path of a given collision.
λ_D	Debye length.
$\mathcal{A}$, $\mathcal{B}$	Matrices of the square linear system solved by NOMADS for updating the electric potential at the MFAM cells.
$\mathcal{I}$	Identity tensor.
$\mathcal{J}, \mathcal{J}_I$	Jacobian and inverse Jacobian matrix of the coordinates transformation between the physical and computational domains.
$\mathcal{J}_l$	Jacobian matrix of the transformation from the arc coordinates (l_η, l_ξ) to the physical variables (z, r).

$\mathcal{Q}_e$	Third order electron heat flow tensor.
$\mathcal{S}$, $\mathcal{R}$	Matrices of the square linear system solved by NOMADS for updating the electron pressure at the MFAM cells.
μ	Electron mobility or magnetic moment, depending on the context.
ν	Collision frequency.
Ω_0	2D (z, r) domain corresponding to the meridian half-plane at $\theta = 0$ (plane referring to the 2D axisymmetric simulation domain).
ω_B	Generic cyclotron frequency.
ω_{ce}	Electron cyclotron frequency.
ω_{pe}	Plasma frequency.
ϕ	Electric potential.
ϕ_A	Anode wall potential.
Π	Macroparticle track matrix.
π	Pi number.
ρ	Charge density.
σ	Collision cross section, surface charge density, magnetic potential function or standard deviation, depending on the context.
σ_t	Replenishment ratio (also called thermalization parameter).
$\tilde{\boldsymbol{j}}_e$, $\tilde{\boldsymbol{j}}_i$	Electron and ion 2D (z, r) current density vectors, respectively.
ε	Partial contributions to mass and power balances presented in Chapter 4.
ξ, η	2D computational coordinates.
ξ, η, ζ	3D computational coordinates.
A	Area of the radial section of a HET chamber, or area of a given MFAM cell face, depending on the context.
A	Atom of a given heavy species.
c_s	Sonic velocity of a given plasma heavy species.
dr	Spatial interval along the radial coordinate.
E	Energy per elementary particle, depending on the context.
e	Electric charge of an electron or normal energy outflux of an impacting population on a material wall boundary, depending on the context.
F	Distribution function or particle list in Chapter 2. Thrust force in Chapter 4 and Appendix B.
f	Velocity distribution function or probability distribution function (depending on the context) of a given plasma species.
f_{sh}	Sheath model function relating the sheath potential drop and the plasma currents collected at the wall.

g_0	Standard acceleration of gravity.
h	Scale functions.
h_{sh}	Sheath model function providing the electron energy flux at the sheath edge.
I	Current.
I_d	Discharge current.
I_{sp}	Specific impulse.
i_{surf}, j_{surf}	Pair of indices identifying a given PIC mesh surface element.
l_η, l_ξ	2D arc coordinates.
M	Total mass of a given heavy species in the simulation domain.
m	Elementary particle mass of a given species.
N	Number of macroparticles (depends on the context).
n	Particle density.
n_d	Exact macroparticle density.
N_k	Number of time-averaging steps used by the extended weighting algorithms.
N_ξ, N_η	Number of nodes along the 2D computational coordinates ξ and η, respectively.
N_{ke}	Number of NOMADS electron-fluid module sub-iterations per simulation (or PIC) timestep.
P	Power or variable corresponding to the Kinetic Bohm Condition presented in Chapter 2.
p	Electron pressure.
P_d	Discharge power.
p_c	Collision probability of a given macroparticle pair.
p_{spec}	Probability of specular reflection of a neutral macroparticle at a given material wall.
Q	Volumetric energy source or sink term.
q	Elementary particle charge of a given species.
R	Random number.
r, θ, z	3D cylindrical coordinates.
R_0	Outermost radius at the initial plane of an expanding plasma plume.
$R_i(T_e)$	Ionization rate.
r_l	Larmor radius.
r_m	HET chamber mean radius in the Appendix A.
S	Particle source term in the continuity equation.
$S_j(\xi, \eta)$	Bilinar shape function associated to the j^{th} PIC mesh node in the computational domain.

T	Temperature (in energy units).
t	Time.
$U(a,b)$	Uniform probability distribution in the interval $[a,b]$.
V	Total volume of the simulation domain or volume of a particular (or several) MFAM cell, as for example V_{cat}, which represents the volume of the volumetric cathode in the context of the electron-fluid model for HETs.
V_d	Discharge voltage.
W	Macroparticle weight.
W_d	Gyrocenter azimuthal energy.
x, y, z	3D Cartesian coordinates.
Z	Charge number.
z_{exit}	Axial coordinate of the thruster exit section in the Appendix A.

Subscripts

$_{1,\ 2}$	Referring to the inner and outer radii of a HET chamber, respectively, in Chapters 5 and 6. Referring to arbitrary directions or timesteps in 2.
$_c$	Referring to the central point of a given PIC mesh surface element or to a collision, depending on the context.
$_j$	Referring to the j^{th} PIC mesh node or surface element, except where otherwise noted (it refers to plasma species in Chapter 5).
$_p$	Referring to the p^{th} macroparticle.
$_r$	Referring to the radial component
$_s$	Referring to the s^{th} heavy species.
$_x$	Referring to the Cartesian x-component
$_y$	Referring to the Cartesian y-component
$_z$	Referring to the axial component.
$_{(ESW)}$	Referring to a time-averaged variable according to the extended surface weighting algorithm presented in Chapter 2.
$_{+,\ -}$	Referring to electron currents collected to the thruster walls along positive or negative radial directions, respectively, in Chapters 5 and 6.
$_0$	Referring to an initial iteration or timestep except where otherwise noted.
$_{2D}$	Referring to a 2D macroparticle velocity in the simulation domain Ω_0.
$_\lambda$	Referring to the magnetic λ coordinate along the B-perpendicular direction.
$_\parallel$	Referring to the B-parallel component except where otherwise noted.
$_\sigma$	Referring to the magnetic σ coordinate along the B-parallel direction.

θ	Referring to the azimuthal component
$\top$	Referring to the B-perpendicular component except where otherwise noted.
$axial$	Referring to the axial transport.
BC	Referring to the Kinetic Bohm Condition.
BS	Referring to the backscattered secondary electrons.
cat	Referring to the cathode.
$cell$	Referring to cell-related variables, such as number of macroparticles per cell.
$coll$	Referring to collisional processes.
$cross$	Referring to the crossing of a given PIC mesh surface element by a macroparticle.
$elec$	Referring to the power transmitted to the electrons by the electric field.
ex	Referring to excitation collisions.
ex	Referring to the expected value of a given magnitude.
e	Referring to the electron population.
gen	Referring to the generation of macroparticles in the domain.
hit	Referring to those macroparticles hitting a non-transparent boundary surface.
i,∞	Referring to the current or power deposited at the free loss domain boundary.
imp	Referring to a property related to an impacting plasma species or particle at a given surface.
$inel$	Referring to the power spent in inelastic collisions (ionization and excitation).
inj	Referring to the injection of macroparticles in the domain.
in, out	Referring to the inner and outer radii of a HET chamber, respectively, in Appendix A.
ion,ex	Referring to the power spent in ionization and excitation collisions.
$ioniz$	Referring to the ionization collisions.
ion	Referring to ionization collisions.
i	Referring to ion species or populations.
min, max	Referring to minumum and maximum values, respectively.
m, l	Referring the m^{th} and l^{th} MFAM face and cell center.
n	Referring to the neutral species or populations.
p, $s1$, $s2$	Referring to the primary and secondary electron populations emitted from the inner and outer thruster walls, respectively, in Chapters 5 and 6.
$reinj$	Referring to the reinjection of macroparticles in the domain from material wall boundaries.
rel	Referring to a relative variable (e.g. the relative velocity v_{rel}).
SEE	Referring to the secondary electron emission.

sh	Referring to the plasma sheaths.
$sinks$	Referring to the power sink terms.
$sources$	Referring to the power source terms.
$spec$	Referring to the specular neutral-wall reflection process.
tg	Referring to a target value.
$ther$	Referring to the thermalization of the electron population.
TS	Referring to the true secondary electrons.
use	Referring to the useful power.
$walls$	Referring to the current or power deposited at the thruster walls.
wet, wef	Referring to the electron currents to and from the thruster walls (see Chapter 5).
W	Referring to a material wall boundary.
w	Referring to the net plasma currents collected to the thruster walls or impact energies at the thruster walls.

Superscripts

(hit)	Referring to those macroparticles hitting a non-transparent boundary surface.
(k)	Referring to the k^{th} iteration or timestep.
(rem)	Referring to those macroparticles to be removed from the simulation domain due to collisional processes.
(SW)	Referring to a surface weighted property or magnitude.
$+$, $++$	Referring to a singly or doubly charged ion, respectively.
$coll$	Referring to collisional processes.
$Coul$	Referring to Coulomb collisions.
el	Referring to an elastic collision.
ex	Referring to an excitation collision.
fw	Referring to fluxes from the boundary walls to the bulk plasma.
ion	Referring to ionization collisions.
tw	Referring to fluxes from the bulk plasma to the boundary walls.

Accents

$\bar{\psi}$	Average value of a given property ψ.
ψ^*	Effective or optimal value of a given property ψ, except where otherwise noted.

ψ'	Fluctuation a given property ψ. In Chapter 3 refers to relative computational coordinates inside a given computational PIC mesh. In Chapter 5 it refers to conventionally weighted variables, except where otherwise noted.
$\tilde{\psi}$	Normalized value of a given property ψ. This does not apply to the variables $\tilde{\boldsymbol{j}}_e$ and $\tilde{\boldsymbol{j}}_i$.

Acronyms

1D	One Dimensional.
1Dp	One Dimensional planar.
1Dr	One Dimensional radial.
2D	Two Dimensional.
3D	Three Dimensional.
ACD	Axially-Controlled Discharge.
BS	Backscattered Secondary electrons.
CC-FVM	Cell Centered Finite Volume Method.
CEX	Charge-EXchange collision.
CFL	Courant-Friedrichs-Lewy.
CIC	Cloud-In-Cell.
CSL	Charge Saturation Limit.
D	Diffuse (referring to neutral-wall reflection type).
DSMC	Direct Simulation Monte Carlo.
ECRA	Electron-Cyclotron-Resonance Accelerator
EP	Electric Propulsion.
EP2	Equipo de Propulsión Espacial y Plasmas.
EP2PLUS	Extensible Parallel Plasma PLUme Simulator.
ESW	Extended Surface Weighting.
EVW	Extended Volumetric Weighting.
GIT	Gridded Ion Thruster.
GR	Gradient Reconstruction.
HallMA	Hall Madrid.
HDF5	Hierarchical Data Format (current version 5).
HEMPT	High Efficiency Multi-stage Plasma Thruster.
HET	Hall Effect Thruster.
HPHall	Hybrid PIC Hall.

HPHall-2	Hybrid PIC Hall-2.
HPT	Helicon Plasma Thruster.
HYPHEN	Hybrid Plasma thruster Holistic simulation ENvironment.
ICD	Ionization-Controlled Discharge.
IP	Initial Population.
KBC	Kinetic Bohm Condition.
KBF	Kinetic Bohm Forcing.
LEO	Low Earth Orbit.
MCC	Monte Carlo Collision.
MD	Minimum Density.
MEX	Momentum-EXchange collision.
MFAM	Magnetic Field Aligned Mesh.
NASA	National Aeronautics and Space Administration.
NOMADS	NOn-structured Magnetically Aligned electron Discharge Simulator.
NSTAR	NASA Solar Electric Propulsion Technology Application Readiness.
NWC	Near-Wall Collisionality.
Open-MP	Open Multi-Processing.
PARDISO	PARallel Sparse Direct and multi-recursive Iterative linear SOlvers.
PIC	Particle-In-Cell.
PID	Proportional-Integral-Derivative.
RLC	Resistor-Inductor-Capacitor.
ROI	Region Of Influence.
S	Specular (referring to neutral-wall reflection type).
S/C	Spacecraft.
SEE	Secondary Electron Emission.
SPT	Stationary Plasma Thruster.
SSM	Self-Similar Method.
TAL	Thruster-with-Anode-Layer.
TCL	Thruster Center Line.
TDD	Test Driven Design
TS	True-Secondary electrons.
UC3M	Universidad Carlos III de Madrid.
VDF	Velocity Distribution Function.
WLSM	Weighted Least Squares Method.

Chapter 1

Introduction

Electric propulsion (EP) has become a well-established and mature technology successfully covering a wide range of in-space propulsive needs with remarkable performance. An EP system basically uses electric energy provided by the S/C power system to ionize the propellant generating plasma and accelerate it producing thrust [1–5]. The main advantage with respect to a conventional chemical propulsion system is the fact that the specific impulse (i.e. the propellant exhaust velocity) is not limited by nature of the propellant (i.e. its calorific energy per unit mass), which allows for important mass savings, thus enabling more ambitious propulsive missions. However, since the produced thrust is limited by the available on-board power delivered by the S/C power system (e.g. solar arrays), electric rockets are constrained to in-space operations.

Among the large variety of existing plasma thrusters, the gridded ion thruster (GIT) and the Hall effect thruster (HET) constitute well-established, reliable and successfully flown technologies. The next generation of these thrusters is being designed for larger on board power (∼20-100 kW), different control schemes, such as direct-drive [6], and new mission scenarios ranging from station keeping to space tugs or planetary exploration [7]. On the other hand, new promising technologies such as the Helicon plasma thruster (HPT) [8–15] or the electron-cyclotron-resonance accelerator (ECRA) [16–21] are under current development. Therefore, there is a need for a versatile multi-thruster simulation platform aiming at (*i*) facilitating and complementing the design of new prototypes, (*ii*) revealing optimization opportunities so as to improve the thruster performance and lifetime, and (*iii*) providing a deeper insight on the already proven technologies.

Several different approaches may be considered for the simulation of plasma discharges. First, fully kinetic models [22] attempt to solve Boltzmann equation for the species distribution function in the phase space coupled with Maxwell equations. However, the complexity introduced by the high dimensional phase space formulation and the difficulties in the modeling of the collisional processes constrain its application to simplified low dimensional studies [23–27]. Second, full particle-in-cell (PIC) models [28–38] represent an alternative Lagrangian-Eulerian approach which discretizes the species distribution function in terms of macroparticles, whose trajectories are integrated consistently with the existing electromagnetic fields. Nevertheless, the time and spatial scales to be resolved must be below the plasma frequency and the Debye length, which greatly increases the computational cost. Third, multi-fluid models solve a simplified set of equations resulting from taking moments of Boltzmann equation [39–43]. However, the low collisionality regime characterizing most plasma discharges in the EP context limits the multi-fluid models applicability due to (*i*) the deviation of the species distribution function from the Maxwellian one, which questions the typical Maxwellian-based model closure, and (*ii*) the high number of independent fluid species needed to better represent possible deviations of the species distribution function from a Maxwellian one. Finally, hybrid PIC-fluid models [44–55] represent an optimal choice suitable for the simulation of a large variety of plasma discharges, gathering the advantages of both full-PIC and multi-fluid models. Typically, a PIC approach is considered for the heavy species (i.e. ions and neutrals), while the electron population is modeled as a fluid. This strategy reduces significantly the computational cost with respect to full-PIC or fully kinetic codes, since it permits much longer integration timesteps. Furthermore, it does not presume any distribution function for those species. Nonetheless, the closure of the fluid set of equations describing the electron population still imposes strong assumptions on its dynamics which are not always fully satisfied in complex scenarios such as HETs.

Considering the advantages of a hybrid PIC-fluid formulation, and based on its broad expertise with previous simulations codes such as HPHall [44], HPHall-2 [45] or HallMA [46], the Plasma and Space Propulsion Team (EP2) at Universidad Carlos III de Madrid (UC3M) has developed HYPHEN, which stands for HYbrid Plasma thruster Holistic simulation ENvironment: a new two-dimensional axisymmetric hybrid PIC-fluid code devoted to the simulation of the plasma physics inside the chamber and in the near plume of various plasma thrusters. Although the focus of this Thesis is on HET simulations, HYPHEN is potentially extensible to HPT, ECRA or high efficiency multi-stage plasma thruster (HEMPT) [56, 57]. In addition, HYPHEN has greatly benefited from the parallel development of the hybrid 3D plasma plume code EP2PLUS by F. Cichocki in the frame of his Thesis [52, 53, 58], and, as a result, is also able to simulate axisymmetric plasma thruster plumes, yielding valuable estimates of the slow ion backflow responsible for S/C sensitive surfaces contamination and sputtering. Regarding HET simulations, HYPHEN incorporates numerous improvements in both the PIC treatment of the heavy species and the electron-fluid formulation, which significantly increase its capabilities with respect to those of previous legacy codes such as HPHall, HPHall-2 or HallMA. As for the PIC segment, the main modeling novelties aim at (*i*) limiting the PIC-related statistics noise through a new efficient particle population control algorithm and (*ii*) the extension of the code capabilities with an improved treatment of charge-exchange (CEX) collisions, essential for simulating plasma plume scenarios. On the other hand, the HYPHEN electron-fluid model for HETs has been originally developed by Pérez-Grande [59, 60] for the case of an anisotropic electron pressure tensor. Its name is NOMADS, standing for NOn-structured Magnetically Aligned plasma Discharge Simulator, and it solves a fully 2D axisymmetric formulation for the electron population in a Magnetic Field Aligned Mesh (MFAM), which permits (*i*) the simulation of complex magnetic topologies featuring magnetic field singular points or magnetically shielded regions present in new HET designs and HEMPTs, and (*ii*) the extension of the domain boundaries for assessing the plasma physics in the near plume region, thus enabling the synergy with plasma plume codes as EP2PLUS. In this Thesis, an improved version of NOMADS for the isotropic electron pressure case is presented.

Despite the fact that HETs are already a mature technology successfully covering the propulsive needs of a wide variety of space missions, there still exist an important number of open problems related to relevant physical phenomena driving the HET plasma discharge in the thruster chamber and its near plume which are insufficiently known. In particular, one of the main issues affecting the thruster performance and its operational lifetime is related to the plasma interaction with the thruster walls, which is responsible for the plasma recombination, energy losses and walls erosion. Moreover, the low collisionality regime typical of a HET discharge prevents from reaching a full replenishment of the high-energy electron velocity distribution function (VDF) tails collected to the walls. This fact, along with the high secondary electron emission (SEE) caused by the electron impact on the typical thruster ceramic walls enhances the departure of the electron from a Maxwellian one. Another central open problem in HET research corresponds to the electron anomalous transport, which is still far from being well understood. Among the various physical mechanisms behind this phenomena, correlated azimuthal fluctuations of the plasma density and the electric potential have been postulated to be the main responsible for the experimentally reported enhanced axial electron transport in typical HET operation. In this context, full-PIC models represent a suitable approach that could bring more light to these still open problems in HET research. Furthermore, hybrid PIC-fluid simulation tools such as HYPHEN can greatly benefit from macroscopic laws derived from reduced full-PIC simulations implemented as auxiliary models.

1.1 Objectives of this Thesis

The main objectives of this Thesis may be divided in two complementary groups. The former includes (*i*) the development and testing of a new 2D axisymmetric PIC model for heavy species (i.e. ions and neutrals), (*ii*) its integration with an improved electron-fluid model for HET discharges for the isotropic electron pressure case, thus establishing the basis of HYPHEN, and (*iii*) the application of HYPHEN to the simulation of different simulation scenarios of interest, including HET discharges and plasma plumes. On the other hand, the latter corresponds to a new improved version of a 1D radial PIC model for the simulation of a HET discharge originally developed by Taccogna [30–32], with the main goals of (*i*) getting a deeper insight on the physics of the discharge, and (*ii*) analyzing the radial dynamics of both the primary and secondary electron populations obtaining valuable information from their respective VDFs, which will enable a future improvement of the plasma-wall interaction models implemented in HYPHEN.

1.2 Thesis outline

The present Thesis is organized as follows:

- Chapter 2 describes the HYPHEN code general architecture and structure, details the PIC model for heavy species included in HYPHEN, which represents one of the major contributions of this Thesis, and presents an improved electron-fluid model for HETs for the isotropic electron pressure case to be coupled with the particle module for the heavy species in the frame of the hybrid PIC-fluid HYPHEN code. The contents of this Chapter are based mainly on two peer-reviewed journal publications [53, 54] and on three conference papers [59, 61, 62].

- Chapter 3 reproduces the contents published in the peer-reviewed journal Plasma Sources Science and Technology [54]. The simulation of a typical plasma plume expansion scenario based on an ion thruster has been considered to compare and benchmark HYPHEN (mainly focusing on the PIC module) against the 3D code EP2PLUS, and show their capabilities. An excellent agreement is found between the codes, which are both capable of reproducing, with an acceptable noise level, the properties of heavy particle populations with densities differing by several orders of magnitude (i.e. the injected and CEX ions populations).

- Chapter 4 demonstrates HYPHEN capabilities for the simulation of axisymmetric plasma discharges in two different scenarios. First, the simulation of an unmagnetized discharge with isothermal electrons in a cylindrical channel has permitted a further assessment of the HYPHEN hybrid code performance. The second part of the Chapter is devoted to SPT-100 HET discharges simulations making use the improved electron-fluid model presented in Chapter 2. The discharge structure is analyzed in detail. The effect on the breathing mode characteristic frequency of the neutral-wall reflection type is investigated. The performance of the volumetric cathode model is tested, and preliminary results for different values of the electron anomalous transport parameter are shown.

- Chapter 5 reproduces the contents published in the peer-reviewed journal Plasma Sources Science and Technology [35]. A new improved version of the 1D radial PIC model of an annular HET discharge with SEE from the walls and a radial magnetic field is presented. The temperature anisotropy ratio of the VDF of both primary and secondary electrons, and the asymmetries introduced by cylindrical geometry effects (which include the geometrical expansion, the centrifugal force, and the magnetic mirror) are analyzed in detail.

- Chapter 6 focuses on a parametric study of the 1D radial PIC model presented in Chapter 5 exploring different scenarios of particular interest in order to both further validate the 1D radial particle model and get a deeper insight on the physics of the response. The contents of this Chapter are based on a conference paper [63] and have been submitted for their publication to the peer-reviewed journal Journal of Physics D: Applied Physics [64].

- Chapter 7 summarizes the main conclusions of this Thesis and proposes a number of activities and relevant research lines for future work.

- Appendix A details the complete set of individual and integrated tests developed during this Thesis, which are mainly related to the algorithms included in the HYPHEN PIC module described in Chapter 2.

- Appendix B contains additional data corresponding to the different SPT-100 HET simulation cases analyzed in Chapter 4 for further analysis and discussion.

Chapter 2

The HYPHEN simulation platform

This Chapter provides a detailed description of HYPHEN: a new two-dimensional, axisymmetric hybrid PIC-fluid code devoted to the simulation of the plasma physics inside the chamber and in the near plume of various plasma thrusters, such as HETs and HPTs, which can be also applied to the study of the expansion of axisymmetric plasma thruster plumes in vacuum. One of the main contributions of this Thesis is the development and testing of the PIC module, which has been successfully integrated with the electron-fluid subcode. Regarding HETs, Pérez-Grande [59, 60] presented the electron-fluid equations for the case of an anisotropic electron pressure tensor. The electron-fluid module implemented in HYPHEN by Pérez-Grande features an isotropic electron pressure. In this Chapter, an improved electron fluid model formulation for the isotropic electron pressure case is presented, with the main purposes of identifying the role of the electron turbulence in the different model equations, and enabling a future treatment of the electron inertial effects. The contents of this Chapter are based mainly on two peer-reviewed journal publications [53, 54] and on three conference papers [59, 61, 62].

2.1 General code structure

2.1.1 Methodology, standards and overall architecture

HYPHEN overall architecture and structure are based on modularity, aiming to be a more flexible and capable simulation platform. Modularization strategy also facilitates code development and debugging, and the integration of new capabilities. Thus, the versatile plasma discharge simulator is potentially extensible to HPT, ECRA or HEMPT, as well as HET. Moreover, in order to maximize code sharing and standardization, HYPHEN has been designed with the same overall architecture, data structure and interfaces as those of the hybrid 3D plasma plume code EP2PLUS, developed by Cichocki [52,53,58]. Both simulation tools make use of common baseline modules and dedicated subroutines whenever possible. As a result of the synergy between the two codes above (especially regarding the PIC module), HYPHEN is also able to simulate 2D axisymmetric plasma thruster plumes, as it is shown in Chapter 3.

The different programming languages used are Python/Matlab for data pre and post-processing and results analysis, and Fortran for the main numerical computations. Additionally, industry-level standards such as HDF5 technology for high-performance data management and Open-MP for code parallelization are considered. The code development process follows a strict Test Driven Design (TDD) philosophy and a wide specific documentation (development document and user manual) is constantly updated. Therefore, HYPHEN is distributed with a complete suite of modular and integrated tests specifically designed to check each of the code functionalities. All tests regarding the HYPHEN PIC segment can be found in the Sec. A. Moreover, the simulation tool development is carried out under version control through a standard Mercurial online repository which can be cloned to any number of local machines.

As depicted in Fig. 2.1, HYPHEN features three independent program units, which can be run separately:

- SET: Pre-processing unit, coded in Python/Matlab. It takes as input the file set.inp, which contains all the simulation settings edited by the user. The SET produces two output files: a text file named sim_params.inp containing the simulation parameters and a HDF5 file called SimState.hdf5, which stores the miminum set of variables needed to start (or restart) a simulation. The SET is composed of different sub-utilities, each of them producing different output files containing information about the domain meshes, the fields or the propellants, for example, which are then gathered and stored into the file SimState.hdf5. The SET sub-utilities are:
  - The magnetic field generator, developed by deSaavedra [65], which provides the magnetic field in a preliminar square mesh covering the thruster simulation domain.
  - The PIC mesh generator, developed in the frame of this Thesis, which generates the *ad hoc* structured mesh used by the PIC module (see Sec. 2.2.1).
  - The magnetic field aligned mesh (MFAM) generator, which produces the unstructured mesh used by the electron-fluid module, whose elements are aligned with the magnetic field lines [60, 66].

  - The electron-fluid initializator, in charge of giving initial values to the electron-fluid module related variables in order to start the simulation.
  - The propellants data generator, which provides all the information related to the different propellants used by the hybrid simulator.
  - The sheath data generator, in charge of generating all the information related to the sheath model used in the simulations.

- CORE: Simulation core unit, coded in Fortran, which carries out the actual simulation of the plasma physics. It takes as inputs both files sim_params.inp and SimState.hdf5 and produces two output files in HDF5 format: PostData.hdf5, containing the time evolution of different variables of interest, and SimState.hdf5, which is an updated version of the corresponding input file at the last simulation step, thus enabling a future simulation restart.

- POST: Post-processing unit, coded in Python/Matlab. It takes as inputs a user defined configuration file named post.inp and the CORE output files, and produces as outputs the required plots, diagrams and statistics of the simulation results.

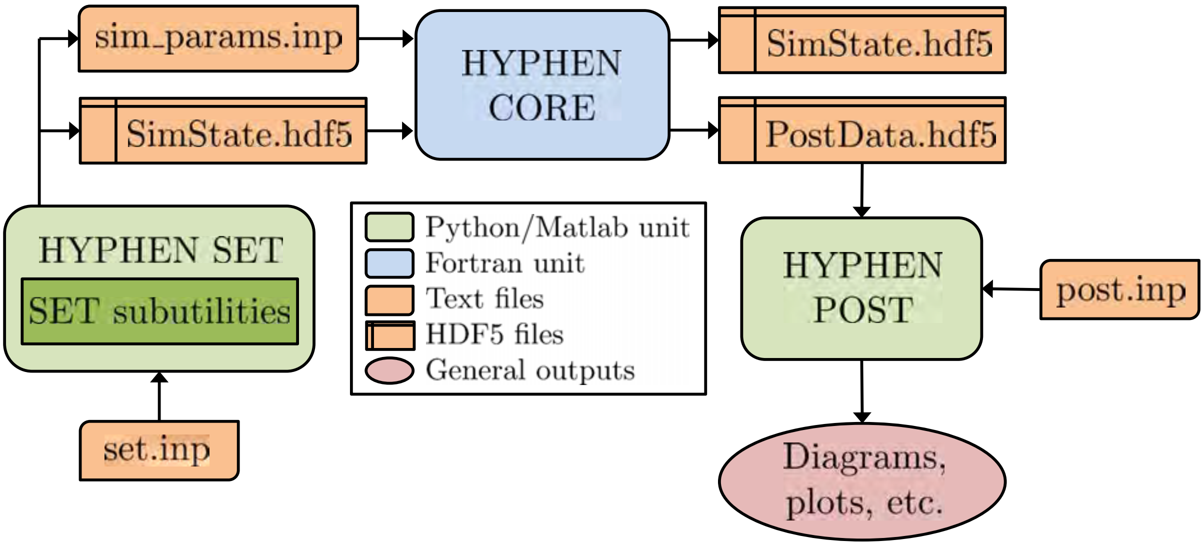

Figure 2.1: HYPHEN overall architecture.

2.1.2 The hybrid code loop

The CORE unit is composed of different dedicated modules, each of them in charge of performing predefined tasks and containing the necessary functions and subroutines with the different numerical algorithms implemented. Fig. 2.2 sketches the main simulation loop. The two central modules of the hybrid simulator are the PIC module and the electron-fluid module. The former, taking as inputs the electric potential and the electron temperature, follows a PIC approach to propagate the heavy species (neutrals and ions) one simulation timestep forward obtaining the particle densities and fluxes. The latter, taking those values from the PIC module and considering quasineutrality, solves

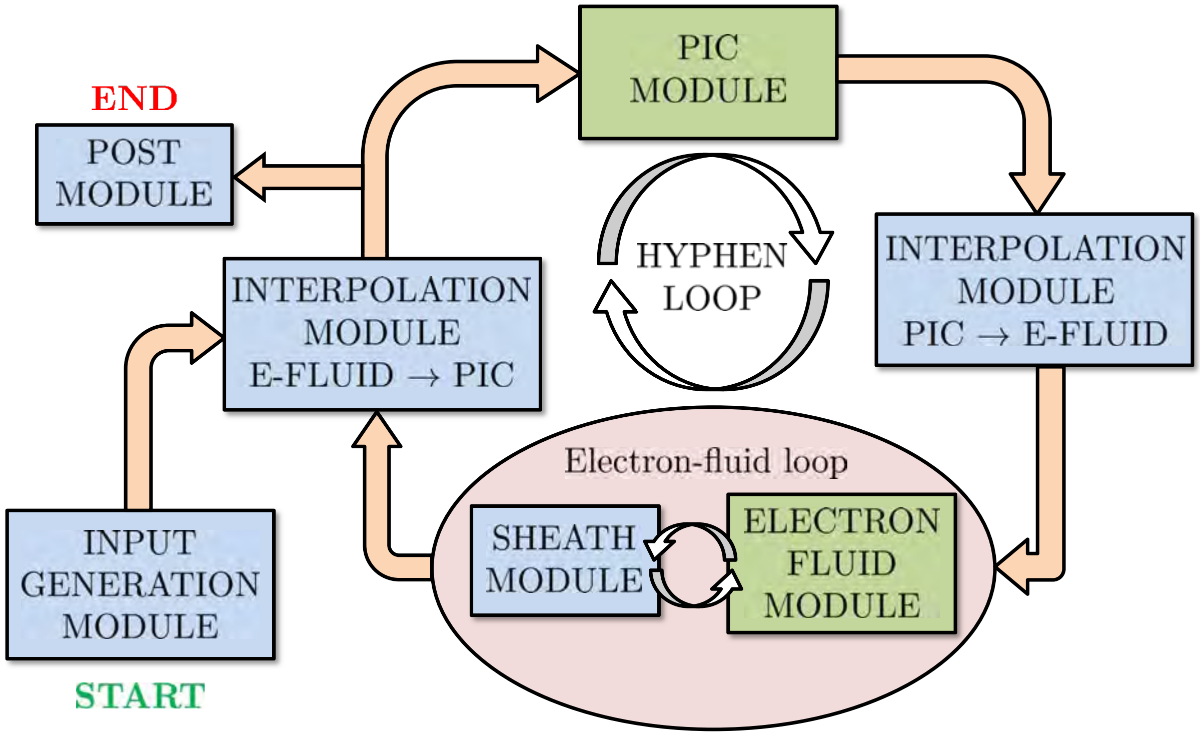

Figure 2.2: HYPHEN general simulation loop.

a given fluid model of the electron population computing the electric potential and the electron population related variables (e.g. the electron temperature), thus closing the loop. However, in general, each of those central modules operates on a different mesh of the simulation domain: a structured mesh for the PIC module (referred to as the PIC mesh hereafter), and an unstructured MFAM for the electron-fluid module. Therefore, both modules communicate each other through a dedicated bidirectional interpolation module. Here a brief description of the main CORE modules is provided:

- Input generation module: it is in charge of reading and initializing all CORE variables at the beginning of the simulation with the information contained in the input files sim_params.inp and SimState.hdf5.

- Interpolation module: it performs the bidirectional interpolation of different CORE variables from the PIC mesh to the MFAM and vice versa.

- PIC module: it carries out the simulation of the heavy species (ions and neutrals), thus performing the injection, propagation, sorting, weighting and removal of particles from domain. It also carries out the different particle collisions modeled and includes the Bohm condition forcing algorithm. Sec. 2.2 details all those processes.

- Electron-fluid module: it solves a given fluid model for the electron population obtaining the electric potential and the electron population related magnitudes such as the electron temperature. While the HYPHEN PIC formulation for the heavy species is standard for most of the foreseen simulation scenarios including plasma plumes and various plasma thrusters, the electron-fluid module has been designed to include different models of the electron population depending on the particular physical processes driving its behavior on each case. Regarding HET simulations, an electron-fluid model for the isotropic electron pressure case has been incorporated by Pérez-Grande [59, 60]. An improved version of this model is presented in Sec. 2.3. Besides, in order to simulate near-collisionless and unmagnetized plasma plumes, HYPHEN includes the simple polytropic electron-fluid closure [39] of EP2PLUS, which is detailed in Sec. 3.2. Furthermore, 2D axisymmetric models for highly magnetized electrons both in the chamber and the near plume of HPT [67] and ECRA [68] are currently under development by the EP2 research group at UC3M, thus making HYPHEN a potential multi-thruster simulation platform.

- Sheath module: this module is coupled with the electron module and relates the sheath potential drop with the electron and ion currents to the boundary walls (see Sec. 2.3.7.1).

- Post module: this module is dedicated to the diagnostic and post-processing of the CORE results. Besides, it writes out all those results to the output files PostData.hdf5 and SimState.hdf5.

2.2 The PIC model

2.2.1 The structured PIC mesh

The 3D physical domain to be simulated by the hybrid code comprises, in the general case of a HET, the thruster chamber where the plasma is produced and accelerated and the near thruster plasma plume, as shown in Fig. 2.3.

Assuming axisymmetry, the simulation domain is reduced to the meridian half-plane of the whole 3D physical domain mentioned above, obtaining a 2D (z, r) domain corresponding to a plane at $\theta = 0$ which shall be hereinafter referred to as Ω_0. In general, PIC algorithms obtain macroscopic magnitudes of the simulated species at the mesh nodes of the simulation domain through a weighting process. Therefore, a spatial discretization of the simulation domain into nodes and cells is needed, which can be obtained considering both unstructured or structured meshes. In HYPHEN, the PIC subcode makes use of a structured mesh, thus taking advantage of its higher computational efficiency in terms of macroparticle sorting algorithms. A new PIC mesh generator has been developed and integrated as a SET sub-utility of the hybrid code for obtaining, in the general case, 2D structured, non-uniform meshes of the typical simulation domain of HETs, HPTs and ECRAs. Besides, simple cylindrical meshes can be also generated for plasma thruster plumes simulations. The boundaries of the 2D PIC mesh represent 3D annular surfaces and the quadrilateral cells corresponds to 3D annular volumes. As shown on Fig. 2.4, a uniform computational mesh featuring square elements can be defined so that every point in the physical domain has unique computational coordinates in the computational domain. Thus, a given physical point $\boldsymbol{r} = (z, r)$ has computational coordinates $\boldsymbol{\xi} = (\xi, \eta)$, where $\xi \in [0, N_\xi - 1]$ and $\eta \in [0, N_\eta - 1]$ are the computational coordinates, taking integer values at the nodes, and N_ξ and N_η are the corresponding number of nodes along each coordinate.

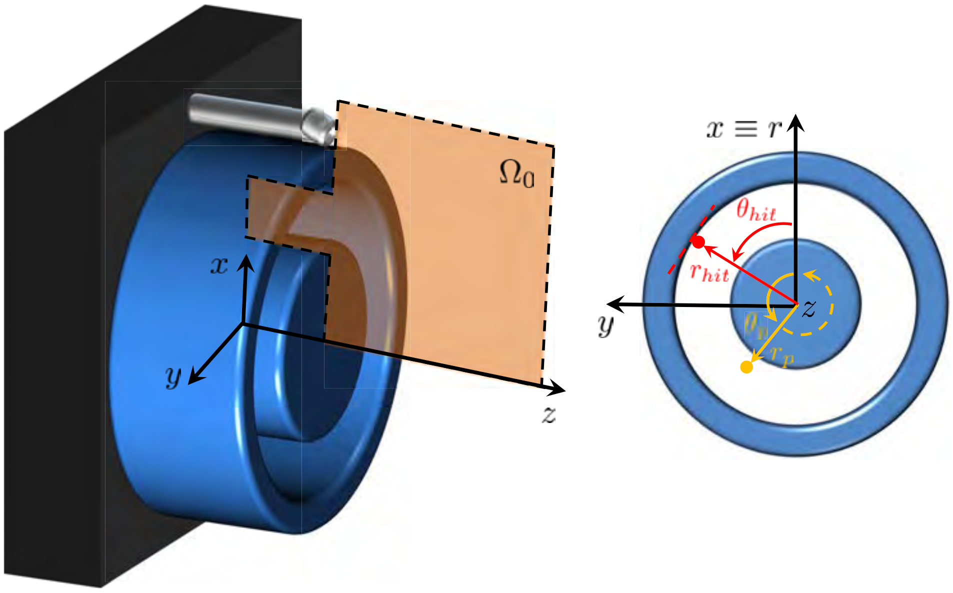

Figure 2.3: Figure of 3D physical domain to be simulated.

Given the computational coordinates of the p^{th} macroparticle $\boldsymbol{\xi}_p = (\xi_p, \eta_p)$, obtaining its corresponding physical coordinates $\boldsymbol{r}_p = (z_p, r_p)$ in the 2D domain Ω_0 is straightforward through a simple bilinear interpolation from the known physical coordinates of the nodes of the mesh cell containing the particle. The bilinear shape function associated to the j^{th} mesh node is defined in the computational domain as

$$S_j(\xi,\eta) = \begin{cases} (1-|\xi-\xi_j|)(1-|\eta-\eta_j|) & \text{with} \quad \{\xi,\eta\} \in \{[\xi_j-1,\xi_j+1],[\eta_j-1,\eta_j+1]\} \\ 0 & \text{otherwise} \end{cases} \tag{2.1}$$

where $\boldsymbol{\xi}_j = (\xi_j, \eta_j)$ are the node computational coordinates (see Fig. 2.4). In the structured PIC mesh, the mesh cell where the particle is located is identified by its lower left node, with computational coordinates $\boldsymbol{\xi}_0 = \text{floor}(\boldsymbol{\xi}_p)$. Therefore, the particle physical coordinates are:

$$\boldsymbol{r}_p = \sum_{j=0}^{3} \boldsymbol{r}_j S_j(\xi_p, \eta_p), \tag{2.2}$$

where j runs over the four nodes of the cell containing the particle with physical coordinates $\boldsymbol{r}_j = (z_j, r_j)$.

On the other hand, given the physical coordinates of the particle $\boldsymbol{r}_p$, obtaining its corresponding computational coordinates in the general case of a non-uniform physical mesh requires much larger computational cost, since an iterative process must be carried out following a Newton-Raphson method. The algorithm starts by considering an initial guess $\boldsymbol{\xi}^{(0)} = (\xi^{(0)}, \eta^{(0)})$ for the computational coordinates to be computed, which may be a point in the middle of the domain or the particle computational coordinates from the step before (in case they are known). After obtaining the corresponding physical

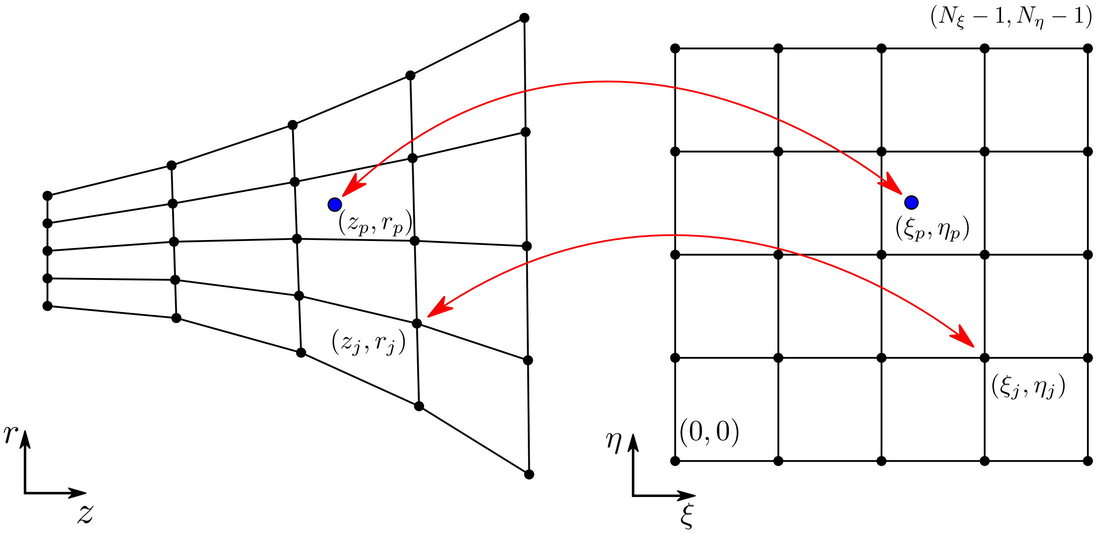

Figure 2.4: Bidirectional relation between the physical and computational PIC meshes.

coordinates $\boldsymbol{r}^{(0)} = (z^{(0)}, r^{(0)})$ through the bilinear interpolation as explained above, the initial estimation error is given by

$$\boldsymbol{\epsilon}^{(0)} = \boldsymbol{r}_j - \boldsymbol{r}^{(0)}, \tag{2.3}$$

and, if the error magnitude is above a minimum tolerance, a correction loop is entered in which, at each iteration k, the computational coordinates are corrected by an amount

$$\Delta\boldsymbol{\xi}^{(k)} = \mathcal{J}_I^{(k-1)} \cdot \boldsymbol{\epsilon}^{(k-1)} \tag{2.4}$$

where $\boldsymbol{\epsilon}^{(k-1)}$ is the reconstruction error defined in Eq. (2.3) at the $(k-1)^{th}$ iteration and $\mathcal{J}_I \equiv \mathcal{J}^{-1}$, being $\mathcal{J}$ the Jacobian matrix of the transformation $\{z, r\} = \{z(\xi, \eta), r(\xi, \eta)\}$, defined as

$$\mathcal{J} = \frac{\partial(z, r)}{\partial(\xi, \eta)} = \begin{pmatrix} \frac{\partial z}{\partial \xi} & \frac{\partial z}{\partial \eta} \\ \frac{\partial r}{\partial \xi} & \frac{\partial r}{\partial \eta} \end{pmatrix}, \tag{2.5}$$

and computed at the PIC mesh nodes by the PIC mesh generator through second order finite difference (FD) schemes. The bilinear interpolation function of Eq. (2.1) is used to obtain the value $\mathcal{J}_I^{(k-1)}$ in Eq. (2.4) at the position $\boldsymbol{\xi}^{(k-1)}$.

The weighting nodal volumes associated to each PIC mesh node used by the volumetric weighting schemes explained in Sec. 2.2.5.2 are computed according to Ref. [69]. The j^{th} mesh node with computational coordinates $\boldsymbol{\xi}_j = (\xi_j, \eta_j)$ has a weighting volume

$$\Delta V_j = \iint_{\mathrm{ROI}} 2\pi r(\xi, \eta) S_j(\xi, \eta) |\mathcal{J}(\xi, \eta)| d\xi d\eta, \tag{2.6}$$

where $S_j(\xi, \eta)$ is the nodal bilinear shape function defined in Eq. (2.1), $|\mathcal{J}(\xi, \eta)|$ is the determinant of the Jacobian matrix of Eq. (2.5), and the integral is performed in the computational domain in the node Region Of Influence (ROI) according to the nodal shape function S_j. The radial coordinate $r(\xi, \eta)$ and the Jacobian $\mathcal{J}(\xi, \eta)$ are expressed in terms of the shape function S_j considering their known values at the nodes.

Surface type	**Effects on ions**	**Effects on neutrals**
Transparent	None	None
Material wall	Recombination	Specular/diffuse reflection with a given probability of specular reflection p_{spec}
Free loss	Removal	Removal
Injection	Stochastic injection	Stochastic injection

Table 2.1: PIC mesh surface elements types and IDs and corresponding effects on macroparticles.

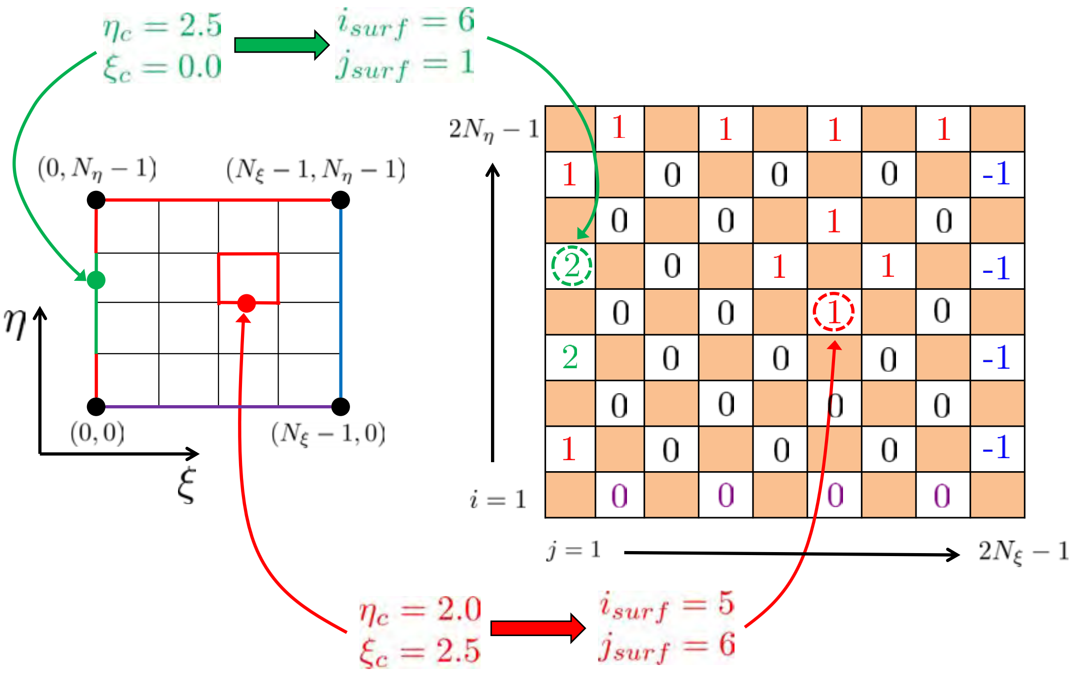

Figure 2.5: PIC mesh surface elements indexing logic. The free loss (blue), material wall (red), injection (green) and transparent (black) surface elements have ID equal to -1, 1, 2 and 0, respectively. The purple surface elements are those at the symmetry axis at $r = 0$, which are also transparent for the macroparticles (see Sec. 2.2.4.1). The shaded matrix elements identify those non-existing surface elements acording to their indexation in Eq. (2.7).

A new capability of the hybrid simulator is the possibility of including active inner surfaces in the simulation domain. Such surfaces can inject a propellant mass flow with given properties into the domain as part of an injection boundary (see Sec. 2.2.5.1.1), collect ions recombining them into neutrals to be reinjected in the simulation domain or reflect neutrals impinging on them (see Sec. 2.2.5.1.2). The PIC mesh surface elements are defined as the lines between two consecutive nodes along ξ and η coordinates. Thus, they correspond to the PIC mesh cell faces. The structured mesh allows to identify each

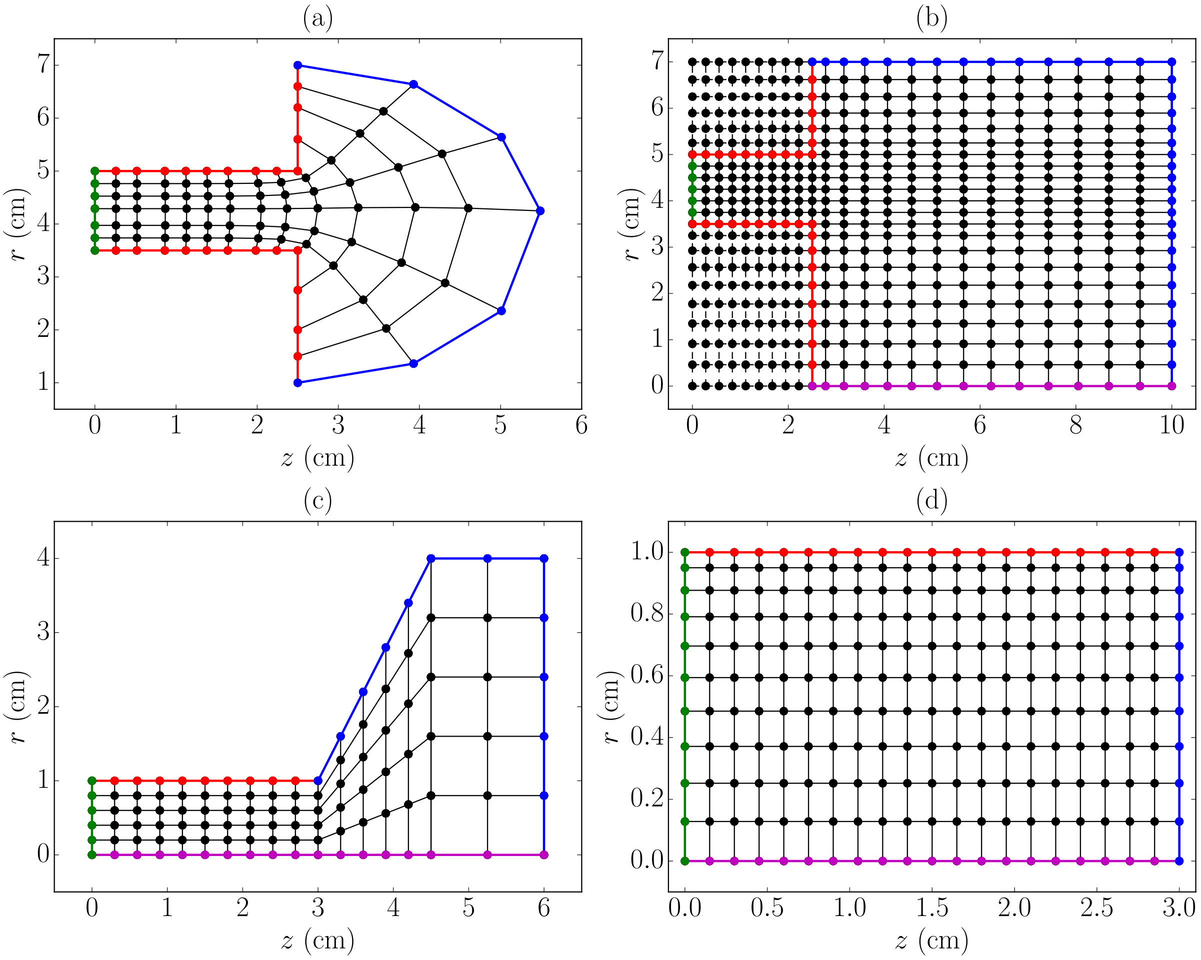

Figure 2.6: Sketch of (a) a typical HET PIC mesh used in HPHall-2 and HallMA, and (b)-(d) HET, HPT and cylindrical PIC meshes obtained with the new PIC mesh generator, respectively. The red, green, blue and magenta lines indicate the material wall, injection, free loss and symmetry axis at $r = 0$ boundaries, respectively. In (b), the ghost nodes of the mesh are those located out of the material wall boundaries, plotted with dashed lines.

surface element with a set of two indices as

$$\begin{aligned} i_{surf} &= 2\eta_c + 1, \\ j_{surf} &= 2\xi_c + 1, \end{aligned} \tag{2.7}$$

where matrix indices start at 1 following Fortran convention and (ξ_c, η_c) are the computational coordinates of the surface element central point. Thus, as shown in Fig. 2.5, a 2D matrix stores an ID flag that indicates the surface element type and thus determines how it interacts with with simulation particles. The different surface elements considered are listed in Tab. 2.1. Additionally, some other properties such as the surface elements area and its normal and tangential versors are stored into matrices following the same logic thus optimizing the memory access. The surface elements area take into account the complete 3D cylindrical surface represented by each 2D PIC mesh surface element.

Fig. 2.6(a) shows a typical structured PIC mesh used in previous legacy codes such as HPHall [44] and its later improved versions such as HPHall-2 [45] or HallMA [46]. Those meshes were generated with Tecplot 10.0 and usually contained some highly deformed mesh cells, especially at the corners of the chamber exit plane. Besides, given the simulation domain geometry, it was imposible to simulate the symmetry axis at $r = 0$. On the contrary, as shown in Figs. 2.6(b)-(d), the new PIC mesh generator enables the simulation of the symmetry axis in HET-like, HPT-like and cylindrical domains, producing meshes with reduced cell deformation, thus improving PIC derived statistics. As shown in Figs. 2.6(b) and 2.6(d), the mesh resolution near the material walls can be increased through an exponential node distribution. Moreover, in case of HET-like and HPT-like domains, a different number of nodes along the radial and axial directions can be considered in the chamber and in the thruster near plume regions, so that the spatial resolution in both zones above is decoupled. Therefore, the mesh generator is able to produce optimized meshes of the prescribed simulation domain, featuring a higher spatial resolution inside the chamber than in the near plume. This ensures a better reconstruction of the generally steeper spatial gradients of the differents plasma magnitudes inside the thruster chamber. On the other hand, it helps keeping a higher number of particles per cell along the plume expansion, thus limiting the PIC statistical noise and the computational cost while still reproducing satisfactorily the plasma gradients there.

Taking advantage of the surface element indexation commented above, it basically defines the material wall boundary [red lines on Figs. 2.6(b)-(d)] by setting the corresponding surface elements ID flags in the surface element matrix. Ghost nodes and cells [plotted with black dashed lines in Fig. 2.6(b)] are needed in order to keep the mesh structured while minimizing cell deformation, and are properly identified so that they are not considered by any CORE unit algorithm.

2.2.2 The electric field reconstruction

The integration of the macroparticles trajectory requires the knowledge of the electric field at the PIC mesh nodes. A common approach in HET simulations [44, 70–72] is to neglect the plasma self-induced magnetic field with respect to the dominant, stationary, externally applied magnetic field. Therefore, according to Maxwell equations, the self-adjusted electric field is irrotational and thus may be written as

$$\boldsymbol{E} = -\nabla\phi, \tag{2.8}$$

where ϕ is the electric potential. In HYPHEN, ϕ is computed by the electron module at the MFAM and is later interpolated to the PIC mesh nodes. The electric field is thus reconstructed at the PIC mesh nodes through the computation of the spatial gradient of Eq. (2.8). The arc parameter variables l_η and l_ξ introduced in Ref. [72] are considered to improve the accuracy of the spatial gradient reconstruction in general non-uniform structured meshes. These variables measure the physical distance when going along each curve $\eta =$ const and $\xi =$ const, respectively, and constitute a set of curvilinear coordinates. The Jacobian matrix $\mathcal{J}_l$ of the transformation $\{z, r\} = \{z(l_\eta, l_\xi), r(l_\eta, l_\xi)\}$ is given by

$$\mathcal{J}_l = \frac{\partial(z,r)}{\partial(l_\eta, l_\xi)} = \begin{pmatrix} \frac{\partial z}{\partial l_\eta} & \frac{\partial z}{\partial l_\xi} \\ \frac{\partial r}{\partial l_\eta} & \frac{\partial r}{\partial l_\xi} \end{pmatrix}, \tag{2.9}$$

Considering $\phi(z(l\eta, l_\xi), r(l\eta, l_\xi))$ and applying the chain rule in Eq. (2.8), the electric field at the PIC mesh nodes is obtained as

$$\begin{pmatrix} E_z \\ E_r \end{pmatrix} = -\left(\mathcal{J}_l^{-1}\right)^T \begin{pmatrix} \frac{\partial \phi}{\partial l_\eta} \\ \frac{\partial \phi}{\partial l_\xi} \end{pmatrix} \tag{2.10}$$

The matrix $\mathcal{J}_l$ is calculated by the PIC mesh generator at the PIC mesh nodes. Second order FD schemes are used for its computation and for the derivatives $\partial\phi/\partial l_k$ with $k = \eta, \xi$. It is worth mentioning that in case of uniform PIC meshes the approach below coincides with that using the computational coordinates (ξ, η) (see Ref. [52] for 3D domains), so that

$$\begin{pmatrix} E_z \\ E_r \end{pmatrix} = -\left(\mathcal{J}_I\right)^T \begin{pmatrix} \frac{\partial \phi}{\partial \xi} \\ \frac{\partial \phi}{\partial \eta} \end{pmatrix} \tag{2.11}$$

An example of the performance of both approaches above can be found in Sec. A.1.

2.2.3 The PIC model overall structure

The different tasks carried out by the PIC model every simulation timestep may be classified into *particle-wise* and *mesh-element-wise* algorithms. The particle-wise algorithms, detailed in Sec. 2.2.4, are applied to every single simulated macroparticle and include:

- Interpolation of electric and magnetic fields to the macroparticle position (only performed for ions).
- Macroparticle trajectory integration and update of its velocity and position.
- Check for crosses with the PIC mesh surface elements.
- Macroparticle sorting to the PIC mesh cells.
- Removal of those macroparticles that have left the simulation domain.

The mesh-element-wise algorithms, explained in detail in Sec. 2.2.5, are evaluated for each PIC mesh element (volume cell or surface element) and involve:

- Collisions simulation through Monte Carlo Collision (MCC) or Direct Simulation Monte Carlo (DSMC) approaches.
- Surface interaction between macroparticles and surface elements. This includes the simulation of the effects on the macroparticles (injection of new particles, ion recombination and neutral reinjection and reflection), and the surface weighting of the emitted or hitting macroparticles in order to update their related macroscopic magnitudes at the corresponding surface elements.
- Volumetric weighting of sorted macroparticles to obtain the required macroscopic magnitudes of the simulated heavy species at the mesh nodes.

- Boundary correction tasks including the Bohm condition forcing algorithm at material wall surfaces and the interpolation of surface weighted magnitudes from the boundary surface elements (cell faces centers) to the corresponding mesh nodes.
- Population control of the simulated heavy species to maintain the number of macroparticles per cell within a specified interval in stationary conditions.

Fig. 2.7 shows a scheme of the ion module loop. F_s represents the distribution function of the s^{th} particle population (ion or neutral) or equivalently a list storing all necessary macroparticles data such as their computational, 2D physical and 3D physical position, velocity and weight (here represented by $\boldsymbol{\xi}_p$, $\boldsymbol{r}_p$, $\boldsymbol{x}_p$, $\boldsymbol{v}_p$ and W_p, respectively, for the p^{th} macroparticle). The ion and neutral macroparticles are grouped into different populations (or particle lists), respectively, depending on their atomic mass m, which determines the atomic species, their charge number Z (singly and doubly charged ions have $Z = 1$ and $Z = 2$, respectively, while neutrals have $Z = 0$) and their origin or energy content (e.g. slow ions or fast neutrals resulting from a CEX collision)[1]. This subdivision of the different species facilitates the population control during the simulation and the treatment of the various particle collisions between different particle lists, thus contributing to reduce the numerical noise in the PIC related statistics. Likewise, $F_s^{(hit)}$ and $F_s^{(rem)}$ are lists storing those macroparticles that have hit a non-transparent surface element and those ones to be removed due to collisional events, for the s^{th} population. The IDs of the particles contained in each PIC mesh cell are identified in a particle track Π_s, for the s^{th} population.

2.2.4 Particle-wise algorithms

Given the large number of macroparticles of a typical simulation ($\sim 10^5$-10^6), these algorithms are optimized in order to reduce the computational time.

2.2.4.1 Particle mover

The HYPHEN particle trajectory integrator is described in detail in Sec. 3.2.2 for the case of a plasma thruster plume simulation on a cylindrical mesh, and it is directly applicable to HET or HPT simulations featuring the non-uniform PIC meshes shown in Fig. 2.6. HYPHEN uses the 3D Cartesian leap-frog algorithm implemented in EP2PLUS [52] for advancing every integration (or PIC) timestep Δt the 3D Cartesian particle velocity $\boldsymbol{v} = (v_x, v_y, v_z)$ and position $\boldsymbol{x} = (x, y, z)$, by solving Newton equation considering the electromagnetic force acting on every particle.

As indicated in Sec. 3.2.2, before weighting every particle to the PIC mesh (see Secs. 2.2.5.1.3 and 2.2.5.2), its 2D axisymmetric position $\boldsymbol{r} = (z, r)$ at the plane Ω_0 is obtained and its particle velocity is rotated to Ω_0 an angle given by $\cos\theta = x/r$ and $\sin\theta = y/r$, with $r = \sqrt{x^2 + y^2}$. The particle computational coordinates $\boldsymbol{\xi} = (\xi, \eta)$ are then computed for particle sorting and weighting purposes as indicated in Sec. 2.2.1.

In order to maintain the stability of the integration scheme, un upper threshold is set to the integration (or PIC) timestep Δt. Actually, in full-PIC codes, the most restrictive condition on Δt between the following is applied [22, 33, 36, 37, 73, 74]:

---

[1] In the following the terms *population* and *species* shall be both used indistinguishably to refer to a given particle list.

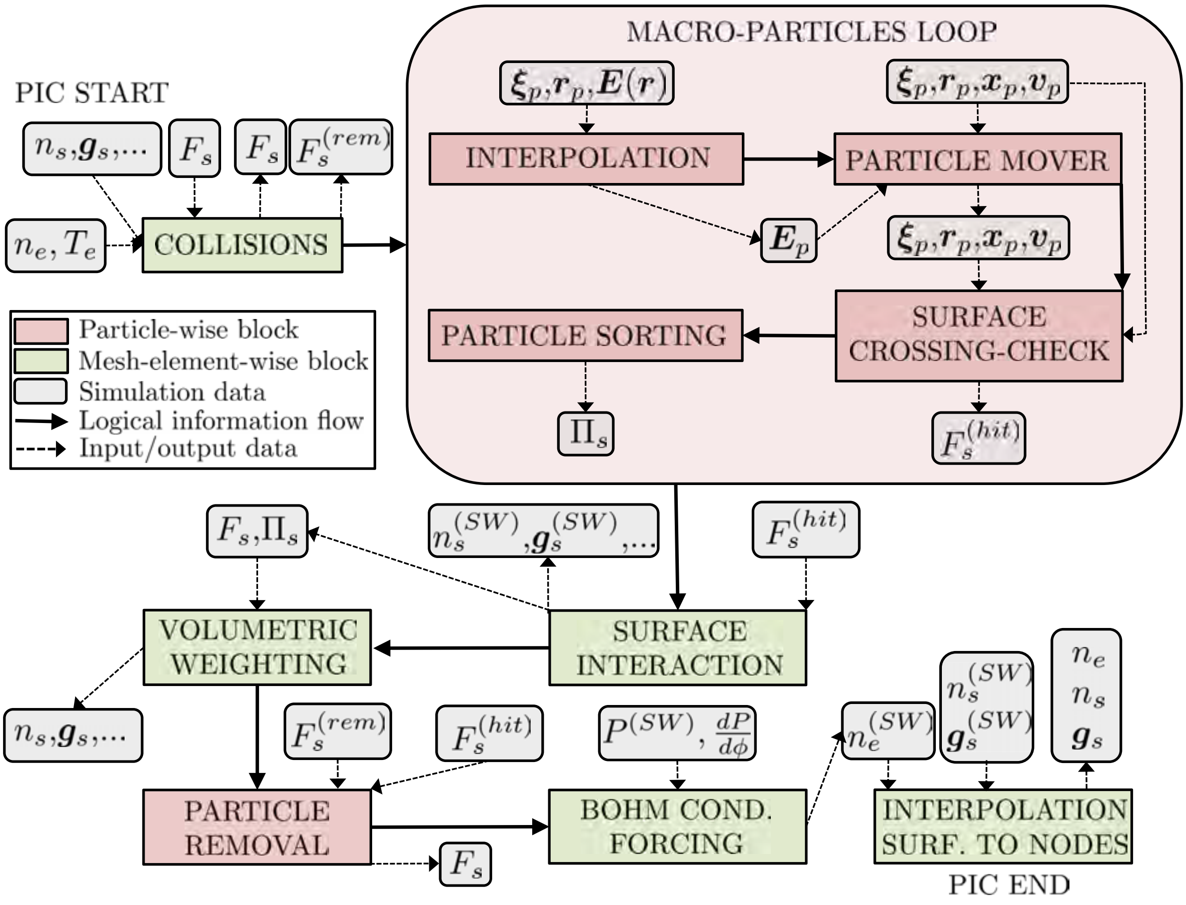

Figure 2.7: PIC model loop.

- The Courant-Friedrichs-Lewy (CFL) condition on the wave propagation $c\Delta t < \Delta x$, c being the speed of light, and Δx the grid size.
- The CFL condition on crossing less than one cell $v\Delta t < \Delta x$, with v the maximum particle velocity.
- The gyromotion condition $\omega_B \Delta t < 0.35$, where ω_B is the cyclotron frequency.
- The condition for capturing plasma oscillations $\omega_{pe}\Delta t < 0.2$, with ω_{pe} the plasma frequency.
- The collisional processes condition $\Delta t \ll \Delta t_{coll}$, so that it is possible to decouple the collisionless motion of each macroparticle (obtained through the integration of the Newton equation considering the corresponding electromagnetic force acting on it, as explained in Sec. 3.2.2) from the collisional processes (between macroparticles and with the domain material boundaries), which are simulated as instantaneous events.

Except for the first condition above, all the others are checked in the full-PIC 1D radial code presented in Chapter 5. In HYPHEN, however, a fluid model is considered for the electron population, while the PIC segment deals with un-magnetized heavy populations (typical in HETs and HPTs, for example). Therefore, the most restrictive condition on the particles integration timestep is the second one above based on the fastest heavy particles (usually the ions). As mentioned in Sec. 3.3.1, a common approach consist on select the timestep so that, on average, the fastest macroparticle does not cross more than one cell every simulation loop. A test case validating the HYPHEN particle mover algorithm can be found in Sec. A.2.

2.2.4.2 Particle crossing check

After moving every particle, the crossing check algorithm detects those macroparticles that leave the domain crossing the PIC mesh boundary surfaces. Fig. 2.8 shows a scenario in which a given macroparticle crosses several PIC mesh cells (a very rare case if the timestep is low enough). The algorithm tracks the particle along its motion during the timestep identifying all those surface elements that the particle has crossed. The macroparticle is then collected at the first surface element found with ID different from zero (non-transparent), thus updating the corresponding particle hit list $F^{(hit)}$. After the macroparticles loop, the surface interaction algorithm performs the surface weighting of the exited particles contained on the updated hit lists (thus obtaining for example the particle outflows) and carries out the pertinant effects of the domain boundary on the macroparticles (see Sec. 2.2.5.1).

The crossing check algorithm makes the reasonable assumption (for low enough PIC timestep) of considering the particle trajectory in the 2D domain Ω_0 during the timestep as a straight line between the 2D initial and final particle positions $\boldsymbol{r}_0$ and $\boldsymbol{r}_1$, respectively (blue line on Fig. 2.8). Therefore, for each crossed cell (those whose lower left node is circled with a dashed orange line in Fig. 2.8), the crosses between the particle trajectory and the cell faces are obtained by computing the intersection points between two straight lines in the plane Ω_0. For each crossed cell, the crossing time with each cell face is computed as

$$\Delta t_{cross} = \left| \frac{\mathbf{1}_{\top} \cdot (\boldsymbol{r}_j - \boldsymbol{r}_0)}{\mathbf{1}_{\top} \cdot \boldsymbol{v}_{2D}} \right| \tag{2.12}$$

where $\boldsymbol{r}_j$ is the position vector of one of the nodes of the considered cell face, $\mathbf{1}_{\top}$ is the corresponding cell face normal versor and $\boldsymbol{v}_{2D} = (\boldsymbol{r}_1 - \boldsymbol{r}_0)/\Delta t$. The cell face crossed is that with minimum crossing time.

If the particle is collected at any non-transparent surface element, the corresponding hit list is updated with the hitting time within the PIC timestep Δt_{hit}, the 2D and 3D particle position at the hitting point $\boldsymbol{r}_{hit}$ and $\boldsymbol{x}_{hit}$, respectively (see Fig. 2.3), and the hitting particle velocity $\boldsymbol{v}_{hit}$, which coincides with the current 3D Cartesian particle velocity in the timestep (not to be confused with $\boldsymbol{v}_{2D}$). The particle crossing check algorithm has been validated through a dedicated test case which can be found in Sec. A.3.

2.2.4.3 Particle sorting

After the particle crossing check algorithm, a particle sorting algorithm is executed with the main purpose of assigning the existing macroparticles in the domain (those which have not been collected by a non-transparent surface element) to the PIC mesh cells where they are located, thus updating the corresponding particle track Π.

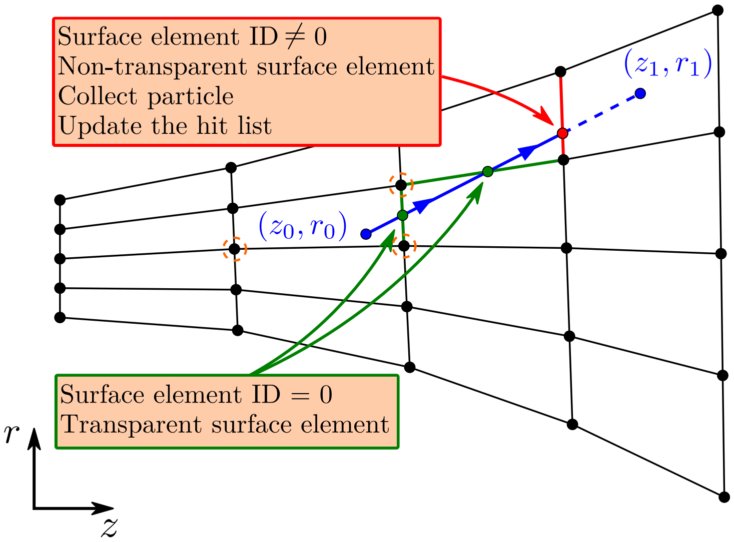

Figure 2.8: Particle crossing check algorithm. The points $\boldsymbol{r}_0 = (z_0, r_0)$ and $\boldsymbol{r}_1 = (z_1, r_1)$ represent the initial and final macroparticle position at plane Ω_0 at a given timestep. The different PIC mesh cell crossed are those whose lower left node is circled with a dashed orange line.

As already mentioned in Sec. 2.2.1, the cell containing the p^{th} macroparticle at a given simulation timestep is identified by its lower left mesh node indices $\boldsymbol{i}_0 = (i_0, j_0)$, obtained as

$$\begin{aligned} i_0 &= \text{floor}(\eta_p) + 1, \\ j_0 &= \text{floor}(\xi_p) + 1 \end{aligned} \tag{2.13}$$

where $\boldsymbol{\xi}_p = (\xi_p, \eta_p)$ are the particle computational coordinates (see Fig. 2.4) and matrix indices start from 1 according to Fortran convention.

2.2.5 Mesh element-wise algorithms

The algorithms hereinforth outlined perform its main operations following a cell-wise or a surface-element-wise loop.

2.2.5.1 Particle surface interaction

The particle surface interaction algorithm performs the injection of new macroparticles into the domain through the prescribed injection surfaces with given injection properties, carries out the effects that the domain boundary cause on the impinging macroparticles and updates the species macroscopic properties by surface weighting the hitting or emitted macroparticles to the boundary surfaces.

2.2.5.1.1 Particle injection

In the hybrid code, new particles are injected into the domain through dedicated injection surface elements (see Tab. 2.1). The injection properties, which can vary linearly across the injection surface elements, are provided at their corresponding nodes. At the current development stage of the code, a drifted Maxwellian injection of the corresponding species is performed, defined by the injected particle flux g_{inj}, the injection macroscopic velocity $\boldsymbol{u}_{inj}$ and the injection temperature T_{inj}. For each injection surface element and every simulation timestep, the injection algorithm basically determines the number of macroparticles to be injected of the given species and the particle weight, position and velocity with which are introduced in the simulation domain. The number of macroparticles of the corresponding species to be injected in the current timestep is obtained as

$$N_{inj} = \frac{\bar{g}_{inj} \Delta S \Delta t}{W_{gen}}, \tag{2.14}$$

where ΔS is the injection surface element area, Δt is the PIC timestep, $\bar{g}_{inj}$ is the mean injection flux at the injection surface element center and W_{gen} is the macroparticle generation weight in the corresponding cell (see Sec. 2.2.5.6). The injected macroparticles are uniformly distributed along the injection surface element. For a given injected macroparticle at position $\boldsymbol{r}_{inj}$, its macroparticle weight is obtained as

$$W_{inj} = \frac{g_{inj}(\boldsymbol{r}_{inj})}{\bar{g}_{inj}} W_{gen}, \tag{2.15}$$

where $g_{inj}(\boldsymbol{r}_{inj})$ is the actual injection particle flux interpolated to the particle injection position. Since the injected macroparticles are uniformly distributed along the injection surface element, an additional correction on the macroparticle weight is required to cancel out cylindrical effects. The generation weight in the cell is then considered as the mean injection weight at the center of the injection surface element, so that the actual injected macroparticle weight is

$$W_{inj}(\boldsymbol{r}_{inj}) = \frac{r_{inj}}{\bar{r}_{inj}} W_{inj}, \tag{2.16}$$

where r_{inj} is the random radial coordinate of the injected particle and $\bar{r}_{inj}$ is the radius of the injection surface element center.

Considering the values of the macroscopic injection velocity and temperature interpolated to the particle position $\boldsymbol{u}_{inj}(\boldsymbol{r}_{inj})$ and $T_{inj}(\boldsymbol{r}_{inj})$, respectively, the macroparticle injection velocity is obtained stochastically from a Maxwellian VDF following the algorithms of Ref. [38], and may be written as

$$\boldsymbol{v}_{inj} = v_{\top} \mathbf{1}_{\top} + v_{\parallel 1} \mathbf{1}_{\parallel 1} + v_{\parallel 2} \mathbf{1}_{\parallel 2}, \tag{2.17}$$

where the normal $v_{\top}$ and tangential components $v_{\parallel 1}$ and $v_{\parallel 2}$ to the surface element are obtained separately, with $\mathbf{1}_{\top}$, $\mathbf{1}_{\parallel 1}$ and $\mathbf{1}_{\parallel 2}$ the injection surface element normal and tangential versors (perpendicular to each other), respectively. On the one hand, the stochastic normal velocity component is computed applying the acceptance-rejection method considering a probability distribution function given by

$$f(v_{\top}) \propto v_{\top} \exp\left(-\frac{m(v_{\top} - u_{\top})^2}{2T_{inj}}\right), \tag{2.18}$$

where $u_{\top} = \mathbf{1}_{\top} \cdot \boldsymbol{u}_{inj}$ and the linear dependency with $v_{\top}$ indicates that particles from the injection reservoir with larger normal velocity to the injection surface are more likely to cross it and thus to be injected into the simulation domain in a given timestep. According to the acceptance-rejection method, a uniformly distributed random normal velocity $v_\top \sim U(v_{\top\,min}, v_{\top\,max})$ is then accepted only if a uniform random number $R \sim U(0,1)$ is lower or equal than than $\tilde{f}(v_\top)$. The minimum and a maximum particle normal velocity values $v_{\top min}$ and $v_{\top max}$ are computed as $u_\top \pm 4\sqrt{T_{inj}/m}$, where $v_{\top\,min} \geq 0$ (semi-Maxwellian injection from the surface element into the simulation domain), and $\tilde{f}(v_\top)$ is the normalized probability distribution function is defined as

$$\tilde{f}(v_\top) = \frac{f(v_\top)}{f(v_\top^*)}, \tag{2.19}$$

with $v_\top^*$ the normal velocity that maximizes Eq. (2.18):

$$v_\top^* = \frac{u_\top + \sqrt{u_\top^2 + 4T_{inj}/m}}{2}. \tag{2.20}$$

Once the normal particle velocity has been computed, the stochastic tangential velocity components are directly obtained from a 2D Maxwellian distribution with the injection properties. Therefore, the probability distribution function for the tangential velocity vector is given by

$$f(v_{\parallel 1}, v_{\parallel 2}) \propto \exp\left(\frac{-m\left[(v_{\parallel 1} - u_{\parallel 1}) + (v_{\parallel 2} - u_{\parallel 2})\right]^2}{2T_{inj}}\right), \tag{2.21}$$

which can be directly integrated and inverted as described in the Appendix C of Ref. [38]. Finally, a continuous injection is simulated by advancing each macroparticle along its injection velocity direction through a random fraction of the PIC timestep. A dedicated test of the injection algorithm performance can be found in Sec. A.5.

2.2.5.1.2 Surface interaction effects on impacting macroparticles

In general terms, the different effects that the domain boundary walls cause on the macroparticles depend on both the type of boundary wall and the type of macroparticle, and are outlined in Secs. 2.2.5.1.2.1-2.2.5.1.2.4.

2.2.5.1.2.1 Axis $r = 0$

Particles suffer specular reflection when crossing the axis $r = 0$ in the 2D domain Ω_0, which takes place naturally since a 3D Cartesian particle mover is implemented (see Secs. 2.2.4.1 and 3.2.2).

2.2.5.1.2.2 Free loss surface

Macroparticles are simply removed from the simulation domain when crossing a free loss boundary.

2.2.5.1.2.3 Injection surface

Ion and neutral macroparticles collected at an injection surface from the plasma are reinjected as neutrals of the corresponding propellant. Therefore, all impacted ions are recombined and reemited as neutrals with the corresponding injection properties (see Sec. 2.2.5.1.1).

2.2.5.1.2.4 Material wall surface

At the material walls of the simulation domain, ions are recombined into neutrals which are diffusely reinjected from the wall into the domain, while the neutrals may suffer either a specular or diffuse reflection, p_{spec} being the specular reflection probability [38] (see Tab. 2.1). The neutral specular reflection is performed simply by inverting the surface normal velocity component of the macroparticle:

$$\boldsymbol{v}_{spec} = \boldsymbol{v}_{hit} + 2(\boldsymbol{v}_{hit} \cdot \mathbf{1}_{\top hit})\mathbf{1}_{\top hit} \tag{2.22}$$

where $\boldsymbol{v}_{hit}$ and $\boldsymbol{v}_{spec}$ are the 3D Cartesian particle velocities before and after the specular reflection and $\mathbf{1}_{\top hit}$ is the 3D Cartesian normal versor to the material wall surface element at the 3D Cartesian particle hitting point $\boldsymbol{x}_{hit}$, stored in the corresponding hit list by the particle crossing check algorithm (see Sec. 2.2.4.2). Considering the axisymmetric domain, this last versor is obtained by rotating the corresponding 2D normal versor at the plane Ω_0 an angle given by $\cos(\theta_{hit}) = x_{hit}/r_{hit}$ and $\sin(\theta_{hit}) = y_{hit}/r_{hit}$ (see Fig. 2.3). The particle position after the specular reflection is

$$\boldsymbol{x}_{spec} = \boldsymbol{x}_{hit} + \boldsymbol{v}_{spec}\delta t_{spec} \tag{2.23}$$

where $\delta t_{spec} = \Delta t - \Delta t_{cross}$, with Δt_{cross} given by Eq. (2.12).

Regarding the neutral diffuse emission from the walls due to both the neutral diffuse reflection and the ion recombination, a semi-Maxwellian reinjection from the wall is performed by applying the injection algorithm explained in Sec. 2.2.5.1.1 but with $\boldsymbol{u}_{inj} = 0$, and $T_{inj} = \bar{E}_{reinj}/2$ (thus equivalent to assuming a thermal cosine emission law for the injection probability distribution function), where

$$\bar{E}_{reinj} = 2T_W\alpha_W + (1-\alpha_W)\bar{E}_{imp} \tag{2.24}$$

is the reinjection mean energy, being T_W the wall temperature (in energy units), and α_W and $\bar{E}_{imp}$ are, respectively, the wall accommodation coefficient [38], and the time-averaged wall-impact total energy (per elementary particle) of the impacting population on each case (the recombined ions or the diffusely reflected neutrals). The computation of this last quantity is detailed in Sec. 2.2.5.1.3.

In case of the ion recombination process, at every material surface element the total impacted ion mass Δm_{reinj} is computed. If W_{gen} and m are, respectively, the corresponding generation weight for the recombined neutrals (see Sec. 2.2.5.6) and their elementary mass, two possible scenarios are considered: if $mW_{gen} \leq \Delta m_{reinj}$, a number of neutrals $N_{reinj} = \mathrm{int}(\Delta m_{reinj}/mW_{gen})$ are reinjected from the surface element and the value Δm_{reinj} is reduced accordingly and kept for next steps; otherwise, Δm_{reinj} is kept for next steps. Additionally, if the number of reinjected neutrals in the cell is below the prescribed minimum during a number of steps N_k, then the total stored mass Δm_{reinj} is reinjected divided into the necessary number of neutrals to reach the target number of neutrals per cell. This approach is similar to that implemented in previous codes such as HallMA [46, 71, 72], HPHall-2 [45, 70] and HPHall [44], but with the advantage of conserving mass instantaneously (and not only on average). As in the case of the injection of new particles in the simulation domain (see Sec. 2.2.5.1.2.3), the reinjected neutrals are uniformly distributed along the corresponding surface element and their macroparticle weight is corrected according to Eq. (2.16) to cancel out cylindrical effects.

The ion recombination and neutral specualar and diffuse reflection algorithms have been validated through a dedicated test outlined in Sec. A.7.

2.2.5.1.3 Particle surface weighting

Extended Surface Weighting (ESW) algorithms were introduced in Refs. [75, 76] and provide more accurate macroscopic magnitudes than the conventional volumetric weighting at the domain material wall boundary. Every simulation timestep, not only the hitting macroparticles (stored in the dedicated hit lists $F^{(hit)}$) but also all those injected or reflected ones are weighted to the central point of the corresponding boundary surface elements applying zeroth-order surface weighting schemes. As already commented on section 2.2.4.1, the macroparticles are rotated to the plane Ω_0 before being weighted to the PIC mesh surface elements so that all surface weighted magnitudes are computed at that plane. Considering the j^{th} PIC mesh surface element and a given particle population, the particle density, the particle flux vector and the particle momentum flux vector, which may be used to compute the thrust, are computed at its central point as

$$n_j^{(SW)} = \frac{1}{\Delta t \Delta S_j} \sum_p \frac{W_p}{v_{\top p}}, \tag{2.25}$$

$$\boldsymbol{g}_j^{(SW)} = \frac{1}{\Delta t \Delta S_j} \sum_p \boldsymbol{v}_p \frac{W_p}{v_{\top p}}, \tag{2.26}$$

$$\dot{\boldsymbol{p}}_j^{(SW)} = \frac{1}{\Delta t \Delta S_j} \sum_p m_p \boldsymbol{v}_p W_p. \tag{2.27}$$

where ΔS_j is the surface element area and m_p, W_p and $v_{\top p}$ stand for the elementary mass, the weight and the magnitude (i.e. absolute value) of the normal velocity to the surface element of the p^{th} macroparticle, respectively. The sum in p is for the particles crossing the surface element in any direction (i.e. hitting, injected or reflected) in the current timestep. Omitting the subindex j, additional macroscopic magnitudes of interest are the normal particle and energy outfluxes $g_{imp}^{(SW)}$ and $e_{imp}^{(SW)}$, respectively (only accounting for the hitting particles from the bulk plasma):

$$g_{imp}^{(SW)} = \frac{1}{\Delta t \Delta S} \sum_p W_p, \tag{2.28}$$

$$e_{imp}^{(SW)} = \frac{1}{\Delta t \Delta S} \sum_p E_{imp,p} W_p. \tag{2.29}$$

with $E_{imp,p}$ the wall-impact energy per elementary particle of the p^{th} macroparticle. For neutral particles, this energy coincides with the particle kinetic energy at the hitting point.

However, at the material boundaries, the sheath potential fall $\Delta\phi_{sh}$ (see Sec. 2.3.7.1) and the Bohm condition potential drop $\Delta\phi_{BC}$ (see Sec. 2.2.5.4) must be included for all the ion populations considered, so that

$$E_{imp,p} = \frac{1}{2} m_p v_p^2 + eZ_p(\Delta\phi_{sh} + \Delta\phi_{BC}), \tag{2.30}$$

where Z_p is the charge number of the p^{th} macroparticle. Finally, it is worth noting that for an ion macroparticle to hit the material wall it is necessary that

$$E_{\top Q} + eZ\Delta\phi_{sh} > 0, \tag{2.31}$$

where $E_{\top Q}$ represents its kinetic energy (per elementary particle) perpendicular to the sheath edge Q, and $\Delta\phi_{sh} \equiv \phi_Q - \phi_W$, with ϕ_Q and ϕ_W the sheath edge and wall potentials, respectively.

In order to reduce the statistical noise, a time-extended (i.e. time-averaged) version of the above magnitudes is considered. Therefore, similarly to Eq. 2.25, the ESW particle density at the j^{th} PIC mesh surface element is defined as

$$n_j^{(ESW)} = \frac{1}{N_k \Delta t \Delta S_j} \sum_k \sum_p \frac{W_p}{v_{\top p}}, \tag{2.32}$$

where now the sum in k is for the last N_k simulation timesteps[2]. In order to optimize the memory storage, the following time-averaging scheme is used (again j subindex is dropped for simplicity):

$$\bar{n}^{(k)}_{(ESW)} = \frac{\bar{n}^{(k-1)}_{(ESW)}(N_k - 1) + n^{(k)}_{(SW)}}{N_k}, \tag{2.33}$$

The time-averaging scheme of Eq. (2.33) tends to the moving average based on N_k timesteps as $N_k \to \infty$ while avoiding the storage of the last N_k simulation timesteps related data. It is applied for all the surface weighted variables defined above, so that the time-averaged wall impact energy in Eq (2.24) is computed as

$$\bar{E}_{imp} = \frac{\bar{e}^{(ESW)}_{imp}}{\bar{g}^{(ESW)}_{imp}}. \tag{2.34}$$

A test of the HYPHEN surface weighting algorithm performance can be found in Sec. A.6.

2.2.5.2 Particle volumetric weighting

The volumetric particle weighting algorithm implemented in HYPHEN is detailed in Sec. 3.2.3. Similarly to the case of the particle surface weighting, and as already commented on section 2.2.4.1, the macroparticles are rotated to the plane Ω_0 before obtaining all the weighted variables at the PIC mesh nodes. A dedicated test case validating the particle volumetric weighting algorithm can be found in Sec. A.4.

---

[2] An analogous approach for the volumetric weighting variables is described in Chapter 5.

2.2.5.3 Particle collisions

The collisional processes involving the heavy species are treated in HYPHEN at the beginning of every simulation timestep (see Fig. 2.7). The different collisions modeled are:

- Single and double ionization collisions, which are essential for the plasma generation inside the thrusters chamber:

$$A + e \rightarrow A^{+} + 2e \tag{2.35}$$

$$A + e \rightarrow A^{++} + 3e \tag{2.36}$$

$$A^{+} + e \rightarrow A^{++} + 2e \tag{2.37}$$

- Symmetric CEX collisions, which are especially important in the thrusters plasma plume near region:

$$A^{+}(\text{fast}) \;+\; A(\text{slow}) \rightarrow A^{+}(\text{slow}) \;+\; A(\text{fast}) \tag{2.38}$$

$$A^{++}(\text{fast}) \;+\; A(\text{slow}) \rightarrow A^{++}(\text{slow}) \;+\; A(\text{fast}) \tag{2.39}$$

Due to their higher ionization energy and hence lower reaction rates, higher ionization degrees are very unlikely at the usual operation conditions of most plasma thrusters and thus have not been considered. Previous studies have shown that CEX dominates over the ion-neutral Momentum EXchange (MEX) collisions in the plasma plume scenarios of interest [77, 78]. Therefore, MEX collisions have not been included in the present code version. Regarding CEX, only the symmetric resonant reactions are considered since they have higher collisional cross sections than the asymmetric non-resonant reaction $\text{Xe}^{++}(\text{fast}) + \text{Xe}(\text{slow}) \rightarrow \text{Xe}^{+}(\text{fast}) + \text{Xe}^{+}(\text{slow})$ [39, 79, 80]. The momentum exchange is neglected and thus the CEX is modeled as an identity switch between the corresponding particles [81]. This assumption is a good approximation recovered by more complex ion-neutral collision models combining CEX and elastic Momentum EXchange collisions (MEX) [82]. A cell-wise particle collider algorithm performs all the collisions above. The validation tests of the collisional algorithms described in Secs. 2.2.5.3.1 and 2.2.5.3.2 can be found in Secs. A.8 and A.9, respectively.

2.2.5.3.1 Ionization collisions

Based on the particular method developed in HPHall [44], the approach implemented is described here for the case of the ionization process of Eq. (2.35). Considering a given PIC mesh cell, a deterministic sampling of the existing neutral macroparticles is performed so that all of them suffer the ionization collision. On a given timestep, the total mass of new singly charged ions to be generated in the cell is

$$\Delta m_i = m n_e n_n R_i(T_e) \Delta V \Delta t, \tag{2.40}$$

where m is the propellant atom mass, n_e and n_n are the plasma and neutral densities, respectively, $R_i(T_e)$ is the corresponding ionization rate evaluated at the cell center and ΔV is the cell physical volume. The ionization rate depends on the electron temperature

T_e according to the Drawin model [83] (Drawin and Bell [84] models are used for the ionization reactions of Eqs. (2.36) and (2.37), respectively). Similarly to the case of the neutral reinjection due to the ion recombination at the walls (see Sec. 2.2.5.1.2.4), the number of ion macroparticles to be generated in the cell is obtained as follows. If W_{gen} and m are, respectively, the corresponding output ion population generation weight in the cell (see Sec. 2.2.5.6) and its elementary mass, two possible scenarios are considered: if $mW_{gen} \leq \Delta m_i$, a number of ions $N_{ion} = \text{int}(\Delta m_i / mW_{gen})$ are generated in the cell and the value Δm_i is reduced accordingly and kept for next steps; otherwise, Δm_{ion} is kept for next steps. The ion macroparticles velocity is sampled from a Maxwellian distribution with the neutral mean velocity and temperature in the corresponding cell while particles positions are uniformly distributed within the cell. Their particle weights are affected by a cylindrical radial correction as that of Eq. (2.16). Finally, every neutral in the cell suffers a macroparticle weight reduction proportional to their current weight, so that the total neutral mass loss in the cell equals the actual generated ion mass $mN_{ion}W_{gen}$.

2.2.5.3.2 Charge-exchange collisions

The CEX collisions model incorporated in HYPHEN presents important improvements with respect to that of previous legacy codes such as HPHall-2 [45]. The new algorithm allows for a more accurate simulation of the CEX collisions effects on the heavy species macroscopic magnitudes not only in the thruster chamber, but also in its near plume. Moreover, it extends the code capabilities enabling HYPHEN to simulate plasma plumes, in which CEX collisions are essential for determining the backscattering ion flux impinging sensitive S/C surfaces [85, 86]. The CEX collisions algorithm implemented in HYPHEN shares most of its characteristics with that of EP2PLUS [52] and, as shown in Chapter 3, an excellent agreement has been found between both codes results in a benchmarking plasma plume simulation scenario.

The CEX collisions algorithm samples two input heavy populations (e.g. fast ions and slow neutrals) and generates the resulting macroparticles in two output populations (e.g. slow ions and fast neutrals) which may coincide or not with the input ones. Finally the input populations are updated accordingly. The different sampling/generation approaches are illustrated in Fig. 2.9 and detailed hereafter. Regarding the particle sampling phase, two approaches may be followed:

1. Direct Simulation Monte Carlo (DSMC) sampling: on every cell, input macroparticles pairs (e.g. one fast ion and one slow neutral) are sampled following an efficient DSMC method [38] so that a given pair collides if $R < p_c/p_c^{max}$, being $R \sim U(0,1)$ and p_c the pair collision probability

   $$p_c = \frac{1 - \exp\left(-\sigma_c(v_{rel}) n_n v_{rel} \Delta t\right)}{N_{n,cell}}, \tag{2.41}$$

   where $\sigma_c(v_{rel})$ is the collision cross section, which depends on the magnitude of the relative velocity between the two macroparticles of the pair $v_{rel} = |\boldsymbol{v}_i - \boldsymbol{v}_n|$ with $\boldsymbol{v}_i$ and $\boldsymbol{v}_n$ the velocities of the colliding ion and neutral particles, respectively, and n_n and $N_{n,cell}$ are the input neutral population particle density and number of macroparticles in cell, respectively. The number of possible input pairs undergoing

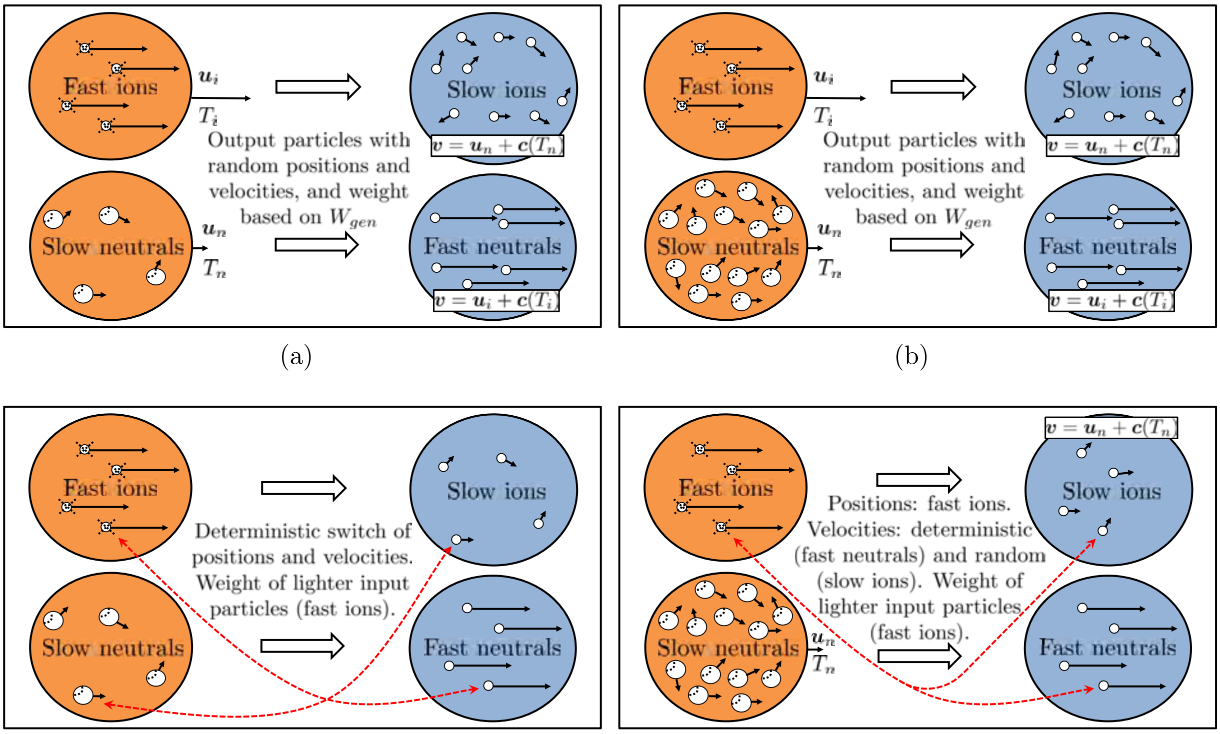

(a) (b)

(c) (d)

Figure 2.9: CEX collisions in a PIC mesh cell showing the sampling and updating of input species (left), and the output particles generation (right). The input fast ions undergoing the collision are removed from the simulation while the slow neutrals weights are reduced correspondingly. The random generation is shown in (a) for DSMC sampling and in (b) for MCC/deterministic sampling. Analogously, the deterministic generation is depicted in (c) for DSMC sampling and (d) for MCC/deterministic sampling. The values $\boldsymbol{c}(T_n)$ and $\boldsymbol{c}(T_i)$ represent thermal velocities of the output populations, depending on the temperature of the corresponding neutral on ion input population, respectively.

a collision in a given cell and timestep is limited to $p_c^{max} N_{i,cell} N_{n,cell}$ with $p_c^{max} = p_c(\{v_{rel}\sigma_c(v_{rel})\}_{max})$ and $N_{i,cell}$ the number of input ion macroparticles in cell.

2. Monte Carlo Collision (MCC)/deterministic sampling: in this case, all the neutrals in the cell are affected by the collision (as in case of ionization collisions), while for the ions, the probability of undergoing a collision with any of the neutrals in the cell is

$$p_c = 1 - \exp\left(-\sigma(v_{rel}) n_n v_{rel} \Delta t\right), \tag{2.42}$$

where $v_{rel} = |\boldsymbol{v}_i - \boldsymbol{u}_n|$, with $\boldsymbol{v}_i$ the ion velocity and $\boldsymbol{u}_n$ the average macroscopic velocity of the input neutral population in the cell (i.e. at the cell center).

The CEX cross section $\sigma_c(v_{rel})$ is taken from Miller's model for Xenon gas [79]. The collision output particles generation can also follow two different approaches:

1. Random generation: the output particles of each output population are generated following a similar approach to that explained in Sec. 2.2.5.3.1 for the ionization collisions. In this case, the total sampled mass undergoing the collision in the cell Δm_{coll} is generated for each output species. The particles velocity are sampled

from a local Maxwellian distribution with the mean velocity and temperature of the corresponding input population in the cell. Therefore, the slow ions have the fluid velocity and temperature of the input slow neutrals, while the fast neutrals feature the fluid properties of the fast input ions. This scenario is depicted in Figs. 2.9(a) and 2.9(b) for DSMC and MCC/deterministic sampling of the input species, respectively. Although the linear momentum and energy are only conserved on average, this approach permits controlling the number of particles in cell of the output populations through the generation weight (see Sec. 2.2.5.6).

2. Deterministic generation: if DSMC sampling is applied for the input populations, as shown in Fig. 2.9(c), the output particles of each output population have the exact position and velocities of the sampled macroparticles of their corresponding input populations. Therefore, slow ions feature the positions and velocities of the sampled slow neutrals, while fast neutrals have the positions and velocities of the sampled fast ions. Regarding their weights, both the slow ion and fast neutral generated from every colliding input pair have the weight of the sampled ion macroparticle (tipically the lighter). Although the number of macroparticles cannot be actively controlled, this approach permits the exact conservation of the linear momentum and energy of the macroparticles. If, on the other hand, as depicted in Fig. 2.9(d), the slow neutrals input population is deterministically sampled (in the MCC/deterministic approach), both the output slow ions and fast neutrals are generated at the positions and with the weights of the sampled fast ions. However, in this case, while the fast neutrals feature the velocities of the fast ions, the slow ions velocity is taken from a local Maxwellian distribution with the fluid properties of the slow neutrals population in the cell.

After generating the output particles, the input populations are updated according to the sampling type. If DSMC sampling has been selected, the weight of the heavier particle of each input pair is reduced by an amount equal to that of the lighter one, while the lighter macroparticle is removed from the simulation thus ensuring mass conservation. In order to prevent the generation of too small macroparticles while conserving mass on average, an acceptance-rejection method removes the heavier particle when the input pair have very similar weights. On the other hand, when MCC/deterministic sampling is applied, the sampled fast ions are simply removed from the simulation while the weights of all slow neutrals in the cell are reduced proportionally to their current values with a total mass reduction equal to the sampled (i.e. generated) mass Δm_{coll}.

2.2.5.4 Kinetic Bohm condition forcing algorithm

Due to the different inertia of electrons and ions in a quasineutral plasma, an ion-attracting sheath with extension of several Debye leghts develops at the boundary between the plasma and a given absorbing boundary wall [87–89]. In typical cases (those considered in the hybrid simulator), the sheath is quasiplanar, quasisteady, collisionless and unmagnetized. If ϕ_Q and ϕ_W are the electric potential at sheath edge and wall, respectively, for the stable existance of such sheath with $\Delta\phi_{sh} = \phi_Q - \phi_W > 0$, the ions must satisfy the Kinetic Bohm Condition (KBC) at the sheath edge [75, 76, 90–92]

$$P \equiv \sum_{s=1}^{N_i} \int_0^{\infty} \left(\frac{Z_s}{T_e} - \frac{Z_s^2}{m_s v_\top^2} \right) F_s(v_\top) dv_\top \geq 0, \tag{2.43}$$

where N_i is the total number of wall-attracted ion populations, $v_\top$ is the ions particle velocity perpendicular to the sheath edge (i.e. perpendicular to the wall), T_e is the electron temperature at the sheath edge, and m_s, Z_s and F_s are the mass, charge number and distribution function at the sheath edge (integrated over parallel velocities) of the s$^{\text{th}}$ wall-attracted ion population, respectively. Using the ESW schemes the equivalent PIC version of Eq. (2.43) is

$$P \equiv \frac{1}{N_k \Delta t \Delta S} \sum_k \sum_p \left(\frac{Z_p}{T_e} - \frac{Z_p^2}{m_p v_{\top p}^2} \right) \frac{W_p}{v_{\top p}} \geq 0, \tag{2.44}$$

where the sum in p extends to all wall-attracted ion macroparticles.

The ion supersonic conditions implicitly imposed by Eqs. (2.43) and (2.44) are not automatically met at the domain boundaries of quasineutral hybrid PIC-fluid codes for usual PIC mesh sizes and standard linear weighting algorithms. Since in the quasineutral scale the sheaths are surface discontinuities (the HYPHEN simulation domain for both the PIC and the electron-fluid segments extends up to the sheath edge), provided that the KBC is satisfied and the sheath existence is assured, the interest is more on the sheath jump conditions (i.e the potential fall through the sheath and the energy fluxes deposited to the walls) than on the sheath inner structure. In HYPHEN, the Kinetic Bohm Forcing (KBF) algorithm proposed in Ref. [76] is applied. The quantity P in Eq. (2.44) is computed on every PIC mesh material wall surface element applying the ESW schemes described in Sec. 2.2.5.1.3. Whenever $P < 0$, a thin collisionless Bohm condition forcing layer is included with a potential fall $\Delta\phi_{BC} \geq 0$ that imposes

$$P(\Delta\phi_{BC}) = \frac{1}{N_k \Delta t \Delta S} \sum_k \sum_p \left(\frac{Z_p}{T_e} - \frac{Z_p^2}{m_p v_{\top p}^2(\Delta\phi_{BC})} \right) \frac{W_p}{v_{\top p}(\Delta\phi_{BC})} = 0, \tag{2.45}$$

where

$$v_{\top p}^2(\Delta\phi_{BC}) = v_{\top p}^2(\Delta\phi_{BC} = 0) + \frac{2eZ_p\Delta\phi_{BC}}{m_p}. \tag{2.46}$$

The value $\Delta\phi_{BC}$ is obtained by linearizing Eq. 2.45 under the assumption $e\Delta\phi_{BC} \ll T_e$. The plasma density at the sheath edge (obtained at the wall material boundary through the ESW algorithm) is then reduced accordingly in order to adapt the electric potential and satisfy the KBC at the sheath edge increasing the ion perpendicular velocity to the wall. It is worth mentioning that the correction above is not applied when $P > 0$ in Eq. 2.44, and that the value $\Delta\phi_{BC}$ tends to zero in stationary conditions as shown in Ref. [76].

The corresponding KBF algorithm HYPHEN validation test can be found in Sec. A.12.

2.2.5.5 Interpolation from surface elements centers to mesh nodes

The surface weighted variables such as the particle density (modified by the Bohm correction algorithm if necessary) and fluxes are interpolated from the PIC mesh surface elements where they are computed to its corresponding PIC mesh nodes. This operation is performed in order to make these variables visible for all the PIC mesh cell algorithms, and also for the simple polytropic electron-fluid closure described in Sec. 3.2, which takes as inputs the quasineutral plasma density at the PIC mesh nodes.

Every boundary node belongs to up to two material surface elements. The nodal values are obtained as the average of the surface weighted properties of the corresponding surface elements sharing the node. For example, after the KBF algorithm, the corrected plasma density is obtained at the corresponding boundary PIC mesh nodes as

$$n_e = \frac{1}{N_F} \sum_{f}^{N_F} \bar{n}_{ef}^{(SW)} \tag{2.47}$$

where N_F is the number of surface elements affecting every PIC mesh node and $\bar{n}_{ef}^{(SW)}$ is the corrected plasma density at the center of the f^{th} surface element above.

2.2.5.6 Population control

In order to improve the PIC-derived statistics and reduce its associated noise, a minimum number of macroparticles per cell of each simulated population is needed. On the other hand, this number must be below a given maximum so as to limit the computational time and memory required by the simulation. On each PIC mesh cell, the population control algorithm implemented in HYPHEN maintains the number of macroparticles in the cell of each simulated particle population within a specified range $[N_{min}, N_{max}]$ in stationary conditions while minimizing the macroparticle weights dispersion. Therefore, for each cell and particle population, whenever the number of macroparticles in the cell is out of the above range, it modifies the generation weight in the cell W_{gen} used by the surface interaction and collisional algorithms (see Secs. 2.2.5.1 and 2.2.5.3, respectively) as

$$W_{gen} = \overline{W} \frac{N_{cell}}{N_{tg}}, \tag{2.48}$$

where $N_{tg} \in [N_{min}, N_{max}]$ is the desired number of macroparticles in the cell and N_{cell} and $\overline{W}$ are the current number of macroparticles and time-averaged [according to the scheme in Eq. (2.33)] macroparticle weight in the cell, respectively. This algorithm makes N_{cell} tend asymptotically to the desired value N_{tg} in steady conditions in all those cells where there exists a relevant generation of new particles, (e.g. due to the injection or the different collisional processes). Thus, the generation weight represents the target value that a renormalization algorithm should consider when splitting or merging macroparticles in order to achieve the target number of particles in the cell. A minimum generation weight is also set per PIC mesh cell and population so that the generation of too many particles with negligible macroparticle weight is avoided.

A further analysis of the population control algorithm combined with the particle generation and distribution in 2D axisymmetric simulation domains is detailed in Sec. 3.2.4.

A dedicated test case validating the population control algorithm can be found in Sec. A.10.

2.3 A fluid electron model for HETs

As commented in Sec. 2.1.2, the HYPHEN electron-fluid module for HETs implemented by Pérez-Grande [59, 60] features an isotropic electron pressure tensor. Its name is NOMADS, standing for NOn-structured Magnetically Aligned plasma Discharge Simulator, and it closes the hybrid PIC-fluid code simulation loop by updating the electric potential and the electron population related variables from the knowledge of the different heavy species macroscopic magnitudes, and assuming quasineutrality. In this section, an improved model formulation is presented with the main purposes of identifying the role of the electron turbulence in the different model equations, and enabling a future treatment of the electron inertial effects. The main model improvements and contributions of the author of this Thesis are summarized in Sec. 2.3.8, which have been partially benefited from the work of J. Zhou in the context of his Thesis on a simulation code for HPTs [93].

2.3.1 The applied magnetic field

In HETs, the stationary externally applied magnetic field $\boldsymbol{B}$, which is generated by the thruster magnetic circuit, dominates over the much smaller magnetic field induced by the plasma discharge currents, which is generally neglected. Therefore, the magnetic field is not only solenoidal but also irrotational. Besides, considering an axisymmetric problem and a cylindrical orthonormal reference system $\{\mathbf{1}_r, \mathbf{1}_\theta, \mathbf{1}_z\}$, since the magnetic field is assumed to be longitudinal, i.e. $B_\theta = 0$, it is possible to define magnetic potential and stream functions satisfying

$$\frac{\partial \sigma}{\partial r} = B_r, \quad \frac{\partial \sigma}{\partial z} = B_z, \quad \frac{\partial \lambda}{\partial r} = -rB_z, \quad \frac{\partial \lambda}{\partial z} = rB_r, \tag{2.49}$$

where $\sigma(r,z)$ and $\lambda(r,z)$ are the magnetic potential and stream functions, respectively. It is well known that the magnetic field introduces a large anisotropy in the transport properties of electrons [1,89]. The associated numerical diffusion when solving the electron transport equations was quantified by Pérez-Grande *et al.* [66], showing that the use of a MFAM can greatly mitigate the induced numerical error. Therefore, a magnetic orthonormal reference system $\{\mathbf{1}_\parallel, \mathbf{1}_\theta, \mathbf{1}_\top\}$ is defined, so that

$$\mathbf{1}_\alpha = \frac{1}{h_\alpha}\frac{\partial \boldsymbol{x}}{\partial \alpha}, \quad h_\alpha \equiv \left|\frac{\partial \boldsymbol{x}}{\partial \alpha}\right|, \quad \alpha = \sigma, \theta, \lambda, \tag{2.50}$$

where $\boldsymbol{x} = \boldsymbol{x}(\sigma, \theta, \lambda)$ is a generic position vector in the magnetic reference system and $\mathbf{1}_\parallel$ and $\mathbf{1}_\top$ represent the versors along the magnetic field parallel and perpendicular directions in the plane Ω_0, respectively, defined as (see Fig. 2.10)

$$\mathbf{1}_\parallel \equiv \boldsymbol{B}/B = \mathbf{1}_r \cos\alpha_B - \mathbf{1}_z \sin\alpha_B, \quad \mathbf{1}_\top = \mathbf{1}_r \sin\alpha_B + \mathbf{1}_z \cos\alpha_B, \tag{2.51}$$

with $B \equiv |\boldsymbol{B}|$, α_B the local magnetic angle, and the magnetic reference system scale functions being

$$h_\sigma = \frac{1}{B}, \quad h_\theta = r, \quad h_\lambda = \frac{1}{rB}. \tag{2.52}$$

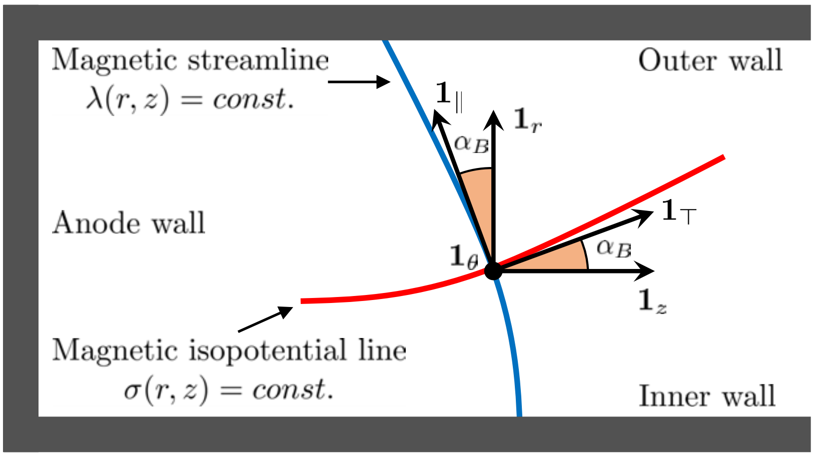

Figure 2.10: Magnetic reference system definition. A typical HET chamber is represented, including the chamber inner and outer walls and the anode wall.

Therefore, any vector field (e.g. the total plasma current $\boldsymbol{j}$) may be written in terms of its magnetic field parallel and perpendicular components as

$$\boldsymbol{j} = j_\parallel \mathbf{1}_\parallel + \boldsymbol{j}_\perp, \quad \boldsymbol{j}_\perp = j_\top \mathbf{1}_\top + j_\theta \mathbf{1}_\theta. \tag{2.53}$$

The derivatives of a scalar field (e.g. the electric potential ϕ) along each direction below are defined as

$$\frac{\partial \phi}{\partial \mathbf{1}_\parallel} = \frac{1}{h_\sigma}\frac{\partial \phi}{\partial \sigma}, \quad \frac{\partial \phi}{\partial \mathbf{1}_\theta} = \frac{1}{h_\theta}\frac{\partial \phi}{\partial \theta}, \quad \frac{\partial \phi}{\partial \mathbf{1}_\top} = \frac{1}{h_\lambda}\frac{\partial \phi}{\partial \lambda}. \tag{2.54}$$

2.3.2 The particle and current conservation equations

Let n_s, Z_s, and $\boldsymbol{u}_s$ be the particle density, charge number, and macroscopic velocity of any independent species s (electrons, and different neutral and ion species, the latter being treated by the PIC model as independent particle populations, as described in Sec. 2.2.3). The continuity equation for the species s is

$$\frac{\partial n_s}{\partial t} + \nabla \cdot n_s \boldsymbol{u}_s = S_s, \tag{2.55}$$

with S_s the net source function for the species s, grouping all possible contributions. For example, for the electron population, considering the ionization collisions and the contribution from a volumetric cathode [94] as the only source of electrons, the total electron source term may be written as

$$S_e = n_e(\nu_e^{ion} + \nu_{cat}), \tag{2.56}$$

where

$$\nu_e^{ion} = \sum_{s \neq e} \Delta Z_s^{ion} \nu_{es}^{ion} \tag{2.57}$$

is the total ionization collisions frequency, being ΔZ_s and ν_{es}^{ion} the charge number jump of the atom (i.e. the number of electrons generated) and the ionization collision frequency, respectively, per each considered reaction, and ν_{cat} is the cathode equivalent electron emission frequency, so that the total electron current emitted by the cathode (i.e. the discharge current) is

$$I_d = e \int_{V_{cat}} n_e \nu_{cat} dV, \tag{2.58}$$

where the integral extends to the volumetric cathode region, featuring a volume V_{cat}. It is stressed that $\nu_{cat} = 0$ outside the volumetric cathode region.

The electron, ion and net electric current densities, and the net electric charge density are defined, respectively, as

$$\boldsymbol{j}_e = -en_e\boldsymbol{u}_e, \quad \boldsymbol{j}_i = e\sum_{s\neq e} Z_s n_s \boldsymbol{u}_s, \quad \boldsymbol{j} = \boldsymbol{j}_e + \boldsymbol{j}_i, \quad \rho = e\sum_{s} Z_s n_s. \tag{2.59}$$

Except for the very thin plasma sheath regions close to the walls, which are treated separately (see Sec. 2.3.7.1), quasineutrality applies in most of the domain in a typical HET, so that $|\rho| \ll \epsilon_0 |\nabla \cdot \boldsymbol{E}|$, and the electron density is given by

$$n_e = \sum_{s\neq e} Z_s n_s. \tag{2.60}$$

Finally, adding the contributions of all species, the current continuity equation is

$$\frac{\partial \rho}{\partial t} + \nabla \cdot \boldsymbol{j} = -en_e\nu_{cat}. \tag{2.61}$$

2.3.3 The electron momentum equation

Considering an isotropic electron pressure tensor, the electron momentum equation is

$$\frac{\partial}{\partial t}(m_e n_e \boldsymbol{u}_e) + \nabla \cdot (m_e n_e \boldsymbol{u}_e \boldsymbol{u}_e) = -\nabla p_e + en_e\nabla\phi + \boldsymbol{j}_e \times \boldsymbol{B} + \boldsymbol{M} \tag{2.62}$$

where m_e and p_e are the electron mass and scalar pressure, respectively, and

$$\boldsymbol{M} = \sum_{s\neq e} m_e n_e \nu_{es}^{el}(\boldsymbol{u}_s - \boldsymbol{u}_e) + \sum_{s\neq e} m_e n_e \Delta Z_s^{ion} \nu_{es}^{ion} \boldsymbol{u}_s \tag{2.63}$$

is the collisional momentum transfer term, with ν_{es}^{el} and ν_{es}^{ion} the electron elastic and ionization collisions frequencies with the heavy species s, respectively. Making use of Eq. (2.55), Eq. (2.62) may be re-written as

$$\boldsymbol{0} = -\nabla p_e + en_e\nabla\phi + \boldsymbol{j}_e \times \boldsymbol{B} + \mu_e^{-1}(\boldsymbol{j}_e + \boldsymbol{j}_c) + \boldsymbol{F} \tag{2.64}$$

where

$$\boldsymbol{M} - m_e \boldsymbol{u}_e S_e = \mu_e^{-1}(\boldsymbol{j}_e + \boldsymbol{j}_c), \tag{2.65}$$

being the electron parallel mobility and the total electron collisional frequency

$$\mu_e = \frac{e}{m_e \nu_e}, \quad \nu_e = \nu_{cat} + \sum_{s\neq e} \nu_{es}, \tag{2.66}$$

respectively, with $\nu_{es} = \nu_{es}^{el} + \Delta Z_s^{ion} \nu_{es}^{ion}$, and

$$\boldsymbol{j}_c = \frac{en_e}{\nu_e} \sum_{s \neq e} \nu_{es} \boldsymbol{u}_s, \tag{2.67}$$

which represents the heavy species total collisional force per unit volume in terms of equivalent current density. On the other hand, $\boldsymbol{F}$ groups the inertial force $\boldsymbol{F}_I$ plus the stationary, axisymmetric force $\boldsymbol{F}_t$ accounting for the plasma turbulence effects

$$\boldsymbol{F} = \boldsymbol{F}_t - \boldsymbol{F}_I, \quad \boldsymbol{F}_I = m_e n_e \frac{D\boldsymbol{u}_e}{Dt}. \tag{2.68}$$

Projecting Eq. (2.64) in the magnetic reference system,

$$0 = -\frac{\partial p_e}{\partial \mathbf{1}_\parallel} + en_e \frac{\partial \phi}{\partial \mathbf{1}_\parallel} + \mu_e^{-1}(j_{\parallel e} + j_{\parallel c}) + F_\parallel, \tag{2.69}$$

$$0 = j_{\top e} B + \mu_e^{-1}(j_{\theta e} + j_{\theta c}) + F_\theta, \tag{2.70}$$

$$0 = -\frac{\partial p_e}{\partial \mathbf{1}_\top} + en_e \frac{\partial \phi}{\partial \mathbf{1}_\top} - j_{\theta e} B + \mu_e^{-1}(j_{\top e} + j_{\top c}) + F_\top, \tag{2.71}$$

and solving for the current density components,

$$j_{\parallel e} = \mu_e \left(\frac{\partial p_e}{\partial \mathbf{1}_\parallel} - en_e \frac{\partial \phi}{\partial \mathbf{1}_\parallel} \right) - j_{\parallel c} - \mu_e F_\parallel, \tag{2.72}$$

$$j_{\theta e} = -\chi j_{\top e} - j_{\theta c} - \mu_e F_\theta, \tag{2.73}$$

$$j_{\top e} = \mu_e \left(\frac{\partial p_e}{\partial \mathbf{1}_\top} - en_e \frac{\partial \phi}{\partial \mathbf{1}_\top} \right) + \chi j_{\theta e} - j_{\top c} - \mu_e F_\top, \tag{2.74}$$

where $\chi \equiv \omega_{ce}/\nu_e = \mu_e B$ is the Hall parameter, $\omega_{ce} = eB/m_e$ being the electron cyclotron frequency. Introducing Eq. (2.73) in Eq. (2.74), the perpendicular component of the electron current density is

$$j_{\top e} = \frac{\mu_e}{1+\chi^2} \left(\frac{\partial p_e}{\partial \mathbf{1}_\top} - en_e \frac{\partial \phi}{\partial \mathbf{1}_\top} \right) - \frac{j_{\top c} + \chi j_{\theta c}}{1+\chi^2} - \mu_e \frac{F_\top + \chi F_\theta}{1+\chi^2}, \tag{2.75}$$

where $\mu_e/(1+\chi^2)$ is the electron perpendicular mobility.

According to Eq. (2.59), for the sake of convenience the generalized Ohm law for the net electric current density $\boldsymbol{j}$ is obtained by adding the ion current density $\boldsymbol{j}_i$,

$$j_\parallel = \mu_e \left(\frac{\partial p_e}{\partial \mathbf{1}_\parallel} - en_e \frac{\partial \phi}{\partial \mathbf{1}_\parallel} \right) + j_{\parallel i} - j_{\parallel c} - \mu_e F_\parallel, \tag{2.76}$$

$$j_\theta = -\chi j_{\top e} + j_{\theta i} - j_{\theta c} - \mu_e F_\theta, \tag{2.77}$$

$$j_\top = \frac{\mu_e}{1+\chi^2} \left(\frac{\partial p_e}{\partial \mathbf{1}_\top} - en_e \frac{\partial \phi}{\partial \mathbf{1}_\top} \right) + j_{\top i} - \frac{j_{\top c} + \chi j_{\theta c}}{1+\chi^2} - \mu_e \frac{F_\top + \chi F_\theta}{1+\chi^2}. \tag{2.78}$$

This formulation facilitates the solution of the current continuity equation in Eq. (2.61), specially for the case of a single ion species with dominant electron-ion collisions, in which, $\boldsymbol{j}_c = \boldsymbol{j}_i$ [recall Eqs. (2.59) and (2.67)].

2.3.3.1 The turbulent contribution

The experience with HET seems to show that Eq. (2.78) for $j_\top$ is not satisfied if $\boldsymbol{F} = 0$ [95, 96]. The wall collisionalty or near-wall conductivity (NWC) [97] and the turbulent transport have been postulated as the main mechanisms behind the anomalous electron diffusion. Regarding the former, Ahedo *et al.* [98] obtained estimations of the wall collisionality from radial analysis of the discharge [99, 100]. Later, Escobar [101] presented a wall collisionality model based on the integration of the electron azimuthal momentum equation along the magnetic field lines. Both analysis concluded that the NWC seems to amount only up to 10% of the total perpendicular electron transport reported by experiments, thus in accordance with other studies [102, 103] which found it to be a second order contribution to the electron anomalous diffusion in typical HET operation conditions. Based on this and on the fact that it is not simple to include that wall phenomenon in the 2D formulation, it has been omitted from the development presented here, and a devoted investigation of its effects on the discharge is left for future work.

On the other hand, among the numerous and well identified oscillation modes present in typical HET operation [104–107], correlated azimuthal fluctuations of plasma magnitudes would be responsible for an enhanced axial electron transport [95, 98, 101]. Neglecting here inertial effects, so that, according to Eq. (2.68), $\boldsymbol{F} = \boldsymbol{F}_t$, of the two turbulent contributions in Eq. (2.78), $F_\top$ and χF_θ, the latter seems to be the most important one. This is because (a) $\chi \gg 1$ and (b) the fact that F_θ can be very relevant in Eq. (2.70) while $F_\top$ is likely marginal in Eq. (2.71), where there are several terms to balance the dominant magnetic force, $j_{\theta e} B$, in particular the electric field. However, in Eq. (2.70), the only term balancing the *small* magnetic force $j_{\top e} B$ is the resistive force. It makes then sense that any small contribution from other azimuthal effects could play a significant role. Therefore, F_θ seems to be the key term for the anomalous turbulent transport.

Distinguishing between (i) time and azimuthal-averaged magnitudes and (ii) their fluctuations, and performing a time and azimuthal-average in Eq. (2.62), the resulting stationary and axisymmetric equation can contain correlated products of two or more averaged variables. Furthermore, unless the fluctuations are very large, their resultant average effect will be relevant only if the corresponding $\theta-$average quasi-steady term is negligible or zero. This is precisely the case for the azimuthal electric force and pressure derivative,

$$\left\langle -\frac{\partial p_e}{\partial \mathbf{1}_\theta} + e n_e \frac{\partial \phi}{\partial \mathbf{1}_\theta} \right\rangle = -e \left\langle n_e' E_\theta' \right\rangle , \tag{2.79}$$

where n_e' and E_θ' represent the electron density and azimuthal electric field fluctuations, and $\langle\ \rangle$ means averaging on both t and θ. While it is assumed that $\langle n_e' E_\perp' \rangle \ll n_e E_\perp$ in Eq. (2.71), the turbulent contribution in Eq. (2.79) can be important in Eq. (2.70). As a consequence the only contribution from turbulence in the right hand side of Eq. (2.62) comes from the turbulent azimuthal force in Eq. (2.79) [98], so that

$$F_{\theta t} = -e \langle n_e' E_\theta' \rangle . \tag{2.80}$$

2.3.3.2 The inertial contribution

Electron inertial effects on a HET discharge were already studied by Ahedo *et al.* [108]. The dominant inertial term, coming from the azimuthal electron motion, yields an equivalent collisionality that can significantly contribute to the anomalous electron transport in the near plume region, where the magnetic field becomes residual. Moreover, electron inertia has been shown to play a non-negligible role in the anode sheath vanishing process [109]. If the Hall parameter is still large at the anode, these effects are only relevant in a thin quasineutral region near the anode, and bound the electron azimuthal drift velocity to values of the order of the electron thermal velocity. Furthermore, as detailed in Chapter 5, the centrifugal force is of the order of the magnetic mirror and radial temperature gradient contributions in the electron radial momentum equilibrium in the acceleration region. As a first approximation, in the present model the magnitude of the electron drift velocity has been limited to a fraction of the thermal one $\sqrt{T_e/m_e}$, with $T_e = p_e/n_e$ the electron temperature, so that unbounded drift velocities presumably arising not only around the anode, but also in the near plume regions are avoided. A more rigorous treatment of the inertial effects is outside the scope of this Thesis and is left for future work.

2.3.3.3 The mechanical energy equation

The electron mechanical energy equation is obtained by multiplying Eq. (2.62) by $\boldsymbol{u}_e$, yielding

$$m_e n_e \frac{D}{Dt}\left(\frac{u_e^2}{2}\right) = -\boldsymbol{u}_e \cdot \nabla p_e + \boldsymbol{j}_e \cdot \boldsymbol{E} + \mu_e^{-1} \boldsymbol{u}_e \cdot (\boldsymbol{j}_e + \boldsymbol{j}_c). \tag{2.81}$$

On the other hand, this equation can also be obtained by multiplying Eq. (2.64) by $\boldsymbol{u}_e$, so that

$$\boldsymbol{u}_e \cdot \boldsymbol{F}_I = -\boldsymbol{u}_e \cdot \nabla p_e + \boldsymbol{j}_e \cdot \boldsymbol{E} + \mu_e^{-1} \boldsymbol{u}_e \cdot (\boldsymbol{j}_e + \boldsymbol{j}_c) + \boldsymbol{u}_e \cdot \boldsymbol{F}_t, \tag{2.82}$$

where the inertial and turbulent contributions have been separated according to Eq. (2.68). Applying the same postulates as in Sec. 2.3.3.1 and considering Eq. (2.80), the relevant quasi-steady axisymmetric turbulent terms in Eqs. (2.81) and (2.82) are, respectively

$$m_e n_e \frac{D}{Dt}\left(\frac{u_e^2}{2}\right) = -\boldsymbol{u}_e \cdot \nabla p_e + \boldsymbol{j}_e \cdot \boldsymbol{E} + \mu_e^{-1} \boldsymbol{u}_e \cdot (\boldsymbol{j}_e + \boldsymbol{j}_c) + \left\langle j'_{\theta e} E'_\theta - u'_{\theta e} \frac{\partial p'_e}{\partial \theta} \right\rangle, \tag{2.83}$$

$$\boldsymbol{u}_e \cdot \boldsymbol{F}_I = -\boldsymbol{u}_e \cdot \nabla p_e + \boldsymbol{j}_e \cdot \boldsymbol{E} + \mu_e^{-1} \boldsymbol{u}_e \cdot (\boldsymbol{j}_e + \boldsymbol{j}_c) - e u_{\theta e} \langle n'_e E'_\theta \rangle, \tag{2.84}$$

so that equating the turbulent contributions above,

$$\left\langle u'_{\theta e} \frac{\partial p'_e}{\partial \theta} \right\rangle = \langle j'_{\theta e} E'_\theta \rangle + e u_{\theta e} \langle n'_e E'_\theta \rangle = -e n_e \langle u'_{\theta e} E'_\theta \rangle \tag{2.85}$$

2.3.4 The electron energy equation

The equation for the total (internal plus mechanical) electron energy is [87–89]

$$\frac{\partial}{\partial t}\left(\frac{3}{2} n_e T_e + \frac{1}{2} m_e n_e u_e^2\right) + \nabla \cdot \left[\left(\frac{5}{2} T_e + \frac{1}{2} m_e u_e^2\right) n_e \boldsymbol{u}_e + \boldsymbol{q}_e\right] = \boldsymbol{j}_e \cdot \boldsymbol{E} + Q_e, \tag{2.86}$$

where $\boldsymbol{q}_e$ is the electron temperature and heat flux vector, respectively, and Q_e groups the source and sinks of electron energy. Considering the ionization collisions and the volumetric cathode contributions,

$$Q_e = Q_{ion} + Q_{ex} + \frac{3}{2} n_e \nu_{cat} T_{cat}, \tag{2.87}$$

T_{cat} being the temperature of the electrons emitted from the volumetric cathode in energy units, and $Q_{ion}, Q_{ex} < 0$ the energy sink terms due to the ionization and excitation collisions. The electron internal energy equation is obtained by substracting from Eq. (2.86) the mechanical energy in Eq. (2.81), yielding

$$\frac{\partial}{\partial t}\left(\frac{3}{2} n_e T_e\right) + \nabla \cdot \left(\frac{5}{2} n_e T_e \boldsymbol{u}_e + \boldsymbol{q}_e\right) = \boldsymbol{u}_e \cdot \nabla p_e - \mu_e^{-1} \boldsymbol{u}_e \cdot (\boldsymbol{j}_e + \boldsymbol{j}_c) + Q_e - \frac{1}{2} m_e u_e^2 S_e. \tag{2.88}$$

Again, applying the postulates stated in Sec. 2.3.3.1 and considering Eq. (2.85), the relevant quasi-steady axisymmetric turbulent terms in Eqs. (2.86) and (2.88) are, respectively

$$\begin{aligned} \frac{\partial}{\partial t}\left(\frac{3}{2} n_e T_e + \frac{1}{2} m_e n_e u_e^2\right) + \nabla \cdot \left[\left(\frac{5}{2} T_e + \frac{1}{2} m_e u_e^2\right) n_e \boldsymbol{u}_e + \boldsymbol{q}_e\right] = \\ \boldsymbol{j}_e \cdot \boldsymbol{E} + \langle j'_{\theta e} E'_\theta \rangle + Q_e \end{aligned} \tag{2.89}$$

$$\begin{aligned} \frac{\partial}{\partial t}\left(\frac{3}{2} n_e T_e\right) + \nabla \cdot \left(\frac{5}{2} n_e T_e \boldsymbol{u}_e + \boldsymbol{q}_e\right) = \\ \boldsymbol{u}_e \cdot \nabla p_e - e n_e \langle u'_{\theta e} E'_\theta \rangle - \mu_e^{-1} \boldsymbol{u}_e \cdot (\boldsymbol{j}_e + \boldsymbol{j}_c) + Q_e - \frac{1}{2} m_e u_e^2 S_e. \end{aligned} \tag{2.90}$$

2.3.5 The electron heat flow equation

A proposed equation for the electron heat flux vector $\boldsymbol{q}_e$ is [89, 110, 111]

$$\boldsymbol{0} = -\frac{5 p_e}{2e} \nabla T_e - \boldsymbol{q}_e \times \boldsymbol{B} - \frac{5 p_e}{2 e n_e} \mu_e^{-1} (\boldsymbol{j}_e + \boldsymbol{j}_c) - \mu_e^{-1} \boldsymbol{q}_e + \boldsymbol{Y}_q + \boldsymbol{Q}_t, \tag{2.91}$$

where the Krook collision model (or relaxation model) for rate of change of the electron heat flux due to collisional processes, together with the contribution from the electron continuity equation yields the term $-\mu_e^{-1} \boldsymbol{q}_e$, $\boldsymbol{Q}_t$ accounts for turbulent effects on the electron heat flux equation, and

$$\boldsymbol{Y}_q = -\frac{m_e}{e}\left[\frac{D \boldsymbol{q}_e}{D t} + (\mathcal{Q}_e \cdot \nabla \boldsymbol{u}_e) : \mathcal{I} + \boldsymbol{q}_e \nabla \cdot \boldsymbol{u}_e + \boldsymbol{q}_e \cdot \nabla \boldsymbol{u}_e\right] \tag{2.92}$$

is the complete inertial term in the electron heat flux equation, with $\mathcal{Q}_e$ the third order electron heat flow tensor, defined as

$$\mathcal{Q}_e = \int m_e \boldsymbol{c}_e \boldsymbol{c}_e \boldsymbol{c}_e f_e d\boldsymbol{v}_e, \tag{2.93}$$

where $\boldsymbol{c}_e = \boldsymbol{v}_e - \boldsymbol{u}_e$ is the electron thermal velocity representing the random component of the electron particle velocity $\boldsymbol{v}_e$, f_e is the electron VDF and $\mathcal{I}$ the identity tensor.

Eq. (2.91) is a generalized Fourier law for the electron heat flux with an anisotropic conductivity tensor, analogous to the Ohm law for the current density expressed in Eqs. (2.76)-(2.78), or in Eqs. (2.72), (2.73) and (2.75) considering only the electron current density. Making use of Eqs. (2.64) and (2.68), Eq. (2.91) may be re-written as

$$\mathbf{0} = -\nabla\left(\frac{5p_eT_e}{2e}\right) + \frac{5p_e}{2}\nabla\phi - \left(\boldsymbol{q}_e + \frac{5p_e}{2}\boldsymbol{u}_e\right) \times \boldsymbol{B} - \mu_e^{-1}\boldsymbol{q}_e + \boldsymbol{Y} + \boldsymbol{Q}_t, \tag{2.94}$$

where the turbulent term $\boldsymbol{F}_t$ in Eq. (2.68) has been merged with the electric potential and electron pressure gradients in Eq. (2.64), and

$$\boldsymbol{Y} = \boldsymbol{Y}_q - \frac{5T_e}{2e}\boldsymbol{F}_I \tag{2.95}$$

groups all inertial terms. Projecting Eq. (2.94) onto the magnetic reference system retaining only the azimuthal quasi-steady axisymmetric turbulent transport contribution yields

$$0 = -\frac{\partial}{\partial \mathbf{1}_\parallel}\left(\frac{5p_eT_e}{2e}\right) + \frac{5p_e}{2}\frac{\partial\phi}{\partial \mathbf{1}_\parallel} - \mu_e^{-1}q_{\parallel e} + Y_\parallel, \tag{2.96}$$

$$0 = -\left(q_{\top e} + \frac{5p_e}{2}u_{\top e}\right)B - \mu_e^{-1}q_{\theta e} + Q_{\theta t} + Y_\theta, \tag{2.97}$$

$$0 = -\frac{\partial}{\partial \mathbf{1}_\top}\left(\frac{5p_eT_e}{2e}\right) + \frac{5p_e}{2}\frac{\partial\phi}{\partial \mathbf{1}_\top} + \left(q_{\theta e} + \frac{5p_e}{2}u_{\theta e}\right)B - \mu_e^{-1}q_{\top e} + Y_\top, \tag{2.98}$$

and solving for the electron heat flux components,

$$q_{\parallel e} = \mu_e\left[-\frac{\partial}{\partial \mathbf{1}_\parallel}\left(\frac{5p_eT_e}{2e}\right) + \frac{5p_e}{2}\frac{\partial\phi}{\partial \mathbf{1}_\parallel} + Y_\parallel\right], \tag{2.99}$$

$$q_{\theta e} = -\chi\left(q_{\top e} + \frac{5p_e}{2}u_{\top e}\right) + \mu_e(Q_{\theta t} + Y_\theta), \tag{2.100}$$

$$q_{\top e} = \mu_e\left[-\frac{\partial}{\partial \mathbf{1}_\top}\left(\frac{5p_eT_e}{2e}\right) + \frac{5p_e}{2}\frac{\partial\phi}{\partial \mathbf{1}_\top} + Y_\top\right] + \chi\left(q_{\theta e} + \frac{5p_e}{2}u_{\theta e}\right), \tag{2.101}$$

Introducing Eq. (2.97) in Eq. (2.98), the perpendicular heat flux is

$$\begin{aligned} q_{\top e} = \frac{\mu_e}{1+\chi^2}\left[-\frac{\partial}{\partial \mathbf{1}_\top}\left(\frac{5p_eT_e}{2e}\right) + \frac{5p_e}{2}\frac{\partial\phi}{\partial \mathbf{1}_\top} + Y_\top + \chi(Y_\theta + Q_{\theta t})\right] + \\ + \frac{5p_e}{2}\frac{\chi}{1+\chi^2}(u_{\theta e} - \chi u_{\top e}). \end{aligned} \tag{2.102}$$

Invoking the postulates considered in Sec. 2.3.3.1, the turbulent contribution in Eq. (2.97) is

$$Q_{\theta t} = \left\langle -\frac{\partial}{\partial \mathbf{1}_\theta}\left(\frac{5p_eT_e}{2e}\right) + \frac{5p_e}{2}\frac{\partial\phi}{\partial \mathbf{1}_\theta}\right\rangle = \frac{5}{2}\left\langle p_e\frac{\partial\phi}{\partial \mathbf{1}_\theta}\right\rangle = -\frac{5}{2}\left\langle p_e' E_\theta'\right\rangle. \tag{2.103}$$

2.3.6 The collisional version of turbulent transport

The turbulent contribution to the electron transport has been generally modeled by adding an anomalous frequency to the total electron collisional frequency [44, 107]. Recent multi-fluid simulations performed by Mikellides and Ortega [43], and hybrid PIC-fluid simulations carried out by Garrigues *et al.* [55] have followed this strategy trying to reproduce the experimental data through the fitting of an anomalous term acting only in the electron momentum equation. Here it is remarked that, as shown in Secs. 2.3.3-2.3.5, there are three electron turbulent contributions acting in the electron momentum, energy and heat flow equations, which can be modeled through three corresponding anomalous transport parameters, which, in principle, may be different from each other. Although this approach cannot help in the understanding of the physical mechanism behind the enhanced electron transport reported by experiments, it allows the incorporation to the electron-fluid equations of effective electron cross-field mobility models obtained from kinetic studies [34, 112–115].

Regarding the turbulent effects on the electron momentum, Ahedo *et al.* [98] defined the turbulent parameter α_{tm} as

$$\alpha_{tm} = \frac{F_{t\theta}}{j_{\theta e} B} = \frac{\langle n_e' E_\theta' \rangle}{n_e u_{\theta e} B}, \tag{2.104}$$

which relates the quasi-steady axisymmetric turbulent force $F_{\theta t}$ defined in Eq. (2.80) to the dominant magnetic force in Eq. (2.71), and is much less than one for a weakly turbulent discharge. Neglecting inertial effects, Eq. (2.73) becomes

$$j_{\theta e} = -\frac{\chi}{1+\alpha_{tm}\chi} j_{\top e} - \frac{j_{\theta c}}{1+\alpha_{tm}\chi} = -\frac{\omega_{ce}}{\nu_e + \alpha_{tm}\omega_{ce}} j_{\top e} - \frac{j_{\theta c}}{1+\alpha_{tm}\chi}, \tag{2.105}$$

so that the effective electron collision frequency is $\nu_e + \alpha_{tm}\omega_{ce}$. Making use of Eqs. (2.104) and (2.105) and neglecting inertial effects, Eqs. (2.72) and (2.75) turn into

$$j_{\parallel e} = \mu_e \left(\frac{\partial p_e}{\partial \mathbf{1}_\parallel} - e n_e \frac{\partial \phi}{\partial \mathbf{1}_\parallel} \right) - j_{\parallel c}, \tag{2.106}$$

$$j_{\top e} = \frac{\mu_e (1+\alpha_{tm}\chi)}{1+\alpha_{tm}\chi+\chi^2} \left(\frac{\partial p_e}{\partial \mathbf{1}_\top} - e n_e \frac{\partial \phi}{\partial \mathbf{1}_\top} \right) - \frac{(1+\alpha_{tm}\chi) j_{\top c} + \chi j_{\theta c}}{1+\alpha_{tm}\chi+\chi^2}, \tag{2.107}$$

and the generalized Ohm law represented by the set of Eqs. (2.76)-(2.78) becomes

$$j_\parallel = \mu_e \left(\frac{\partial p_e}{\partial \mathbf{1}_\parallel} - e n_e \frac{\partial \phi}{\partial \mathbf{1}_\parallel} \right) + j_{\parallel h}, \tag{2.108}$$

$$j_\theta = -\frac{\chi}{1+\alpha_{tm}\chi} j_{\top e} + j_{\theta h}, \tag{2.109}$$

$$j_\top = \frac{\mu_e (1+\alpha_{tm}\chi)}{1+\alpha_{tm}\chi+\chi^2} \left(\frac{\partial p_e}{\partial \mathbf{1}_\top} - e n_e \frac{\partial \phi}{\partial \mathbf{1}_\top} \right) + j_{\top h}, \tag{2.110}$$

with

$$j_{\parallel h} = j_{\parallel i} - j_{\parallel c}, \quad j_{\theta h} = j_{\theta i} - \frac{j_{\theta c}}{1+\alpha_{tm}\chi}, \quad j_{\top h} = j_{\top i} - \frac{(1+\alpha_{tm}\chi) j_{\top c} + \chi j_{\theta c}}{1+\alpha_{tm}\chi+\chi^2}. \tag{2.111}$$

Regarding Eq. (2.90) for the electron internal energy, the turbulent effects may be modeled through the parameter

$$\alpha_{te} = \frac{en_e \left\langle u'_{\theta e} E'_\theta \right\rangle}{\boldsymbol{j}_e \cdot \boldsymbol{u}_e B}, \tag{2.112}$$

which relates the turbulent contribution in Eq. (2.90) to the main *heating* term from Eq. (2.71), where the total electron current density and velocity vectors have been considered. Introducing Eq. (2.112) in Eq. (2.90), and writing it in terms of electron pressure and current density for later convenience, it becomes

$$\begin{aligned} &\frac{\partial}{\partial t}\left(\frac{3}{2}p_e\right) + \nabla\cdot\left(-\frac{5p_e}{2en_e}\boldsymbol{j}_e + \boldsymbol{q}_e\right) = \\ &\qquad = -\left(\frac{\boldsymbol{j}_e}{en_e}\right)\cdot\nabla p_e + \eta_e^* j_e^2 + \eta_e \boldsymbol{j}_e \cdot \boldsymbol{j}_{\boldsymbol{c}} + Q_e - \frac{m_e j_e^2 S_e}{2e^2 n_e^2}, \end{aligned} \tag{2.113}$$

where the electron resistivity and the electron effective resistivity are defined, respectively, as

$$\eta_e = \frac{1}{en_e\mu_e}, \qquad \eta_e^* = \eta_e + \frac{m_e \alpha_{te}\omega_{ce}}{e^2 n_e}, \tag{2.114}$$

so that the turbulent heating requires $\alpha_{te} > 0$.

Finally, the quasi-steady axisymmetric turbulent term $Q_{\theta t}$ defined in Eq. (2.103) may be related to the dominant term in Eq.(2.98) by defining

$$\alpha_{tq} = -\frac{Q_{\theta t}}{q_{\theta e} B} = -\frac{5}{2}\frac{\left\langle p'_e E'_\theta \right\rangle}{q_{\theta e} B}, \tag{2.115}$$

so that neglecting the inertial term in Eq. (2.100), it becomes

$$q_{\theta e} = -\frac{\chi}{1+\alpha_{tq}\chi}\left(q_{\top e} + \frac{5p_e}{2}u_{\top e}\right) = -\frac{\omega_{ce}}{\nu_e + \alpha_{tq}\omega_{ce}}\left(q_{\top e} + \frac{5p_e}{2}u_{\top e}\right), \tag{2.116}$$

which is analogous to Eq. (2.105) for the case of momentum. Neglecting inertial terms and considering Eqs. (2.115) and (2.116), the parallel and perpendicular electron heat flux components from Eq. (2.91) are

$$q_{\parallel e} = -\frac{5\mu_e p_e}{2e}\frac{\partial}{\partial \mathbf{1}_\parallel}\left(\frac{p_e}{n_e}\right) - \frac{5p_e}{2en_e}(j_{\parallel e} + \mathrm{J}_{\parallel c}), \tag{2.117}$$

$$\begin{aligned} q_{\top e} = &-\frac{\mu_e(1+\alpha_{tq}\chi)}{1+\alpha_{tq}\chi+\chi^2}\frac{5p_e}{2e}\frac{\partial}{\partial \mathbf{1}_\top}\left(\frac{p_e}{n_e}\right) + \\ &+\frac{5p_e}{2en_e}\frac{\left[\chi^2 - (1+\alpha_{tq}\chi)\right] j_{\top e} - (1+\alpha_{tq}\chi)\, j_{\top c}}{1+\alpha_{tq}\chi+\chi^2}, \end{aligned} \tag{2.118}$$

where, again, they have been written in terms of electron pressure and current density for later convenience.

2.3.7 Numerical resolution of the electron-fluid model

Given the three turbulent parameters defined in Eqs. (2.104), (2.112) and (2.115), the collisions models providing the total electron collision frequency in Eq. (2.66) and the collisional energy sink term in Eq. (2.87) (see Sec. 2.3.7.1), and all the relevant magnitudes characterizing the heavy species (particle and current densities provided by the PIC module), Eqs. (2.61),(2.105)-(2.111), (2.113) and (2.116)-(2.118) represent a closed set of equations for the electric potential, the electric current density, and the electron current density, temperature (or pressure), and the heat flux vector when the quasineutrality condition expressed in Eq. (2.60) is applied. The HYPHEN electron-fluid module discretizes these equations in a non-structured MFAM through a cell centered finite volume method (CC-FVM). As shown in Fig. 2.11, two types of MFAM cells may be distinguished. The inner cells are enclosed by two pairs of faces that are magnetic lines. The boundary cells have at least one boundary face which in general is not magnetically aligned. The cell center of the inner cells is always the magnetic center, while for boundary cells the geometric center is considered instead. On the other hand, the MFAM faces can be classified into inner faces and boundary ones (see Fig. 2.11). Similarly, the faces are represented by their magnetic and geometric centers, for inner and boundary faces, respectively. The model discretization through the CC-FVM requires the application of gradient reconstruction (GR) techniques to express the value of a function and its derivatives along a given set of directions at the face centers in terms of its values at the cell centers (i.e. the actual computational points). The weighted least squares method (WLSM) introduced by Sozer [116] has been implemented in NOMADS [59, 60, 66]. Considering for example the electric potential, this method yields

$$\phi_m = \sum_l c_{ml}\phi_l, \qquad \left.\frac{\partial \phi}{\partial \mathbf{1}_\alpha}\right|_m = \sum_l c^\alpha_{ml}\phi_l, \qquad \left.\frac{\partial \phi}{\partial \mathbf{1}_\alpha}\right|_{l'} = \sum_{l\neq l'} c^\alpha_{l'l}\phi_l, \tag{2.119}$$

where c_{ml}, c^α_{ml} and $c^\alpha_{l'l}$ are the corresponding GR coefficients at the l^{th} MFAM cell center for obtaining the electric potential and its derivative with respect to a given direction $\mathbf{1}_\alpha$ at the MFAM face center m and cell center l'.

In NOMADS, the generalized Ohm law expressed in Eqs. (2.108)-(2.110) is solved along with the current continuity equation in Eq. (2.61) neglecting its time derivative term, and considering an already known solution for the electron pressure (and thus the electron temperature) [59, 60]. Therefore, applying the CC-FVM to the steady Eq. (2.61) at a given MFAM cell featuring a volume V,

$$\int_V \nabla\cdot\boldsymbol{j}dV = \oint_{S\in V}\boldsymbol{j}\cdot\boldsymbol{n}dS = \sum_m \boldsymbol{j}_m\cdot\boldsymbol{n}_m A_m = -e\int_V n_e\nu_{cat}dV, \tag{2.120}$$

where the Gauss theorem permits to approximate the volume integral in the left hand side as the sum of electric currents normal to the MFAM element faces, $\boldsymbol{j}_m$ being the electric current density evaluated at the center of the face m, and $\boldsymbol{n}_m$ and A_m the normal versor and area of the MFAM cell face m. The term $j_{nm} \equiv \boldsymbol{j}_m\cdot\boldsymbol{n}_m$ is either $\pm j_\parallel$ or $\pm j_\top$ at inner faces (see the inner faces normal versors in Fig. 2.11), while it is provided by the boundary conditions at boundary faces (see Sec. 2.3.7.1). Applying Eq. (2.120) for all the MFAM cells, and considering Eq. (2.58) for the right hand side of Eq. (2.120), leads

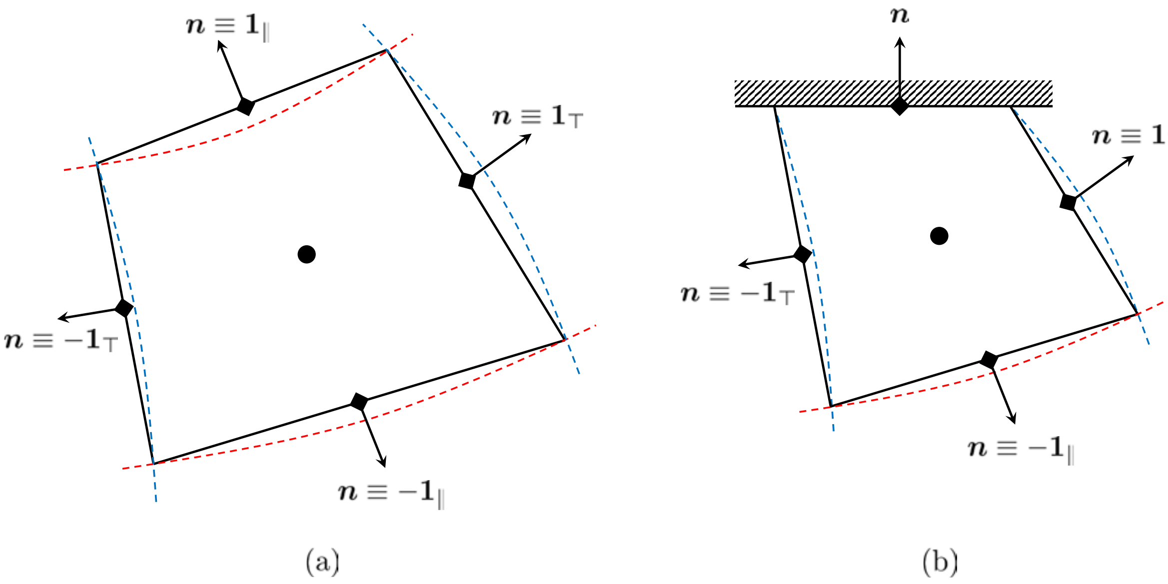

Figure 2.11: MFAM inner (a) and boundary (b) cells. Circles and squares represents the cell and face centers, respectively. The inner faces normal versors coincide with either $\pm\mathbf{1}_{\parallel}$ or $\pm\mathbf{1}_{\top}$. Dashed blue and red lines corresponds to magnetic isopotential and streamfunction lines, respectively (i.e. $\sigma = const.$ and $\lambda = const.$ lines, respectively).

to the non-square matrix relation

$$\mathcal{A}_1 \left\{ j_{nm} \right\} = \mathcal{B}_1 I_d, \tag{2.121}$$

where $\{j_{nm}\}$ is a vector grouping the electric current densities normal to all the MFAM faces, $\mathcal{A}_1$ is a matrix collecting the faces areas, $\mathcal{B}_1$ is a vector containing information related to the MFAM cells representing net current sink/sources, and zeros for the rest of MFAM cells, and I_d is the discharge current, which is also defined for a HET as

$$I_d = \int_A \boldsymbol{j} \cdot \boldsymbol{n} dS = \sum_{m \in A} \boldsymbol{j}_m \cdot \boldsymbol{n}_m A_m, \tag{2.122}$$

where the integral is performed over the anode wall, so that the sum extends to the m MFAM faces belonging to the anode wall boundary (A). It is worth noting here that, while in the constant discharge current HET operation mode I_d is given as a simulation parameter [60], in the most usual constant voltage HET operation mode I_d is unknown. This operation mode shall be considered hereafter. Therefore, using Eq. (2.122), the right hand side of Eq. (2.121) can be integrated in the left hand side. Now, the vector $\{j_{nm}\}$ in Eq. (2.121) can be obtained by combining (a) the generalized Ohm law in Eqs. (2.108) and (2.110) at the inner faces using the GR relations in Eq. (2.119), and (b) the known boundary conditions at the boundary faces (see Sec. 2.3.7.1), so that

$$\left\{ j_{nm} \right\} = \mathcal{A}_2 \left\{ p_{el} \right\} + \mathcal{A}_3 \left\{ \phi_l \right\} + \mathcal{B}_2, \tag{2.123}$$

with $\{p_{el}\}$ and $\{\phi_l\}$ vectors gathering the electron pressure and the electric potential values at the center of the MFAM cells l, $\mathcal{A}_2$ and $\mathcal{A}_3$ matrices containing plasma, boundary conditions and geometric information, and $\mathcal{B}_2$ a vector collecting information about (i)

the j_h terms at the inner faces, defined in Eq. (2.111), which depend on $\boldsymbol{j}_i$ and $\boldsymbol{j}_c$, given in Eqs. (2.59) and (2.67), respectively, and provided by the PIC module given the corresponding electron properties, and (*ii*) the boundary conditions (see Sec. 2.3.7.1). As mentioned before, in order to keep the system of equations linear, the electron pressure is supposed known when solving for the current continuity and generalized Ohm equations. Therefore, introducing Eq. (2.123) in Eq. (2.121) yields a square matrix system for the electric potential at center of the MFAM cells,

$$\mathcal{A}\left\{\phi_l\right\} = \mathcal{B}, \tag{2.124}$$

where $\mathcal{A} = \mathcal{A}_1\mathcal{A}_3$ and $\mathcal{B} = \mathcal{B}_1 - \mathcal{A}_1\left[\mathcal{A}_2\left\{p_{el}\right\} + \mathcal{B}_2\right]$. It can be proven that the square matrix $\mathcal{A}$ does not feature its maximum possible rank, so that the resolution of Eq. (2.124) requires to set a reference potential at a given MFAM cell (see Sec. 2.3.7.1).

Proceeding analogously for the electron internal energy equation in Eq. (2.113), the CC-FVM at an MFAM cell with volume V yields

$$\begin{aligned}\left.\frac{\partial p_e}{\partial t}\right|_V = &-\frac{2}{3V}\sum_m \left.\left(-\frac{5p_e}{2en_e}\boldsymbol{j}_e + \boldsymbol{q}_e\right)\right|_m \cdot \boldsymbol{n}_m A_m - \left.\frac{2\boldsymbol{j}_e}{3en_e}\cdot\nabla p_e\right|_V + \\ &+\frac{2}{3}\left.\left(\eta_e^* j_e^2 + \eta_e \boldsymbol{j}_e\cdot\boldsymbol{j}_c + Q_e - \frac{m_e j_e^2 S_e}{2e^2 n_e^2}\right)\right|_V,\end{aligned} \tag{2.125}$$

where $\boldsymbol{j}_e$ and $\boldsymbol{q}_e$ are given at the inner faces by Eqs. (2.105)-(2.107), and (2.116)-(2.118), respectively, and by the corresponding boundary conditions at the boundary faces (see Sec. 2.3.7.1). According to the semi-implicit treatment described in Ref. [60], in order to solve a linear system for the electron pressure (temperature), the electron current terms and the electron pressure term multiplying the derivatives in the electron heat flux parallel and perpendicular components [Eqs. (2.117) and (2.118), respectively] are treated explicitly (i.e. known from a previous electron-fluid module sub-iteration k). Applying Eq. (2.125) for all the MFAM cells considering a first order FD scheme for the electron pressure time derivative, and introducing again the GR relations in Eq. (2.119), yields a square matrix system for updating the electron pressure at the MFAM cells,

$$\mathcal{S}\left\{p_{el}\right\}^{(k+1)} = \left\{p_{el}\right\}^{(k)} + \mathcal{R}, \tag{2.126}$$

where $\left\{p_{el}\right\}^{(k+1)}$ and $\left\{p_{el}\right\}^{(k)}$ groups the electron pressure values at the MFAM cells centers evaluated at the current $k+1$ and previous k electron-fluid module sub-iterations. $\mathcal{S}$ is a square matrix containing all the information coming from all those implicit pressure terms in Eq. (2.125). Those include (1) the implicit pressure term in the left hand side of Eq. (2.125), (2) the first term in the right hand side of Eq. (2.125) at the inner faces [expressed in terms of the MFAM cell centers through Eq. (2.119)], representing the electron energy flux term, including the electron energy advection and the electron heat flux term, and (3) the second term in the right hand side of Eq. (2.125), corresponding to the electron pressure work. On the other hand, $\mathcal{R}$ is a vector containing the first term in the right hand side of Eq. (2.125) at the boundary faces, coming from the boundary conditions (see Sec. 2.3.7.1), and the third term in the right hand side of Eq. (2.125), which represents the total Joule heating and the complete energy sink/source term. Both

$\mathcal{S}$ and $\mathcal{R}$ depend on the electron-fluid sub-iterations timestep, defined from the PIC (or simulation) timestep as

$$\Delta t_e = \frac{\Delta t}{N_{ke}}, \tag{2.127}$$

where N_{ke} is the number of sub-iterations of the electron-fluid module per PIC or simulation timestep. Considering two successive solutions for the heavy species given by the PIC module at the simulation times t_0 (e.g. an initial state) and $t_1 = t_0 + \Delta t$, and an initial solution for all the electron fluid variables at t_0 (i.e. at the electron-fluid module sub-iteration $k = 0$), the electron-fluid module performs an inner loop of N_{ke} sub-iterations so as to update the electron population variables to the simulation time $t_1 = t_0 + N_{ke}\Delta t_e$, according to Eq. (2.127). For each sub-iteration k, Eq. (2.126) is applied first, thus obtaining the updated electron pressure at $k+1$ from the already known electron-fluid solution and the boundary conditions for the electron energy flux at k. Then, Eq. (2.124) solves for the electric potential at $k+1$ considering the updated electron pressure and the corresponding boundary conditions for the current density. The electron current density and heat flux are then updated by Eqs. (2.105)-(2.107), and (2.116)-(2.118), respectively, at the sub-iteration $k+1$. It is underlined that, on every electron-fluid module sub-iteration k, the heavy species magnitudes are evaluated at $k+1$ through a linear interpolation of their known values at t_0 and t_1. In addition, in every sub-iteration, after solving Eqs. (2.124) and (2.126) for the electric potential and the electron pressure, respectively, Eq. (2.119) is applied for obtaining those magnitudes at the MFAM boundary faces. As a final comment, in order to solve the matrix systems of equations in Eqs. (2.124) and (2.126), NOMADS makes use of the PARDISO [117, 118] parallel direct solver.

2.3.7.1 Boundary conditions and ancillary models

Considering the usual constant voltage operation mode of a HET, the HYPHEN electron-fluid model takes as input the discharge voltage, defined as

$$V_d = \phi_A - \phi_{cat}, \tag{2.128}$$

where ϕ_A is the electric potential of the anode wall, and ϕ_{cat} is the cathode potential. At the current state of the code [60], the volumetric cathode is represented only by one MFAM cell which, for the sake of simplicity, is also set as the reference potential cell, so that $\phi_c at = 0$. This condition is consistently included in the matrix system in Eq. (2.124).

Regarding the boundary conditions for the electric current and the electron energy flux, Fig. 2.6(b) shows a typical HET simulation domain in which the red, green, blue and magenta lines indicate the dielectric (D) wall, the anode (A) wall, the free loss (FL) boundary and symmetry axis at $r = 0$ (Ax), respectively. As commented in Sec. 2.3.7, at the simulation domain boundary, the boundary condition for j_{nm} at every MFAM boundary face m constitutes a row in Eq. (2.123), which is later introduced in Eq. (2.121), thus yielding the linear matrix system in Eq. (2.124) solving for the electric potential at the MFAM cells. Similarly, the information about the electron energy flux term at the MFAM boundary faces is contained in the vector $\mathcal{R}$ of Eq. (2.125). The symmetry condition at the axis yields

$$\left.\begin{aligned}\{j_{nm}\} &= \mathbf{0}\\ \left.\left(-\frac{5p_e}{2en_e}\boldsymbol{j}_e + \boldsymbol{q}_e\right)\right|_m \cdot \boldsymbol{n}_m &= 0\end{aligned}\right\} \forall m \in \text{Ax}. \tag{2.129}$$

It is worth noting that, since the MFAM faces at the axis feature zero area [i.e. $A_m = 0$ in Eqs. (2.120) and (2.125) for the m^{th} MFAM face beloging to the symmetry axis], they do not contribute either in Eqs. (2.120) or (2.125).

The free loss boundary fulfills the current free condition for $\boldsymbol{j}$ and the adiabatic condition for $\boldsymbol{q}_e$, so that

$$\left.\begin{aligned}\{j_{nm}\} &= \mathbf{0}\\ \boldsymbol{q}_e \cdot \boldsymbol{n}|_m &= 0\end{aligned}\right\} \forall m \in \text{FL}. \tag{2.130}$$

As already commented on Sec. 2.2.5.4, the different inertia of electrons and ions in a quasineutral plasma leads to the development of a plasma sheath between the plasma and a given boundary wall, which adjusts the ion and electron currents reaching the wall. The sheath region is outside the quasineutral simulation domain of the HYPHEN hybrid simulator, and is thus treated as a boundary condition. The sheath model presented by Ahedo and de Pablo [119] has been adapted and implemented by Pérez-Grande [60] in HYPHEN. In typical cases (those considered in the hybrid simulator), the sheath is quasiplanar, quasisteady (i.e. the sheath response is much faster than the quasineutral bulk plasma typical time scales), collisionless and unmagnetized. Except for the charge saturation limit (CSL) [91], after which the sheath is no longer monotonic, which is not considered in the model, a positive (i.e. ion attracting) potential fall $\Delta\phi_{sh}$ develops at the dielectric (i.e. non-conducting) walls so that they feature zero net electric current at steady conditions. Under the collisionless sheath assumption, the zero net electric current is fulfilled at the sheath edge, which coincides with the HYPHEN simulation domain boundary, so that

$$\{j_{nm}\} = \mathbf{0}, \quad \forall m \in \text{D}, \tag{2.131}$$

and the sheath potential fall at the dielectric boundary walls is given by

$$\Delta\phi_{sh,m} = f_{sh,\text{D}}(\boldsymbol{j}_i \cdot \boldsymbol{n}, n_e, T_e)|_m\,, \quad \forall m \in \text{D}, \tag{2.132}$$

where $f_{sh,D}$ is the sheath model function for $\Delta\phi_{sh}$ at dielectric walls (see Ref. [60]), which depends on the total ion current density reaching the wall, and the quasineutral plasma density and the electron temperature at the sheath edge, the later being known when solving for the electric potential, as already commented in Sec. 2.3.7. Additionally, the sheath model function $h_{sh,\text{D}}$ (see Ref. [60]) provides the total electron energy flux at the sheath edge of a dielectric wall

$$\left.\left(-\frac{5p_e}{2en_e}\boldsymbol{j}_e + \boldsymbol{q}_e\right)\right|_m \cdot \boldsymbol{n}_m = h_{sh,\text{D}}(\boldsymbol{j}_i \cdot \boldsymbol{n}, n_e, T_e)|_m\,, \quad \forall m \in \text{D}, \tag{2.133}$$

which is introduced in the first term on the right hand side of Eq. (2.125) at the dielectric wall boundary faces as the corresponding boundary condition. It is underlined that Eq. (2.133) is treated explicitly when solving Eq. (2.126) for the electron pressure, so that it is evaluated considering the electron temperature from a previous electron-fluid module sub-iteration.

On the other hand, the sheath model provides a non-linear relation $f_{sh,\mathrm{A}}$ (see Ref. [60]) between the electron current density collected by the anode and the sheath potential drop there, which, adding the ion current density reaching the anode, may be written as

$$\{j_{nm}\} = f_{sh,\mathrm{A}}(\Delta\phi_{sh}, n_e, T_e)\big|_m + \boldsymbol{j}_i \cdot \boldsymbol{n}\big|_m, \quad \Delta\phi_{sh,m} = \phi_m - \phi_A, \quad \forall m \in \mathrm{A}, \tag{2.134}$$

where, again, the electron temperature is known when solving for the electric potential. In order to solve a linear system of equations for the electric potential at the MFAM cells, the function $f_{sh,\mathrm{A}}$ is linearized around a given value $\Delta\phi^*_{sh}$ through a first order Taylor expansion. Besides, expressing ϕ_m in Eq. (2.134) in terms of the electric potential at the MFAM cells through Eq. (2.119), the linearized Eq. (2.134) corresponds to the rows of Eq. (2.123) referring to the anode MFAM boundary faces, for which $\mathcal{A}_2$ features zero rows, $\mathcal{A}_3$ collects the information about the linearized sheath function $f_{sh,\mathrm{A}}$ around $\Delta\phi^*_{sh}$ and geometry (i.e. corresponding GR coefficients), and $\mathcal{B}_2$ contains information about the linearized sheath function $f_{sh,\mathrm{A}}$ around $\Delta\phi^*_{sh}$, the values of $\Delta\phi^*_{sh}$ and ϕ_A, and the ion current density collected by the anode wall. Hence, the linear system of Eq. (2.124) depends on $\Delta\phi^*_{sh}$, so that the following iterative process is performed in order to solve for the electric potential at the MFAM cells:

a) Consider an initial guess $\Delta\phi^*_{sh} = \Delta\phi_{sh0}$.

b) Obtain and solve the linear system of equations in Eq. (2.124) for the electric potential at the MFAM cells $\{\phi_l\}$.

c) Compute the new sheath potential fall $\Delta\phi_{sh1}$ from the solution $\{\phi_l\}$ and applying Eqs. (2.134) and (2.119).

d) Repeat step b) with $\Delta\phi^*_{sh} = \Delta\phi_{sh1}$ until Eq. (2.120) at every anode boundary MFAM cell is satisfied within a given tolerance.

In addition, similarly to the case of a dielectric wall, the sheath function $h_{sh,\mathrm{A}}$ (see Ref. [60]) provides the total electron energy flux at the sheath edge

$$\left(-\frac{5p_e}{2en_e}\boldsymbol{j}_e + \boldsymbol{q}_e\right)\bigg|_m \cdot \boldsymbol{n}_m = h_{sh,\mathrm{A}}(\Delta\phi_{sh}, n_e, T_e)\big|_m, \quad \forall m \in \mathrm{A}, \tag{2.135}$$

whose explicit treatment is analogous to the case of a dielectric wall, considering known values of $\Delta\phi_{sh}$ at the anode faces from a previous electron-fluid module sub-iteration when solving for the electron pressure.

Finally, considering Xenon as propellant, the elastic electron-neutral collision frequency is obtained from the model proposed by Mitchner and Krueger [83], while the corresponding values for the elastic electron-ion collisions are based on a Coulomb interaction model from Goldston [87]. For inelastic collisions, which imply an energy sink for the electron population, the models for the ionization collisions were already commented in Sec. 2.2.5.3.1, while the Hayashi model [120] for the excitation reaction $\mathrm{Xe} + e \to \mathrm{Xe}^*$ is added.

2.3.8 Summary of the main improvements on the electron-fluid model

The electron-fluid model presented in Sec. 2.3 features a number of improvements with respect to that originally developed by Pérez-Grande [59, 60], which are listed below:

1) A preliminary treatment of electron inertial effects through the implementation of an electron drift velocity limiter, as described in Sec. 2.3.3.2, which avoids unphysically high electron drift velocities arising in the original model.

2) The incorporation to the electron internal energy equation of the equivalent Joule heating term corresponding to the anomalous electron transport through the definition of the electron effective resistivity η_e^* in Eq. (2.114), according to the collisional version of turbulent effects.

3) The improved treatment of the volumetric cathode source term in the electron conservation equations, which eliminates unphysical effects present in the original version of the code when changing the location of the MFAM cell corresponding to the volumetric cathode in the simulation domain.

4) A simple and precise redefinition of the turbulent electron transport parameters α_{tm}, α_{te} and α_{tq} related to the electron momentum, energy and heat flux, respectively, as shown in Sec. 2.3.6.

5) The improved grouping of the collisional term in the electron momentum equation through the definition of the heavy species equivalent collisional current density $\boldsymbol{j}_c$, which simplifies the model formulation and treats separately every collision process between the electron population and a given heavy species s (corresponding to an independent PIC particle population, as described in Sec. 2.2.3), thus defining the total (i.e. elastic plus ionization) collision frequency ν_{es} between the electron population and the heavy species s, and considering the heavy species s drift velocity $\boldsymbol{u}_s$. In contrast, in the original NOMADS version [59,60], the ionization collision frequencies were neglected with respect to the elastic ones. In addition, (i) for a given propellant, all neutral and singly and doubly charged ion PIC particle populations (i.e. independent particle lists, as explained in Sec. 2.2.3) were merged in a single species, respectively, thus mixing their respective origins and energy contents (especially for those populations coming from CEX collisions), and (ii) the neutral species drift velocity was neglected with respect to that of the electron population, while those of the ion species were considered. This is not consistent when fast neutrals coming from CEX collisions are simulated.

6) The improved identification in Eq. (2.113) [or, equivalently in Eq. (2.125)] of the boundary conditions for the electron energy flux given by the sheath module in Eqs. (2.133) and (2.135).

While the improvements 1), 2) and 3) have already been implemented in the current version of NOMADS in the frame of this Thesis, the actual incorporation to the code of those stated in 4), 5) and 6) is left for future work.

Chapter 3

Simulation of axisymmetric plasma plumes

This Chapter reproduces the contents published in the peer-reviewed journal Plasma Sources Science and Technology [54]. The typography has been adapted to the style of this thesis.

Abstract

The expansion of a rarefied axisymmetric plume emitted by a plasma thruster is analyzed and compared with a 3D Cartesian-type and a 2D cylindrical-type simulation code, both based on a particle-in-cell formulation for the heavy species and a simple Boltzmann-type model for the electrons. The first part of the paper discusses the 2D code numerical challenges in the moving of particles, their generation within the cells, and the weighting to the nodes, caused by the radial non-uniformity and the singular and boundary character of the symmetry axis. The second part benchmarks the 2D code against the 3D one for a high-energy, unmagnetized plume with three major species populations (injected neutrals, singly charged and doubly charged ions) and three minor species populations (constituted by particles coming from collisional processes, such as the charge-exchange reactions). The excellent agreement found in the results proves that both plume codes are capable of simulating, with a reasonable noise level, heavy particle populations differing by several orders of magnitude in number density. For simulations with a comparable level of accuracy, the 2D code presents a ten-fold gain in computational cost, although the symmetry axis remains its weakest point, due to particle depletion there and the related weighting noise.

3.1 Introduction

Nowadays, the number of spacecraft (S/C) with onboard electric propulsion (EP) is increasing rapidly. The physics of the ejected high-energy plasma plumes has therefore become a subject of extreme interest, given the criticality of their interaction with the satellite surfaces like solar arrays, especially from a system engineering point of view. In fact, the surface erosion and contamination due to the impact of secondary ions generated within these plumes is a key issue to take into account at a preliminary stage of the satellite design. This has led to the development of a large number of plasma thruster plume simulators [48–50, 74, 121–127] featuring a detailed modeling of the physics in the near-region of the plume, where most of the slow ion backflow responsible for S/C sputtering and contamination is generated [53].

One such code is EP2PLUS, [52, 53, 58], a 3D code that has already been successfully used to analyze different phenomena, such as the plasma plume interaction with a space debris, in the context of the ion beam shepherd concept [128], or the expansion of the plasma plume of either a gridded ion thruster (GIT) [53] or a high efficiency multi-stage plasma thruster (HEMPT) [51]. EP2PLUS adopts a hybrid approach, opting for a particle-in-cell (PIC) formulation for the heavy species (e.g. ions and neutrals), while relying on a fluid model for the electrons, with a kinetic-type closure at the level of the pressure tensor. In many aspects and problems with rarefied plumes, hybrid codes offer the best trade-off in terms of computational time, generality of geometries and conditions, and reliability of results [53].

Although the interaction of a plasma plume with the satellite is clearly an asymmetric phenomenon that depends on the complex geometry of the S/C, most plasma plumes are quasi-axisymmetric (except perhaps for a small asymmetry introduced by a non-centered neutralizer), so that the computation of their properties, including the critical ion backflow at the emission plane, could largely benefit from a 2D (axisymmetric) formulation instead of a 3D one. This work attempts to assess these potential benefits, together with the drawbacks arising from cylindrical effects. To this effect an axisymmetric plume code is developed and its performances and results are compared with those of EP2PLUS. The 2D plume code is an adaptation of a 2D hybrid multi-thruster simulation platform, currently under development, for the analysis of the plasma discharge inside the chamber and the very-near plume of various electromagnetic thrusters, such as the Hall effect thruster (HET) [59] and the Helicon plasma thruster (HPT) [12].

This paper limits the study to unmagnetized plumes, with the electrons modeled as a near-collisionless polytropic fluid [39], and focuses the analysis on the PIC formulation, which is more affected by the change from 3D to 2D and more open to innovative approaches. In fact, the two codes will be tested to operate satisfactorily with up to six heavy species populations with very different densities and energies. Such benchmarking is also beneficial for the 2D multi-thruster simulator, thus further justifying the development of the 2D plume code.

While the 3D PIC module of EP2PLUS operates naturally in a Cartesian spatial mesh, the 2D PIC module of the axisymmetric code uses a 2D cylindrical mesh, which has several important implications on the particle modeling and management. First of all, the cylindrical mesh consists of ring-like cells and the radial coordinate introduces a non-uniformity that needs to be considered in the numerical algorithms. Then, each macroparticle represents a ring of elementary particles (with a uniform distribution along the azimuthal direction), with one rotational (around the symmetry axis) and two translational degrees of freedom, along the radial r and axial z coordinates. Contrary to a uniform Cartesian mesh, the macroparticle contribution to the species density depends strongly on its radius: as it moves radially, its volume of influence (i.e. the volume of the occupied mesh cell) changes, and so does the represented elementary species density.

The radial non-uniformity has also strong implications on the macroparticle weighting scheme: standard weighting schemes like those employed in 3D Cartesian codes [53] can produce systematic errors on the species density. To prevent them, Ruyten [129] proposed density-conserving PIC and cloud-in-cell (CIC) shape factors in cylindrical coordinates, while Larson [130] applied correction factors to the nodal weighted density. In order to generalize these approaches to a non-uniform cylindrical mesh, Verboncoeur suggested the use of corrected nodal weighted volumes in a generalized weighting scheme [69], which has later been applied to general non-uniform and unstructured meshes with triangular and quadrilateral elements by Vázquez and Castellanos [131] and Araki and Wirz [132].

Secondly, the symmetry axis ($r = 0$) introduces difficulties in particle moving and affects the noise level of the PIC-related statistics. Regarding the macroparticles trajectory integration, the axis $r = 0$ is a singularity in the radial equation of motion, in cylindrical coordinates, which may lead to unphysical accelerations at low radii [36]. As to the PIC noise, the weighted (macroscopic) magnitudes at the nodes in the axis are determined by the macroparticles of only two neighboring cells, instead of the 8 cells considered in a 3D Cartesian mesh [see Fig.3.1(a)]. In addition, the lower number of cells surrounding the symmetry axis in the 2D cylindrical domain mesh leads to a quicker macroparticle depletion there.

Sec. 3.2 discusses the most suitable algorithms for an axisymmetric PIC code in order to deal with the above mentioned effects of a cylindrical mesh. Then, Sec. 3.3 cross-validates the 2D code by comparing its maps of the plume expansion with those of EP2PLUS for a high-energy plume, analyzes the spatial evolution of the number of macroparticles per cell, and compares the respective computational times. Finally, the conclusions are drawn in Sec. 3.4.

3.2 The axisymmetric code

Like in EP2PLUS, the axisymmetric code assumes plasma quasineutrality except in the very thin Debye sheaths around material surfaces, treated as discontinuities of the electric potential. In this work, the electron density and temperature follow the simple polytropic law

$$T_e/T_{e0} = (n_e/n_{e0})^{\gamma-1}, \tag{3.1}$$

where n_{e0} and T_{e0} are respectively the electron density and temperature at the reference location where the electric potential ϕ is zero, and γ is the constant polytropic coefficient. For this equation of state, the collisionless electron momentum balance equation leads to an analytical expression for the electric potential [39]:

$$\frac{e\phi}{T_{e0}} = \begin{cases} \ln\left(\frac{n_e}{n_{e0}}\right) & \text{if} \quad \gamma = 1 \\ \frac{\gamma}{\gamma-1}\left[\left(\frac{n_e}{n_{e0}}\right)^{\gamma-1} - 1\right] & \text{if} \quad \gamma > 1 \end{cases}. \tag{3.2}$$

The PIC module of the code follows a Lagrangian description for the heavy species populations (ions and neutrals) [53] and its outputs, after each timestep, are the node-weighted densities, fluxes, and temperatures of all the heavy species under consideration. Then n_e is obtained from plasma quasineutrality and Eq. (3.2) determines ϕ.

Once the electric potential map has been obtained, the electric field $\boldsymbol{E}$ is computed at the PIC mesh nodes and fed back to the PIC module for the next timestep simulation.

The PIC module features two classes of algorithms: *particle-wise* and *mesh-element-wise* algorithms. The former are applied to every macroparticle and include (i) interpolation of electromagnetic fields to the macroparticle position, (ii) integration of the macroparticle trajectory with a leap-frog algorithm, and (iii) macroparticle sorting to the mesh cells. The latter are run for each PIC mesh volume cell or cell-face and involve: (i) the collisional processes between the heavy species particles and with the electrons (i.e. charge exchange and ionization collisions), (ii) the injection of new macroparticles through the corresponding boundary cell-faces, (iii) the volumetric weighting of sorted macroparticles, and (iv) the update of the macroparticle generation weight for each simulated heavy species population to appropriately control the number of macroparticles per cell within a specified interval in stationary conditions. All these algorithms have already been described in detail in Ref. [53] and, in the following, only changes on them due to the axisymmetric geometry are discussed.

3.2.1 Axisymmetric mesh

Both 3D and 2D codes use a structured PIC mesh in order to speed up different particle-to-mesh algorithms (such as the particle sorting and weighting to the mesh nodes) and the mesh-to-particle algorithms (such as the interpolation of the electromagnetic fields from the mesh nodes to the particles position). Fig. 3.1(a) shows a rectangular simulation scenario consisting in a 3D (x, y, z) Cartesian prismatic domain and the corresponding cylindrical 2D (z, r) domain identified by the half meridian plane of the 3D circumscribed cylinder, hereinafter referred to as Ω_0. In the general case, the 3D PIC mesh is composed of prismatic cells with quadrilateral cell-faces, while the 2D cylindrical mesh features quadrilateral cells corresponding to 3D annular or conical volumes and their corresponding cell-faces.

In both cases, it is possible to identify a uniform computational mesh with rectangular elements (cubes in 3D, squares in 2D), with a bijective relation between physical and computational coordinates. As shown in Fig. 3.1(b) for the 2D case, a given physical point $\boldsymbol{r} = (z, r)$ has computational coordinates $\boldsymbol{\xi} = (\xi, \eta)$, where $\xi \in [0, N_\xi - 1]$ and $\eta \in [0, N_\eta - 1]$ are the computational coordinates taking integer values at the nodes, and N_ξ and N_η are the corresponding number of nodes along each coordinate. macroparticles are quickly sorted to the PIC mesh nodes from the knowledge of their computational coordinates, since their integer part provides directly the occupied cell indices.

3.2.2 Particle mover

The Lagrangian description of the heavy species requires computing the trajectory of the p^{th} macroparticle from the integration of Newton equation of motion:

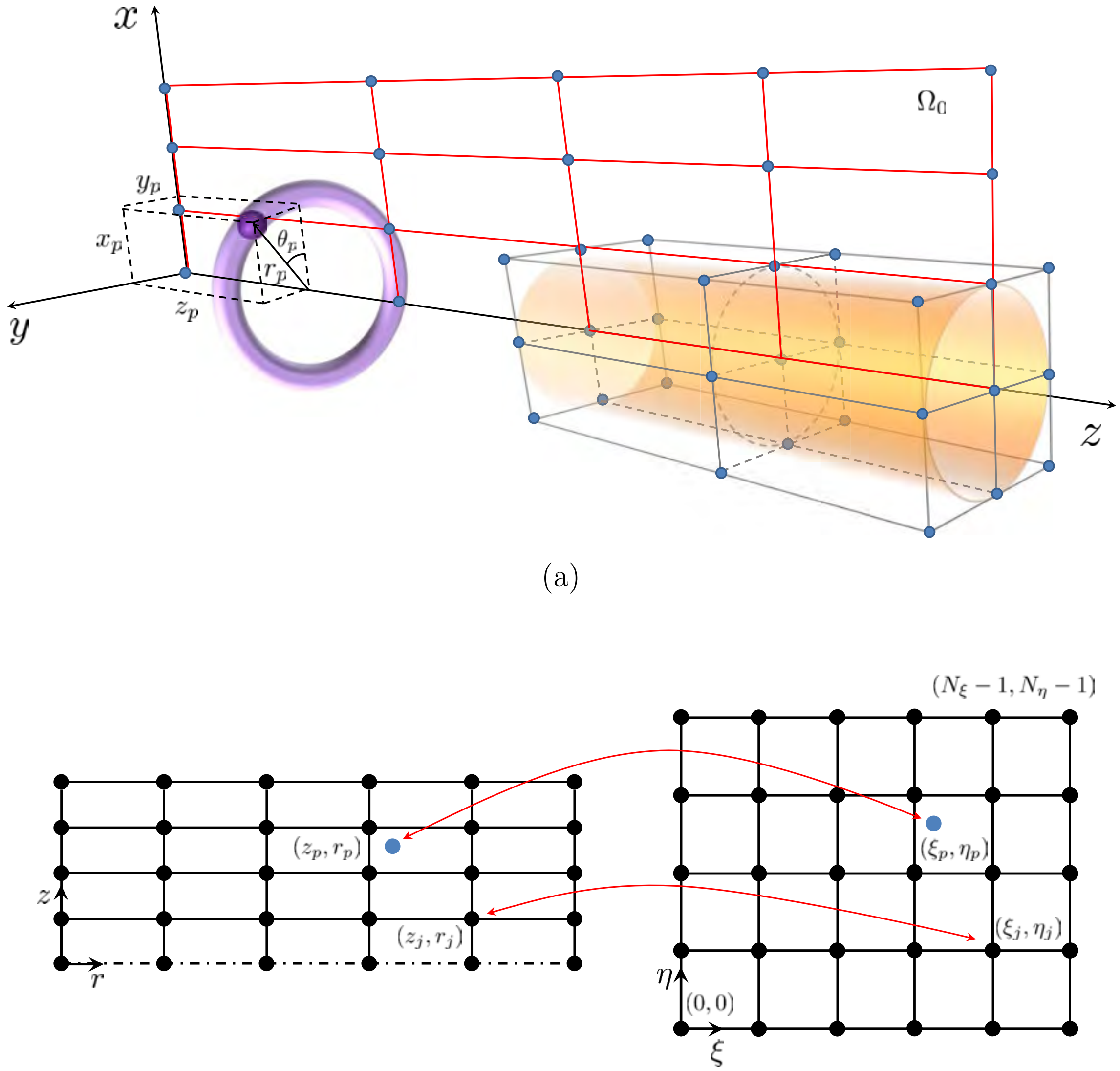

(a)

(b)

Figure 3.1: (a) Simulation scenario consisting in a 3D (x, y, z) Cartesian prismatic domain and the corresponding cylindrical 2D (z, r) domain identified by the half meridian plane of the 3D circumscribed cylinder, Ω_0. The 3D prismatic cells are compared to the 2D cylindrical ones at the axis $r = 0$. A ring-shaped 2D mesh macroparticle is represented, featuring a 3D Cartesian position (x_p, y_p, z_p) equivalent to the cylindrical position (r_p, θ_p, z_p), being $r_p = \sqrt{x_p^2 + y_p^2}$ and $\cos(\theta_p) = x_p/r_p$, $\sin(\theta_p) = y_p/r_p$. (b) Sketch of the physical and computational 2D structured meshes used for plume simulations. The dot-dashed line indicates the symmetry axis.

$$m_p \frac{d\boldsymbol{v}_p}{dt} = eZ_p \left(\boldsymbol{E}_p + \boldsymbol{v}_p \times \boldsymbol{B}_p \right), \tag{3.3}$$

where $\boldsymbol{E}_p$ and $\boldsymbol{B}_p$ are respectively the electric and magnetic fields at the macroparticle position ($\boldsymbol{B}_p = \boldsymbol{0}$ in the present work), e is the electron charge, and m_p and Z_p the elementary particle mass and charge number. In EP2PLUS, a 3D particle mover based on the Boris CYLRAD algorithm [22] integrates the ion and neutral macroparticles trajectories, solving Eq. (3.3) through a generalized second order leap-frog algorithm, which leads to a time shift $\Delta t/2$ between the particles position and velocity, Δt being the PIC integration timestep. Therefore, if k is the current timestep index, the particles position is known at time k while the particles velocity at time $k - 1/2$. Direct integration in cylindrical coordinates yields non-physically large azimuthal accelerations when a particle moves close to the axis $r = 0$ [36]. In order to avoid this problem, the 2D code integrates the particles trajectories using the same 3D Cartesian particle mover algorithm, thus obtaining, for every particle, its 3D Cartesian velocity $\boldsymbol{v} = (v_x, v_y, v_z)$ and position $\boldsymbol{x} = (x, y, z)$. Then, in order to perform the particle sorting and weighting to the PIC mesh nodes, every particle is projected into the 2D plane Ω_0 [see Fig. 3.1(a)], in which the 2D cylindrical particle position $\boldsymbol{r} = (z, r)$ is obtained taking $r = \sqrt{x^2 + y^2}$.

Thus, the radial turning point of the particle near the axis $r = 0$ is automatically reproduced. The particle computational coordinates $\boldsymbol{\xi} = (\xi, \eta)$ are then computed from its 2D physical position (z, r) and used to sort the particle to the PIC mesh cells and weight it to the corresponding nodes. The computation of the higher order moments of the velocity distribution function (e.g. species fluxes and temperatures) requires to rotate the particle velocity to the plane Ω_0 from the particle actual azimuthal position θ, defined by $\cos\theta = x/r$ and $\sin\theta = y/r$. Note that, at Ω_0, $v_x \equiv v_r$ and $v_y \equiv v_\theta$, being this last velocity component responsible for the azimuthal rotation of the ring-like particles in a 2D cylindrical domain.

3.2.3 Particle volumetric weighting

The macroscopic magnitudes characterizing the simulated populations, such as the densities, the fluxes, and the temperatures, are obtained by weighting the particle distributions to the nodes of the PIC mesh. This process links the macroparticles with the domain mesh and implies some form of interpolation from the macroparticles to the mesh nodes and viceversa. An ensemble of N macroparticles in a 2D cylindrical domain can be described by the exact macroparticle density

$$n_d(\boldsymbol{r}) = \sum_{p=1}^{N} \frac{W_p}{2\pi r_p} \delta(\boldsymbol{r} - \boldsymbol{r}_p), \tag{3.4}$$

where $\boldsymbol{r}_p = (z_p, r_p)$ is the position of the p^{th} macroparticle, which actually represents a ring of W_p elementary particles uniformly distributed along the azimuthal direction [see Fig. 3.1(a)], and $\delta(z, r)$ is the Dirac function (which gives 1 when integrated in a volume containing r_p). In PIC codes, the corresponding smoothed particle density at the mesh node j is obtained by integrating in space the exact macroparticle density n_d of Eq. (3.4) weighted by a nodal shape function $S_j(\boldsymbol{r}')$, and then dividing by the weighting volume ΔV_j associated to the node as

$$n_j = \frac{1}{\Delta V_j}\int_{ROI} n_d(\boldsymbol{r})S_j(\boldsymbol{r}')2\pi r\, dr dz = \frac{1}{\Delta V_j}\sum_p W_p S_j(\boldsymbol{r}'_p), \tag{3.5}$$

where $\boldsymbol{r}' = \boldsymbol{r} - \boldsymbol{r}_j$ is the physical position relative to the node and the integral extends throughout the nodal region of influence (ROI).

In order to deal with general non-uniform cylindrical meshes, the weighting process is performed in the uniform computational domain considering the bilinear shape function defined in Ref. [45], $S_j(\boldsymbol{\xi}')$, which, for the j^{th} node with computational coordinates $\boldsymbol{\xi}_j = (\xi_j, \eta_j)$, depends on the macroparticles relative computational coordinates $\boldsymbol{\xi}' = (\xi', \eta') = (\xi - \xi_j, \eta - \eta_j)$.

Regarding the weighting volume associated to the nodes, as it was already considered in Ref. [45], systematic errors in cylindrical coordinates are avoided using the corrected weighted nodal volumes of Ref. [69], defined as

$$\Delta V_j = \iint_{ROI} 2\pi r(\xi,\eta) S_j(\xi - \xi_j, \eta - \eta_j)|\mathcal{J}(\xi,\eta)| d\xi d\eta, \tag{3.6}$$

where $|\mathcal{J}(\xi,\eta)| = |\partial(z,r)/\partial(\xi,\eta)|$ is the determinant of the Jacobian matrix, which, along with the radial coordinate $r(\xi,\eta)$, is interpolated from its known values at the nodes using again the same shape function S_j. (Note that the same integral scheme should be applied to a generic irregular 3D mesh, with the only difference of a now missing $2\pi r$ term, and an extra coordinate ζ.) For the inner nodes of a 3D uniform Cartesian mesh, Eq. (3.6) (generalized to 3D) yields the constant physical volume of the cells [53] (at the boundaries, the weighting volume reduces with the number of applicable cells).

3.2.4 Particle distribution and population control

As explained in Ref. [53], new macroparticles are introduced in the simulation domain from the boundary cell-faces (either injection or material wall) and are generated in the bulk domain due to the different collisional processes, the main ones being ionization and charge exchange (CEX) collisions. In both 3D and 2D codes, all these processes involve the generation and distribution of macroparticles inside a given mesh cell, and use an appropriate cell-wise generation weight W_{gen}.

Let N_{gen} be the number of new macroparticles to be produced in a given timestep inside a given cell, and W_{gen} the corresponding generation macroparticle weight in the cell. In both 3D and 2D codes, the particles are uniformly distributed inside the regular computational cells, which greatly reduces the computational cost in the general case of non-uniform domain meshes. However, unlike in the 3D code, in which all particles in the cell are generated with the same macroparticle weight W_{gen}, in the axisymmetric formulation the cylindrical geometry is taken into account by introducing a linearly varying macroparticle weight with the radius within the cell, so that W_{gen} now represents the average macroparticle generation weight in the cell, and the p^{th} macroparticle, generated at the radius r_p, takes the weight:

$$W_p = \frac{r_p}{\overline{r}_{cell}} W_{gen} \tag{3.7}$$

where $\overline{r}_{cell}$ is the cell mean radius, or the average generation radius for the considered uniform distribution. It is worth mentioning that this radius dependence is considered

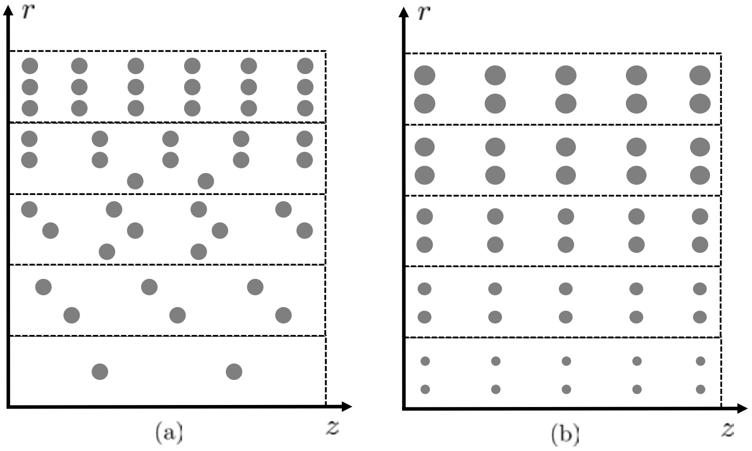

Figure 3.2: Two different approaches for the global population control. In (a) the macroparticle weight is uniform while the number of macroparticles per cell grows linearly with the cells volume (in this case with the radius). In (b) the number of macroparticles per cell is constant, and the weight grows linearly with the mean cell radius.

only for the weight at the generation stage; once generated, the macroparticle conserves its weight until the next collisional event.

In order to limit the PIC noise, especially critical at the symmetry axis of the 2D cylindrical simulation scenario, the EP2PLUS population control is here adapted to the 2D code as well. As explained in Ref. [53], the number of macroparticles per cell is kept within a specified range by updating appropriately the generation weight W_{gen}. This approach can only work properly for those mesh cells featuring a dominant particle generation process (i.e. injection, neutral reinjection due to ion recombination, or collisional processes), and, for a plasma plume simulation like the one shown in Sec. 3.3, provides satisfactory results with a minimum computational effort (when compared to particle resampling or merging/splitting approaches [133, 134]).

The 2D code can then feature different approaches for what concerns the targeted number of macroparticles per cell. While a constant density field n_0 can be reproduced in the Cartesian 3D case with uniform values for the macroparticle weight and number per cell, in a uniform 2D cylindrical mesh, the linearly increasing cells volume with the radius must be taken into account. In order to reproduce the constant density field n_0, two choices are available. The first one, hereinafter named (A), shown in Fig. 3.2(a), is to set a constant macroparticle weight per cell and let the targeted number of macroparticles per cell vary linearly with the cell volume (or equivalently in this case with the radius). The second approach, referred to as (B), illustrated in Fig. 3.2(b), considers a constant number of macroparticles per cell in the whole domain, and includes the cylindrical effect on the macroparticle weight.

The performance of both approaches is compared considering two populations: (i) a monoenergetic singly charged ion population injected radially with a Gaussian profile [see Eq. (3.8)] and with zero temperature, and (ii) a thermal neutral population injected with a flat density profile and sonic conditions. Both populations are injected at $z = 0$, between $r = 0$ and $r = 14$cm. The ion injection properties are the same as those of Tab. 3.1 (except for the zero injection temperature), while the neutrals feature the same injected mass flow

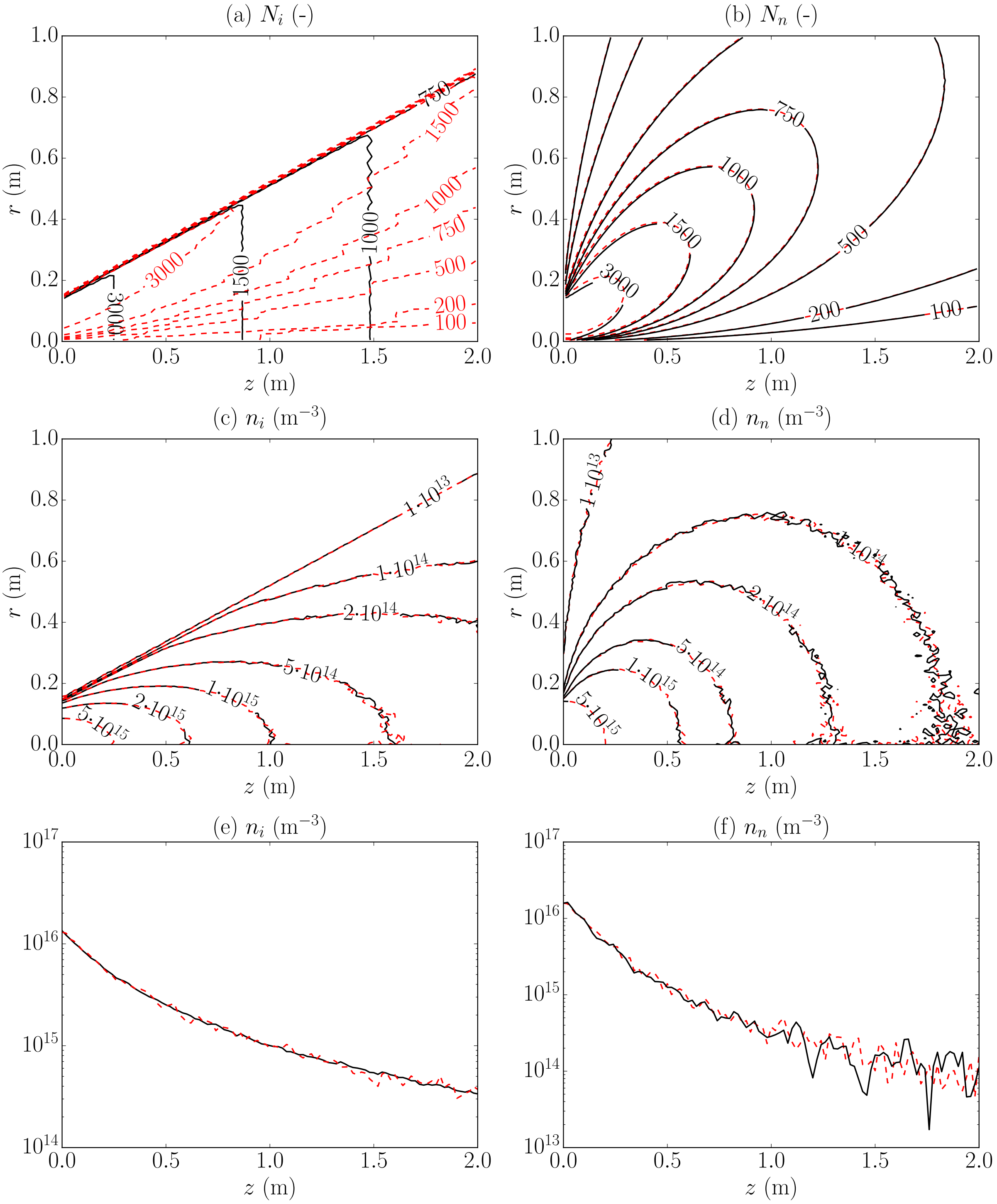

Figure 3.3: Comparison of population control approaches (A) (red dashed lines) and (B) (black solid lines). Number of particles per cell for (a) monoenergetic ions and (b) thermal neutrals. Weighted particle density for (c) monoenergetic ions and (d) thermal neutrals. Axial evolution of the weighted particle density at the symmetry axis for (e) monoenergetic ions and (f) thermal neutrals.

as the ions, the same axial fluid velocity and a temperature $T_n = (3/5)m_n u_n^2$, where m is the neutral elementary mass (xenon is considered) and u_n the injection axial velocity. Both populations and control approaches feature the same average number (5000 here) of macroparticles at injection cells. While this is constant in the approach (B) for all injection cells, the approach (A) features a linearly varying number with the injection cell radius.

The number of macroparticles per cell and the weighted species density obtained with both approaches are shown in Fig. 3.3. Time-averaged values over 2000 simulation timesteps are considered for the number of macroparticles per cell, while instantaneous ones (i.e. at the last simulation timestep) are shown for the species densities. As expected, the monoenergetic ion population clearly benefits from the constant number of macroparticles per cell in the approach (B), which, for the same total number of macroparticles in the domain, keeps a higher number of macroparticles in the cells at $r = 0$, and thus helps keeping low the noise level along the axis.

On the contrary, the local particle weight dispersion (i.e. the standard deviation of particle weights in a given cell) in approach (B) leads to a higher noise level in the weighted density at the symmetry axis for the thermal neutrals. Unlike for the injected ions (or ions generated inside an ionization chamber), which are pushed radially outwards from the symmetry axis by the ambipolar electric fields, large neutral macroparticles (injected far from the symmetry axis) can cross radially the domain and reach the symmetry axis, thus producing large variations in the weighted magnitudes there. Contrary to the case of the monoenergetic ions, the number of neutral macroparticles per cell tends to the same value downstream regardless of the considered distribution, albeit with a different weight dispersion. Therefore, the choice of the optimal population control strategy depends on the dynamics of the injected population. Following these conclusions, the results from the 2D code shown in Sec. 3.3 have been obtained with the approach (A) for the injected thermal neutral population, and approach (B) for the quasi monoenergetic ion populations.

3.3 Code benchmarking and discussion of the results

3.3.1 Simulation settings

The 2D axisymmetric code is validated by simulating an expanding plasma plume similar to that of the NASA's NSTAR gridded ion thruster [135, 136], and comparing its results with those obtained by the 3D EP2PLUS code for the same plume. The simulation domain is a 2 m side cube for the 3D simulation and a cylinder of 1 m radius and 2 m length for the 2D one. The mesh spacing, the number of nodes along each direction and the main simulation parameters are listed in Tab. 3.1. The thruster injection area is circular with a 14 cm radius.

Three different heavy species based on xenon are injected: neutrals, singly charged and doubly charged ions. A flat injection density profile and a sonic velocity (based on its own temperature) is considered for the neutrals. On the other hand, the injection profiles of the density n, the axial and radial velocities u_z and u_r of singly and doubly charged ions, follow a generalized Parks-Katz radial plume profile [39, 137, 138]:

$$n(r) = n_0 \exp\left(-\frac{C}{2}\frac{r^2}{R_0^2}\right), \quad u_z(r) = u_{z0}\left(\frac{n}{n_0}\right)^{\frac{\gamma-1}{2}}, \quad u_r(r) = u_z \frac{r}{R_0}\tan\alpha_0, \tag{3.8}$$

where n_0 and u_{z0} are the density and axial velocity at $r = 0$, γ is the electron polytropic coefficient, $C = 5.44$, and α_0 represents the ion streamline divergence angle at the outermost radius $R_0 = 14$ cm. This angle is set to 20.5 and 30 degrees for, respectively, the singly and doubly charged ions. While the resulting divergence efficiency matches the values found in the literature, the choice of the divergence angles of both species is not unique: since the ion grid optics of the thruster are presumably optimized for the singly charged ions, they here feature a lower divergence angle. Regarding the doubly charged ion current, it amounts to 9.1% of the singly charged ion current [135, 136].

The following collisional reactions are considered [53]:

- Ionization collisions: $\mathrm{Xe} + e \to \mathrm{Xe}^+ + 2e$, $\mathrm{Xe} + e \to \mathrm{Xe}^{++} + 3e$, and $\mathrm{Xe}^+ + e \to \mathrm{Xe}^{++} + 2e$
- Symmetric CEX collisions: $\mathrm{Xe}^+(\mathrm{fast}) + \mathrm{Xe}(\mathrm{slow}) \to \mathrm{Xe}^+(\mathrm{slow}) + \mathrm{Xe}(\mathrm{fast})$, and $\mathrm{Xe}^{++}(\mathrm{fast}) + \mathrm{Xe}(\mathrm{slow}) \to \mathrm{Xe}^{++}(\mathrm{slow}) + \mathrm{Xe}(\mathrm{fast})$

It is underlined that the asymmetric non-resonant CEX reaction [$\mathrm{Xe}^{++}(\mathrm{fast}) + \mathrm{Xe}(\mathrm{slow}) \to \mathrm{Xe}^+(\mathrm{fast}) + \mathrm{Xe}^+(\mathrm{slow})$] has not been included since its cross section is much lower than that of the symmetric reactions [79]. The above reactions create populations with very different densities and energies from those of the injected particles. To have an adequate population control and correct macroscopic magnitudes of the minor species, we consider six particle populations, each one with its own computational list. They are detailed in Tab. 3.2, with their corresponding subscripts.

The timestep in Tab. 3.1 is set so that, on average, a fast doubly charged ion crosses no more than one PIC cell per simulation step, while the simulation duration (set to 50000 timesteps, equivalent to 15 ms) is sufficiently long to reach stationary conditions for the slowest particle population (injected neutrals, with a residence time of about 8 ms). Regarding the population control algorithm, the targeted number of macroparticles per cell for all populations is 500 (with control range of ±10%), except for the fast CEX neutrals, generated deterministically (i.e. directly taking the particle properties of the corresponding colliding fast ion) and therefore featuring no active population control. In fact, the intermittent generation and the monoenergetic distribution of such neutrals makes the monitoring of their macroparticle weight and number nearly ineffective, in terms of noise control. On the other hand, a proper visualization of their density requires an extremely large number of averaging timesteps, which is here set to 2000.

Finally, regarding the electrons, we have chosen a polytropic coefficient of $\gamma = 1.2$, consistent with experimental observations and implying a mild cooling along the plume (i.e. the temperature drops by 37% when the density decreases by a factor of 10), and a temperature $T_{e0} = 3.5$ eV at the potential reference node, located 6cm downstream of the injection plane $z = 0$.

Simulation parameter	**Units**	**Value**
3D (x, y, z) mesh number of nodes	-	$201 \times 201 \times 101$
2D (r, z) mesh number of nodes	-	101×101
3D mesh number of cells	-	$4 \cdot 10^6$
2D mesh number of cells	-	10^4
Mesh spacing ($\Delta x = \Delta y \equiv \Delta r$, Δz)	cm	1, 2
Simulation timestep	s	$3 \cdot 10^{-7}$
Number of simulation steps	-	50000
Time-averaging steps number	-	2000
Number of macroparticles per cell	-	500
Injected Xe velocity	m/s	247 (sonic)
Injected Xe temperature	eV	0.05
Injected Xe mass flow	mg/s	0.265
Injected Xe$^+$ kinetic energy	eV	1040
Injected Xe$^+$ temperature	eV	0.1
Injected Xe$^+$ mass flow	mg/s	2.40
Injected Xe^{++} kinetic energy	eV	2080
Injected Xe^{++} temperature	eV	0.2
Injected Xe^{++} mass flow	mg/s	0.109

Table 3.1: Main simulation parameters. The considered meshes are uniform for both 2D and 3D simulations. The number of macroparticles per cell is controlled at injection cells for the injected populations and where collisional effects are not negligible for collisional populations. The reference electron temperature refers to the position $r = 0, z = 6$ cm, slightly downstream of the injection plane, where $\phi = 0$.

Population subscript	**Description**
$i1s$	Slow Xe$^+$ ions from ionization and CEX
$i1f$	Fast injected Xe$^+$ ions
$i2s$	Slow Xe^{++} ions from ionization and CEX
$i2f$	Fast injected Xe^{++} ions
ns	Slow injected Xe neutrals
nf	Fast Xe neutrals from CEX

Table 3.2: Different macroparticles populations considered in the simulations, with a dedicated computational particle list for each of them.

3.3.2 Simulation results and discussion

The results shown in this section refer to time-averaged quantities over 2000 PIC timesteps. The electric potential in the meridian plane Ω_0 ($z - r$ plane) is shown for both 2D and 3D simulations in Fig. 3.4(a). It is monotonically decreasing both axially and radially except for the bump on the side of the main plume, which is due to the formation of CEX ions. Far downstream, when vacuum is reached, the total potential drop is $\gamma T_{e0}/[e(\gamma - 1)] = 21$ V, according to Eq.(3.2). Such a value is approached in nearly depleted regions of the plasma plume that are located radially outwards at $z = 1$ m. However, at the centerline, 2 m downstream from the injection plane, the potential

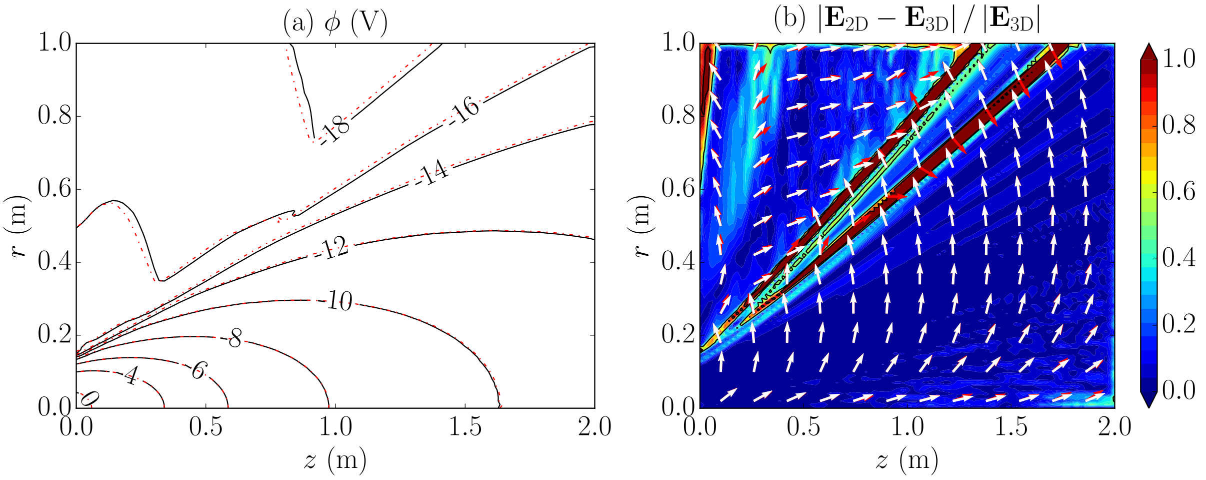

Figure 3.4: Comparison of (a) electric potential and (b) electric field relative reconstruction error at the Ω_0 plane. In (a), the solid black lines refer to the 3D simulation, while the red dash-dot lines to the 2D simulation. In (b) white and red arrows show the direction of the electric field in respectively the 3D and 2D simulation.

fall is just around 11 V.

The relative error in the ambipolar electric field (between 2D and 3D simulations) and the field direction are shown in Fig. 3.4(b). As expected, the electric field vector is directed radially outwards and, at the plume centerline, along the plume expansion. In the areas populated by CEX ions, on the other hand, the axial component of the electric field inverts and produces the well known ion backflow phenomenon [53,128]. The differences between the 2D and 3D electric field are finally negligible everywhere except at the boundaries of the main plume core, where the number of macroparticles is particularly small, and close to the injection plane boundary at large radii, where the effect of the different simulation box geometry (cylinder versus cube) becomes important.

Fig. 3.5 depicts some relevant properties of the six heavy particle populations. All results show a very good agreement between the 2D and 3D codes, and, more importantly, the capability of reproducing with a good level of noise the statistics of populations differing several orders of magnitude in density. In fact the densities of the particle populations produced by collisional events are 2-3 orders of magnitude lower than those of the injected populations.

Xe^+ and the slow CEX Xe^+ densities are shown respectively in Figs. 3.5(a) and (b). The total Xe^+ density is dominated by the injected ions in most of the domain, except at the lateral plume regions where injected ions are totally absent. Their density is maximum at the injection plane centerline, where it is above 10^{16} m^{-3}, and reduces monotonically downstream because of both the injection divergence angle and the effect of the ambipolar electric field. The CEX singly charged ions are mainly generated in the near-region (within 50 cm axially and 20 cm radially from the injection plane centerline), they reach a peak density above 10^{14} m^{-3} and quickly vanish downstream as they are accelerated radially and axially outwards by the electric fields. At the injection plane, their density decays radially to values as low as $3 \cdot 10^{12}$ m^{-3} at $r = 1$ m.

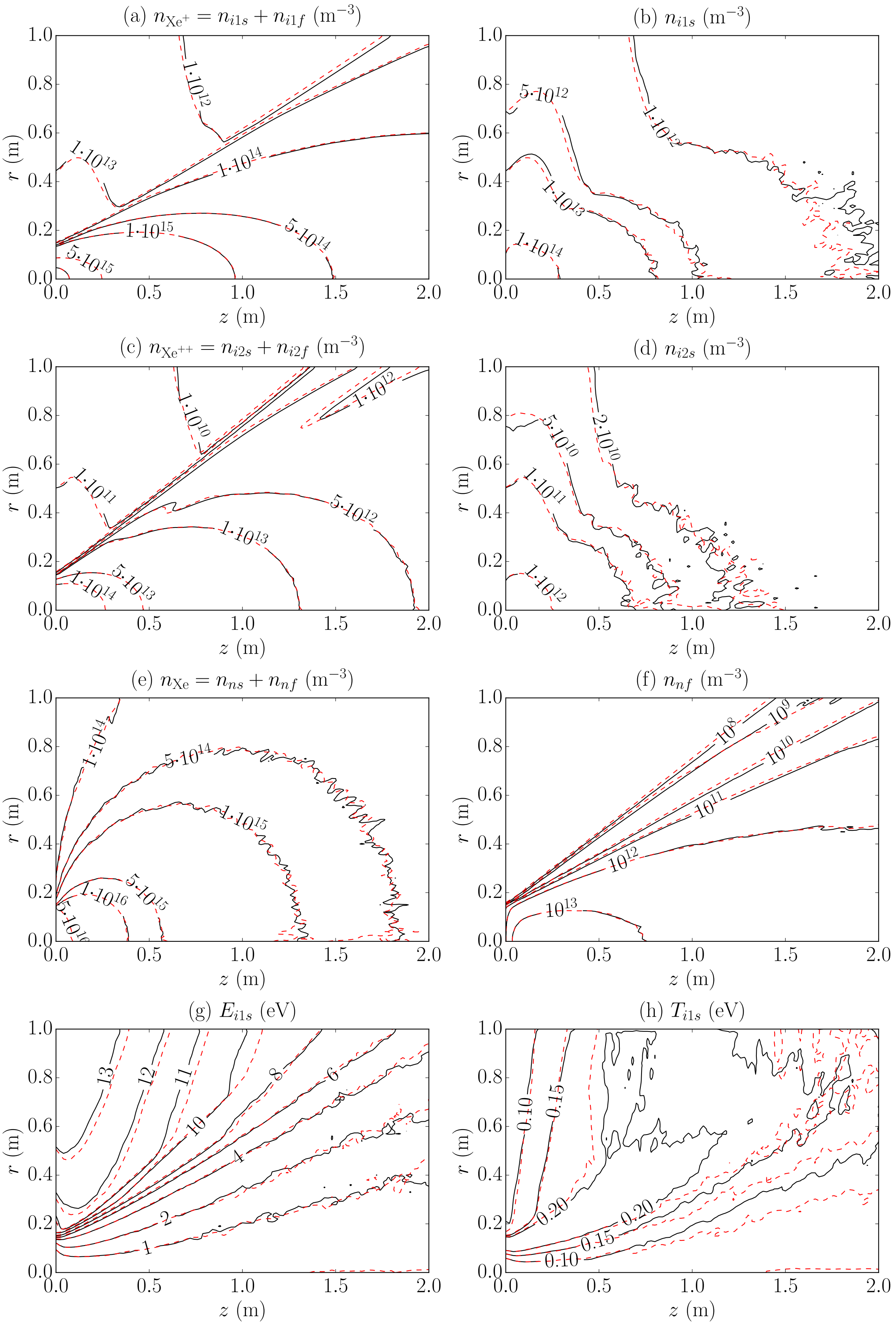
(a) $n_{\mathrm{Xe}^+} = n_{i1s} + n_{i1f}$ (m^{-3})

(b) n_{i1s} (m^{-3})

(c) $n_{\mathrm{Xe}^{++}} = n_{i2s} + n_{i2f}$ (m^{-3})

(d) n_{i2s} (m^{-3})

(e) $n_{\mathrm{Xe}} = n_{ns} + n_{nf}$ (m^{-3})

(f) n_{nf} (m^{-3})

(g) E_{i1s} (eV)

(h) T_{i1s} (eV)

Figure 3.5: Comparison of (a) total Xe$^+$, (b) slow Xe$^+$, (c) total Xe^{++}, (d) slow Xe^{++}, (e) total Xe and (f) fast CEX Xe neutral particle densities, and (g) slow Xe$^+$ average energy (thermal plus average motion) per particle and (h) temperature, at the Ω_0 plane. Both 2D (red dashed lines) and 3D (black solid lines) results are shown.

The total density of doubly charged Xe ions is shown in Fig. 3.5(c). These ions have a larger injection divergence angle than the singly charged ones, and, at the outer periphery of the main plume core, they are repelled by the latter, so that they present a local minimum density around 10^{12} m^{-3} at the upper right corner of the simulation domain. It is underlined that this effect has not been observed experimentally, and is clearly related to our choice of the injection divergence angle for the two ion species. The slow Xe^{++} ions, shown in Fig. 3.5(d), present a peak density of $3 \cdot 10^{12}$ m^{-3} at the centerline, which decreases quickly both radially and axially outwards.

The total neutral density is shown in Fig. 3.5(e) and is dominated clearly by the injected sonic population, which expands almost spherically and whose density decays more quickly than that of the injected ions, from $7 \cdot 10^{16}$ m^{-3} at the injection plane centerline, to $4 \cdot 10^{14}$ m^{-3} at the centerline, 2 m downstream. The CEX neutrals, shown in Fig. 3.5(f), on the other hand, are particularly fast and highly focused so that their density decay is much smaller (a factor of 10 in 2 m axial expansion), and present a peak density above $2 \cdot 10^{13}$ m^{-3} slightly downstream from the injection plane.

Another important property of the plume that the two codes are able to characterize is the average energy of slow ions (thermal plus average motion) generated by CEX collisions, shown in Fig. 3.5(g). The backflow ions (which produce spacecraft sputtering and contamination) have energies in the order of 12-13 eV on average and tend to migrate quickly radially outwards. In fact, the average ion energy does not increase axially downstream, as it should if the CEX ions were accelerated along the corresponding potential drop [$\sim 5-10$ V, as shown in Fig. 3.4(a)]. This means that the downstream slow ions density is primarily dominated by ions produced in the vicinity, with a very small collision cross section, given the extremely low ion and neutral densities there. Finally, Fig. 3.5(h) shows the slow ions temperature, which takes relatively low values, below 0.3 eV, compared to their total energy. This means that the CEX ions are a nearly monoenergetic population. The differences in temperature at larger radii and axial distances can be attributed to a lower number of macroparticles per cell in the 3D case (induced by the setting of a minimum ion generation weight to reduce the total computational cost), which affects the computed statistics.

While the physical plume properties show minimal differences, which validates the 2D simulator, important differences between the 2D and 3D simulations are found in the evolution of the number of macroparticles per cell for both injected populations (ions and neutrals). The number of injected Xe^{+} ion macroparticles per cell is compared in Fig. 3.6(a). While the number of macroparticles per cell is the same at the injection plane (500), the axial decrease in the 3D simulation is much quicker, given the higher dimensionality of the simulation domain (macroparticles have 3 degrees of freedom in position, thus experimenting a larger dispersion). In particular, a number of slightly less than 10 macroparticles per cell is found in 3D, at $z = 2$ m, versus approx. 80 macroparticles per cell in 2D (depending on the considered radius). Nevertheless, the highest value is always found at the centerline for the 3D case, while the 2D case shows a local minimum there. This is also true in Fig. 3.6(b), which shows the number of macroparticles per cell for the injected neutrals. Since this population is sonic at injection, the expansion is nearly spherical and the number of macroparticles per cell drops much quicker than for the ions. Once again, in 3D we observe a quicker drop in number of macroparticles per cell as the plume expands downstream, and a maximum number always at the symmetry axis. In 2D, on the other and, the axis always features a local minimum in number of macroparticles per cell, with a maximum found along the streamline containing 50% of the total axial particle flow [blue solid line in Fig. 3.6(b)].

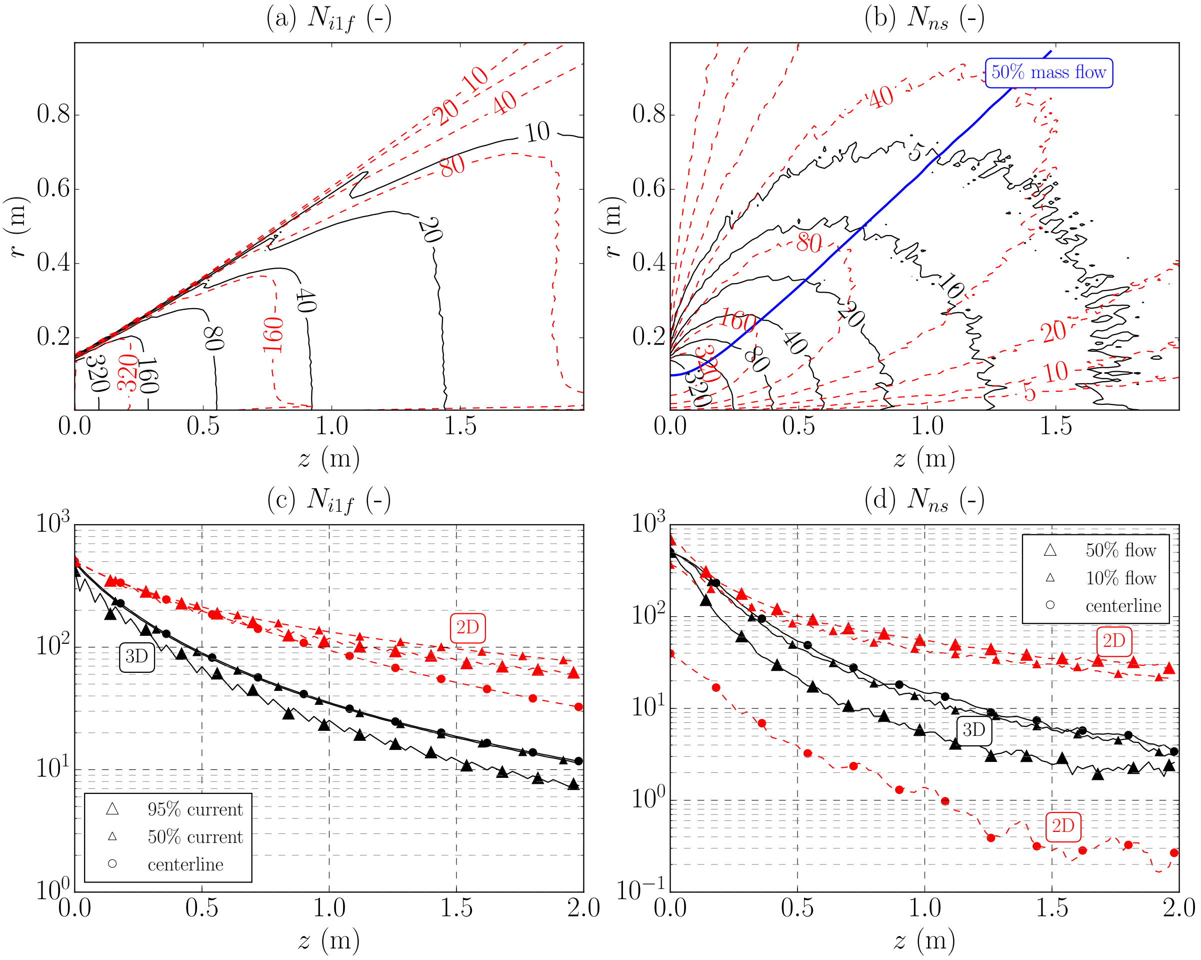

Figure 3.6: Comparison of the number of macroparticles per cell for (a) injected ion and (b) injected neutrals at the Ω_0 plane, (c) injected ions and (d) injected neutrals along different streamlines. Both 2D (red dashed lines) and 3D (black solid lines) simulation results are shown. In (b), the blue solid line shows the radius of the stream tube containing 50% of the total axial neutral flow. In (c), circles are used for the evolution along the centerline, small upwards triangles for the evolution along the 50% flow streamline and big upwards triangles for the evolution along the 95% flow streamlines. In (d), circles are used for the centerline, small upwards triangles for the 10% axial flow streamline, and big upwards triangles for the 50% axial flow streamline.

The evolution of the number of macroparticles per cell along different ion and neutral streamlines is shown respectively in Figs. 3.6(c) and (d). The streamlines are identified in terms of the percentage of the total axial particle flow contained in the corresponding streamtube. In the ion case, at $z = 0$ the number of macroparticles per cell is 500, as set by the simulation parameters, for all streamlines. In the neutral case, this is only true for the 3D simulation, since the 2D code follows the population control approach (A), with a constant injection macroparticle weight (see Sec. 3.2.4), and hence, a linearly variable number of macroparticles per cell (with the cell radius). The centerline depletion of injected neutrals in the 2D simulation is very clear: the number of macroparticles per cell drops to less than 1 (as time-average), for $z > 1$ m, and this decay is quicker there than along any other streamline, because of the smaller cells volume (which is proportional to the radius in a uniform mesh). Moreover, the 2D simulation axis is more critical than the 3D simulation one because the latter presents a much larger number of injected macroparticles that can potentially cross it downstream. In fact, while the probability of crossing a centerline cell is the same for both 2D and 3D macroparticles (the particle mover algorithm is 3D in both cases), the number of macroparticles injected in the radial interval dr of the injection plane is much larger in the 3D case (a ring of 3D cells inject macroparticles between r and $r + dr$, versus only one cell in the 2D case).

Finally, a key feature in the 2D versus 3D comparison is the large difference in computational time, for the same simulation time and comparable PIC noise. The total number of macroparticles of the 3D case is 143 million, versus the 6.48 million particles of the 2D case. This number ratio of 22 is only partially mitigated by the total computational cost per timestep per 2D macroparticle, that is approximately twice as large: 6 μs versus 3 μs (using one single thread). Therefore, the 2D code is approximately 10 times quicker in carrying out a plume simulation with a comparable noise level. This time gain is very significant for extensive research activity, considering that each 3D simulation presented here has required a computational time of around a week, using 40 threads in an up-to-date workstation.

3.4 Conclusions

A new cylindrical axisymmetric code devoted to the simulation of plasma plumes expansion into vacuum has been developed and validated against an already existing 3D plume code. The 2D cylindrical geometry introduces non-trivial difficulties in the particle modeling. The already available 3D Cartesian particle mover is applied to avoid unphysical macroparticles accelerations near the symmetry axis, while the radial expansion is taken into account in both the macroparticles weighting and generation within the domain. Regarding the latter, two different population control approaches have been proposed to limit the noise level, which is especially critical at the 2D domain symmetry axis. It has been found that the optimal algorithm depends on the dynamics of the simulated macroparticle population: monoenergetic populations benefit from a constant target number of macroparticles per cell, while a constant macroparticle generation weight is recommended for thermal populations.

The simulation of a typical plasma plume expansion scenario based on an ion thruster has been considered to compare and benchmark the 2D code against the 3D one, and show their capabilities. An excellent agreement is found between the codes, which are both capable of reproducing, with an acceptable noise level, the properties of heavy particle populations with densities differing by several orders of magnitude (i.e. the injected and CEX ions populations).

As expected, the simulation of a plasma plume expansion into vacuum greatly benefits from a 2D formulation, which allows for a significant reduction of the computational time (a factor of 10) while keeping a similar PIC statistics noise level. However, the symmetry axis still remains the weak point of the 2D code. Further work will deal with the development of a cell-wise particle rezoning algorithm to better control the noise downstream through the resampling of the particle populations from their retrieved distributions. Besides, the particle weighting and population control could benefit from using a domain mesh in the variables (z, r^2), mapped into the computational coordinates (ξ, χ). A bilinear weighting in such computational coordinates would correspond to an area weighting scheme, and the population control could benefit from both a constant number of macroparticles and a constant generation weight per cell. This condition is naturally reproduced with a uniform mesh in (z, r^2), at the cost of a lower resolution at the symmetry axis.

As a final comment, the PIC codes discussed here, with a polytropic closure for electrons, can deal only with unmagnetized plasma plumes, which is the case of ion thrusters and other electrostatic thrusters (e.g. electrospray ones). For Hall effect thrusters and other electromagnetic thrusters, only the far plume is unmagnetized, while the near plume and the in-chamber plasma jet present strongly magnetized electrons, but marginally magnetized ions. This means that the 2D-to-3D PIC comparison discussed here continues to be valid in these cases, but the electron model to be coupled with the PIC one, must be changed. Full 2D axisymmetric models for highly magnetized electrons both in the chamber and the near plume of both Hall effect and Helicon plasma thrusters are being developed [59, 60, 67]. A 3D model of mildly magnetized electrons, to be matched with EP2PLUS, is under development too [139].

Chapter 4

Simulation of axisymmetric plasma discharges

This Chapter is focused on the analysis of axisymmetric plasma discharges in two different scenarios. In the first one, a simple geometrical configuration, typical of the HPT or ECRA, consisting of a cylindrical channel with a high surface-to-volume ratio is considered. The simple case of an unmagnetized discharge with isothermal electrons permits a further assessment of the HYPHEN hybrid code performance and the study of relevant aspects of the discharge. In particular, different discharge ignition procedures are analyzed, and the effect of the neutral gas-wall interaction on the discharge is evaluated in detail. The second part of the Chapter is devoted to HET discharges simulations. In particular, a typical SPT-100 thruster simulation scenario is used as a benchmark case to assess the performance of the electron-fluid model NOMADS, originally developed by Pérez-Grande [59, 60] for the isotropic electron pressure case, to which the improvements described in Chapter 2 have been incorporated. First, in order to limit the computational time of NOMADS, the effects on the simulation results of the NOMADS number of time sub-iterations is addressed. Moreover, several numerical issues are identified, and plausible strategies to solve them are proposed as future work. Second, based on the analysis performed in the first part of this Chapter, the effect on the breathing mode characteristic frequency of the neutral-wall reflection type is investigated. Third, the performance of the volumetric cathode model is tested by placing the cathode at different locations in the thruster near plume region. Finally, preliminary results for different values of the electron anomalous transport parameter are shown.

4.1 Analysis of a plasma discharge in a cylindrical channel

The simulation of an unmagnetized plasma discharge featuring isothermal electrons in a cylindrical channel with a high surface-to-volume ratio is analyzed in detail in this section. Such a simple scenario serves as a benchmark case facilitating a further evaluation of the HYPHEN code performance, and revealing several important modeling issues.

The first one corresponds to the discharge ignition process in quasineutral hybrid codes, which is directly related to the modeling of the ionization collisions, responsible for the plasma generation in the simulation domain. Unlike full PIC codes, in which not only the heavy species but also the electrons are treated as macroparticles following a Lagrangian approach, quasineutral hybrid codes such as HYPHEN consider a fluid model for the electron population, its density being given by Eq. (2.60). Hence, according to Eq. (2.40), in order to perform the ionization collisions at the initial stage of the simulation, the plasma density must be set to a minimum, or, equivalently, the domain must be seeded with given initial ion populations. The former strategy shall be hereinafter referred to as MD (minimum density), while the latter shall be named as IP (initial population). It is stressed that in the MD approach, the minimum plasma density is set for performing the ionization of the neutral population only, so that it does not overwrite the actual plasma density obtained in the domain through the weighting of the resulting ion populations. In both of them, the neutral population may be replaced by a neutral background with given properties[1].

The second issue is related to the particle-surface interaction phenomena, which, given the typically high surface-to-volume ratio of most electric thrusters, play an important role in determining the discharge structure and behavior. Focusing on the neutral gas-surface interaction, the majority of the current models are mostly phenomenological and their application is limited by the nature of the gas and the surface and their relative energy range. The two main figures of merit characterizing the reemitted population from a surface are its angular distribution and its wall energy accommodation, which indicates how closely the energy of the incoming population adjusts to the thermal energy of the surface. Some experiments indicate that the gas diffuse reflection with complete thermal accommodation represents satisfactorily the real gas-wall interaction process in most practical scenarios [38]. However, it is known that some factors such as the relative size of the gas and wall molecules, the surface rugosity and contamination, due for example to gas-surface adsorption, and the gas molecules impact angle and translational energy relative to the surface can have non-negligible effects. Surface contamination due to incident gas molecules adsorption increases the energy accommodation and broadens the angular distribution of the reemitted population [140, 141]. The gas-surface interaction is of crucial importance in the context of satellite drag coefficients computation. On-orbit measurements of the reflected population angular distribution were performed by Gregory and Peters [142], showing about a 97% diffuse and a 2-3% quasi-specular distribution. Moreover, Moe [143] suggested that a predominant diffuse reflection with accommodation factors close to unity dominates at Low Earth Orbits (LEO), while quasi-specular reflection processes become more relevant at higher altitudes, thus reducing the

---

[1] This approach is considered by the 1D radial PIC model presented in Chapter 5.

energy accommodation. Font [144] performed particle simulations of a low earth orbit neutral species sensor with an ionizing element, obtaining 20 times higher neutral density in the sensor ionization chamber in the case of pure diffuse neutral-wall reflection with complete accommodation, with respect to the pure specular reflection case.

Here, a preliminary investigation on the effects of the neutral-wall reflection process in the stationary plasma discharge obtained in the cylindrical channel under study is carried out. As indicated in Tab. 2.1, at material surfaces, in the absence of a better gas-surface interaction model, the neutral-wall interaction process is modeled through a probability p_{spec} of specular reflection, so that pure diffuse and specular neutral-wall reflection scenarios may be reproduced by setting $p_{spec} = 0$ and $p_{spec} = 1$, respectively [38]. For the sake of simplicity, since the development and analysis of a more complex gas-wall interaction model is out of the scope of this thesis, p_{spec} takes a given constant value throughout the simulation, so that the effects of the particle impact angle and energy, and the material surface conditions are neglected. Here, the limit cases of pure diffuse and pure specular neutral-wall reflection scenarios, which shall hereinafter be referred to as D and S cases, respectively, are explored. It is emphasized that zero neutral-wall accommodation is considered in this study for the diffuse reflection process (i.e. it is elastic) so that both the diffusely and specularly reflected neutral populations feature the same average energy content. Therefore, the only difference between both reflection processes lies in the reflection direction, which follows a cosine distribution law in the diffuse case, as already described in Sec. 2.2.5.1.2.4, thus focusing the study on the effects of the angular distribution of the surface reflected populations.

The rest of the section is organized as follows. A simulation reference case for all the studies performed is detailed in Sec. 4.1.1. The two different discharge ignition strategies commented below are analyzed in detail in Sec. 4.1.2.1. Furthermore, a preliminary investigation of the effect of the neutral-wall interaction on the plasma discharge is detailed in Sec. 4.1.2.2. Finally, the conclusions are drawn in Sec. 4.1.3.

4.1.1 Simulation settings

The simulation domain considered corresponds to a cylindrical channel of 1 cm radius and 3 cm length, typical of a HPT or an ECRA, presenting a surface-to-volume ratio of 200 (where only the lateral material wall has been taken into account). Fig. 4.1 shows the PIC mesh, which features an even node distribution along the axial coordinate. In order to increase the mesh resolution near the material wall while limiting the computational cost, the nodes are radially distributed according to an exponential law, so that squared cells are obtained at the material wall boundary, the radial mesh spacing being maximum at the symmetry axis. The mesh spacing, the number of nodes along each direction, and the main simulation parameters are listed in Tab. 4.1.

The reference for the electric potential, where $\phi = 0$, is located at the position $r = 0$, $z = 0$ cm. For the sake of simplicity, isothermal electrons are considered, so that the relation between the plasma density and the electric potential is given by Eq. (3.2) with $\gamma = 1$ and $T_e = 8$ eV. Since no magnetic field is included in the simulations, the electric potential is directly solved at the PIC mesh shown in Fig. 4.1. Assuming xenon as propellant, only neutrals and singly charged ions are simulated. A neutral mass flow $\dot{m}_A$ is injected from the circular injection surface of 1 cm radius at $z = 0$ (green left

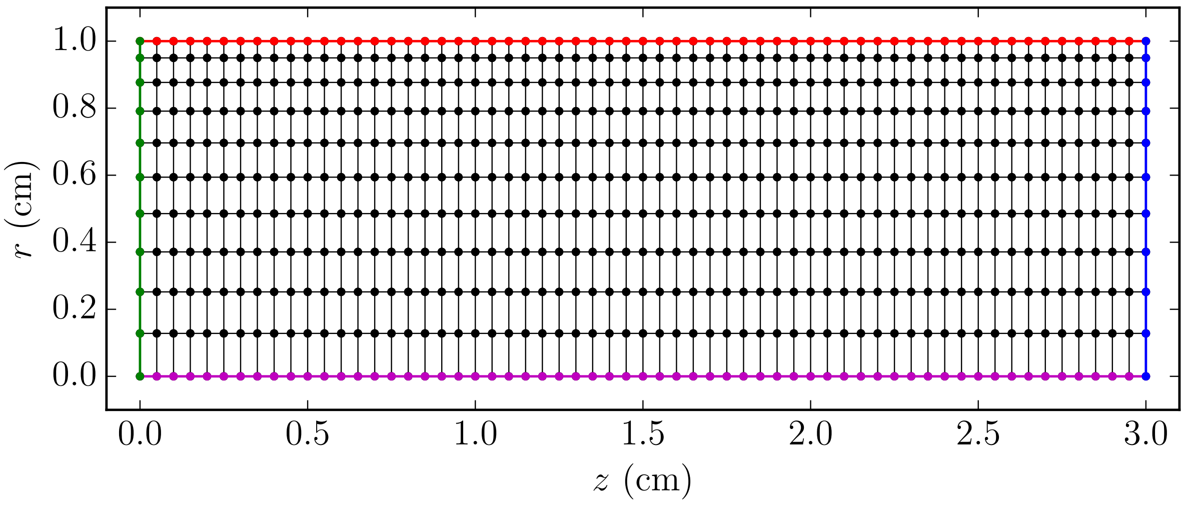

Figure 4.1: PIC mesh of the cylindrical channel simulation domain. The red, green, blue and magenta lines indicate the material wall, injection, free loss and symmetry axis at $r = 0$ boundaries, respectively.

boundary in Fig. 4.1) featuring a flat profile with a sonic axial velocity based on its own temperature. The singly charged ions are generated through the ionization of both the injected neutrals and the reinjected ones due to the ion recombination at the lateral material wall. Both collisional processes follow the ionization reaction $\mathrm{Xe} + e \rightarrow \mathrm{Xe}^{+} + 2e$. Higher ionization degrees and CEX collisions are not considered here. The recombined neutrals are diffusely emitted from the material wall [top red boundary in Fig. 4.1] considering complete accommodation of the impacting ions [i.e. $\alpha_W = 1$ in Eq. (2.24)], as suggested by several authors [72, 145]. Thus, the neutral emission energy is only given by the wall temperature, which is set to 850 K. Pure diffuse neutral reflection (i.e. $p_{spec} = 0$ at material walls according to Tab. 2.1) with zero neutral-wall accommodation [i.e. $\alpha_W = 0$ in Eq. (2.24)] is considered for the reference simulation case here described. Therefore, it is equivalent to a specular reflection featuring a random reflection direction, so that the information about the impacting particle direction is not preserved. In order to improve the PIC-related statistics, the heavy species mentioned above are split into three different particle populations, each one with its own computational list, so that they are independently monitorized. The different particle populations considered are detailed in Tab. 4.2, with their corresponding subscripts.

The timestep (see Tab. 4.1) is set so that, on average, sonic ions take at least two timesteps to cross the lateral material wall boundary cells (smallest ones). The simulation duration (here set to 10000 timesteps, equivalent to 1 ms) is sufficiently long to reach stationary conditions for the slow neutral populations (which are around 8 times slower than the ions). The number of averaging steps considered for the ESW algorithm described in Sec. 2.2.5.1.3 is set so that the surface weighted magnitudes have a similar noise level than the volumetric weighted ones. Therefore, it depends on the particular dynamics of every population, being set to 2 and 16 for ions and neutrals, respectively. Regarding the population control algorithm, the target number of macroparticles per cell is 200 for the ions, and 500 for both neutral populations (with a control range of ±10% on each case). As explained in Sec. 2.2.5.6, the population control algorithm acts

Simulation parameter	**Units**	**Value**
Mesh number of nodes, N_r, N_z	-	11, 61
Mesh number of cells	-	600
Axial mesh spacing, Δz	mm	0.5
Max. and min. radial mesh spacing, Δr	mm	1.3, 0.5
Simulation timestep, Δt	s	10^{-7}
Number of simulation steps	-	10000
Injected Xe velocity	ms^{-1}	300 (sonic)
Injected Xe temperature	eV	$7.35 \cdot 10^{-2}$
Injected Xe mass flow, $\dot{m}_A$	mgs^{-1}	$4 \cdot 10^{-1}$
Electron temperature, T_e	eV	8.0
Material wall temperature, T_W	K	850
Ion/neutral wall accommodation coefficients, α_W	(-)	1/0
Probability of neutral-wall specular reflection, p_{spec}	(-)	0

Table 4.1: Main simulation parameters of the cylindrical channel plasma discharge reference simulation case.

Population subscript	**Description**
ni	Injected Xe neutrals
nr	Recombined Xe neutrals
i	Xe^+ ions from ionization of ni and nr neutrals

Table 4.2: Different macroparticles populations considered in the simulations of a plasma discharge in a cylindrical channel.

through any process generating new particles in the domain. Since there is not any volumetric source of neutrals in the domain, a higher target number of particles per cell is needed at the injection and wall recombination cells in order to properly characterize the population in the whole simulation domain. Finally, all the results shown in the following sections characterizing the steady discharge are time-averaged over 500 simulation timesteps (equivalent to 50 μs of simulation time).

4.1.2 Simulation results and discussion

4.1.2.1 Discharge ignition strategies in hybrid codes

Considering the reference case described in Sec. 4.1.1, Figs. 4.2(a) and 4.2(b) compare the time evolution of the average ion and neutral particle density and number of macroparticles in the simulation domain obtained when applying approaches MD and IP. A minimum plasma density of 10^{14} m^{-3} is set in the MD case for ionization purpose only, while an initial ion population of 50 macroparticles per cell featuring a density of 10^{17} m^{-3} is uniformly distributed in the simulation domain in the IP approach. Interestingly, both of them present a similar transient, especially for the neutral population, and, as expected, the same steady discharge is obtained in both cases, the maximum relative errors on the mass balance for each particle population being of the order of 10^{-5}. It is worth noting that the total computational time in the IP case is around 10% higher than that of the approach MD. Therefore, the latter has been considered for the rest of cases simulated in this Chapter.

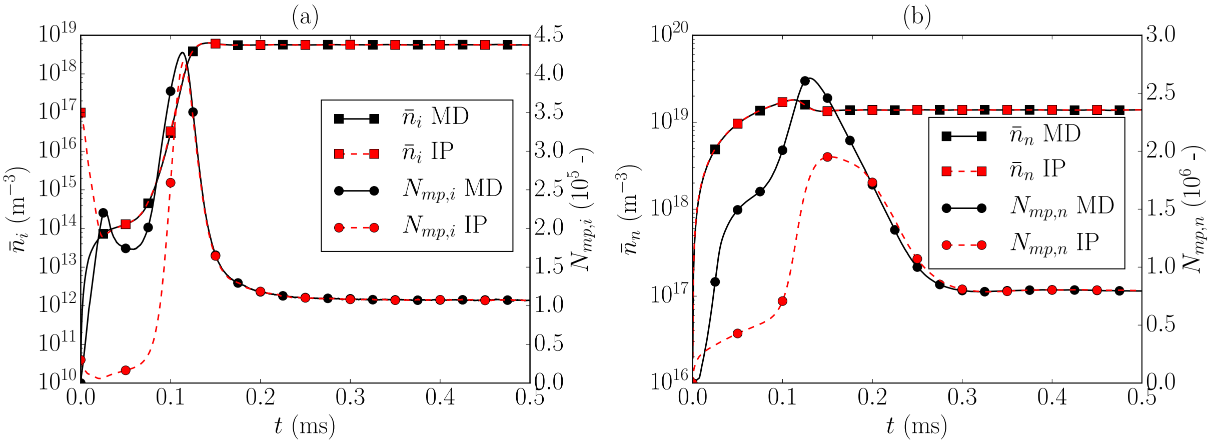

Figure 4.2: Time evolution of the total ion (a) and neutral (b) mass and number of macroparticles in the domain.

Figs. 4.3(a) and 4.3(b) show the electric potential and the electric field magnitude of the stationary discharge. The average radial potential drop in the presheath region along the axial coordinate is 5.5 V, not far from the well known value of $T_e/2$ needed for cold ions to acquire sonic conditions at the sheath edge. The potential reaches a maximum value of 3.35 V at the symmetry axis at $z = 0.25$ cm. The axial potential drop along the axis from that point to the exit plane is 10.81 V. Fig. 4.3(c) depicts the ion density, which, as expected, follows the electric potential distribution, according to the isothermal law. On the other hand, Fig. 4.3(d) shows the magnitude of the ion fluid velocity and the ion streamlines, which all originate at the maximum ionization region, and split the domain into regions with positive and negative axial ion flow. The corresponding ion streamlines are consistent with the electric field represented in Fig 4.3(b). Finally, Figs. 4.3(e) and 4.3(f) plot, respectively, the total neutral density and the recombined-to-injected neutral density ratio, which is equivalent to the ratio of their ionization production terms. The injected neutrals only dominate in an initial region at the center of the channel and close to the injection boundary, while the recombined neutrals are responsible for most of the plasma generated downstream that region. This fact suggests that a shorter channel would yield better performance in terms of plasma production efficiency, although this analysis is out of the scope of this section.

4.1.2.2 Neutral-wall interaction effects on the plasma discharge

Fig. 4.4(a) and 4.4(b) show, respectively, the evolution with the neutral injection mass flow of the average and maximum ion and neutral (including injected and recombined populations) particle density in the simulation domain at stationary conditions for the D and S cases. Likewise, the evolution of the total ionization source term is depicted in Fig.

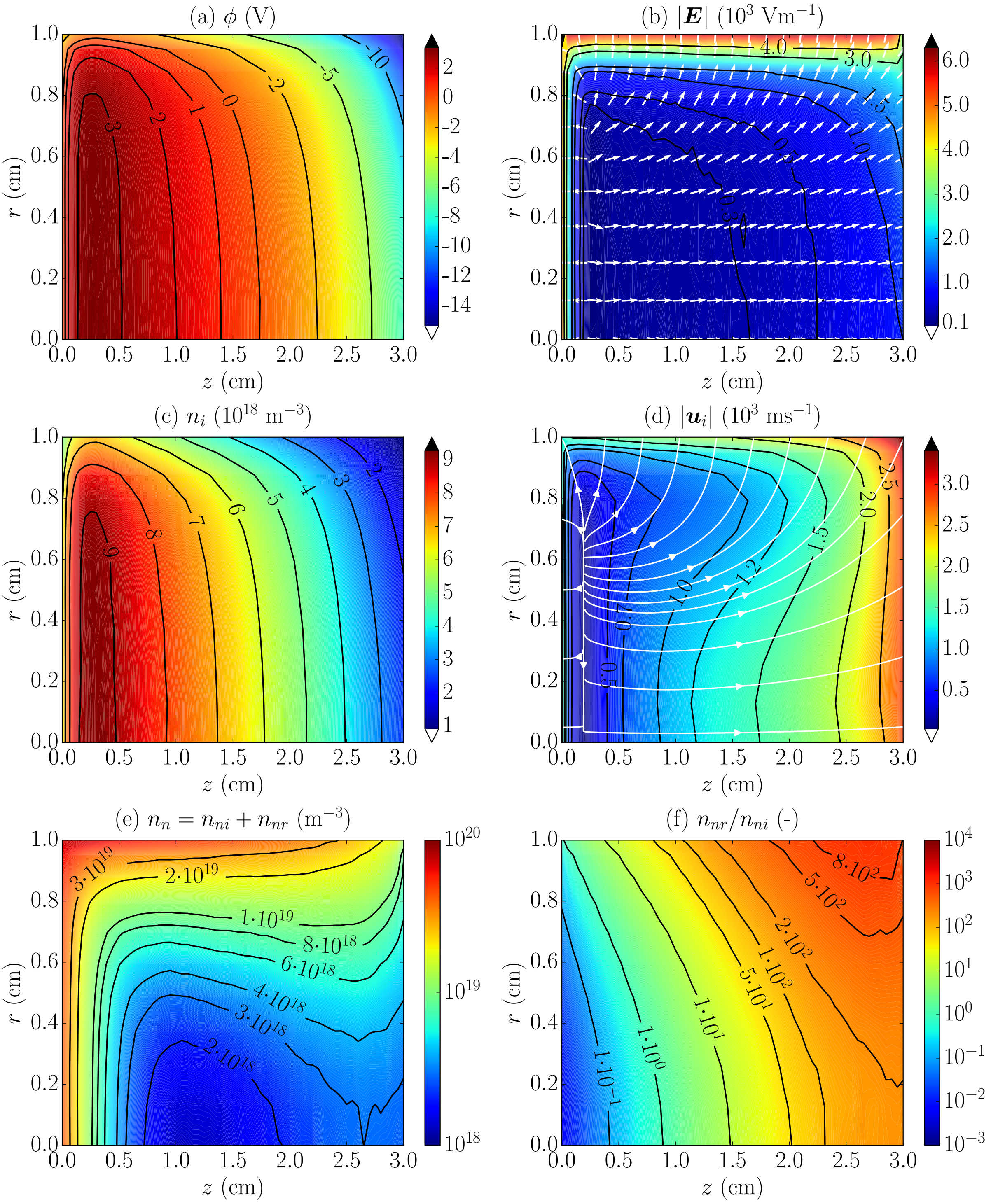

Figure 4.3: Cylindical plasma discharge reference case results: (a) the electric potential, (b) the electric field magnitude, (c) ion (plasma) density, (d) ions fluid velocity magnitude, (e) total neutral density and (f) ratio between the recombined and the injected neutrals density. In (b) the white arrows indicate the direction of the electric field, while in (d) the white lines represent the ion streamlines.

4.4(c). Black (red) solid and dashed lines with square (circle) markers indicate average and maximum values for the D (S) cases, respectively. On the other hand, Fig. 4.4(d) plots the propellant utilization efficiency, defined as

$$\eta_u = \frac{\dot{m}_{i\infty}}{\dot{m}_A}, \tag{4.1}$$

where $\dot{m}_{i\infty}$ stands for the ion mass flow leaving the domain through the channel exit plane (blue right boundary in Fig. 4.1). Taking into account that the MD discharge ignition approach is here applied in all cases with a minimum plasma density of 10^{14} m^{-3} (see Sec. 4.1.2.1), a self-sustained steady plasma discharge requires minimum neutral injection mass flows of ∼0.11 and ∼0.33 mgs^{-1} in the D and S scenarios (vertical black and red dot-dashed lines in Fig. 4.4), respectively, for the present configuration. Interestingly, given a neutral injection mass flow for which ignition is achieved in both scenarios, the stationary plasma discharge obtained is practically the same in terms of average plasma and neutral density, so that it features very similar performances, as revealed in Fig. 4.4(d) for the utilization efficiency. On the other hand, in the range $\dot{m}_A \in [0.11, 0.33]$ mgs^{-1}, a predominant neutral-wall diffuse reflection allows for a significant propellant mass saving while ensuring a self-sustained plasma discharge with reasonably high performance. If a constant value of $p_{spec} \in (0, 1)$ is considered, the minimum neutral injection mass flow needed for the plasma discharge ignition lies within the range mentioned above and, once ignition is achieved, the effect of p_{spec} on the discharge performance is negligible.

In order to clarify this behavior, the ionization collisions are turned off so that only the injected neutrals are simulated. Fig. 4.5(a) plots the trajectories in the plane Ω_0 of two injected neutral macroparticles (with the same injection properties described in Sec. 4.1.1) featuring both diffuse (black line) and specular (red line) neutral reflection. Since both reflection processes are energy conserving, it is evident that the random reflection direction of the diffusely reflected neutral considerably increases its residence time in the channel. Furthermore, this fact significantly affects the neutral macroscopic magnitudes. Figs. 4.5(b) and 4.5(c) show the steady axial profile along the symmetry axis of the injected neutrals particle density and macroscopic axial velocity, respectively, for various neutral injection mass flows in both D and S cases. In particular, the cases shown are those just before and after the discharge ignition for each case, and those corresponding to the maximum $\dot{m}_A$ considered. While a flat neutral density profile develops in the S cases, the diffuse reflection leads to a neutral mass accumulation in the first third of the channel along the axial direction, thus giving rise to axial neutral density gradients along the channel. As expected, the macroscopic axial neutral velocity evolves along the axial coordinate so that the axial neutral flow matches with the prescribed one at the injection boundary for each case. As a consequence, and confirming the phenomenon revealed in Fig. 4.5(a), the neutral average residence time in the channel of around two times higher when diffuse reflection is considered. Finally, Fig. 4.5(d) depicts the evolution with the injection neutral mass flow of the average and maximum neutral density in the simulation domain for the D and S cases. As expected, in both cases the neutral density increases linearly with the injection mass flow, featuring the D cases a slope ∼2.8 times higher than that of the S cases for the average neutral density in the domain. In fact, at the corresponding minimum $\dot{m}_A$ values for ignition for the D and S cases, respectively, the former features an average neutral density ∼8% lower than that of the S case, but it presents a maximum neutral density ∼30% higher, which compensates the plasma

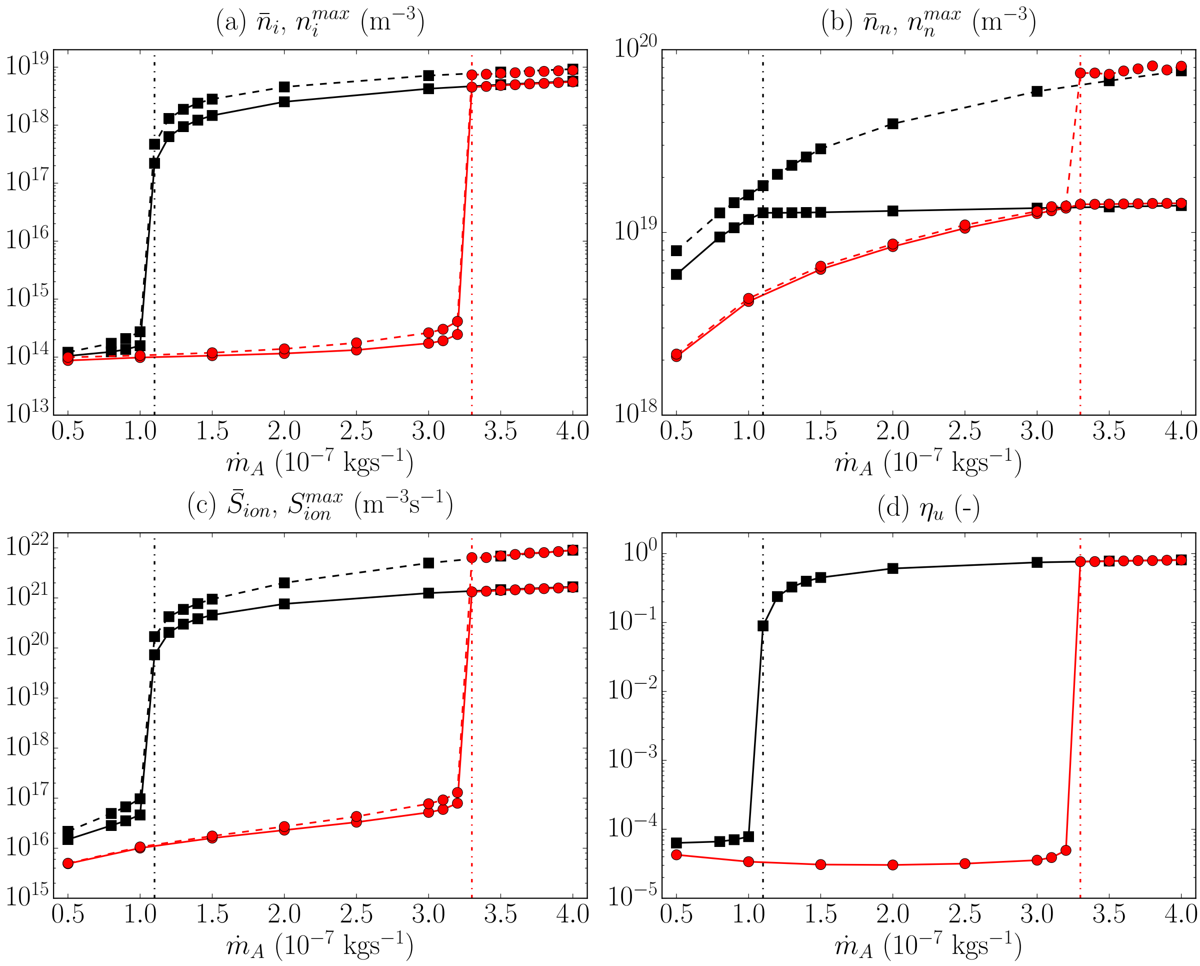

Figure 4.4: Evolution with the neutral injection mass flow of the average and maximum (a) plasma density, (b) total neutral density (including injected and recombined neutrals) and (c) total ionization source term in the simulation domain at stationary conditions for the D and S cases. Black (red) solid and dashed lines with square (circle) markers indicate average and maximum values for the D (S) cases, respectively. (d) Evolution with the neutral injection mass flow of the utilization efficiency at stationary conditions in the D (black solid line with squared markers) and S (red solid line with circle markers) cases. The vertical black and red dot-dashed lines indicate the minimum neutral injection mass flow needed for the plasma discharge ignition in the D and S cases, respectively.

gradients due to the neutral spatial distribution and triggers the discharge ignition. In summary, the neutral-wall diffuse reflection leads to an increase of the average neutral residence time in the channel and shapes its spatial distribution in the domain thus facilitating the discharge ignition.

It is worth noting that, as shown in Fig. 4.3(f), $n_{nr}/n_{ni} > 1$ except for a region close to the injection boundary at the center of the channel (and thus far from the lateral material wall), where the injected neutrals dominate. Thus, downstream that region, the ion population is mostly generated from the ionization of the recombined neutrals, the latter being diffusely emitted from the lateral material wall all along the channel, and mostly ionized in the first cells close to the wall (the recombined neutral density at the axis is, on average, around 30 times lower than that at the material wall for $\dot{m}_A = 0.4$ mgs^{-1}). This explains the fact that, as commented above, once the discharge ignites, the

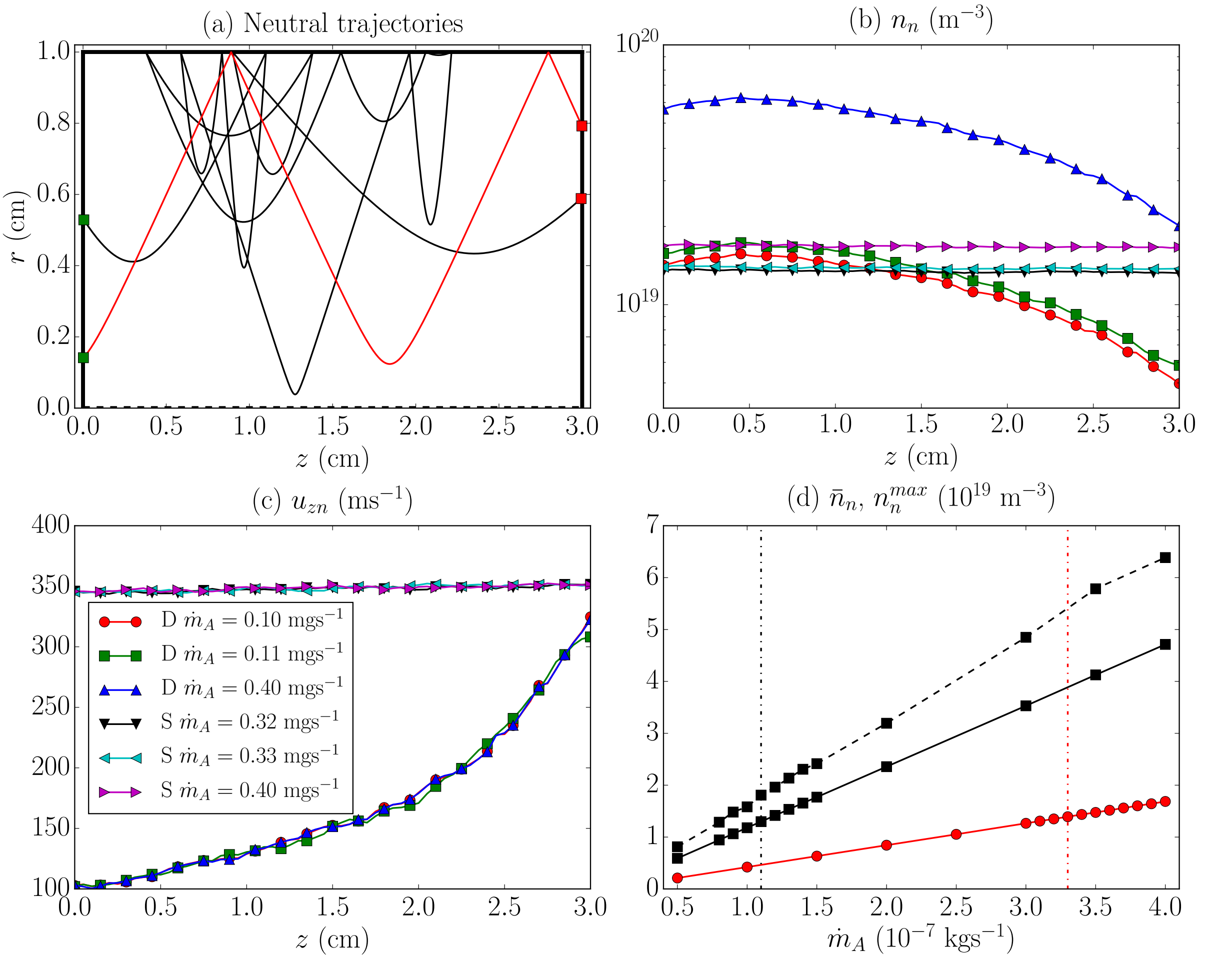

Figure 4.5: (a) Two injected neutrals 2D trajectories in the Ω_0 plane in case of diffuse (black line) and specular (red line) neutral-wall reflection. The green and red squares represent the initial and final neutrals positions for each case. Steady state injected neutrals properties in the cylindrical channel for the D and S cases without ionization collisions: axial evolution at the symmetry axis $r = 0$ of injected neutrals density (b) and macroscopic axial velocity (c); and (d) evolution with the injection mass flow of the average (solid line) and maximum (dashed line) neutral density in the domain in D and S cases (maximum values in the S cases coincide with the average ones since flat neutral density profiles are obtained in these cases). The vertical black and red dot-dashed lines indicate the minimum neutral injection mass flow needed for the plasma discharge ignition in the D and S cases, respectively.

neutral-wall reflection process plays a minor role in the discharge structure in stationary conditions.

4.1.3 Conclusions

The simulation of a simple scenario consisting of an unmagnetized plasma discharge in a surface-dominated cylindrical channel with isothermal electrons has permitted to further assess the performance of HYPHEN. Two main different modeling issues have been addressed, showing their effects on the plasma discharge simulation results. First, two different discharge ignition strategies for hybrid codes have been investigated: a first one based on a minimum background plasma density (MD), and a second one relying on given initial ion populations (IP). As expected, both approaches yield the same steady plasma discharge, the former allowing for a non-negligible computational time saving since no initial particle populations are needed.

On the other hand, special focus has been put on the particle-surface interaction algorithms, which were not included in the validation against the EP2PLUS code in Chapter 3. Particularly, a preliminary investigation on the effect of the neutral-wall interaction on the plasma discharge has been performed considering a simple model for the neutral-wall interaction process based on a constant probability p_{spec} of specular reflection. The limit cases, here named D and S, corresponding respectively to pure diffuse ($p_{spec} = 0$) and pure specular ($p_{spec} = 1$) neutral reflection have been explored, yielding the main following conclusions. First, the minimum propellant injection mass flow for which a steady and self-sustained plasma discharge is obtained greatly depends on the neutral-wall reflection process, being around three times higher in the S case for the surface-dominated simulation domain here considered. Second, the diffuse neutral-wall reflection leads to a significant increase of the neutral residence time with respect to that of the specular reflection cases, thus enhancing the neutral ionization in the channel and explaining the existence of different neutral injection mass flow thresholds for the discharge ignition in the D and S cases. Finally, once the plasma discharge ignition takes place, it becomes dominated by the ion population, which is mostly generated through the ionization of the recombined neutrals, and the neutral-wall reflection type has been found to have a marginal effect on the discharge structure and performance.

As a future work, a more consistent model for the neutral-wall interaction process should be derived. As found in Ref. [128], for a hypersonic flow of Xe ions/atoms on an Al target the specular reflection probability mostly depend on the impacting particle angle relative to the surface. On the other hand, a more consistent plasma-wall interaction model should include the material wall sputtering phenomena as already done in Ref. [128]. This would permit not only to study the wall sputtering effects on the plasma discharge, but also, and more importantly, to quantitative evaluate the thruster walls erosion, which has a direct impact on its operational lifetime.

4.2 HET simulations

An improved version of NOMADS [59, 60] has been presented in Chapter 2 for the isotropic electron pressure case. Only several of the improvements proposed in Sec. 2.3.8 have been actually incorporated in the model in the frame of this Thesis. The main focus of this section is on assessing its performance, revealing its capabilities and identify its limitations in a preliminary and simple simulation scenario corresponding to a SPT-100 HET.

The electron-fluid model for HETs presented in Chapter 2 features a time-dependent electron energy equation [see the time derivative term in Eq. (2.113)]. Therefore, as described in Sec. 2.3.7, NOMADS performs an inner temporal loop of N_{ke} sub-iterations per simulation (PIC) timestep, the electron fluid timestep Δt_e being thus given by Eq. (2.127). The value of N_{ke} has a great impact on the computational time required for the HYPHEN code to complete a standard HET simulation. Here, a preliminary investigation on the effects of N_{ke} on the discharge is performed in order to select an appropriate value for N_{ke} which allows obtaining satisfactory results while limiting the computational cost. It is remarked that the semi-implicit first order Euler scheme used for the time discretization of Eq. (2.113) is used here for all the simulations. Additional temporal schemes were already considered in Ref. [60], and a further investigation in this line is left for future work.

The well-known breathing mode oscillation in the range of 10-30 kHz characterizing the typical HET operation [104,106,107,146] is responsible for the large oscillations of the discharge current I_d. This predator-prey type fluctuation, caused by the strong ionization of the neutral atoms in the HET chamber, is directly related to the neutral average residence time in the thruster chamber, which, as already shown in Sec. 4.1.2.2, depends on the neutral-wall interaction process in the surface-dominated chamber of a HET. Here, the effect on the breathing mode characteristic frequency of pure diffuse and pure specular neutral-wall reflection type is analyzed.

The boundary cathode model originally implemented by Fife in HPHall [44], and used later in HPHall-2 [45,70], made it impossible to extend the simulation domain beyond the neutralization region. Later, the wall cathode model presented in Ref. [147] placed the electron emission surface in a small section of the lateral external thruster wall aiming to a more accurate representation of the actual plasma/cathode interaction physics, thus including a sheath model for high emission electrodes [148], and enabling the simulation of the thruster near plume beyond the cathode. However, numerical convergence problems at the cathode wall favored the development of the volumetric cathode model, detailed in Ref. [94], which was later implemented in HallMA [46], and recently in NOMADS [60]. The cathode position has been shown to have an important influence on the discharge performance, affecting the discharge current oscillation mode [149–151]. After improving the volumetric cathode treatment as described in Chapter 2, preliminary results are presented here for different cathode locations in the thruster near plume region. The simulations reveal the limitations of the volumetric cathode model: the thermal injection performed within the bulk plasma breaks the usual isopotential condition of the magnetic lines near the cathode region.

The physical processes behind the electron anomalous transport phenomenon in HETs are still far from being well understood. The lack of a proper theory explaining the origin of the fluctuations and how they correlate results in a broad range of possible values for the turbulent parameter α_{tm} in Eq. (2.104). Hybrid HET numerical simulations [152] reported a better agreement with experimental measurements of the resulting discharge properties when using the anomalous transport data obtained experimentally by Meezan and Capelli [153–155], in comparison to the case of the Bohm's classical value of $\alpha_{tm} = 1/16$ [156]. On the other hand, lower values of the order of 10^{-2} have been found by Morozov and Savelyev [157], and used in HET simulations [44–46, 76, 98, 158]. In contrast, values of α_{tm} close to 1 have been recently suggested by Mikellides and Ortega [41,159]. Different authors have proposed a variety of functions for α_{tm} including two region step-in and step-out models[2] and quenching profiles [94,160–162]. Hybrid HET simulations performed by Santos [72] showed that step-out profiles with $\alpha_{tm} = 1.75\text{-}10 \cdot 10^{-2}$ in the chamber-near plume regions, respectively, yielded a better fit to the experimental measurements of the discharge current reported in Ref. [163] for a SPT-100 at nominal operation. Recently, Jorns [164] have provided advanced fittings for the turbulent parameter through data-driven machine learning techniques, and multi-fluid simulations performed by Mikellides and Ortega [43] have accurately reproduced experimental measurements using a multiple-coefficient approach for the turbulent parameter spatial profile. Following previous studies [44–46, 59, 60, 72, 101], preliminary results considering an unique electron turbulent parameter $\alpha_t = \alpha_{tm} = \alpha_{te}$, and $\alpha_{tq} = 0$ [see definitions of the electron energy and heat flux turbulent parameters α_{te} and α_{tq} in Eqs. (2.104) and (2.104), respectively] featuring constant values and step-out profiles are shown here.

The structure of the rest of the section is the following. A simulation reference case is defined in Sec. 4.2.1. Sec. 4.2.2.1 shows the effects on the simulation results of the NOMADS number of time sub-iterations N_{ke}, defined in Eq. (2.127), which has a great impact on the computational time. The results for the reference case defined in Sec. 4.2.2.1 are discussed in detail in Sec. 4.2.2.2. Moreover, Sec. 4.2.2.3 analyzes the influence of the neutral-wall reflection type on the typical breathing mode operation typical of a HET. On the other hand, Sec. 4.2.2.4 analyzes the effects on the simulation results of the volumetric cathode location in the near plume region. Furthermore, the simulation results for different electron anomalous transport parameter constant values and step-out profiles are shown in Sec. 4.2.2.5. Finally, the conclusions are presented in Sec. 4.2.3.

4.2.1 Simulation settings

Figs. 4.6(a) and 4.6(b) show the PIC mesh and the MFAM of the typical simulation domain of a SPT-100 HET (already depicted in Fig. 2.3), generated by the HYPHEN SET sub-utilities corresponding to the PIC mesh and the MFAM generators, respectively, as commented in Sec. 2.1.1. The dimensions of the thruster chamber and near plume region, which includes the symmetry axis, are taken from Ref. [60] and are listed in Tab. 4.3, along with the main meshes characteristics and the most relevant simulation parameters. Fig. 4.6 (b) shows the different volumetric cathode locations analyzed in detail in Sec. 4.2.2.4, being their coordinates collected in Tab. 4.3. The cathode position C1 corresponds to the reference case here described. The cathode electron emission temperature is set to 3 eV for all the cases simulated. As mentioned in Sec. 2.3.7.1, the reference for the electric

---

[2] The step-in (out) profiles feature a higher (lower) value of the turbulent parameter α_{tm} inside the thruster chamber than in the near plume region.

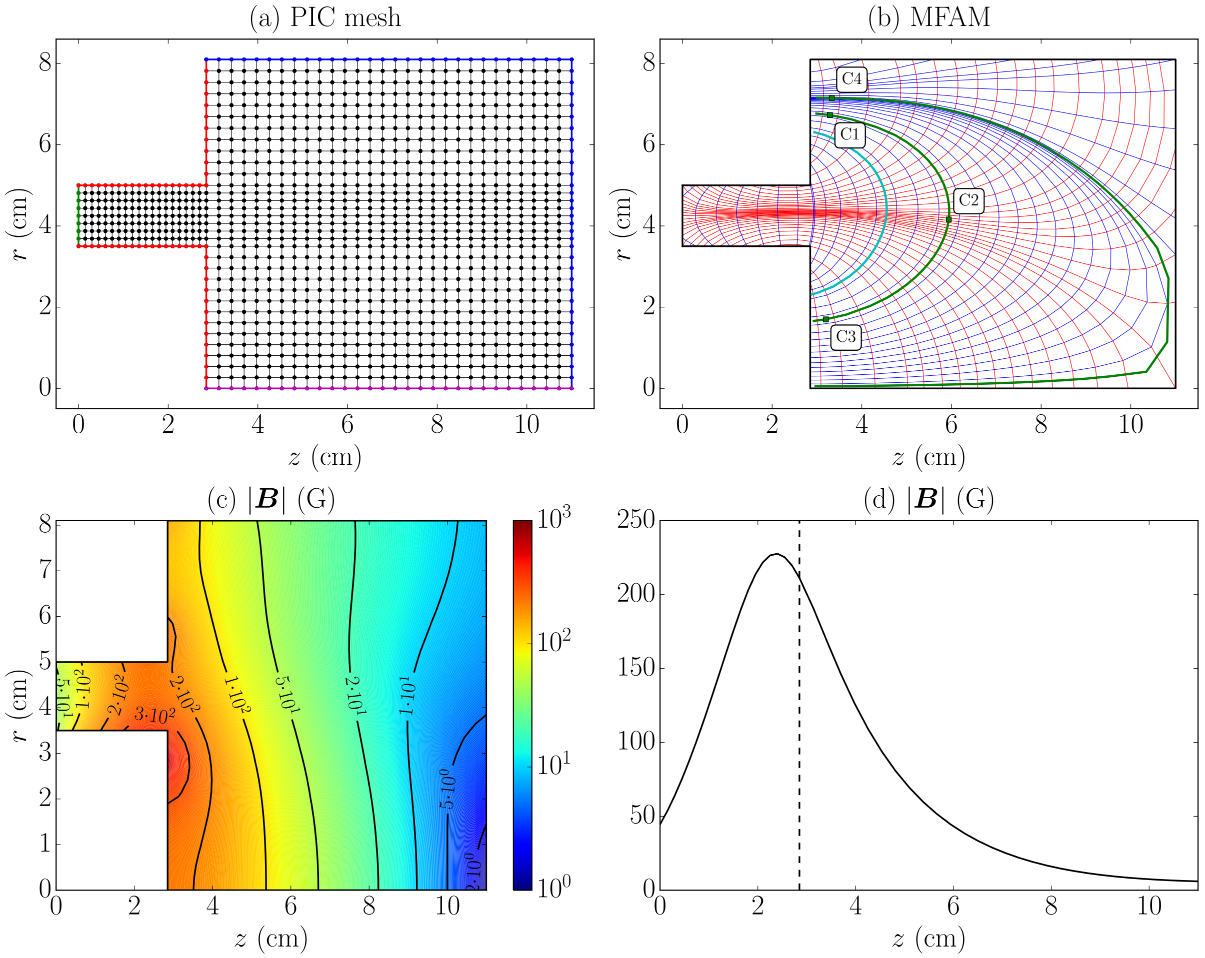

Figure 4.6: (a) The PIC mesh. The red, green, blue and magenta lines indicate the thruster dielectric walls, the anode wall, the free loss boundary and the symmetry axis at $r = 0$, respectively. (b) The MFAM used by NOMADS. The blue and red MFAM faces defining the MFAM cells are aligned along the magnetic field parallel and perpendicular directions, respectively. The green squares indicate the various volumetric cathode positions considered, whose coordinates are listed in Tab. 4.3. The location C1 is considered for the reference case. The green lines correspond to the magnetic field streamlines passing through the different cathode positions, C1, C2 and C3 being upon the same magnetic line. The cyan line refers to an additional magnetic field streamline dealt with in Sec. 4.2.2.4 for checking the isothermal condition along it. (c) The magnetic field intensity in the HET simulation domain. (d) The axial profile of the magnetic field intensity along the simulation domain at a radius $r = 4.63$ cm. The dashed vertical line indicates the axial location of the thruster chamber exit plane, at $z = 2.85$ cm (see Tab. 4.3).

potential (i.e. the point where $\phi = 0$) is set at the center of the MFAM cell representing the volumetric cathode for each case. The base magnetic circuit configuration presented in [60] for the SPT-100 is considered here for all the cases simulated. The magnetic field intensity, and the axial profile of the magnetic field intensity along the simulation domain at a radius $r = 4.63$ cm are shown in Figs. 4.6(c) and 4.6(d), respectively. The value of the maximum magnetic field intensity and its axial location at the thruster center line (TCL), along with the average magnetic field intensity at the free loss boundary downstream [vertical blue boundary line in Fig. 4.6(a)] are listed in Tab. 4.3.

Here, the nominal SPT-100 HET operation parameters reported in [163], already considered by Pérez-Grande [59, 60], are adopted. The constant voltage operation mode is simulated for all cases with a discharge voltage $V_d = 300$ V. Assuming xenon as propellant, a neutral mass flow $\dot{m}_A = 5$ mgs^{-1} is injected through the whole annular wall anode located at $z = 0$ [green left boundary in Fig. 4.6(a)] featuring a flat profile with a sonic axial velocity based on its own temperature (see Tab. 4.3). Singly and doubly charged ions are generated through the ionization of both the injected and the recombined neutrals at the thruster ceramic walls [red boundary lines in Fig. 4.6(a)], according to the ionization reactions shown in Sec. 3.3.1. The same plasma-wall interaction approach and parameters described in Sec. 4.1.1 for the reference simulation case of a plasma discharge in a cylindrical channel are here considered (see Tab. 4.1). All the simulations feature three different particle populations, each one with its own PIC computational list, which are detailed in Tab. 4.4 with their corresponding subscripts. Contrary to the simulation cases shown in Sec. 4.1, both injected and wall-recombined neutrals are treated in the same computational list. Since elastic atom-atom collisions are not included in the simulations, there is no chance for an injected neutral macroparticle to reach the near plume regions along the thruster lateral walls outside of the plasma beam. As a consequence, the injected neutral PIC population would not be accurately represented in those regions. In this scenario, merging in a single population both the injected and the wall-recombined neutrals (which are dominant in those regions) improves the neutral species PIC statistics there. Regarding the population control algorithm, a target number of macroparticles per cell of 500 is considered per particle population, with a control range of $\pm 10\%$. In order to limit the larger macroparticle depletion at the symmetry axis, the two first rows of PIC mesh cells close to the axis feature twice the target number of macroparticles above. On the other hand, following the rationale described in Sec. 4.1.1, and considering that the neutral magnitudes at the thruster ceramic walls are dominated by the ion recombination process, the number of averaging simulation steps considered for the ESW algorithm (see Sec. 2.2.5.1.3) is set to 5 for all the particle populations.

The simulation (or PIC) timestep (see Tab. 4.3) is set so that a doubly charged ion accelerated across the discharge voltage takes at least two simulation timesteps to cross the smallest PIC mesh cell. Every complete HYPHEN simulation of the SPT-100 HET performed here features a total of 60000 simulation steps (equivalent to 900 μs of simulation time), and is divided in two phases. First, an initialization phase of 15000 simulation steps (equivalent to 225 μs of simulation time) provides an initial state solution for NOMADS considering isothermal electrons. As commented in Sec. 4.1.1, during this phase the electric potential is given by Eq. (3.2) with $\gamma = 1$ and $T_e = 8$ eV. Starting from the initial solution above, a second phase featuring 45000 simulation steps using NOMADS for the electron population completes the simulation. Along this period, equivalent to 675 μs of simulation time, the obtained discharge current undergoes around seven oscillations reproducing the HET breathing mode. The NOMADS number of time sub-iterations per simulation step is set to 5 for the reference case here described (see Tab. 4.3). On the other hand, all the HYPHEN results shown in the following sections are time-averaged over 50 simulation timesteps (equivalent to $7.5 \cdot 10^{-1}$ μs of simulation time), which allows for its appropriate visualization while still reproducing oscillation modes of interest. Furthermore, a time-averaging over the last 450 μs of simulation time (time enough for the discharge current to perform around five complete oscillations) is

Simulation parameter	**Units**	**Value**
Thruster chamber length, L	cm	2.85
Thruster chamber inner radius, r_1	cm	3.50
Thruster chamber outer radius, r_2	cm	5.00
Near plume region length	cm	8.15
Near plume region radius	cm	8.10
PIC mesh number of cells, nodes	-	1080, 1161
PIC mesh spacings in chamber Δz, Δr	mm	1.50, 1.88
PIC mesh spacings in near plume Δz, Δr^*	mm	2.81, 2.53
MFAM number of cells, faces	-	1173, 2411
MFAM average cells skewness [60]	-	$2 \cdot 10^{-2}$
MFAM average aspect ratio [60]	-	10^{-1}
C1 cathode location, z, r	cm	3.29, 6.73
C2 cathode location, z, r	cm	5.94, 4.16
C3 cathode location, z, r	cm	3.20, 1.70
C4 cathode location, z, r	cm	3.33, 7.15
Cathode emission temperature, T_{cat}	eV	3
Cathode volume C1, C2, C3, C4	cm^3	1.68,0.697,0.854,0.138
Max. $\|\boldsymbol{B}\|$ along the TCL	G	242.75
Axial location of max. $\|\boldsymbol{B}\|$ at the TCL	cm	2.40
Average $\|\boldsymbol{B}\|$ at the free loss exit plane	G	5.04
Discharge voltage, V_d	V	300
Simulation (PIC) timestep, Δt	s	$1.50 \cdot 10^{-8}$
Total number of simulation steps	-	60000
Number of initialization steps	-	15000
Number of simulation steps with NOMADS	-	45000
NOMADS number of time sub-iterations, N_{ke}	-	5
Injected Xe velocity	ms^{-1}	300 (sonic)
Injected Xe temperature	eV	$7.35 \cdot 10^{-2}$
Injected Xe mass flow, $\dot{m}_A$	mgs^{-1}	5

Table 4.3: Main simulation parameters of the SPT-100 HET reference simulation case. The radial PIC mesh spacing marked with an asterisk (*) represents the average radial spacing in the near plume region.

performed for all the time-averaged variables shown in the following sections. Given the oscillating HET operational regime, the time-average value of every magnitude is obtained from a time range including the largest number of complete cycles, on each case.

As commented in Sec. 4.2, all the HET simulations shown in this Thesis consider an electron turbulent parameter $\alpha_t = \alpha_{tm} = \alpha_{te}$, and $\alpha_{tq} = 0$. While the results for

Population subscript	Description
n	Injected and recombined Xe neutrals
$i1$	Xe^+ ions from ionization of n neutrals
$i2$	Xe^{++} ions from ionization of n neutrals and $i1$ ions

Table 4.4: Different macroparticles populations considered in the HET simulations.

different α_t values and profiles is shown in Sec. 4.2.2.5, the simulation reference case takes $\alpha_t = 2.5 \cdot 10^{-2}$ (i.e. the equivalent electron turbulent collision frequency represents the 2.5% of the electron cyclotron frequency ω_{ce}). As for the electron inertial effects (refer to Sec. 2.3.3.2), the magnitude of the electron drift velocity is limited to twice the electron thermal one, so that the electron drift-to-internal energy ratio $m_e u_e^2/2T_e$, with $u_e \equiv |\boldsymbol{u}_e|$, can take a maximum value of two (see Sec. 4.2.2.2 for further details).

Finally, as commented in Sec. 2.3.7.1, HYPHEN features the sheath model presented by Ahedo and de Pablo [119], which considers a total secondary electron emission (SEE) yield including elastically reflected electrons and true-secondary electrons, and a thermalization or replenishment parameter σ_t for the primary electrons VDF (see Chapter 5). Considering Boron Nitride thruster ceramic (i.e dielectric) walls, the SEE data is taken from Ref. [119], while $\sigma_t = 0.3$ is considered for all the cases presented here. It is underlined that the anode sheath model features no SEE.

4.2.2 Simulation results and discussion

4.2.2.1 Effects of the number of time sub-iterations

The value of N_{ke} has a big impact on the computational time required by NOMADS to complete a simulation step between two PIC states. Aiming to limit this computational time as much as possible, several simulations have been performed based on the reference case described in Sec. 4.2.1 so as to assess the influence of N_{ke} on the simulation results. In particular, values of 5, 10, 20, 50 and 100 sub-iterations have been considered.

Figs. 4.7(a) and 4.7(b) shows the time evolution and the normalized amplitude spectrum of the discharge current for all cases above. After the initialization phase, along which I_d is not obtained, the same oscillating behavior of the discharge current characterizing the typical HET breathing mode is reproduced in all the cases with minimal differences. The largest I_d peak occurs during the first steps with NOMADS due to the initial conditions provided by the initialization phase. After a transient period of about 225 μs, a sustained oscillating regime is reached, with a dominant oscillation frequency of ~11.45 kHz in all cases. On the other hand, Fig. 4.8 shows the evolution of the single core equivalent total computational time with N_{ke}. Given the significant increase with N_{ke} of the total computational time and the fact that a higher value of N_{ke} does not contribute to reduce the large oscillation peaks in the discharge current, a value of $N_{ke} = 5$ is considered for all the simulations shown hereafter.

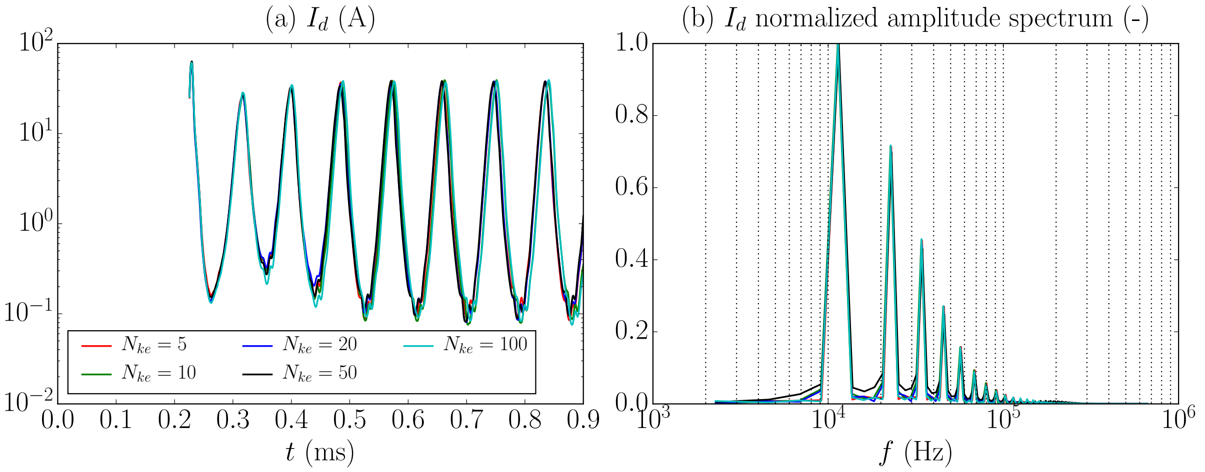

Figure 4.7: Time evolution (a) and normalized amplitude spectrum (b) of the discharge current I_d for the different N_{ke} values.

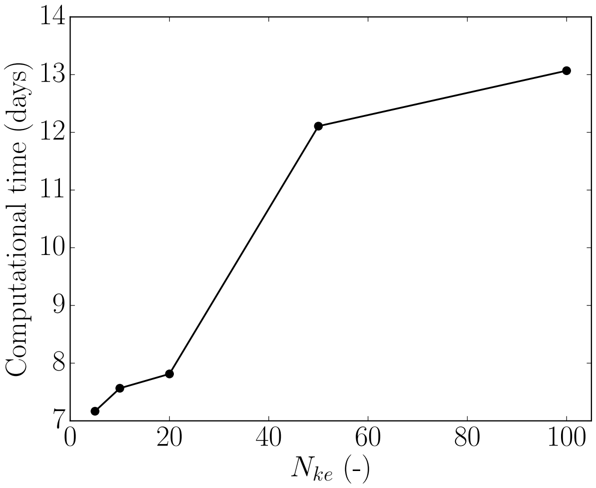

Figure 4.8: Evolution with N_{ke} of the total single core computational time.

4.2.2.2 Reference case results

The results for the SPT-100 HET reference simulation case described in Sec. 4.2.1 are discussed in detail in this section. Tab. 4.5 lists the relevant data of the discharge, which shall be commented on this section along with Figs. 4.9-4.17.

The ionization induced predator-prey type fluctuation characterizing the typical HET breathing mode is revealed in Figs. 4.9(a) and 4.9(b), showing the time evolution and the normalized amplitude spectrum, respectively, of both the average plasma density $\bar{n}_e$ (solid black line) and the average neutral density $\bar{n}_n$ (dashed black line) in the simulation domain. The average plasma density features a phase delay of 76.13 degrees with respect to the average neutral density, presenting both magnitudes the same dominant oscillation frequency of 11.45 kHz, thus coincident with that of the discharge current, already given in Sec. 4.2.2.1. This result is very close to that obtained in previous simulations [146, 152, 165], and is in the 10-30 kHz range reported by experiments [104, 106, 107]. The time-averaged mean, maximum and mininum values of both $\bar{n}_e$ and $\bar{n}_n$ are listed in Tab.

Variable	**Units**	**Value**
$\bar{n}_e$ min., max., mean	m^{-3}	$9.23 \cdot 10^{15}$, $3.96 \cdot 10^{17}$, $1.53 \cdot 10^{17}$
$\bar{n}_n$ min., max., mean	m^{-3}	$3.12 \cdot 10^{17}$, $1.10 \cdot 10^{18}$, $7.51 \cdot 10^{17}$
$\bar{n}_e$, $\bar{n}_n$ frequency, phase shift	kHz, deg	11.45, 76.13
I_d min., max., mean	A	$1.01 \cdot 10^{-1}$, $3.79 \cdot 10^{1}$, $6.41 \cdot 10^{0}$
$I_{i\infty}$ min., max., mean	A	$1.00 \cdot 10^{-1}$, $2.87 \cdot 10^{1}$, $4.84 \cdot 10^{0}$
I_d, $I_{i\infty}$ frequency, phase shift	kHz, deg	11.45, 20.38
I_{wi}, I_{prod}	A	2.95, 7.79
I_{sp}, F	s, mN	1508, 73.96
$P_{zi\infty}$, $P_{i\infty}$	W	654, 792
P_d, $\varepsilon_E^{P_d}$	W, -	1924, 0.51
P_{use}, $\varepsilon_E^{P_{use}}$	W, -	654, 0.17
P_{loss}, $\varepsilon_E^{P_{loss}}$	W, -	1194, 0.32
P_{walls}, $\varepsilon_E^{P_{walls}}$	W, -	1032, 0.27
$P_{ion,ex}$, $\varepsilon_E^{P_{ion,ex}}$	W, -	162, 0.05
η_{thr}, η_u, η_{cur}, η_{div}, η_{prod}	-	0.28, 0.97, 0.76, 0.83, 0.62
ν_{cat}, P_{cat}	MHz, W	462, 29

Table 4.5: Main results for the reference simulation case. Mean values represent time-averaged values over the number of complete cycles within the last 450 μs of simulation time. The maximum and minimum values represent the average of the peak and trough values within that period. Please note that the value of $P_{zi\infty}$ does not contain the contribution of the neutral species. However, since this contribution is negligible compared to that of the ions, $P_{zi\infty}$ takes the value of P_{use} after truncation and approximation.

4.5. On the other hand, Figs. 4.9(c) and 4.9(d) show, respectively, the time evolution and the normalized amplitude spectrum of both the discharge current I_d (solid black line) and the beam current $I_{i\infty}$ (dashed black line), the latter representing the total ion current leaving the simulation domain through the free loss boundary [blue boundary in Fig. 4.6(a)]. As expected, the beam current is lower than the discharge current (see time-averaged mean, maximum and minimum values on Tab. 4.5), and presents a phase delay of 20.38 degrees with respect to the discharge current. The lower phase delay between I_d and $I_{i\infty}$ with respect to that between $\bar{n}_e$ and $\bar{n}_n$ may be related to the faster electron-ion dynamics with respect to the ion-neutral dynamics. Both currents feature the same dominant oscillation frequency commented above. The peak values of the discharge current induced by the ionization instability are around 6 times higher than the mean value, which reveals the need for a future implementation of effective strategies to damp those large oscillations, such as resistor-inductor-capacitor (RLC) networks or proportional-integral-derivative (PID) control algorithms [166, 167]. Furthermore, Figs. 4.9(e) and 4.9(f) depict the time evolution of the utilization efficiency, already defined in Eq. (4.1), and the thrust efficiency

$$\eta_{thr} = \frac{F^2}{2\dot{m}_A P_d}, \tag{4.2}$$

where $P_d = V_d I_d$ is the discharge power and F is the thrust force, obtained as the axial momentum flux of the heavy species [computed according to Eq. (2.27)] integrated over the free loss domain boundary [blue boundary in Fig. 4.6(a)]. The phase shift between the oscillating average plasma and neutral densities in the domain, partially mitigated by the ion recombination at the thruster walls, is responsible for the instantaneous values $\eta_u > 1$, while the mean value over five complete cycles is 0.97. This higher-than-expected value is probably due to the large oscillations of I_d. The temporal evolution of the thrust efficiency yields a mean value of 0.48. Given its non-linear dependence on the oscillating thrust and discharge power, a more representative value of 0.28 is obtained using the properly time-averaged values of those quantities. Moreover, Tab. 4.5 lists the time-averaged values of the current, divergence and production efficiencies, defined respectively as

$$\eta_{cur} = \frac{I_{i\infty}}{I_d}, \quad \eta_{div} = \frac{P_{zi\infty}}{P_{i\infty}}, \quad \eta_{prod} = \frac{I_{i\infty}}{I_{prod}}, \tag{4.3}$$

where $P_{zi\infty}$ and $P_{i\infty}$ are the axial and total ion power deposited to the free loss domain boundary, respectively, and $I_{prod} = I_{wi} + I_{i\infty}$ is the total ion current produced though the ionization processes, with I_{wi} the total ion current collected at the thruster walls (i.e. the anode and dielectric walls). Tab. 4.5 gathers the time-averaged values of all those quantities and of the specific impulse, defined as

$$I_{sp} = \frac{F}{g_0 \dot{m}_A}. \tag{4.4}$$

where $g_0 = 9.80665$ ms^{-2} is the standard acceleration of gravity.

The mass balance of a heavy species s is

$$\frac{dM_s}{dt} = \dot{m}_s^{coll} + \dot{m}_s^{tw} + \dot{m}_s^{fw}, \tag{4.5}$$

where M_s is the total heavy species mass in the simulation domain, $\dot{m}_s^{coll}$ is the mass flow generated or loss through the collisional processes, and $\dot{m}_s^{tw}$ and $\dot{m}_s^{fw}$ are the mass flows *to* and *from* the simulation domain walls, respectively. The error committed on the determination of the mass balance of the heavy species s is defined as

$$\epsilon_{M,s} = \frac{dM_s/dt - (\dot{m}_s^{coll} + \dot{m}_s^{tw} + \dot{m}_s^{fw})}{\dot{m}_A}. \tag{4.6}$$

Fig. 4.10(a) shows the time evolution of the mass balance per heavy species and of the total one considering all the heavy species simulated. The time evolution of the error committed on each mass balance above is depicted in Fig. 4.10(b), while Fig. 4.10(c) plots the two partial contributions to the total heavy species mass flow, defined as

$$\varepsilon_M^{tw} = \frac{|\dot{m}^{tw}|}{|\dot{m}^{tw}| + |\dot{m}^{fw}|}, \quad \varepsilon_M^{fw} = \frac{|\dot{m}^{fw}|}{|\dot{m}^{fw}| + |\dot{m}^{fw}|}, \tag{4.7}$$

where $\dot{m}^{tw}$ and $\dot{m}^{fw}$ represent the total heavy species mass flow to and from the simulation domain, respectively. As expected, ε_M^{tw} and ε_M^{fw} feature a phase shift of 180 degrees revealing the dominant injection and exhaust stages of the discharge.

Variable description	**Symbol**	**Units**
Electron-neutral elastic collision frequency	ν_{en}^{el}	Hz
Electron-ion $i1$ elastic Coulomb collision frequency	ν_{ei1}^{el}	Hz
Electron-ion $i2$ elastic Coulomb collision frequency	ν_{ei2}^{el}	Hz
Electron-neutral ionization Xe → Xe^+ collision frequency	ν_{en}^{ion01}	Hz
Electron-neutral ionization Xe → Xe^{++} collision frequency	ν_{en}^{ion02}	Hz
Electron-ion $i1$ ionization $\mathrm{Xe}^+ \rightarrow \mathrm{Xe}^{++}$ collision frequency	ν_{ei1}^{ion12}	Hz
Total electron collision frequency (sum of the above)	ν_e	Hz
Effective electron collision frequency	$\nu_e^* = \nu_e + \alpha_t\omega_{ce}$	Hz
Hall parameter	$\chi = \omega_{ce}/\nu_e$	-
Effective Hall parameter	$\chi^* = \omega_{ce}/\nu_e^*$	-

Table 4.6: Collision frequencies and Hall parameter definitions for the HET simulations.

The steady total energy balance in the plasma discharge may be written as

$$0 = P_d - P_{ion,ex} - P_{walls} - P_{use}, \tag{4.8}$$

where the discharge power P_d is the power delivered to the system, P_{use} is the useful fraction of that power, invested in the thrust generation through the ions acceleration, $P_{ion,ex}$ represent the power spent in the ionization and excitation processes, and P_{walls} groups the total power deposited by the plasma to the thruster walls (i.e. the anode and the dielectric walls), and the electron energy flow and the heavy species non-axial energy flow through the free loss boundary. The total loss power is $P_{loss} = P_{ion,ex} + P_{walls}$. Fig. 4.10(b) shows the time evolution of the total energy balance in Eq. (4.8) and the terms in its right hand side, with its corresponding sign, while their time-averaged values are listed in Tab. 4.5. Considering the time-averaged values, $P_{use}/P_d = 0.34$, which is close to the thrust efficiency (see Tab. 4.5). Fig. 4.10(d) plots the total energy balance error, defined as

$$\epsilon_E = \frac{P_d - (P_{ion,ex} + P_{walls} + P_{use})}{P_d}. \tag{4.9}$$

Considering the time-averaged quantities, a value of $\epsilon_E \simeq 4\%$ is obtained. On the other hand, similarly to the case of the heavy species mass balance, Fig. 4.10(e) depicts the time evolution of the partial contributions of each term in the right hand side of Eq. (4.8), defined as

$$\varepsilon_E^{P_j} = \frac{|P_j|}{\sum_j |P_j|}, \tag{4.10}$$

where P_j refers to any term in the right hand side of Eq. (4.8). The time-averaged partial contributions are listed in Tab. 4.5.

Figs. 4.11-4.16 show the axial profiles at $r = 4.63$ cm of different magnitudes characterizing the discharge at the simulation stages A, B, C and D indicated in Fig. 4.9(c), along with their time-averaged axial profiles at the same radius and 2D contour maps. In addition, Figs. 4.16(d) and 4.16(f) show the streamlines of the 2D (z, r) electron and ion current densities $\tilde{\boldsymbol{j}}_e$ and $\tilde{\boldsymbol{j}}_i$. In the axial profile figures, the vertical black dashed line at $z = 2.85$ cm indicates the axial position of the thruster chamber exit plane, while the vertical black dot-dashed line at $z = 5.94$ cm indicates the axial position of the magnetic field streamline passing through the cathode, which corresponds to the red line in Fig. 4.11(b). The cathode location (point C1 in Fig. 4.6(b) with coordinates listed in Tab. 4.3) is represented by the black square marker in all the 2D contour figures. For the sake of simplicity, the PIC mesh in Fig. 4.6(a) has been used for plotting all the spatially dependent results shown in this section.

The electric potential axial profiles shown in Fig. 4.11(a) present their global maximum and minimum values at ∼0.3 cm away from the anode wall, and at the axial position of the cathode magnetic line, respectively. The location of the maximum slope between those positions above, which characterizes the HET acceleration region, varies with the I_d cycle stage, and coincides with the location of the maximum axial electric field, shown in Fig. 4.11(c). This displacement of the acceleration region also affects the axial location of the maximum electron temperature, as depicted in Fig. 4.11(e). On average, both the maximum axial electric field and electron temperature are located between the thruster chamber exit plane and the cathode magnetic line. Interestingly, the largest E_z and T_e peaks are found at the trough of I_d (i.e. the stage C). As shown in Fig. 4.9(a), the stage C features an average plasma density very close to its minimum, due to the ion depletion caused by the large axial electric field, which accelerates the ions downstream producing thrust during the stages A to C, as represented in Fig. 4.10(b) by the negative signed P_{use} in that time interval[3]. On the other hand, referring to Fig. 4.9(a), the increasing neutral density from B to C favors the electron Joule heating, thus explaining the large peak in the electron temperature at the stage C in Fig. 4.11(e), which is damped by the wall losses and the increasing ionization from C to a new stage A, passing by the intermediate stage D characterized by a maximum neutral density.

The plasma and neutral density profiles at the different discharge stages analyzed, shown in Figs. 4.11(g) and 4.12(a), respectively, along with the profiles for the singly and doubly charged ion populations depicted in Figs. 4.12(c) and 4.12(e), respectively, are consistent with the low frequency oscillating discharge dynamics commented above. The stages A and C present, respectively, the highest and the lowest plasma density profiles. As expected, the same applies to the singly and doubly charged ion populations. The doubly-to-singly charged ions particle density ratio n_{i2}/n_{i1} is shown in Figs. 4.12(g) and 4.12(h). Regarding the neutral species, it features the highest and the lowest density profiles at the stages D and B, respectively, according to the aforementioned phase shift between $\bar{n}_e$ and $\bar{n}_n$. As for the time-averaged plasma density profile shown in Fig. 4.11(g) it features a maximum upstream the acceleration region, inside the thruster chamber [see the time-average 2D contour in Fig. 4.11(h)], and decreases monotonically towards both the anode wall and the thruster exit plane due to the ion acceleration by the self-adjusted electric field shown in Fig. 4.11(d), thus yielding the ion streamlines shown in Fig. 4.16(f). The ionization region, characterized by the maximum plasma density in the domain, is located closer to the anode wall than expected. This fact is related to the lack of an electric potential plateau along the first part of the thruster chamber [see Figs. 4.11(a) and 4.11(b)], which has been reported by experiments [168–171], and greatly depends on

---

[3] P_{use} defined as the thrust multiplied by the average exhaust velocity of the ion beam is actually positive. However, it has been plotted with negative sign in Fig. 4.10(b) according to the power balance in Eq. (4.8).

the electron turbulent parameter profile simulated (see Sec. 4.2.2.5). In the near plume region, Fig. 4.11(h) reveals a higher plasma density along the symmetry axis with respect to the upper free loss boundary. This fact is due to the *reflection condition* at the axis (see Sec. 2.2.5.1.2.1), which, as expected, increases the singly and doubly charged ions particle density along the axis [see Figs. 4.12(d) and 4.12(f), respectively], thus giving rise to the formation of a single-peaked plasma plume downstream. As commented in Sec. 4.2.1, the ion-wall recombination and subsequent neutral emission from the lateral thruster walls is responsible for most of the neutral particle density in the lateral near plume regions, as shown in Fig. 4.12(b).

On the other hand, Figs. 4.13(a)-(d) and Fig. 4.13(e) show, respectively, the axial profiles at the stages A-D and the time-averaged ones for the different collision frequencies, described in Tab. (4.6). The behavior of the different elastic and ionization collision frequencies are mainly driven by the values of the various heavy species density and the electron temperature, as expected: high values of neutral density and electron temperature increase the electron-neutral collisionality, while the electron-ion Coulomb collisions dominates at low electron temperature. According to Tab. 4.6, the equivalent turbulent collision frequency is proportional to the electron cyclotron frequency through the parameter α_t (see Sec. 2.3.6 for further details), the latter being constant in the whole simulation domain here. From Figs. 4.13, 4.14(a), and 4.14(b) it is clear that the effective electron collision frequency ν_e^* (see Tab. 4.6) is dominated by the B-proportional turbulent contribution, thus featuring very similar profiles along the whole breathing mode cycle. As a result, the effective Hall parameter χ^*, shown in Figs. 4.14(e) and 4.14(f) and defined in Tab. 4.6, is much lower than the classical one χ, depicted in Figs. 4.14(c) and 4.14(d), and features similar profiles at the different stages A-D, presenting larger differences at the anode and near plume regions. The lower electron magnetization characterizing those regions yields lower values of the azimuthal electron current density $j_{\theta e}$, shown in Figs. 4.15(a) and 4.15(b). Moreover, as already observed by Ahedo *et al.* [108,109], Figs. 4.16(a) and 4.16(b) reveal a higher electron drift-to-internal energy ratio $m_e u_e^2/2T_e$ at the anode and near plume regions. According to Sec. 4.2.1, this ratio is here limited to two (see Sec. 2.3.3.2 for further details). Therefore, larger values could arise at those regions if a lower tolerance is set to the electron drift velocity limiter described in Sec. 2.3.3.2, thus suggesting that the electron inertia could play a non-negligible role there. Furthermore, the electron drift energy should be considered in the computation of the ionization rates R_i [see Eq. 2.40] if $m_e u_e^2/2T_e \sim 1$ locally [108].

The discharge current peak and trough stages A and C, respectively, can be clearly distinguished in the axial profiles shown in Figs. 4.15 and 4.16 for the electron current density components, and for the magnitude of the 2D (z, r) electron and ion current densities $\tilde{\boldsymbol{j}}_e$ and $\tilde{\boldsymbol{j}}_i$, respectively. The results for the electron azimuthal and perpendicular current density components shown in Figs. 4.15(a) and 4.15(b), and 4.15(c) and 4.15(d), respectively are in agreement with Eq. (2.105), from which, neglecting collisions, $j_{\theta e} \simeq -\chi^* j_{\top e}$. Both electron current density components $j_{\theta e}$ and $j_{\top e}$ feature a change of sign when crossing the cathode magnetic line. This is consistent with the negative axial component of the electric field that develops in that region [see Fig. 4.11(c)], which has also been reported by experiments [168, 169]. The cathode injection increases the electron parallel current density along the nearby magnetic field lines, as can be seen in Figs. 4.15(e) and 4.15(f). The electron streamlines shown in Fig. 4.16(d) illustrate how the collisional processes taking place in the very near plume region yield a perpendicular electron transport towards both the thruster chamber and the free loss domain boundary. The former constitutes the back-streaming flow of primary electrons in charge of ionizing the neutral gas injected through the anode, which are highly magnetized and feature a diffusive-collisional motion characterized by the dominant azimuthal $\boldsymbol{E} \times \boldsymbol{B}$ drift[4], and a reduced perpendicular motion through the anode. As shown in Fig. 4.11(f), they are heated up by the collisions in the region between the cathode magnetic line and the thruster chamber exit plane. Inside the chamber, the electron temperature decreases due to the neutral gas ionization and excitation processes and the wall losses. On the other hand, the later are responsible for the ion beam neutralization in the near plume region, and is favored by a potential jump of $\sim$25 V between the cathode and the free loss domain boundary [see Fig. 4.11(b)].

Moving now to the anode region, Fig. 4.17 compares the time-averaged axial profiles of various magnitudes at $r = 4.63$ cm (black solid lines) and at $r = 4.25$ cm (red dashed lines), corresponding to the TCL. In particular, the red dashed line in Fig. 4.17(a) reveals a larger electric potential at the anode sheath edge (boundary node of the simulation domain at $z = 0$) than at the next PIC mesh node located inside the domain. As shown in Fig. 4.17(b), this fact leads to the development of a positive axial component of the electric field in the very near anode region, which is responsible for reducing the ion backflow to the anode wall [see the axial component of the ion current density j_{zi} in Fig. 4.17(d)]. As a consequence, Fig. 4.17(e) shows a higher than expected decrease of the plasma density there, which in turns yields a lower electron backflow to the anode [see Fig. 4.17(c)]. This unusual scenario in the nominal operation conditions of a HET is artificially induced by a numerical issue related to the GR techniques commented in Sec. 2.3.7. According to Eq. (2.119), the magnitudes at the MFAM boundary faces are obtained as an extrapolation of their known values at the nearby MFAM cells, so that numerical errors may easily arise. An improved approach for computing the electric potential and the electron temperature at the simulation domain boundary from the corresponding boundary conditions has been proposed in Ref. [93], and will be implemented in future versions of the code.

On the other hand, Fig. 4.15(f) reveals an oscillating pattern in the parallel electron current density component along the magnetic lines in the vicinity of the volumetric cathode in the near plume region. This effect, also present in Fig. 4.15(e), is responsible for the electron streamlines trend change there, as shown in Fig. 4.16(d), and is most probably due to numerical issues related to the abrupt MFAM cells change of size in that region. Future work will deal with the development of improved simulation domain MFAMs featuring a smoother and progressive evolution of the cells size. Besides, special attention will be put to the PIC-mesh-to-MFAM cell size ratio, since important interpolation errors may be present whenever that ratio greatly differs from unity. This issue can be specially critical at the domain boundary.

Moreover, in the near plume region, Figs. 4.11(a) and 4.11(b), and Figs. 4.11(e) and 4.11(f) show a flat evolution of the electric potential and the electron temperature, respectively. The still relatively high magnetization of the electron population there [$\chi^* \sim 40$ according to Figs. 4.14(e) and 4.11(f)] is probably behind this behavior. Future simulation domains featuring an extended near plume up to regions with $|\boldsymbol{B}| \sim 1$ G will

---

[4] The $\boldsymbol{E} \times \boldsymbol{B}$ drift gives rise to the azimuthal Hall current, which gives its name to the thruster, although an opposing $\nabla p_e \times \boldsymbol{B}$ diamagnetic drift is also present [1, 3].

allow to explore the discharge behavior when the magnetic field becomes residual, and to assess the influence of the downstream boundary conditions on the expected decaying profiles of the electric potential and the electron temperature along the expanding plasma plume.

Furthermore, the thermal electron injection performed by the cathode leads to unphysical effects in the region close to its location. According to Figs. 4.11(b) and 4.11(d), the injected electrons through the cathode are accelerated along the magnetic field streamlines in the near cathode region through a ∼15 V potential jump (see Sec. 4.2.2.4 for further details). In fact, the isopotential lines of 5, 10 and 15 V depicted in Fig. 4.11(b) are perpendicular to the red cathode magnetic field streamline. Thus, as detailed in Sec. 4.2.2.4, the magnetic lines are far from being isopotential in that region.

As a final comment, the simulation here described considered a total number of particles of around one million. The total single core computational time for $N_{ke} = 5$ was already shown in Fig. 4.8. Using 10 threads in an up-to-date workstation, the reference simulation here described has required a total computational time of around 17 hours.

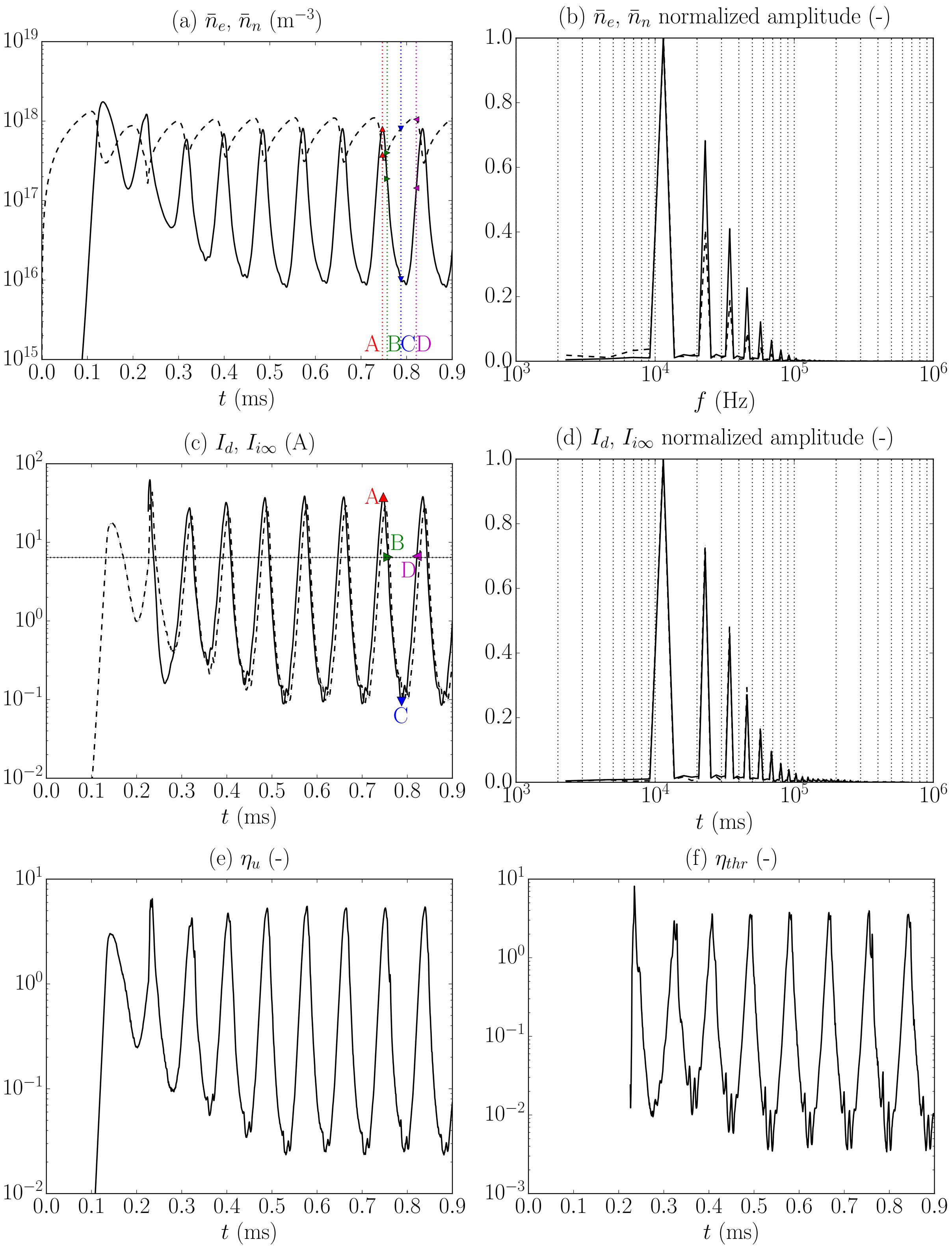

Figure 4.9: Reference simulation case results. Time evolution of (a) $\bar{n}_e$ and $\bar{n}_n$, (c) I_d and $I_{i\infty}$, and (e) η_u and (f) η_{thr}. Normalized amplitude spectrum of (b) $\bar{n}_e$ and $\bar{n}_n$ and (d) I_d and $I_{i\infty}$. Solid and dashed lines in (a) and (b) corresponds to $\bar{n}_e$ and $\bar{n}_n$, respectively, while in (c) and (d) corresponds to I_d and $I_{i\infty}$, respectively. The horizontal dotted line in (c) indicates the time-averaged value of I_d. The red up, green right, blue down and purple left triangle markers in (c) indicate the simulation stages A, B, C and D coinciding with the successive peak, downwards crossing with the time-averaged value, trough and upwards crossing with the time-averaged value of I_d. Dotted vertical lines and corresponding markers indicate those stages in (a).

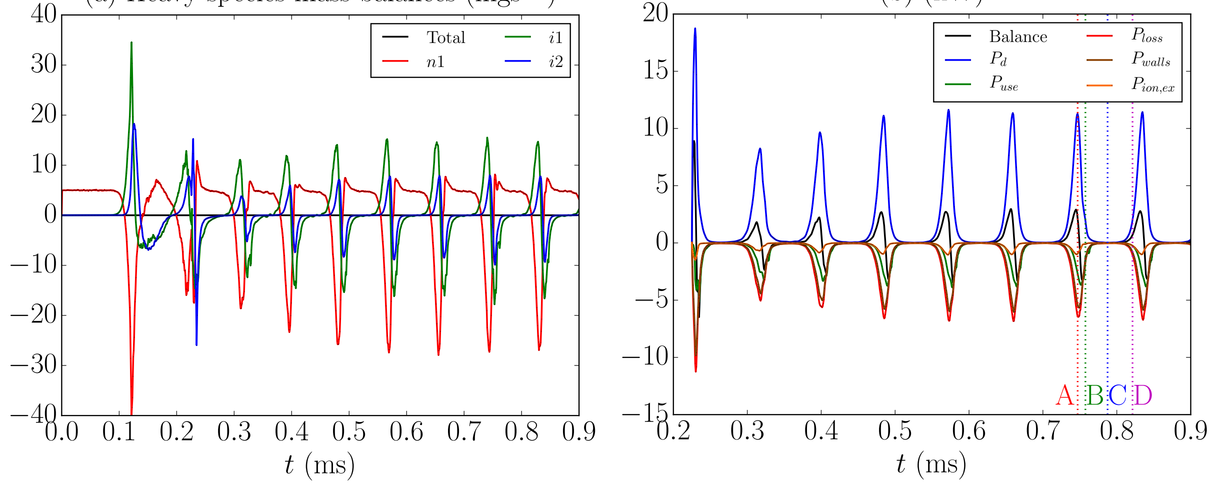

(a) Heavy species mass balances (mgs^{-1})

(b) (kW)

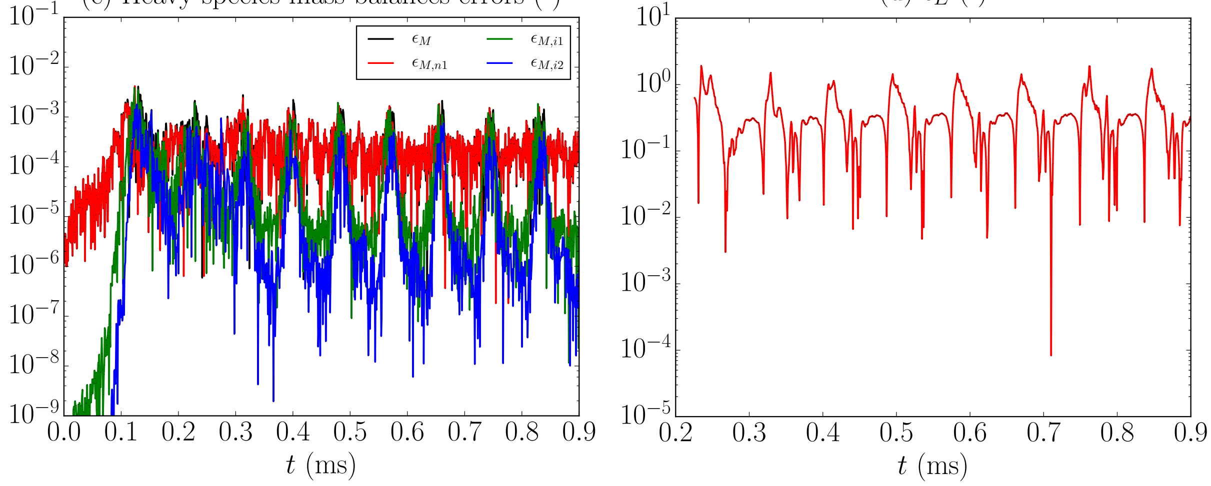

(c) Heavy species mass balances errors (-)

(d) ϵ_E (-)

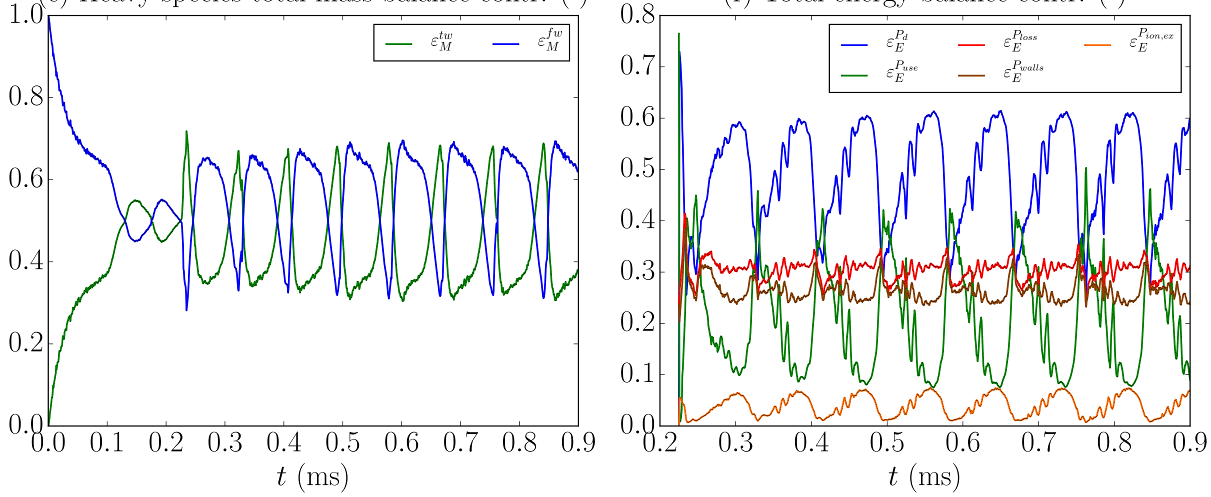

(e) Heavy species total mass balance contr. (-)

(f) Total energy balance contr. (-)

Figure 4.10: Heavy species mass balance and the total energy balance results for the reference simulation case. Time evolution of (a) the heavy species mass balance, (b) the total energy balance, (c) the heavy species mass balance errors, (d) the total energy balance error, (e) the partial contributions to the total mass balance for the heavy species defined in Eq. (4.7) and (f) the partial contributions to the total energy balance defined in Eq. (4.10). The total energy balance is only plotted after the initialization phase (i.e. once NOMADS is active). Dotted vertical lines in (b) indicate the simulation stages A-D defined in Fig. 4.9(c).

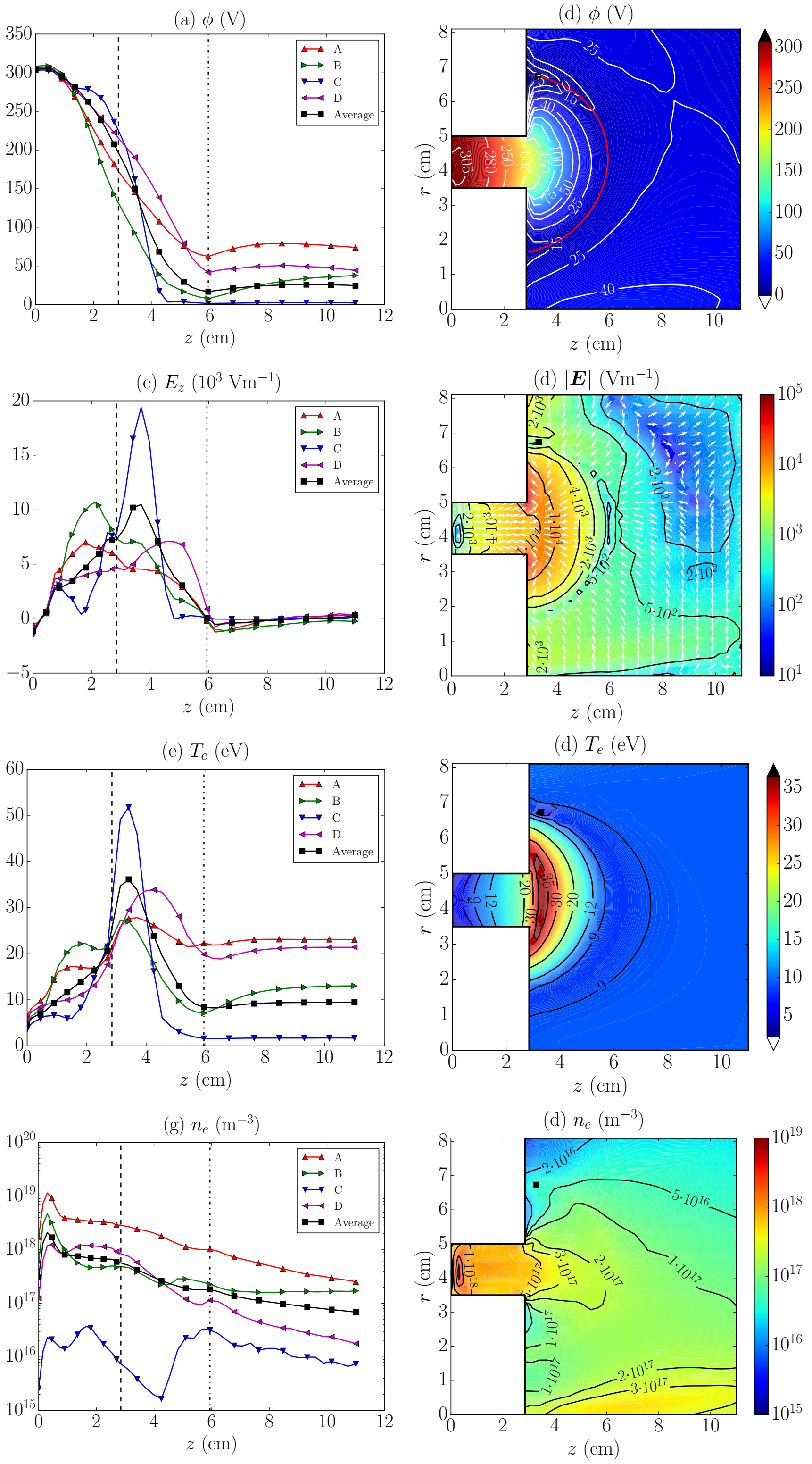

Figure 4.11: Reference simulation case results. Axial profiles at $r = 4.63$ cm and time-averaged 2D contours of the electric potential (a) and (b), the axial electric field (c) and (d), the electron temperature and (e) and (f), and the plasma density (g) and (h). The black square marker in the 2D contours indicates the cathode position at C1. In (b) the red line represents the magnetic field streamline passing through the cathode. In (d) the white arrows show the direction of the electric field. In (a), (c), (e) and (f), the vertical black dashed and dot-dashed lines indicate, respectively, the axial position of both the thruster chamber exit plane at $z = 2.85$ cm, and the magnetic field streamline passing through the cathode at $z = 5.94$ cm.

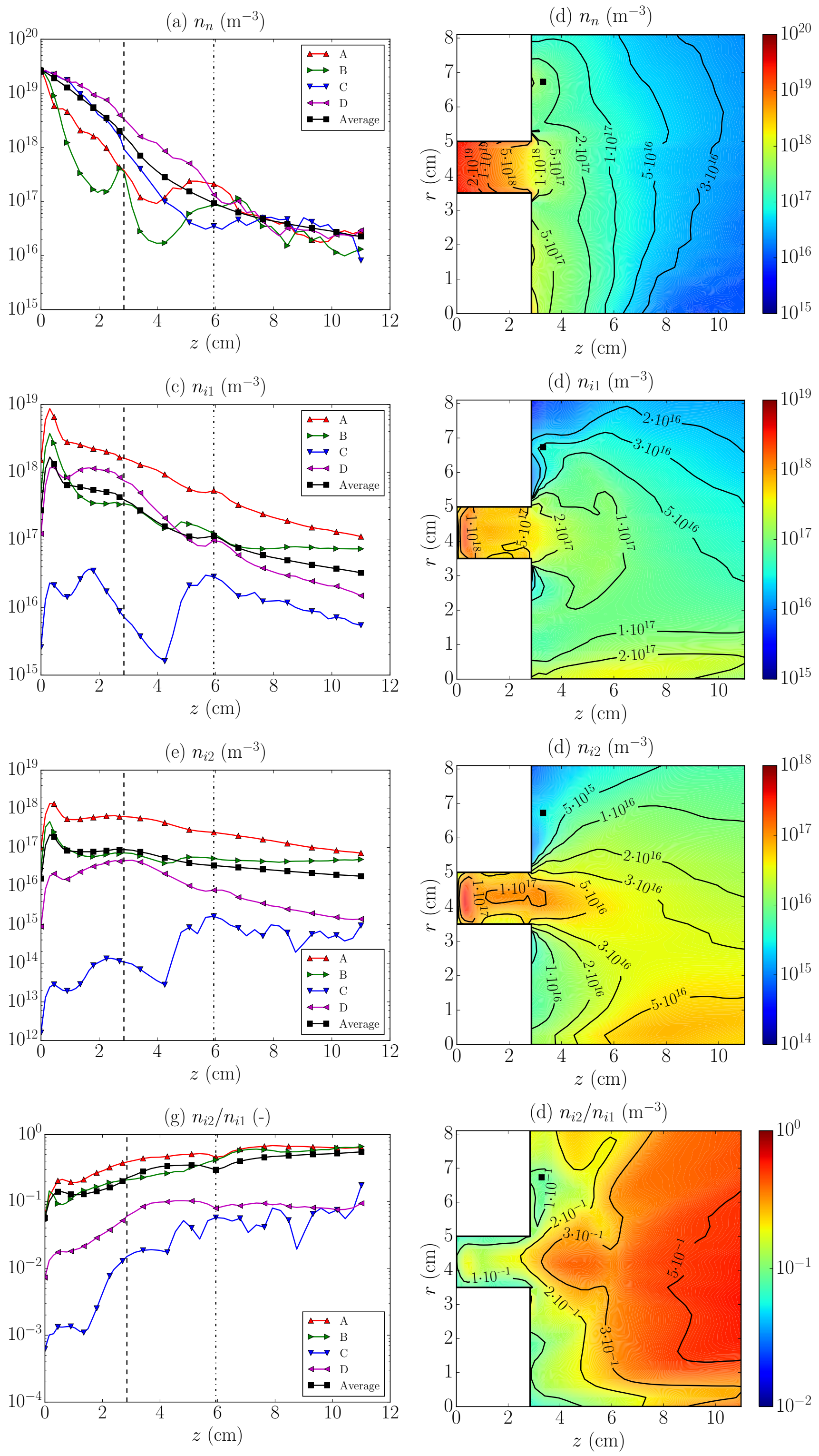

Figure 4.12: Reference simulation case results. Axial profiles at $r = 4.63$ cm and time-averaged 2D contours of the neutrals particle density (a) and (b), the singly charged ions particle density (c) and (d), the doubly charged ions particle density (e) and (f), and the doubly-to-singly charged ions particle density ratio (g) and (h). The black square marker in the 2D contours indicates the cathode position at C1. In (a), (c), (e) and (f), the vertical black dashed and dot-dashed lines indicate, respectively, the axial position of both the thruster chamber exit plane at $z = 2.85$ cm, and the magnetic field streamline passing through the cathode at $z = 5.94$ cm.

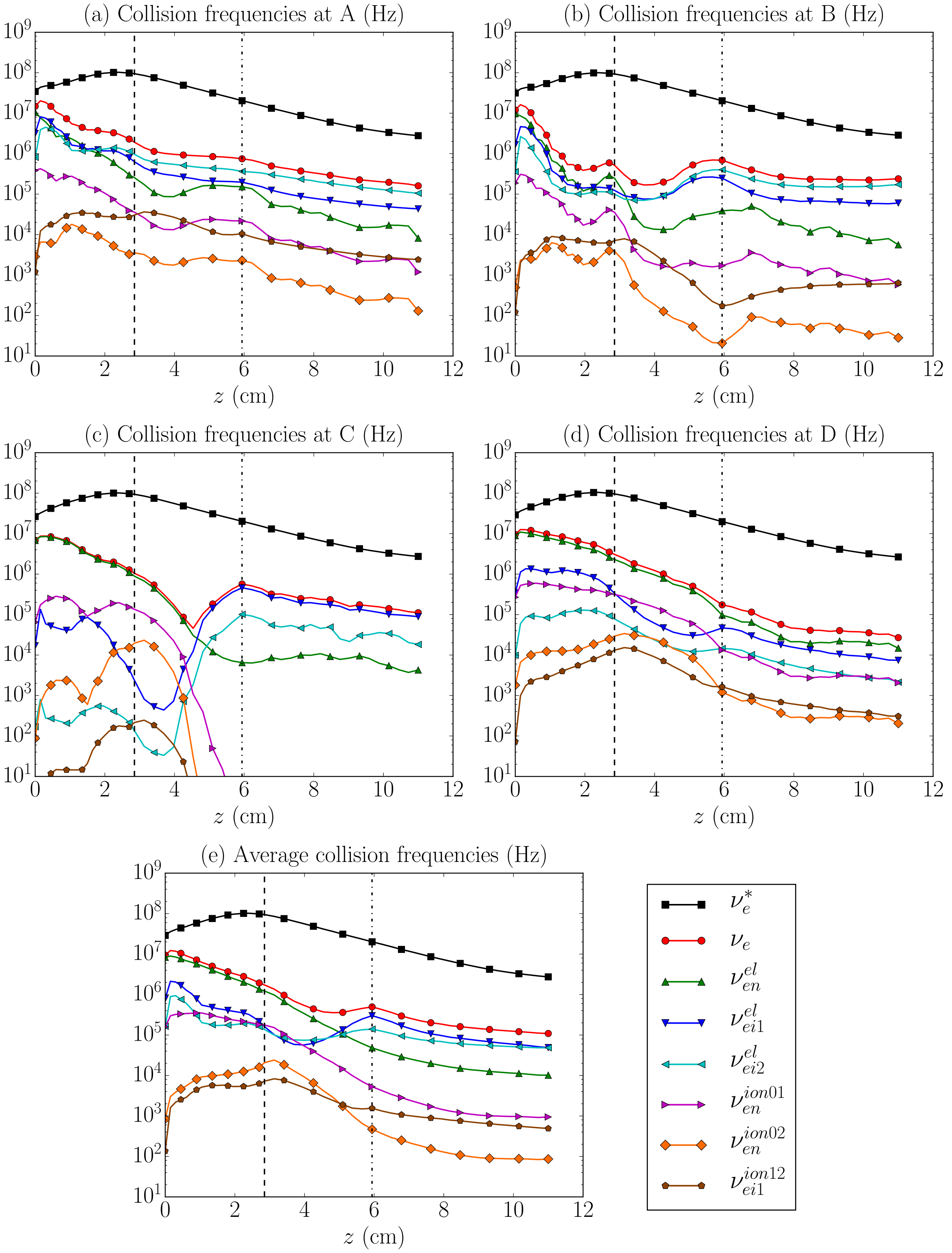

Figure 4.13: Reference simulation case results. Axial profiles at $r = 4.63$ cm of the different collision frequencies defined in Tab. 4.6 at A (a), B (b), C (c) and D (d), and time-averaged (e). The vertical black dashed and dot-dashed lines indicate, respectively, the axial position of both the thruster chamber exit plane at $z = 2.85$ cm, and the magnetic field streamline passing through the cathode at $z = 5.94$ cm.

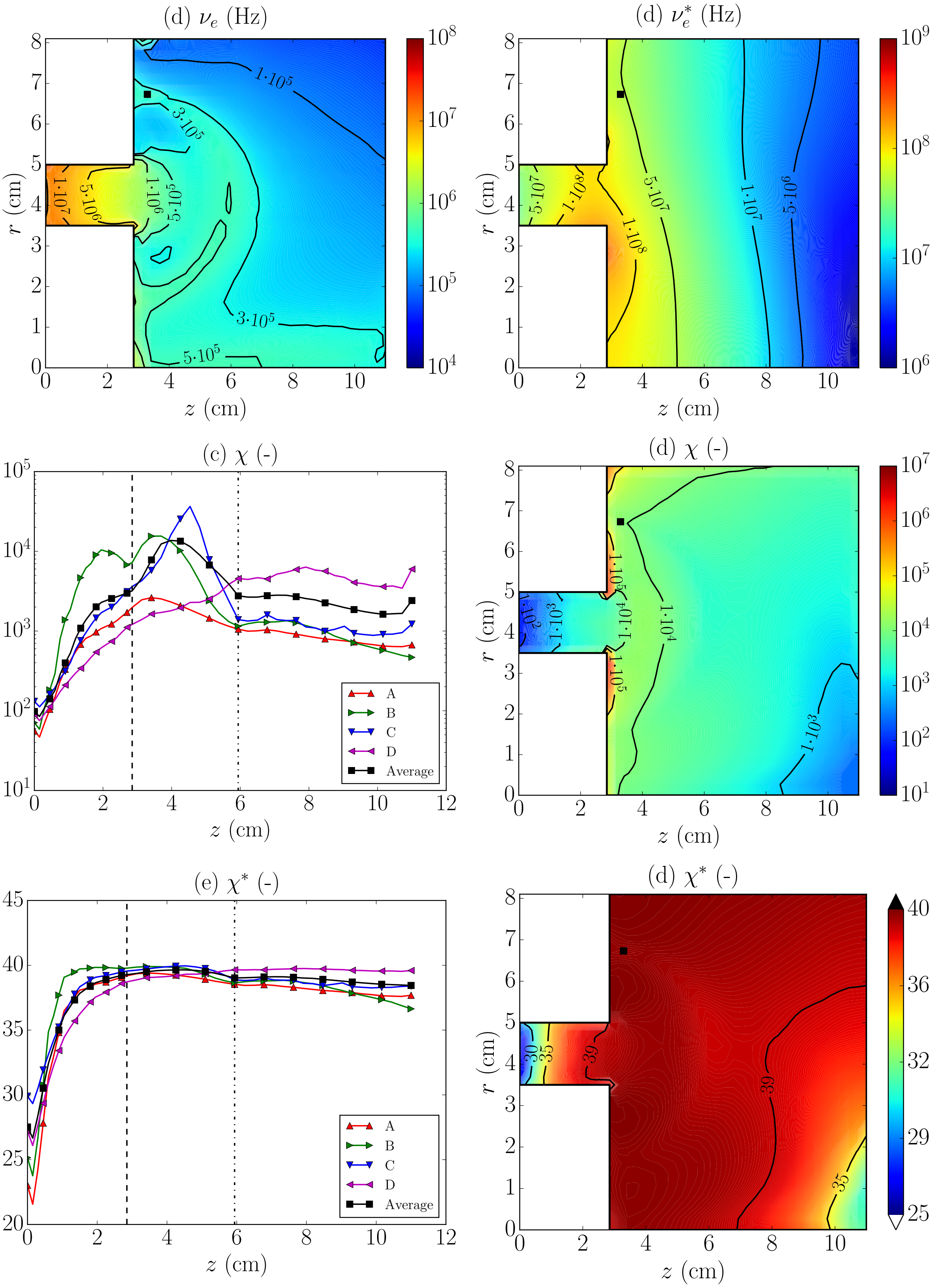

Figure 4.14: Reference simulation case results. 2D contours of the time-averaged total (a) and effective (b) electron collisional frequency, and classical (d) and effective (e) Hall parameters. The black square marker in the 2D contours above indicates the cathode position at C1. Axial profiles at $r = 4.63$ of the classical (c) and effective (d) Hall parameters. The vertical black dashed and dot-dashed lines indicate, respectively, the axial position of the thruster chamber exit plane at $z = 2.85$ cm, and the axial position of the magnetic field streamline passing through the cathode at $z = 5.94$ cm.

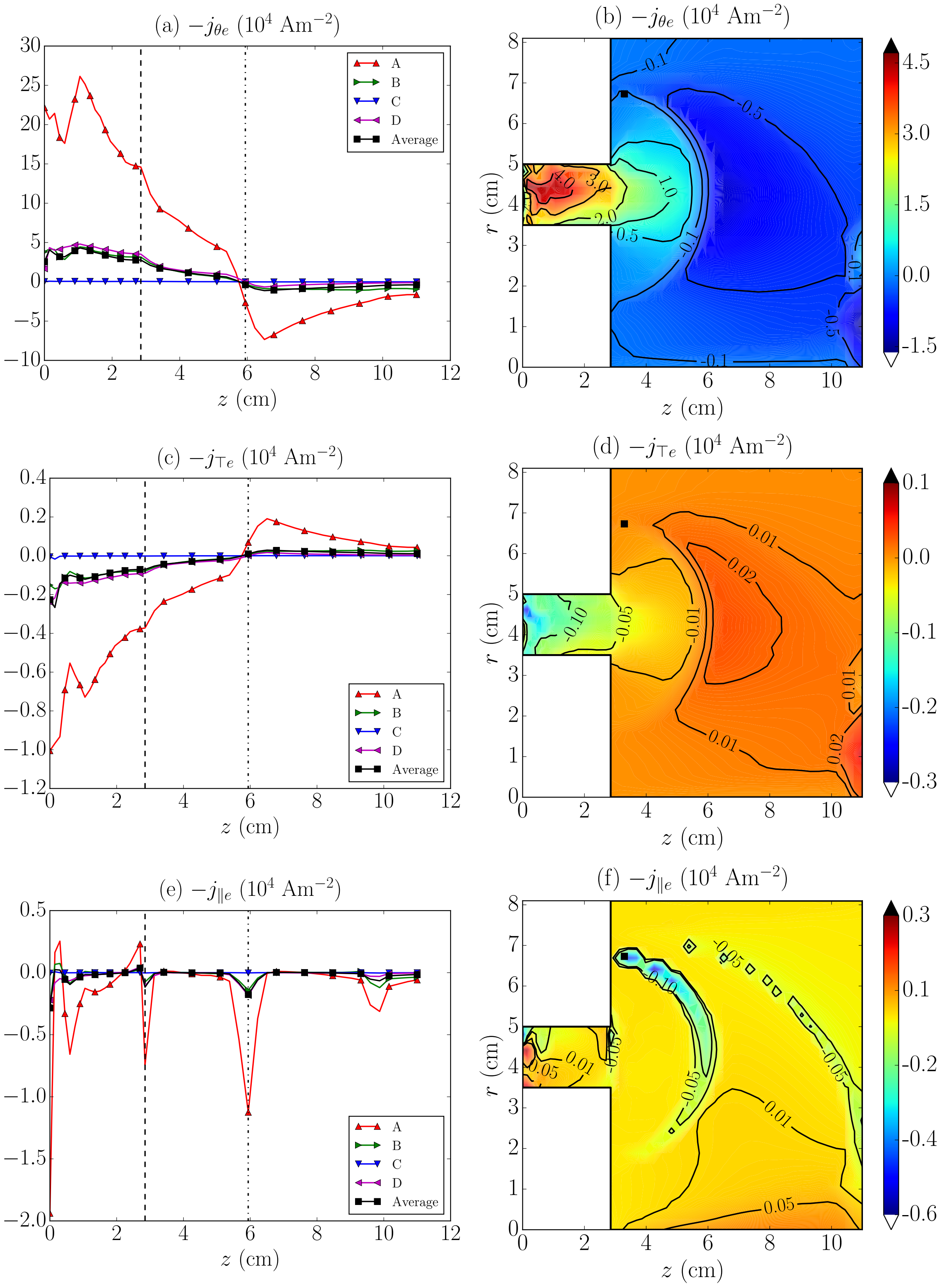

Figure 4.15: Reference simulation case results. Axial profiles at $r = 4.63$ cm and time-averaged 2D contours of the electron current density azimuthal (a) and (b), perpendicular (c) and (d) and parallel components. The black square marker in the 2D contours indicates the cathode position at C1. In (a), (c) and (e) the vertical black dashed and dot-dashed lines indicate, respectively, the axial position of both the thruster chamber exit plane at $z = 2.85$ cm, and the magnetic field streamline passing through the cathode at $z = 5.94$ cm.

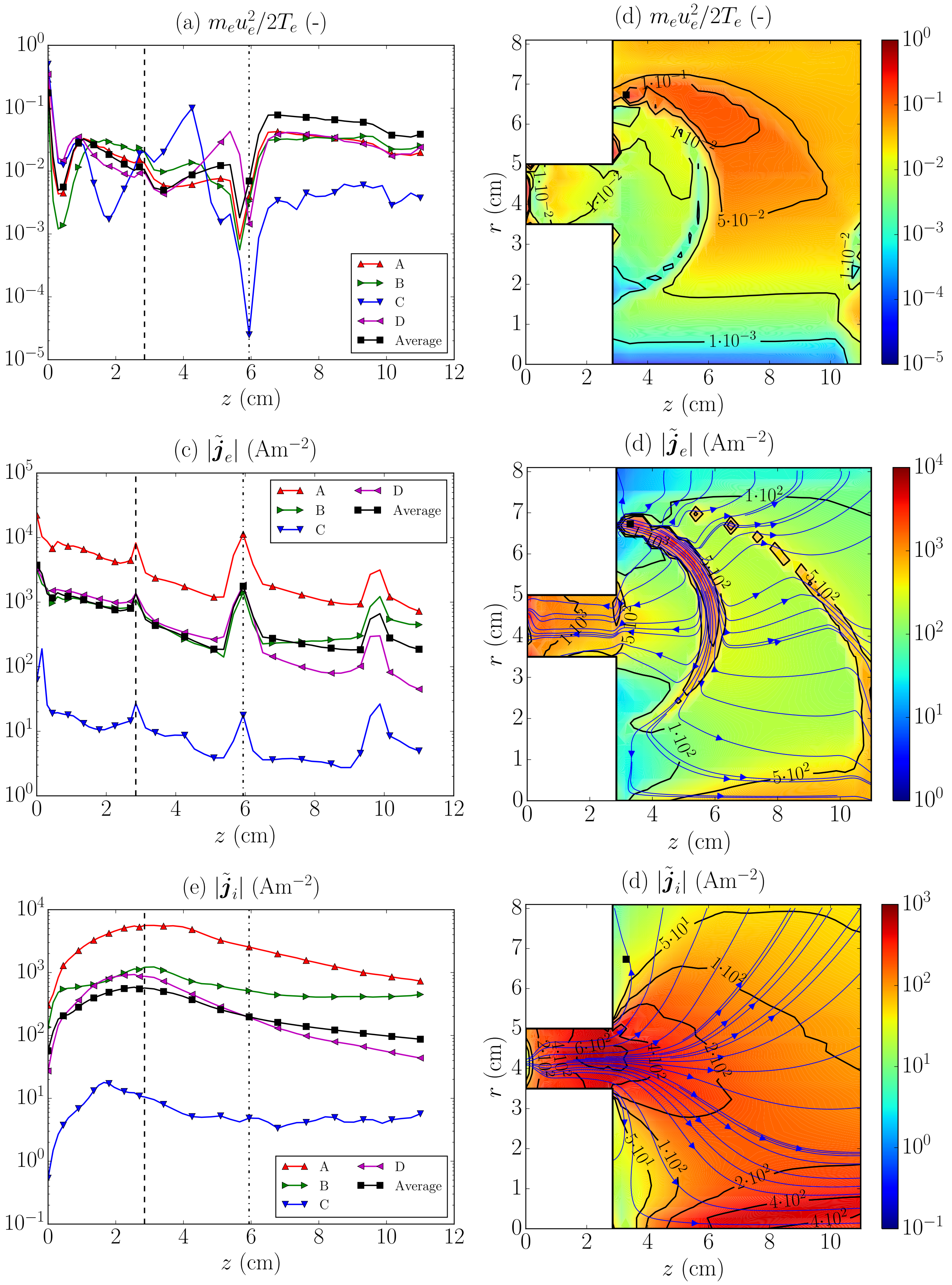

Figure 4.16: Reference simulation case results. Axial profiles at $r = 4.63$ cm and time-averaged 2D contours of (a) and (b) the electron drift-to-inernal energy ratio $m_e u_e^2/2T_e$, (c) and (d) the magnitude of the 2D (z, r) electron current density vector $\tilde{\boldsymbol{j}}_e$, and (e) and (f) the magnitude of the 2D (z, r) ion current density vector $\tilde{\boldsymbol{j}}_i$. The black square marker in the 2D contours indicates the cathode position at C1. The blue lines with arrows in (d) and (f) indicates the $-\tilde{\boldsymbol{j}}_e$ and $\tilde{\boldsymbol{j}}_i$ streamlines, respectively. In (a), (c) and (e) the vertical black dashed and dot-dashed lines indicate, respectively, the axial position of both the thruster chamber exit plane at $z = 2.85$ cm, and the magnetic field streamline passing through the cathode at $z = 5.94$ cm.

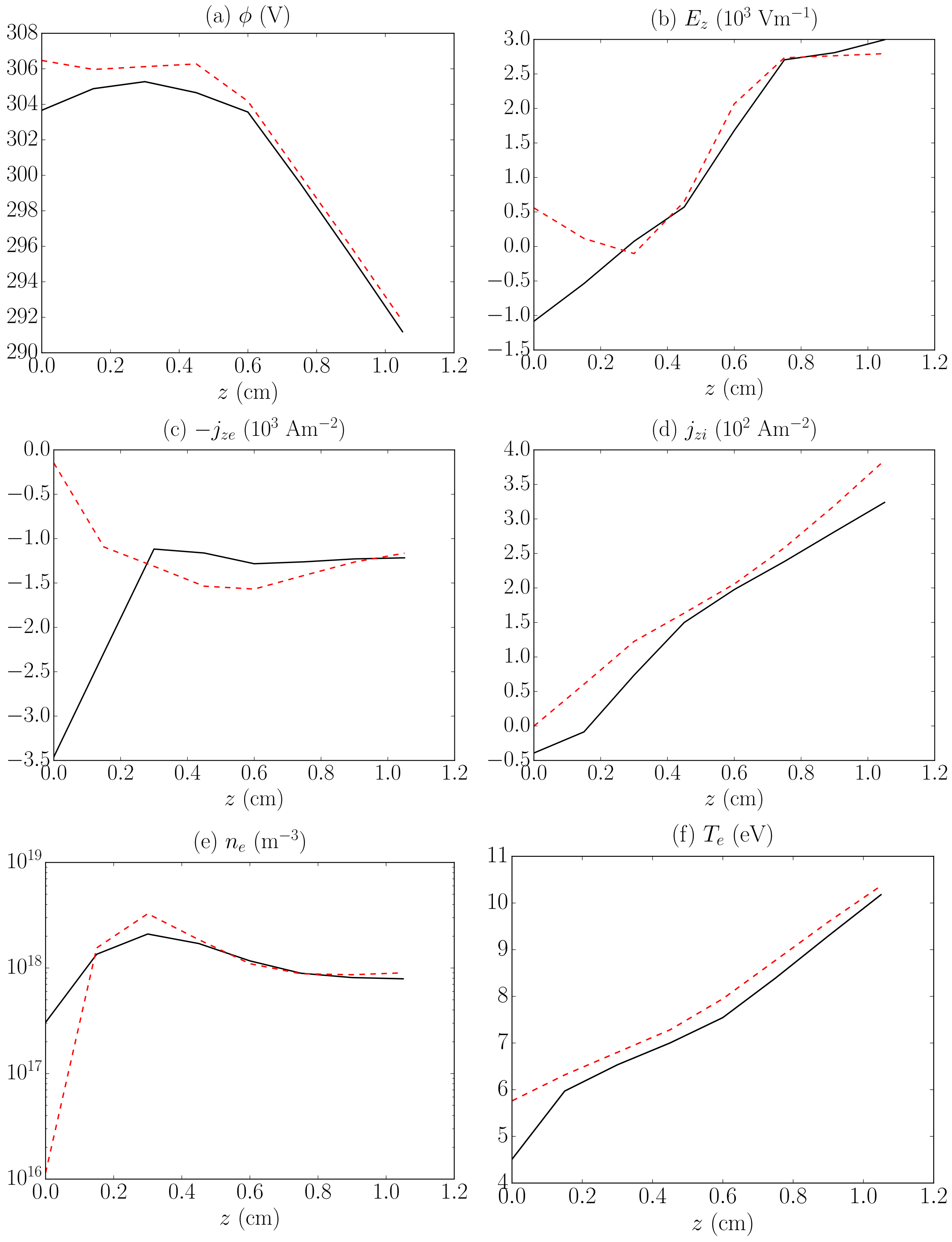

Figure 4.17: Reference simulation case results. Detail at the anode region of the time averaged axial profiles of (a) the electric potential, (b) the axial electric field, the axial component of the electron (c) and ion (d) current density, (e) the plasma density, and (f) the electron temperature. The black solid and the red dashed lines indicate the axial profiles at $r = 4.63$ cm and at $r = 4.25$ cm, corresponding to the TCL, respectively.

4.2.2.3 Influence of the neutral-wall reflection type on the breathing mode

As detailed in Sec. 4.1.2.2, the neutral-wall reflection process has a significant effect on the neutral gas average residence time inside a cylindrical channel with a high surface-to-volume ratio. Here, the reference simulation case of a SPT-100 HET analyzed in detail in Sec. 4.2.2.2 is re-run featuring pure specular neutral-wall reflection.

Fig. 4.18 compares the results of both cases, while Tab. 4.7 contains relevant data for the specular neutral-wall reflection simulation case. In particular Figs. 4.18(a), 4.18(c), 4.18(e) and 4.18(g) compare the time-evolution of the average neutral density, the average plasma density, the discharge current and the ion beam current, respectively, while Figs. 4.18(b), 4.18(d), 4.18(f) and 4.18(h) show their corresponding normalized amplitude spectrum. Black solid and red dashed lines correspond to the reference simulation case featuring diffuse and specular neutral-wall reflection, respectively. As expected, the main differences between both cases are found in the average neutral density in the domain. The faster neutral dynamics in the specular reflection case produces an increase of $\sim$7% of the breathing mode characteristic frequency, which is now 12.25 kHz (the same for all the above magnitudes). This value is very close to the reciprocal of the neutral gas average residence time in the thruster chamber, which yields 13.32 kHz, thus representing a 33.2% increase with respect to the value of 10 kHz obtained in the diffuse case. These results are in agreement with previous studies of low frequency discharge oscillations in HETs [146]. Moreover, in the specular case, the average plasma density phase delay reduces to 73.16 degrees with respect to the average neutral density, and the phase shift between both the discharge and the ion beam current is 23.58 degrees. The time-averaged mean, maximum and mininum values of the magnitudes shown in Fig. 4.18 for the specular case are listed in Tab. 4.7, along with the specific impulse, thrust, powers and efficiencies, which reveal a marginal influence of the neutral-wall reflection type on the thruster performance.

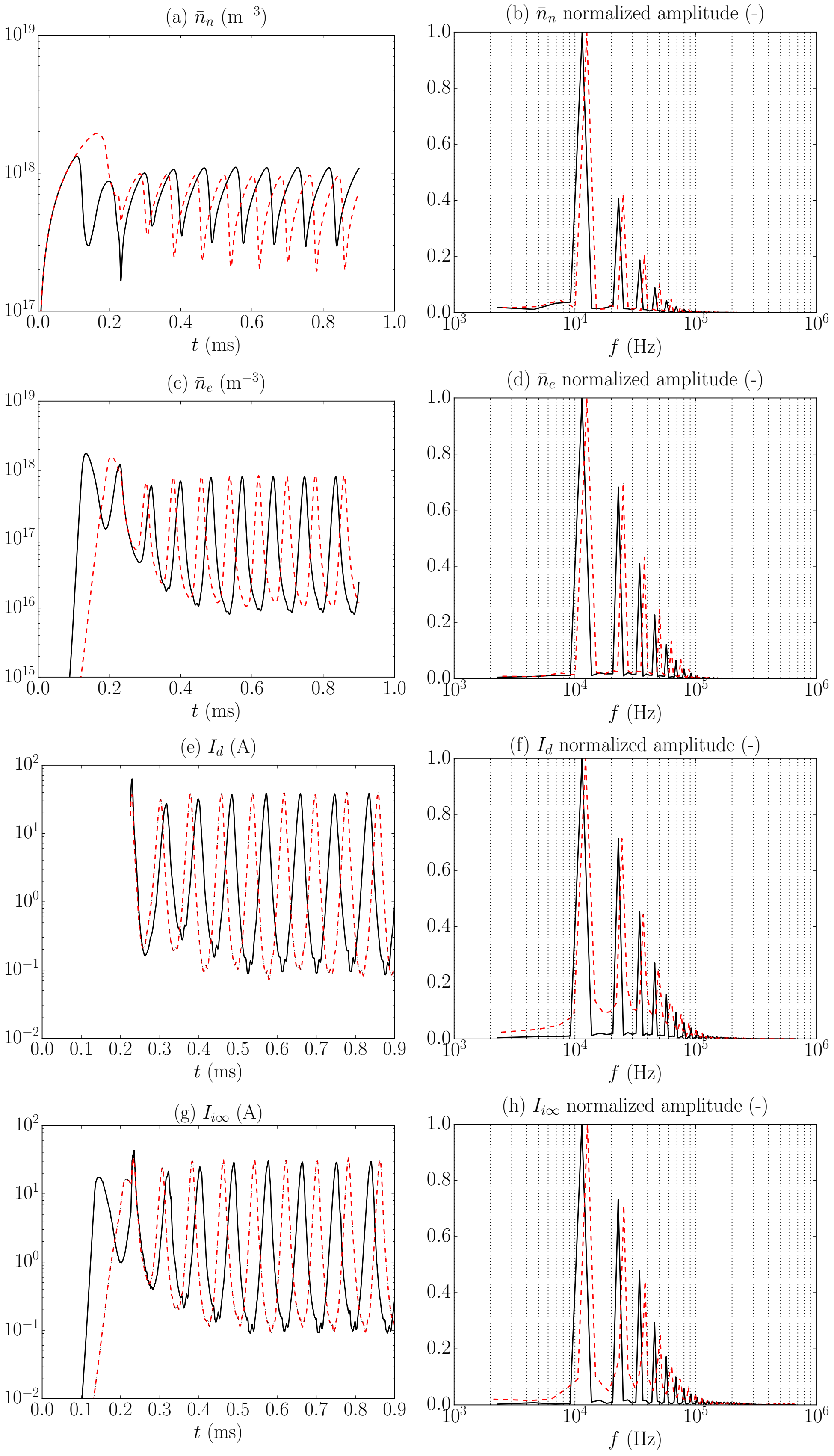

Figure 4.18: Comparison of the reference simulation case results featuring pure diffuse (black solid lines) and pure specular (red dashed lines) neutral-wall reflection. Time evolution of (a) and (c) the average neutral and plasma density in the domain, and (e) and (g) the discharge and ion beam currents. Normalized amplitude spectrum of (b) and (d) the average neutral and plasma density in the domain, and (f) and (h) the discharge and ion beam currents.

Variable	**Units**	**Value**
$\bar{n}_e$ min., max., mean	m^{-3}	$1.15 \cdot 10^{16}$, $6.23 \cdot 10^{17}$, $1.57 \cdot 10^{17}$
$\bar{n}_n$ min., max., mean	m^{-3}	$2.10 \cdot 10^{17}$, $9.64 \cdot 10^{17}$, $6.29 \cdot 10^{17}$
$\bar{n}_e$, $\bar{n}_n$ frequency, phase shift	kHz, deg	12.25, 73.16
I_d min., max., mean	A	$9.00 \cdot 10^{-2}$, $3.86 \cdot 10^{1}$, $6.04 \cdot 10^{0}$
$I_{i\infty}$ min., max., mean	A	$1.06 \cdot 10^{-1}$, $3.14 \cdot 10^{1}$, $5.00 \cdot 10^{0}$
I_d, $I_{i\infty}$ frequency, phase shift	kHz, deg	11.25, 23.58
I_{wi}, I_{prod}	A	2.79, 7.79
I_{sp}, F	s, mN	1449, 71.03
$P_{zi\infty}$, $P_{i\infty}$	W	629, 748
P_d, $\varepsilon_E^{P_d}$	W, -	1812, 0.51
P_{use}, $\varepsilon_E^{P_{use}}$	W, -	629, 0.18
P_{loss}, $\varepsilon_E^{P_{loss}}$	W, -	1118, 0.31
P_{walls}, $\varepsilon_E^{P_{walls}}$	W, -	965, 0.27
$P_{ion,ex}$, $\varepsilon_E^{P_{ion,ex}}$	W, -	153, 0.04
η_{thr}, η_u, η_{cur}, η_{div}, η_{prod}	-	0.28, 0.98, 0.83, 0.84, 0.64
ν_{cat}, P_{cat}	MHz, W	389, 27

Table 4.7: Main results for the specular neutral-wall reflection case. Mean values represent time-averaged values over the number of complete cycles within the last 450 μs of simulation time. The maximum and minimum values represent the average of the peak and trough values within that period. Please note that the value of $P_{zi\infty}$ does not contain the contribution of the neutral species. However, since this contribution is negligible compared to that of the ions, $P_{zi\infty}$ takes the value of P_{use} after truncation and approximation.

4.2.2.4 Effects of the cathode location

Keeping constant the rest of simulation parameters, the simulation results for the cases featuring the cathode locations C2, C3 and C4 indicated in Fig. 4.6(b) are compared to those of the reference case described in Sec. 4.2.1 and analyzed in detail in Sec. 4.2.2.2, whose cathode is located at C1. In this section, the cathode position shall be used to refer to the cases above. The relevant discharge data for the different cases C2-C4 can be found in Sec. B.1 in Tabs. B.1-B.3, respectively, which are analogous to Tab. 4.5 for the reference case C1. These data shall be analyzed in this section along with Figs. 4.19-4.23. Here only the most relevant results are emphasized, while Figs. B.1-B.7 are included in Sec. B.1 for further reference, completing the results presented in this section.

As shown in Fig. 4.6(b), the cases C1, C2 and C3 feature the cathode location along the same magnetic field streamline. On the other hand, in the case C4 the cathode cell center is on the last closing magnetic field streamline in the simulation domain. Figs. 4.19(a) and 4.19(b) compare, respectively, the time evolution and the corresponding normalized amplitude spectrum of the discharge current for the cases C1-C4. The characteristic breathing mode oscillation frequency for the cases C2 and C3 is 11.26 kHz and 11.30 kHz, respectively, thus very close the value of 11.45 kHz of the reference case C1. In contrast, the case C4 presents a lower value of 9.66 kHz and a larger peak-to-peak oscillation amplitude, with discharge current peak values around 7 times higher than the mean value (see Tab. B.3). Nevertheless, the case C2 features the highest peak values of I_d. Figs. 4.19(c)-(f) plot the time evolution of the average plasma and neutral density in the domain, and the cathode equivalent emission frequency and power. Again the largest discrepancies are found for the case C4. According to Eq. (2.58), the value of ν_{cat} is inversely proportional to both the value of the plasma density at the cathode MFAM cell, and its volume V_{cat}. Therefore, considering that all cases C1-C4 feature a similar time-averaged value of I_d (see Fig. 4.19(a) and Tabs. 4.5 and B.1-B.3), the lower volume of the cathode MFAM cell C4 (see Tab. 4.3) and the lower value of the time-averaged plasma density at that region [see Figs. B.3(a)-(d)], could explain both the larger oscillations and mean value of ν_{cat} shown in Fig. 4.19(e). The value of ν_{cat} indicates how concentrated is the volumetric injection of electrons through the volumetric cathode. Therefore, the larger this value, the larger the perturbation that the volumetric cathode induces in the rest of magnitudes.

Given the near-collisionless parallel motion of the confined electron population typical of a HET, the plasma density and the electric potential may be assumed to satisfy the isothermal Boltzmann relation [172]. In particular, along the cathode magnetic field streamline, it may be written as

$$e(\phi(\sigma) - \phi_0) - T_{e0} \ln\left(\frac{n_e(\sigma)}{n_{e0}}\right) = 0 \tag{4.11}$$

where the electron temperature T_{e0}, the plasma density n_{e0} and the electric potential ϕ_0 are constant along the cathode magnetic field streamline (i.e. $\lambda = const.$ line). Tab. 4.8 lists the values of T_{e0}, n_{e0} and $\phi_0 = 0$ at the cathode MFAM cell for the cases C1 and C2. Considering those values, the black and red solid lines in Figs. 4.20(a)-(d) represent, respectively, the isothermal Boltzmann relation of Eq. (4.11), the electron temperature ratio T_e/T_{e0}, the electric potential and the plasma density ratio n_e/n_{e0} along the cathode magnetic streamline corresponding to the cases C1 and C2 [see Fig. 4.6(b)]. Apart from the electron inertial effects, which have not been considered as such in the simulations, the electron temperature gradient along the magnetic line and the collisions are responsible for the deviations of the electron momentum equation from Eq. (4.11), shown in Fig. 4.20(a). From Fig. 4.20(b), it is clear that the cathode magnetic lines are far from being isothermal, specially near the cathode position. The intense injection of thermal electrons with temperature T_{cat} through the volumetric cathode, represented by the equivalent cathode electron emission frequency ν_{cat}, acts as a dominant collisional process and perturbs the plasma solution making the electron temperature tend to T_{cat} in the region near the cathode MFAM cell, whose location along the cathode magnetic streamline is indicated by the orange star markers in Fig. 4.20. Therefore, the electric potential jump along the cathode magnetic lines shown in Fig. 4.20(c) is not only due to the plasma density variations depicted in Fig. 4.20(d). This effect was already commented in Sec. 4.2.2.2 and can be also seen in Figs. B.1(a)-(d). The extension of the volumetric cathode to several MFAM cells could help reducing the cathode perturbation on the plasma properties and will be analyzed in future simulations. Nonetheless, for both cases C1 and C2, the black and red dashed lines with square and circle markers in Fig. 4.20(b), respectively, show that the isothermal condition is satisfied along the magnetic field streamline represented by the cyan line in Fig. 4.6(b), thus confirming that the volumetric cathode perturbation is local. The reference point in that line, represented by the cyan star marker in Fig. 4.20(b), is at $r = 4.24$ cm, $z = 4.54$ cm, and features an electron temperature $T_{e0} = 16.49$ eV.

As for the thruster performances, very similar results for thrust, specific impulse and efficiencies are obtained for the cases C1-C3. The case C4 however, features slightly higher thrust, specific impulse and thrust efficiency values (see Tabs. 4.5 and B.1-B.3). The fact that the cathode magnetic streamline is located further downstream in the case C4 [see Fig. 4.6(b)] results in a smoother electric potential evolution in the near plume region, as shown in Figs. 4.21(a) and B.1(d). As a consequence, the axial component of the electric field shown in Fig. 4.21(b) features a lower peak value, but remains positive in a wider region until the cathode magnetic line [see Fig. B.1(h)], thus yielding a higher thrust. Interestingly, the electron temperature follows the trend of the electric potential and a decaying profile is found for the case C4 in the near plume region, as shown in Fig. 4.21(e), while a very similar electron temperature peak value and evolution inside the thruster chamber is found in all cases. Moreover, the electron drift-to-internal energy ratio shown in Fig. 4.23(a) remains one order of magnitude lower than those of the cases C1-C3 in most of the near plume region, thus indicating the marginal role of the electron inertial effects there. The perturbation on the plasma density shown in Fig. 4.21(g) for the cases C1-C3, produced by the behavior of the electric field around the cathode magnetic line region, does not appear in the case C4. The same applies to the singly and doubly charged ions particle density and their density ratio depicted in Figs. 4.21(b), 4.21(d) and 4.21(f), respectively.

The low electron temperature near the corresponding cathode magnetic lines in the cases C1-C3 and C4 favors the increase of the dominant electron-ion Coulomb collisions in those regions, thus yielding a higher electron collisionality [see the various collision frequencies profiles in Figs. 4.22(c)-(g)] and, as a result, a lower effective Hall parameter there [see Figs. 4.22(a) and 4.22(b)]. As commented in Sec. 4.2.2.2 for the reference simulation case (i.e. the case C1 here), both the azimuthal and perpendicular electron current density components exhibit a change of sign when crossing the cathode magnetic line on each case, as shown in Figs. 4.23(b) and 4.23(c), respectively, in accordance with the sign of the dominant axial component of the electric field there [see Figs. 4.21(b) and B.1(e)-(h)]. The sign of the parallel electron current density component peaks depicted in Fig. 4.23(d) is consistent with the position of the cathode with respect to the axial line at $r = 4.63$ cm (along which all the axial profiles have been obtained), on each case ($-j_{\parallel e}$ features the sign of the electron parallel drift velocity).

Case	$T_{e0}(\lambda)$ (eV)	$n_{e0}(\lambda)$ (10^{16} m^{-3})
C1	6.41	3.83
C2	2.20	21.1

Table 4.8: Time-averaged values of the electron temperature and the plasma density at the cathode MFAM cell for the cases C1 and C2.

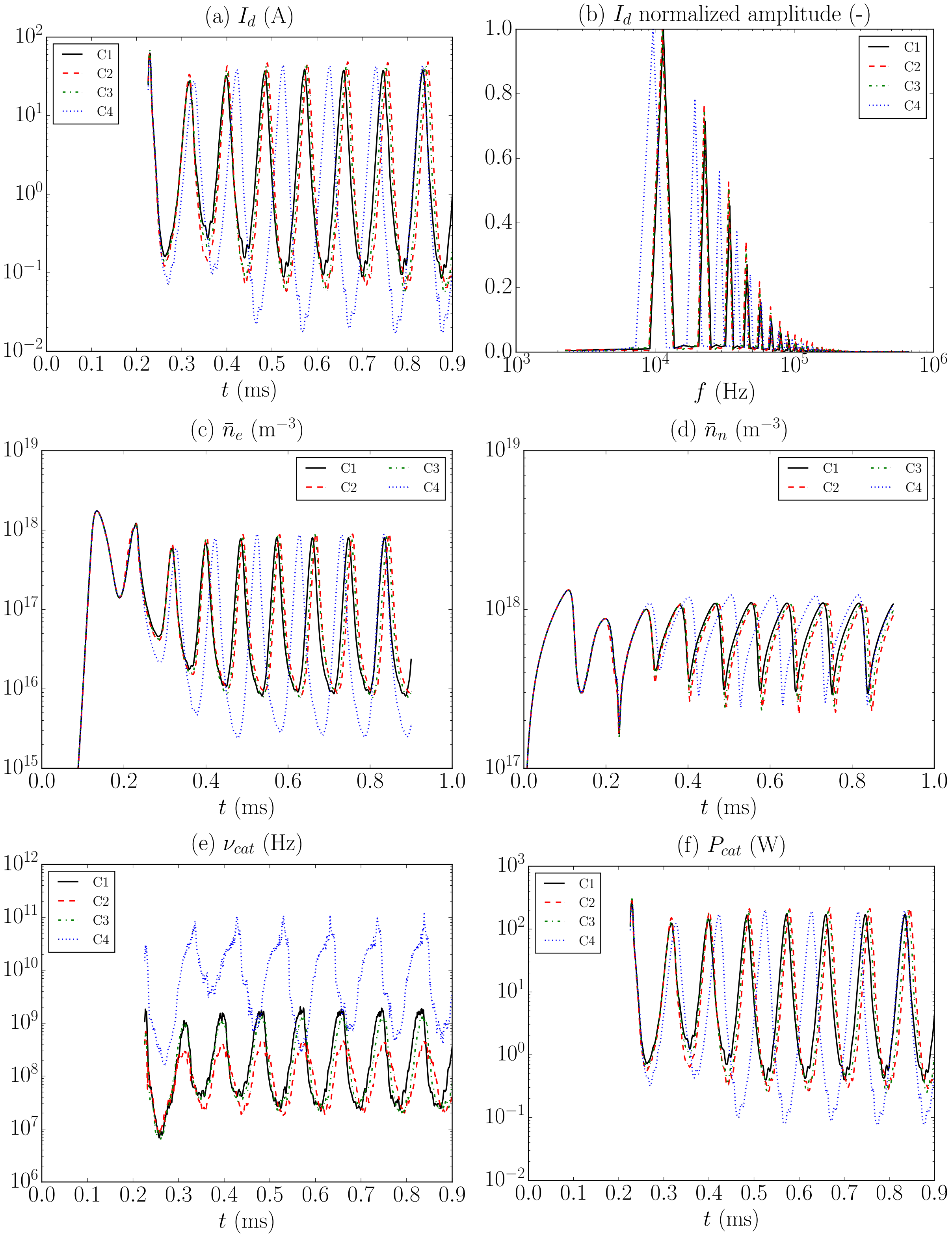

Figure 4.19: Results comparison for the simulation cases C1-C4. Time evolution of (a) I_d, (c) $\bar{n}_e$, (d) $\bar{n}_n$, (e) and ν_{cat}, and (e) P_{cat}. (b) Normalized amplitude spectrum of I_d.

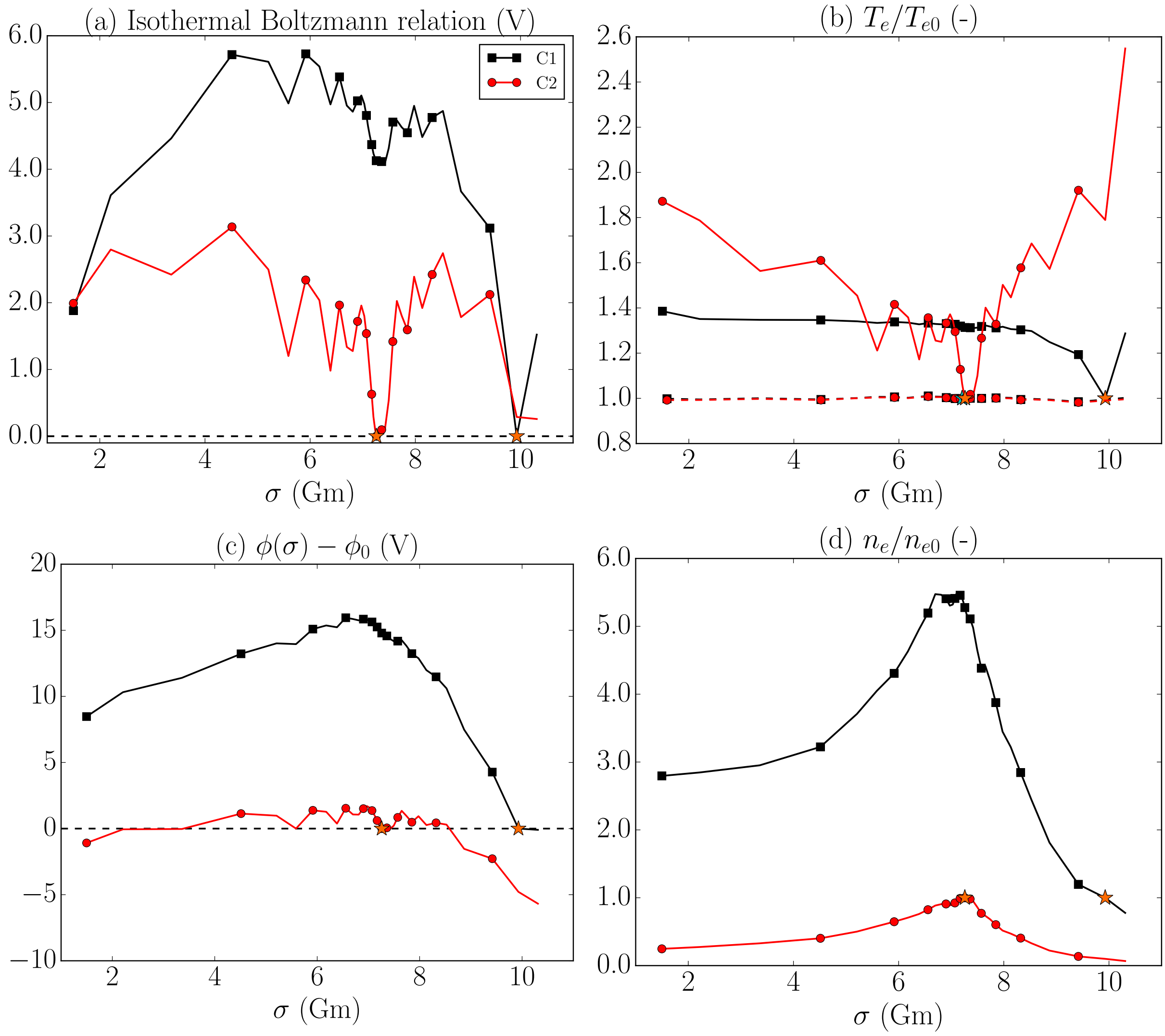

Figure 4.20: Spatial evolution of (a) the isothermal Boltzmann relation in Eq. (4.11), (b) the electron temperature ratio T_e/T_{e0}, (c) the electric potential and (d) the plasma density ratio n_e/n_{e0} along the cathode magnetic field streamline for the cases C1 and C2. The orange star markers indicate the cathode position along the magnetic field streamline. In (b) the black and red dashed lines with square and circle markers correspond to the temperature ratio T_e/T_{e0} along the cyan magnetic line plotted in Fig. 4.6(b) for the cases C1 and C2, respectively. The cyan star marker in (b) indicates the reference point for T_{e0} in that line. The horizontal black dashed lines in (a) and (b) are set at zero volts.

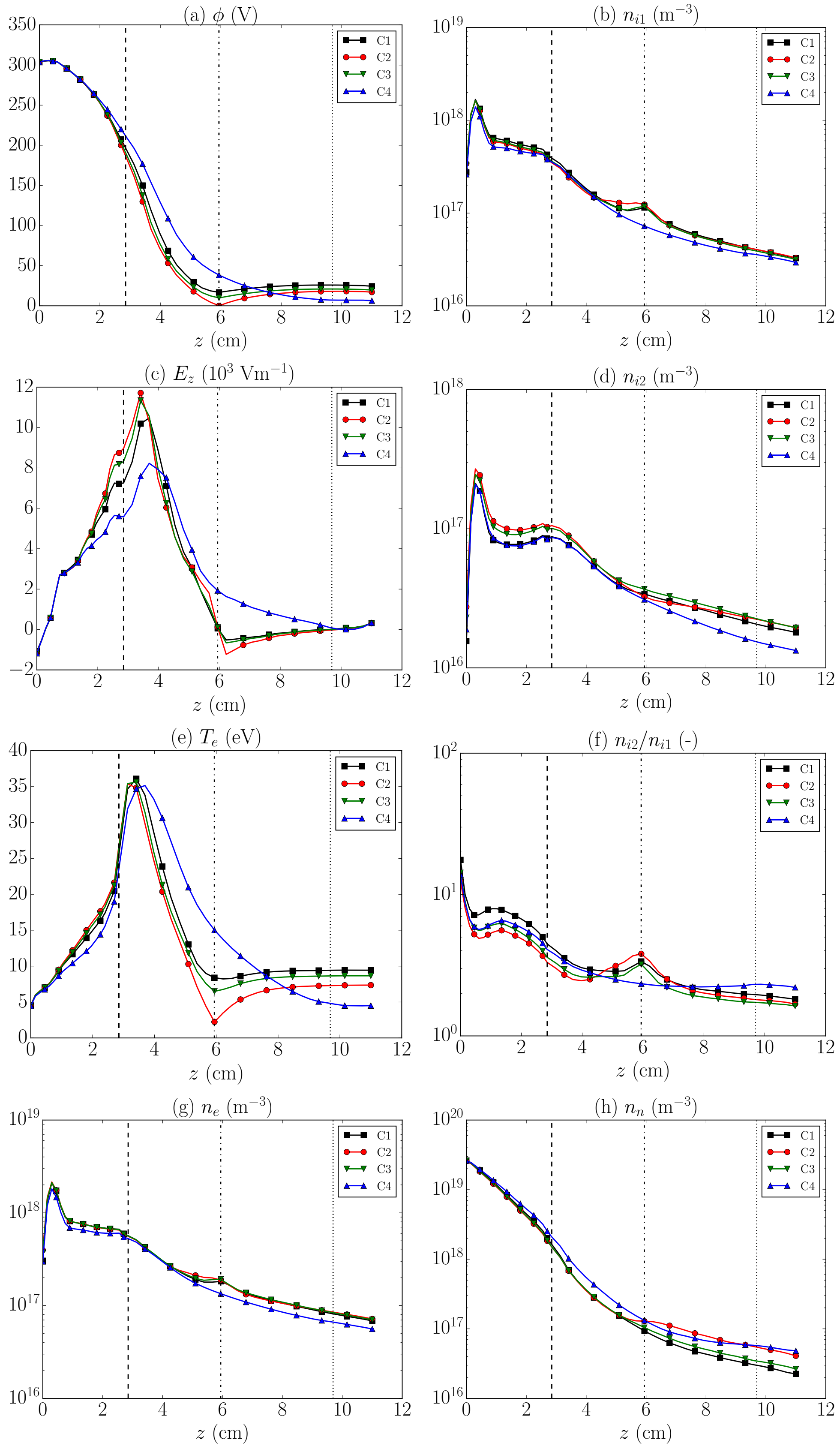

Figure 4.21: Results comparison for the simulation cases C1-C4. Time averaged axial profiles of (a) the electric potential, (b) the singly charged ions particle density, (c) the axial component of the electric field, (d) the doubly charged ions particle density, (e) the electron temperature, (f) the doubly-to-singly charged ions particle density ratio, (g) the plasma density and (h) the neutrals particle density. The vertical black dashed, dot-dashed and dotted lines indicate, respectively, the axial position of the thruster chamber exit plane at $z = 2.85$ cm and the axial position of the magnetic field streamlines passing through the cathode positions C1-C3 at $z = 5.94$ cm, and C4 at $z = 9.69$ cm.

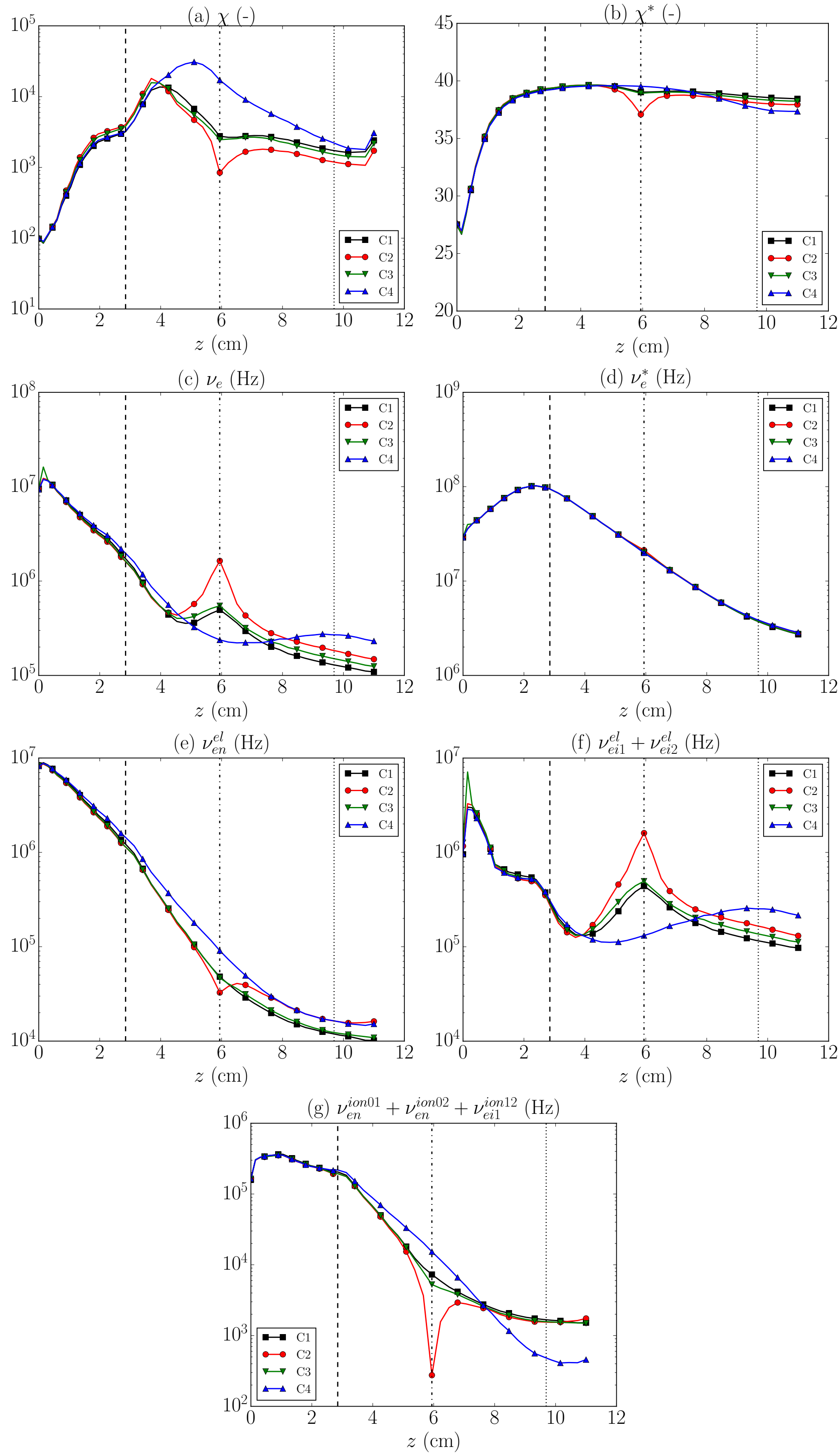

Figure 4.22: Results comparison for the simulation cases C1-C4. Time averaged axial profiles of (a) the classical Hall parameter, (b) the effective Hall parameter, (c) the total electron collision frequency, (d) the effective electron collision frequency, (e) the electron-neutral collision frequency, (f) the total electron-ion Coulomb collision frequency and (g) the total ionization collisions frequency. The vertical black dashed, dot-dashed and dotted lines indicate, respectively, the axial position of the thruster chamber exit plane at $z = 2.85$ cm and the axial position of the magnetic field streamlines passing through the cathode positions C1-C3 at $z = 5.94$ cm, and C4 at $z = 9.69$ cm.

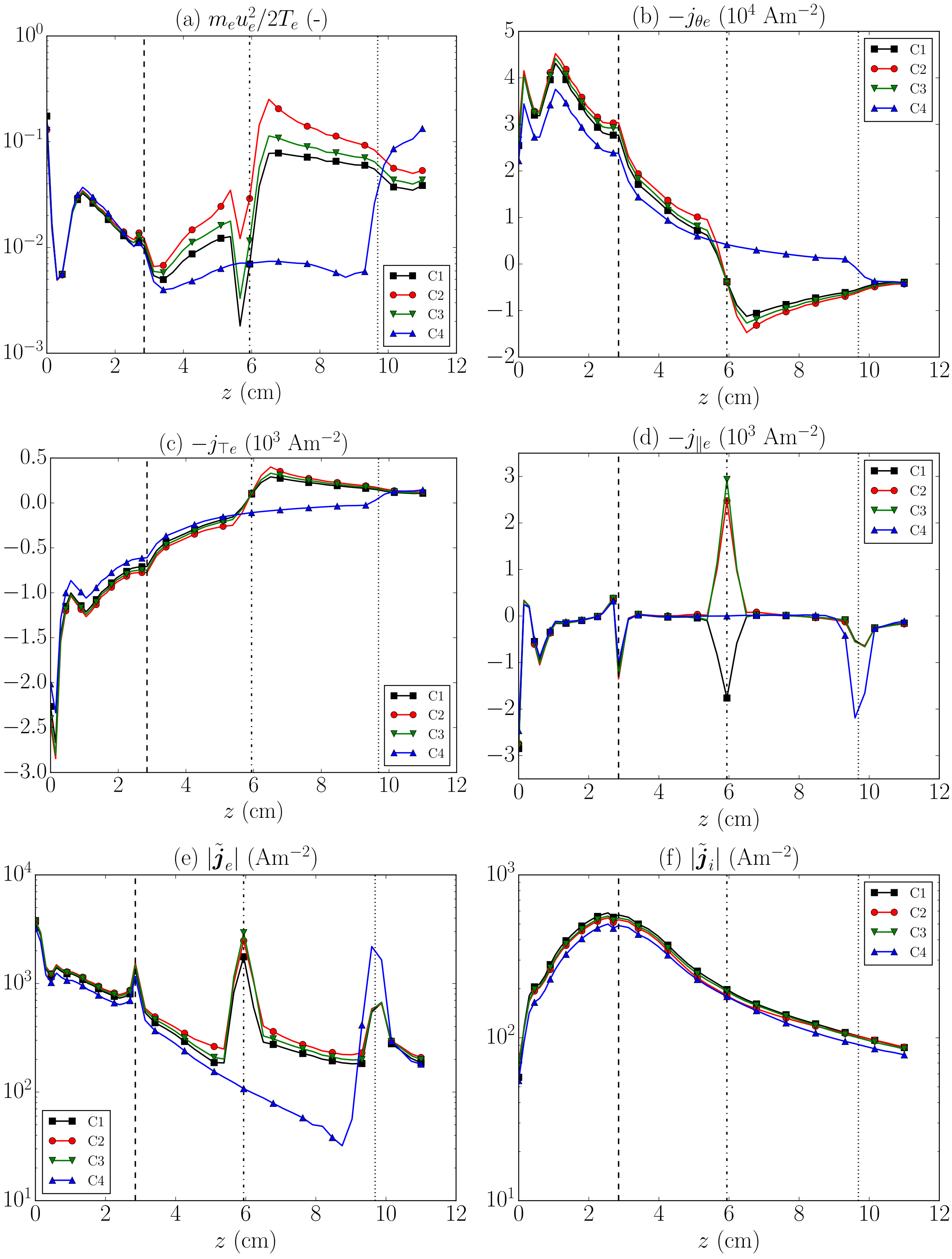

Figure 4.23: Results comparison for the simulation cases C1-C4. Time averaged axial profiles of (a) the electron drift-to-internal energy ratio, (b) the electron azimuthal current density component, (c) the electron perpendicular current density component, (d) the electron parallel current density component, (e) the magnitude of the 2D (z, r) electron current density vector and (f) the magnitude of the 2D (z, r) ion current density vector. The vertical black dashed, dot-dashed and dotted lines indicate, respectively, the axial position of the thruster chamber exit plane at $z = 2.85$ cm and the axial position of the magnetic field streamlines passing through the cathode positions C1-C3 at $z = 5.94$ cm, and C4 at $z = 9.69$ cm.

4.2.2.5 Results for various electron turbulent transport parameter profiles

Tab. 4.9 defines the simulation cases considered in this section featuring various α_t profiles. The rest of simulation parameters are kept constant to those of the reference case described in Sec. 4.2.1, which shall be here referred to as T1. The case T2 features a constant α_t profile with twice the value of the reference case T1. On the other hand, various step-out profiles have been considered following two trends: cases T3-T5 increase the turbulent contribution in the near plume region while keeping it constant inside the thruster chamber; cases T5-T7 decrease the turbulent contribution inside the thruster chamber while keeping it constant in the near plume region. The main simulation results and relevant aspects of all the cases above are commented in this section along with Figs. 4.24-4.30. In order to facilitate the analysis, the results are here presented in two groups, named G1 and G2. The former refers to the cases T1-T5, and the latter gathers the cases T1 and T5-T7. Figs. 4.25, 4.27 and 4.29 correspond to the results for the group G1, while Figs. 4.26, 4.28 and 4.30 present the results for the group G2. Additionally, Sec. B.2 includes the relevant discharge data for the cases T2-T7 in Tabs. B.4-B.9, respectively, along with Figs. B.8-B.21, thus completing the results here presented.

Case	**Turbulent parameter profile type**
T1	Constant profile with $\alpha_t = 2.5\%$
T2	Constant profile with $\alpha_t = 5.0\%$
T3	Step-out profile at $z = 2.85$ cm with $\alpha_t = 2.5 - 5.0\%$
T4	Step-out profile at $z = 2.85$ cm with $\alpha_t = 2.5 - 7.5\%$
T5	Step-out profile at $z = 2.85$ cm with $\alpha_t = 2.5 - 10.0\%$
T6	Step-out profile at $z = 2.85$ cm with $\alpha_t = 2.0 - 10.0\%$
T7	Step-out profile at $z = 2.85$ cm with $\alpha_t = 1.5 - 10.0\%$

Table 4.9: Definition of the SPT-100 HET simulation cases T1-T7 featuring different turbulent parameter profiles. The values of the turbulent parameter α_t refer to the percentage of the electron electron cyclotron frequency ω_{ce} corresponding to the equivalent electron turbulent collision frequency. The axial location of the α_t step is at the thruster chamber exit plane. The hyphen separates the α_t values inside the thruster chamber and in the near plume region.

Figs. 4.24(a) and 4.24(b) show the time evolution of the discharge current for the cases in G1 and G2, respectively. The corresponding normalized amplitude spectrum is depicted in Figs. 4.24(c) and 4.24(d), respectively. As was already commented in Sec. 4.2.2.2, the results highlight the need for a control strategy for the discharge current in order to obtain time-averaged values closer to those reported by experiments [163]. The largest peak values are obtained for the case T2, which also features the lowest breathing mode frequency of 10.65 kHz. As can be seen in Fig. 4.24(c), increasing α_t in the near plume region yields a higher breathing mode frequency, which takes the values of 12.12, 12.74 and 13.20 kHz for the cases T3-T5, respectively. Fig. 4.24(d) shows a similar effect when reducing α_t in the thruster chamber. The breathing mode frequency is 13.61 and 14.04 kHz for the cases T6 and T7, respectively. Figs. 4.24(e) and 4.24(f) show the time evolution of the plasma density for the cases in G1 and G2, while the neutral density is depicted in Figs. 4.24(g) and 4.24(h), respectively. Both magnitudes feature larger oscillations in cases T2-T7 than in the reference case T1 here (see the data detailed in Tabs. B.4-B.9 for the cases T2-T7, respectively).

The time-averaged axial profiles of the various plasma properties are shown in Figs. 4.25, 4.27 and 4.29 for the cases in G1, and in Figs. 4.26, 4.28 and 4.30 for the cases in G2. From Figs. 4.25(a) and 4.26(a) it is clear that the larger the α_t value inside the thruster chamber, the flatter the electric potential profile in the first part of the chamber. This behavior is consistent with experiments [170]. According to previous stationary plasma thruster simulations [5,160], a larger axial potential fall is found within the thruster chamber for both increasing α_t in the near plume region (i.e the cases T3-T5, respectively), and decreasing α_t inside the thruster chamber (i.e. the cases T5-T7, respectively). As shown in Figs. 4.25(c) and 4.26(c), the peak in the axial component of the electric field increases accordingly, and moves upstream into the thruster chamber for all the step-out cases T3-T7, presenting the case T7 the maximum E_z peak value. According to Fig. 4.25(e), the electron temperature peak increases for higher values of α_t in the near plume region due to the enhanced Joule heating there [see the larger electron effective collisionality for cases T3-T5 in Fig. 4.27(d)]. In contrast, it decreases and moves upstream into the thruster chamber when decreasing the turbulent contribution inside the chamber, as depicted in Fig. 4.26(e). The obtained electron temperature peak values are not far from those reported by experiments [168–171], the case T2 presenting the larger discrepancies with respect to the rest of the cases here analyzed.

The behavior of the effective Hall parameter is clearly dominated by the electron turbulent contribution in all cases, as shown in Figs. 4.27(b) and 4.28(b). Fig. 4.29(b) depicts a lower magnitude of $j_{\theta e}$ along the near plume region in the cases T3-T5. This is consistent with the lower magnetization of the electron population due the larger electron effective collisionality in that region [see the corresponding values of the effective Hall parameter in Fig. 4.27(b)]. Consequently, the higher electron magnetization inside the thruster chamber in the cases T5-T7 yields larger $j_{\theta e}$ values there, as shown in Fig. 4.30(b), and reduces the electron perpendicular transport towards the anode, as can be seen in Fig. 4.30(c). This is in line with the decreasing trend of the time-averaged discharge current values listed in Tabs. B.7-B.9 for the cases T5-T7, respectively.

Finally, regarding the main thruster performances listed in Tabs. B.4-B.9, the thrust efficiency increases for lower values of the electron turbulent contribution inside the thruster chamber (i.e. the cases T5-T7). Since all cases here feature both a constant discharge voltage and propellant mass flow, this fact is due to the significant decrease in the time-averaged discharge current from the case T5 to T7, commented above. On the other hand, the thrust efficiency is not significantly affected when increasing α_t in the near plume region (see Tabs. B.5-B.7 for the cases T3-T5, respectively).

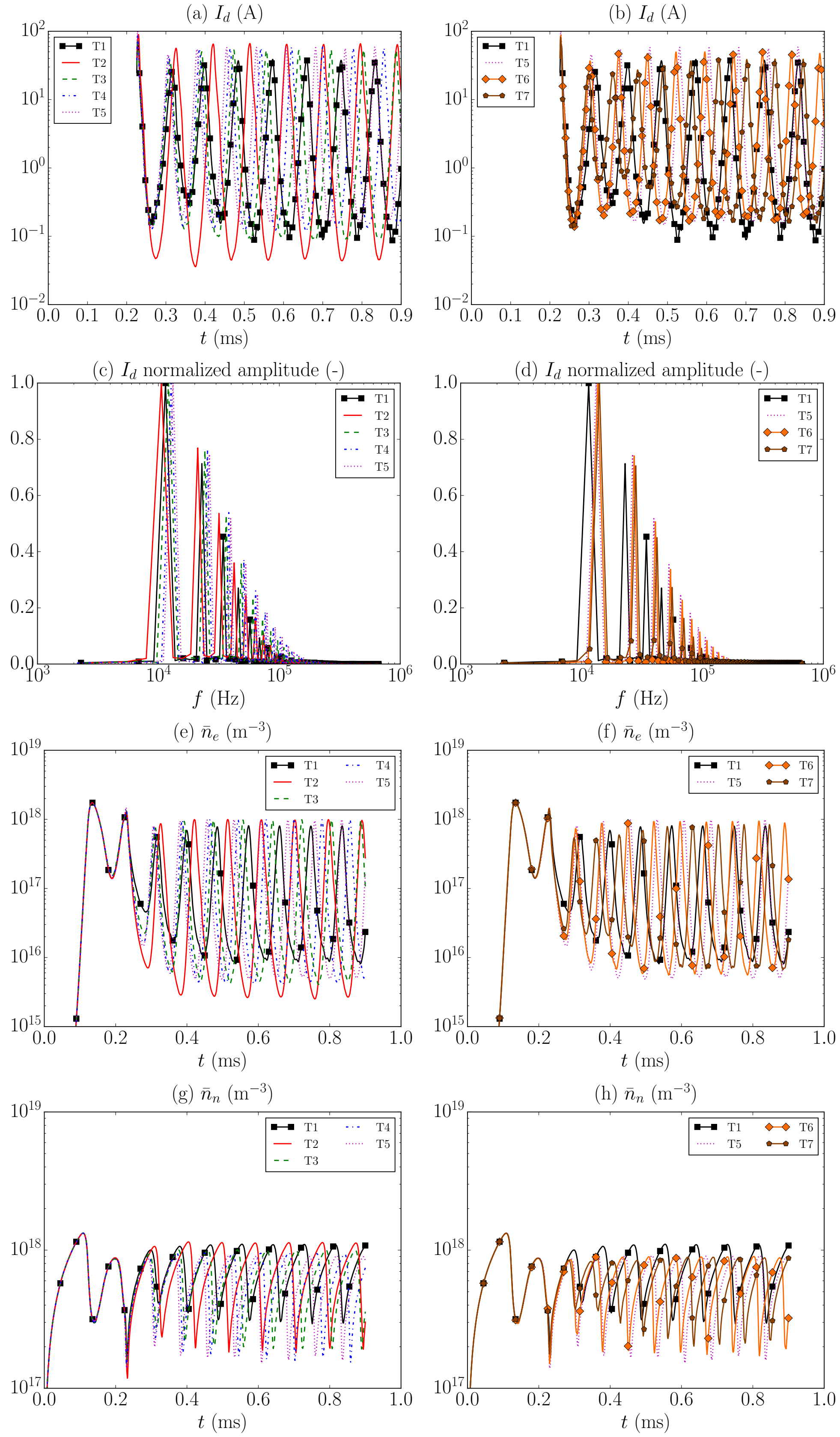

Figure 4.24: Results comparison for the simulation cases T1-T7. Plots for cases T1-T5: time evolution of (a) I_d, (e) $\bar{n}_e$ and (g) $\bar{n}_n$; (c) I_d normalized amplitude spectrum. Plots for cases T1 and T5-T7: time evolution of (b) I_d, (f) $\bar{n}_e$ and (h) $\bar{n}_n$; (d) I_d normalized amplitude spectrum.

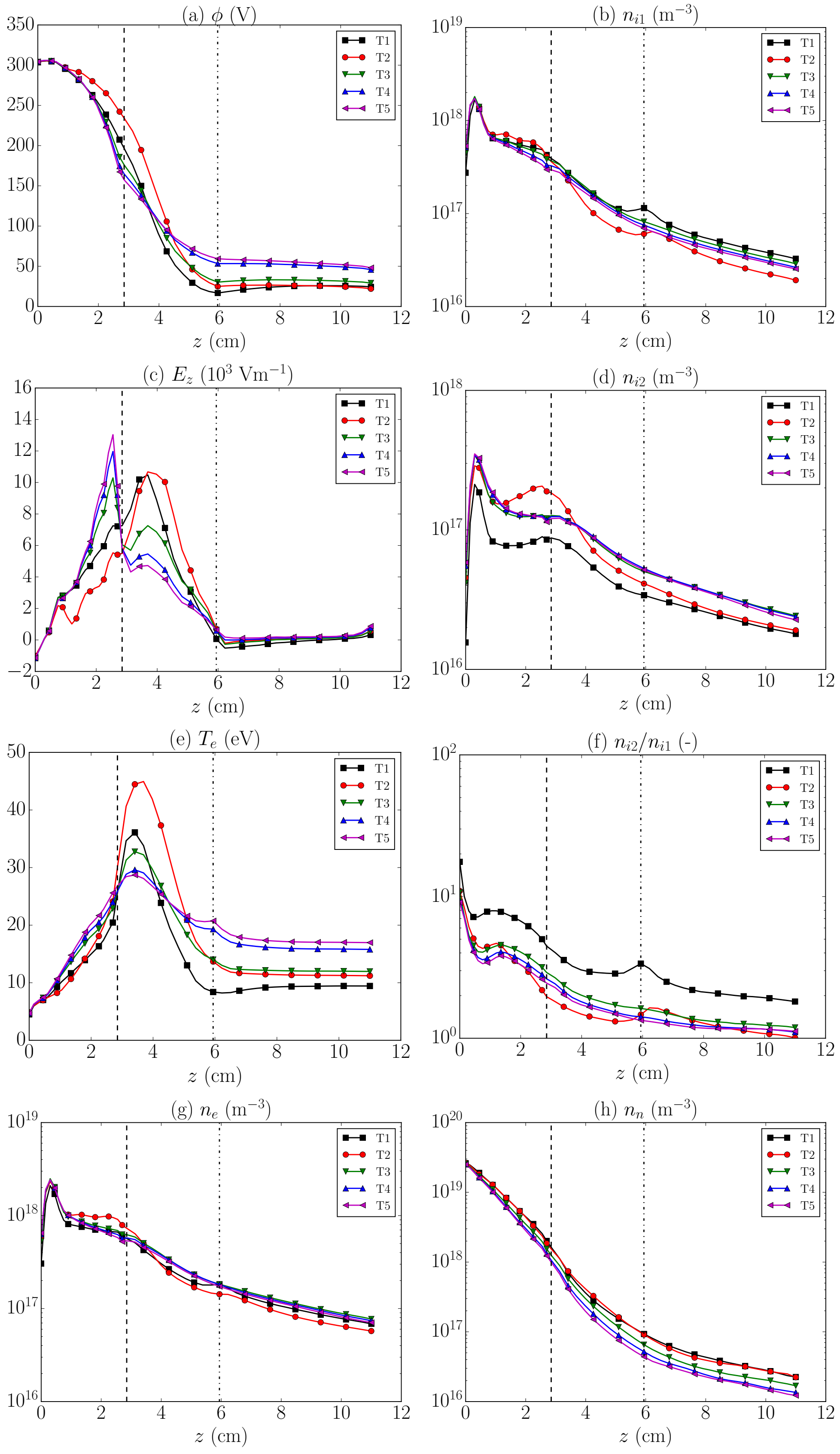

Figure 4.25: Results comparison for the simulation cases in T1-T5. Time averaged axial profiles of (a) the electric potential, (b) the singly charged ions particle density, (c) the axial component of the electric field, (d) the doubly charged ions particle density, (e) the electron temperature, (f) the doubly-to-singly charged ions particle density ratio, (g) the plasma density and (h) the neutrals particle density. The vertical black dashed and dot-dashed lines indicate, respectively, the axial position of the thruster chamber exit plane at $z = 2.85$ cm and the axial position of the magnetic field streamline passing through the cathode at $z = 5.94$ cm.

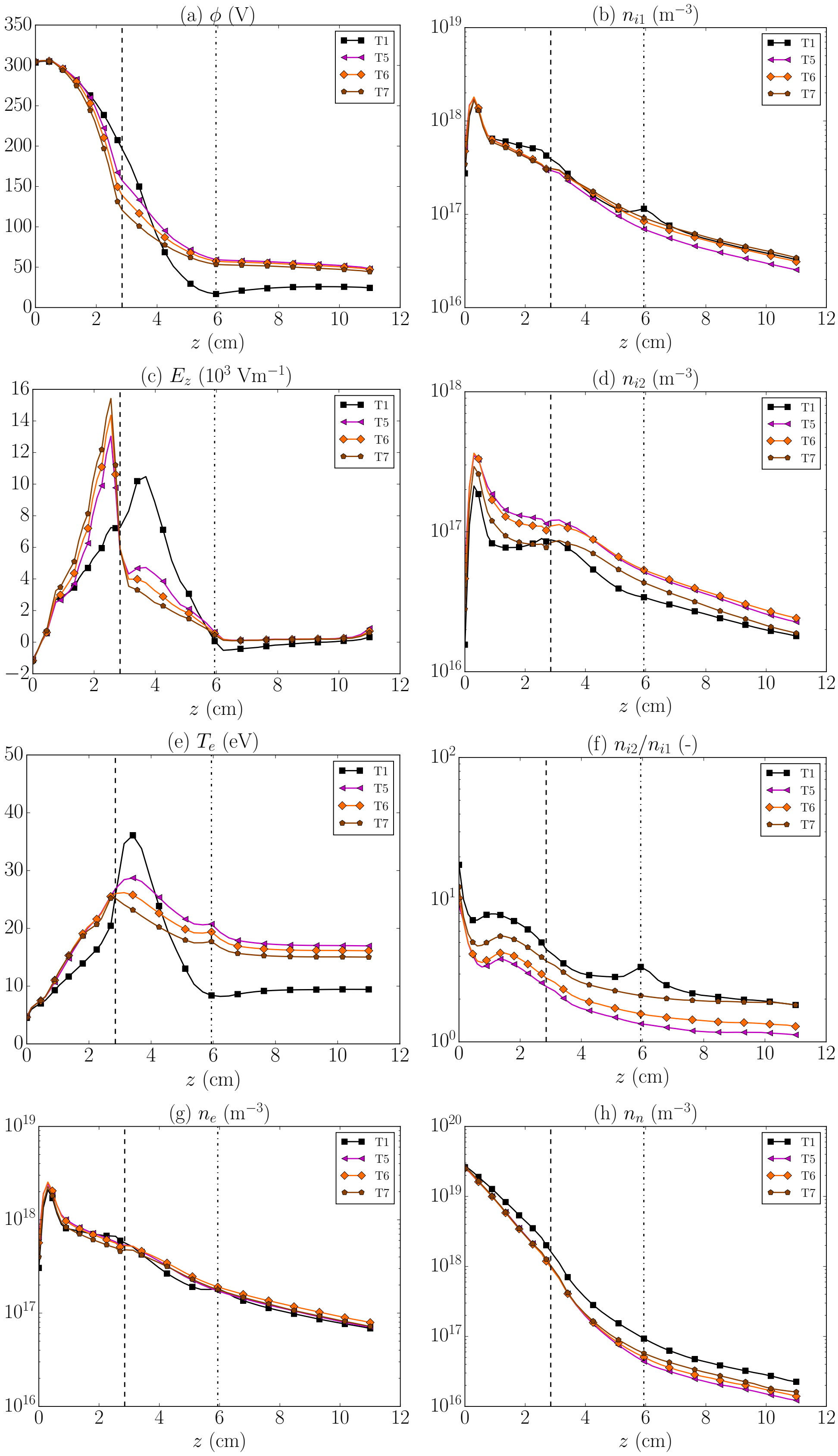

Figure 4.26: Results comparison for the simulation cases in T1 and T5-T7. Time averaged axial profiles of (a) the electric potential, (b) the singly charged ions particle density, (c) the axial component of the electric field, (d) the doubly charged ions particle density, (e) the electron temperature, (f) the doubly-to-singly charged ions particle density ratio, (g) the plasma density and (h) the neutrals particle density. The vertical black dashed and dot-dashed lines indicate, respectively, the axial position of the thruster chamber exit plane at $z = 2.85$ cm and the axial position of the magnetic field streamline passing through the cathode at $z = 5.94$ cm.

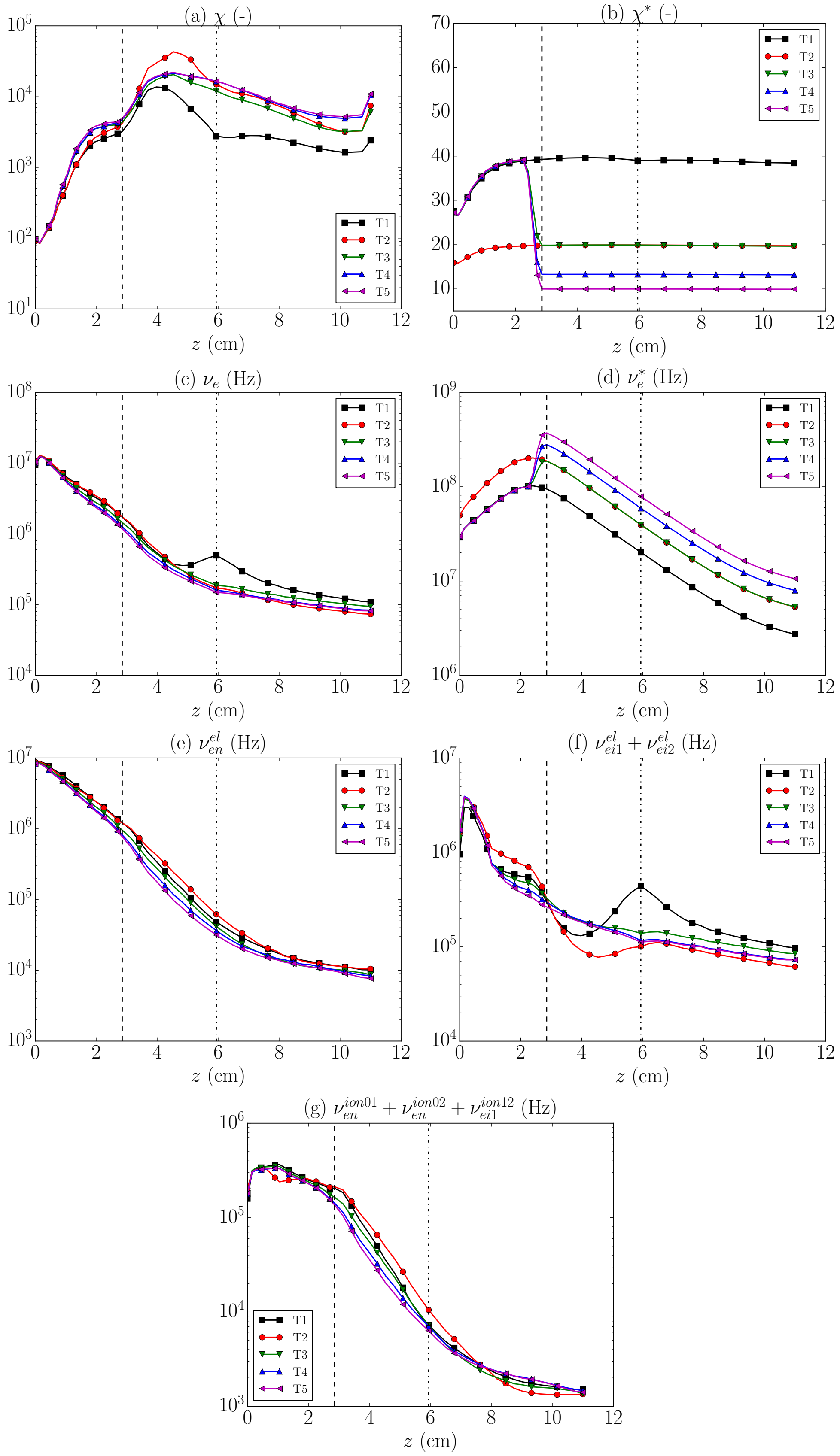

Figure 4.27: Results comparison for the simulation cases T1-T5. Time averaged axial profiles of (a) the classical Hall parameter, (b) the effective Hall parameter, (c) the total electron collision frequency, (d) the effective electron collision frequency, (e) the electron-neutral collision frequency, (f) the total electron-ion Coulomb collision frequency and (g) the total ionization collisions frequency. The vertical black dashed and dot-dashed lines indicate, respectively, the axial position of the thruster chamber exit plane at $z = 2.85$ cm and the axial position of the magnetic field streamline passing through the cathode at $z = 5.94$ cm.

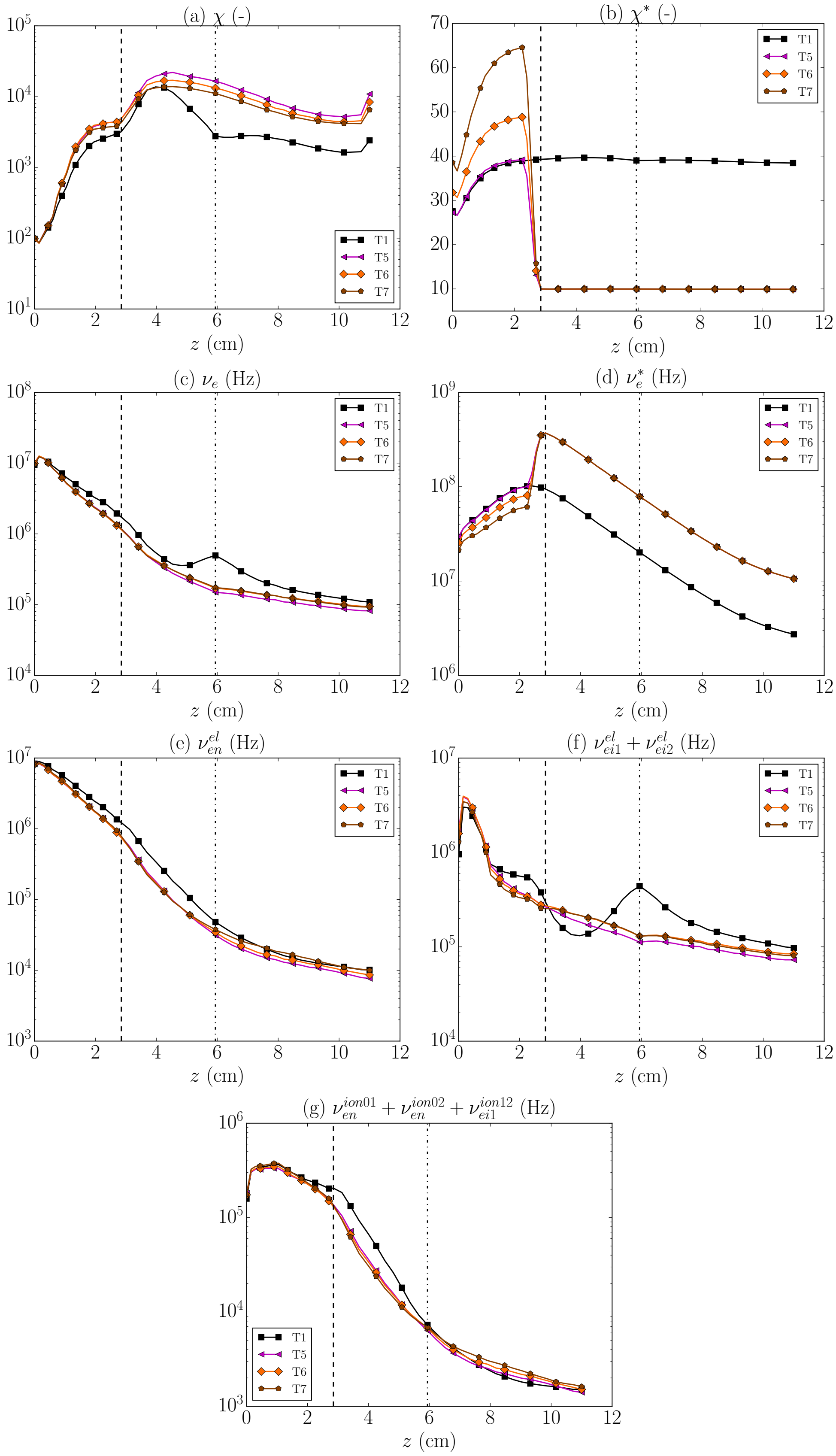

Figure 4.28: Results comparison for the simulation cases T1 and T5-T7. Time averaged axial profiles of (a) the classical Hall parameter, (b) the effective Hall parameter, (c) the total electron collision frequency, (d) the effective electron collision frequency, (e) the electron-neutral collision frequency, (f) the total electron-ion Coulomb collision frequency and (g) the total ionization collisions frequency. The vertical black dashed and dot-dashed lines indicate, respectively, the axial position of the thruster chamber exit plane at $z = 2.85$ cm and the axial position of the magnetic field streamline passing through the cathode at $z = 5.94$ cm.

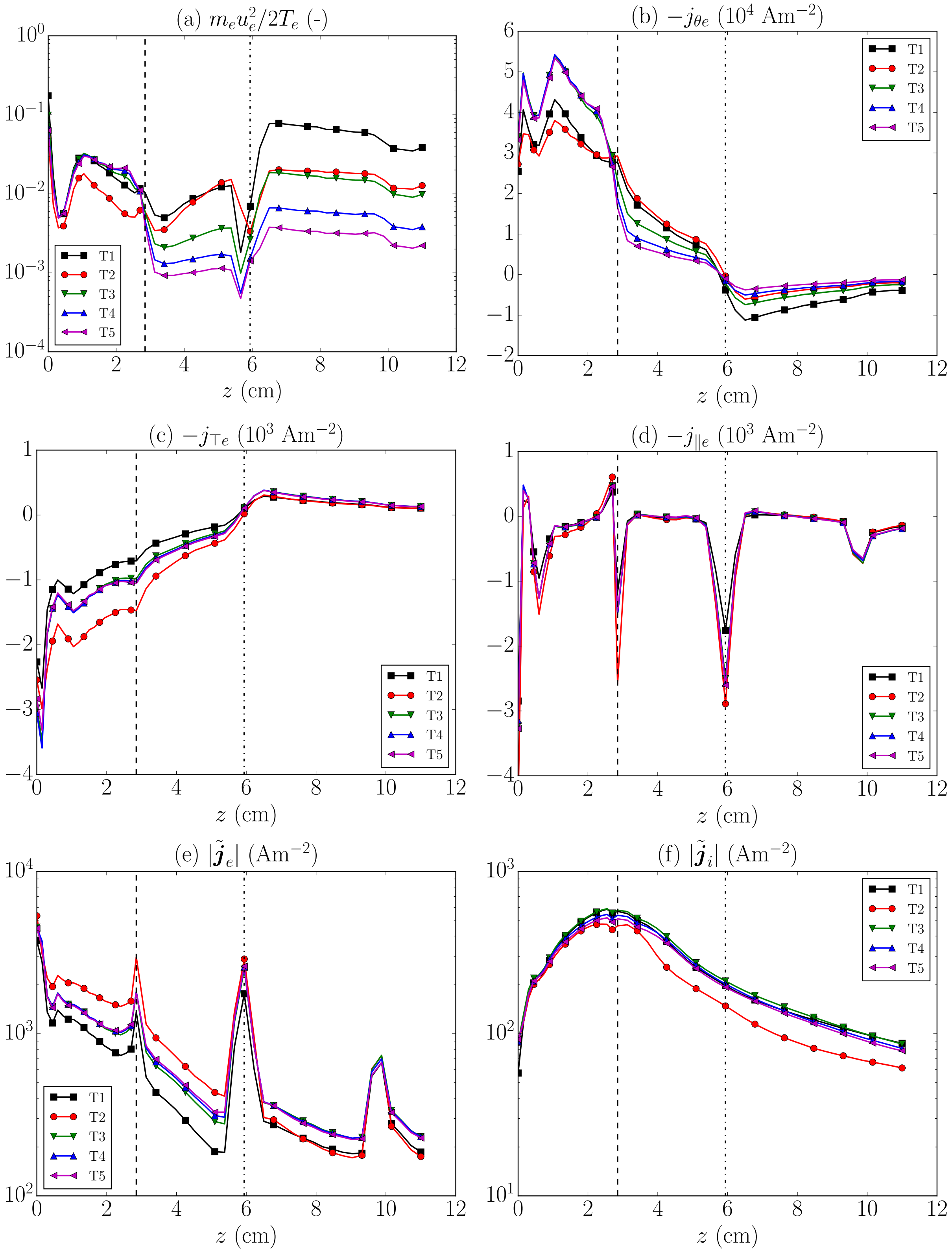

Figure 4.29: Results comparison for the simulation cases T1-T5. Time averaged axial profiles of (a) the electron drift-to-internal energy ratio, (b) the electron azimuthal current density component, (c) the electron perpendicular current density component, (d) the electron parallel current density component, (e) the magnitude of the 2D (z, r) electron current density vector and (f) the magnitude of the 2D (z, r) ion current density vector. The vertical black dashed and dot-dashed lines indicate, respectively, the axial position of the thruster chamber exit plane at $z = 2.85$ cm and the axial position of the magnetic field streamline passing through the cathode at $z = 5.94$ cm.

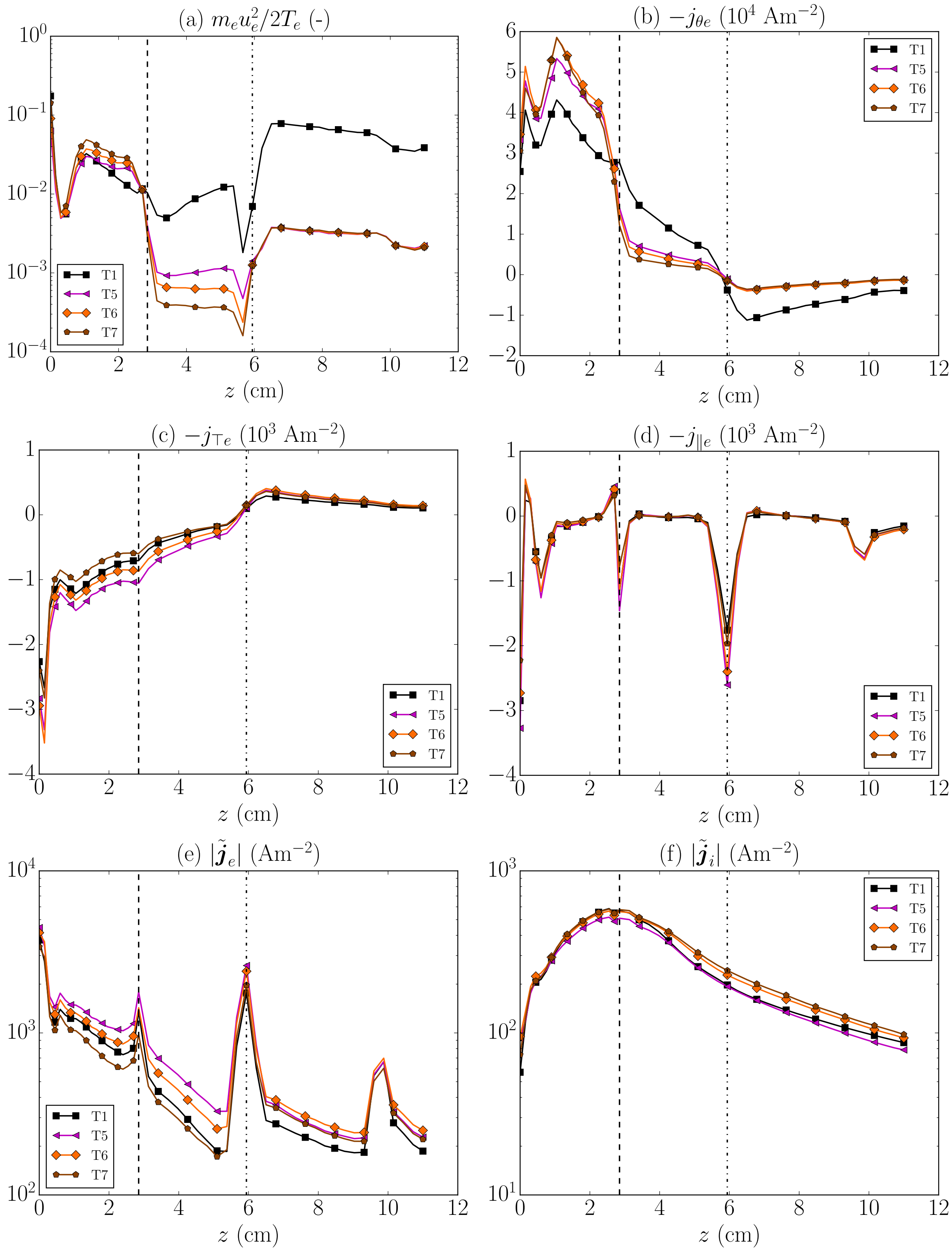

Figure 4.30: Results comparison for the simulation cases T1 and T5-T7. Time averaged axial profiles of (a) the electron drift-to-internal energy ratio, (b) the electron azimuthal current density component, (c) the electron perpendicular current density component, (d) the electron parallel current density component, (e) the magnitude of the 2D (z, r) electron current density vector and (f) the magnitude of the 2D (z, r) ion current density vector. The vertical black dashed and dot-dashed lines indicate, respectively, the axial position of the thruster chamber exit plane at $z = 2.85$ cm and the axial position of the magnetic field streamline passing through the cathode at $z = 5.94$ cm.

4.2.3 Conclusions

The simulation of a typical SPT-100 HET scenario has permitted to assess the performance of an improved version of NOMADS for the isotropic electron pressure case. In order to reveal its capabilities and limitations, different studies have been performed.

First, the impact of the number of NOMADS sub-iterations on the simulation results have been explored, showing that the computational time can be greatly reduced without affecting significantly the simulation results by considering a lower value of NOMADS sub-iterations N_{ke}.

Second, a reference simulation case has allowed both to demonstrate the code capabilities, reproducing the typical HET breathing mode, and to identify numerical issues related to (*i*) the large oscillations of the discharge current induced by the low frequency ionization instability under constant discharge voltage operation mode, (*ii*) the determination of plasma properties such as the electric potential and the electron pressure (or temperature) at the simulation boundary through GR techniques, and (*iii*) the MFAM quality and the relative size of both the PIC and the MFAM cells, which may yield important interpolation errors.

Third, the neutral-wall specular reflection type has been found to increase up to a 7% the breathing mode frequency obtained in the neutral wall diffuse reflection case. This fact is directly connected to the faster neutral dynamics produced by the specular reflection. The reciprocal of the neutral gas average residence time in the thruster chamber has been found to closely approximate the resulting breathing mode frequency.

Fourth, the improved volumetric cathode treatment has permitted to analyze the cathode location effects on the plasma discharge, revealing a local perturbation of the plasma properties in the near cathode region due to the concentrated injection performed by the volumetric cathode. The cathode magnetic line is far from being isothermal, specially near the cathode position. Similar plasma profiles inside the thruster chamber and thruster performances are obtained when moving the cathode position along the same magnetic field streamline (cases C1-C3). In contrast, larger discrepancies with the cases above are found for the case C4 in which the cathode magnetic streamline crosses the simulation domain further downstream, which could be due to the effect of the external boundary.

Finally, preliminary results for different electron turbulent parameter values featuring constant and step-out profiles have been presented. Although a finer tuning of α_t is needed, and despite the high discharge current fluctuations, which yield average I_d values still far from those corresponding to the typical SPT-100 HET nominal operation point, in general terms the results are not far from those reported by experiments. The breathing mode frequency has been found to slightly increase when step-out profiles with both increasing α_t in the near plume region (cases T3-T5) and decreasing α_t in the thruster chamber (cases T5-T7). The largest discharge current peak values and the lowest breathing mode frequency are obtained for the case T2, featuring a constant $\alpha_t = 5\%$ profile. The electric potential flattens in the first part of the thruster chamber for higher α_t values, while a larger potential fall is found for all the step-out profiles in the last part of the chamber. The peak in the axial component of the electric field increases accordingly, and moves upstream into the thruster chamber in those cases. The peak in the electron temperature increases in cases T3-T5 due to the enhanced Joule heating in the near plume region. In contrast, it decreases and moves upstream into the thruster chamber for cases T5-T7. While the thrust efficiency is not significantly affected when increasing α_t in the near plume region, larger values are obtained for lower electron turbulent contribution inside the thruster chamber (i.e. cases T5-T7). This fact is due to the lower average values of I_d obtained for those cases, which is consistent with the reduced electron perpendicular transport inside the chamber.

Several actions are proposed for future work. First, the large oscillations found on the discharge current reveals the need for a future implementation of effective current control strategies, such as resistor-inductor-capacitor (RLC) networks or proportional-integral-derivative (PID) control algorithms [166, 167], so that the discharge voltage V_d is not directly applied between the anode and cathode. This will allow to obtain more reliable results, and will facilitate the tuning of the electron turbulence parameters aiming to better reproduce the reported experimental results in future simulations. Second, a deeper investigation about the effects of different time discretization schemes for the electron-fluid model on the simulation results should be carried out. Third, the determination of the electric potential and the electron temperature at the simulation domain boundary must follow the approach proposed in Ref. [93], which will avoid the numerical extrapolation errors due to the current GR schemes applied. Fourth, the development of improved simulation domain MFAMs featuring a smoother and progressive evolution of the cells size should also be tackled, and special attention should be put to the PIC-mesh-to-MFAM cell size ratio, since important interpolation errors may be present whenever this ratio greatly differs from unity. This issue can be specially critical at the domain boundary. Fifth, the extension of the volumetric cathode to several MFAM cells is a proposed strategy to limit the perturbation produced on the plasma solution by this cathode model. It should be discussed whether this perturbation is purely artificial or not. In this line, the implementation of the wall cathode model presented in Ref. [147], which includes a sheath model for high emission electrodes that adjusts the electric potential there to the conditions imposed by the external plasma [148] could provide more realistic results in the near cathode region. Sixth, simulation domains featuring an extended near plume region will be considered in the future to assess the effects on the plasma discharge of the boundary conditions downstream, and analyze the evolution of the plasma properties when the magnetic field becomes residual. Seventh, future HYPHEN simulations will benefit from more realistic values for the thermalization or replenishment parameter σ_t used in the plasma-wall interaction models, provided by the 1D radial particle model dealt with in Chapters 5 and 6. Eighth, a more detailed implementation of the dominant inertial terms in the electron momentum equation could bring to light their still bad known role in those regions with a lower electron magnetization, such as the anode and the plume region. Finally, dedicated parametric studies of the discharge response for a wide range and combination of three different turbulent parameters introduced in Chapter 2 will be performed in the future, including the analysis of the plasma discharge with α_{te}/α_{tm} different from one.

Chapter 5

A HET discharge 1D radial particle model

This Chapter reproduces the contents published in the peer-reviewed journal Plasma Sources Science and Technology [35]. The typography has been adapted to the style of this Thesis.

Abstract

An improved radial particle-in-cell model of an annular Hall effect thruster discharge with secondary electron emission from the walls and a radial magnetic field is presented. New algorithms are implemented: first, to adjust the mean neutral density to a desired mean plasma density; second, to avoid refreshing of axially accelerated particles; and third, to weigh correctly low density populations (such as secondary electrons). The high-energy tails of the velocity distribution functions of primary and secondary electrons from each wall are largely depleted, leading to temperature anisotropies for each species. The secondary electron populations are found to be partially recollected by the walls and partially transferred to the primary population. A replenishment ratio of the primary high-energy tail is determined based on the sheath potential fall. Significant asymmetries at inner and outer walls are found for the collected currents, the mean impact energy, and the wall and sheath potentials. Radial profiles in the plasma bulk are asymmetric too, due to a combination of the geometric expansion, the magnetic mirror effect, and the centrifugal force (emanating from the $\boldsymbol{E} \times \boldsymbol{B}$ drift). The temperature anisotropy and non-uniformity, and the centrifugal force modify the classical Boltzmann relation on electrons along the magnetic lines.

5.1 Introduction

The Hall effect thruster (HET) [1, 3, 4] is a mature technology, already widely and successfully used as both primary and secondary propulsion system for a variety of space missions. In spite of its success, relevant physical phenomena of the plasma discharge inside the HET chamber and in its near plume are insufficiently known. This shortage drags out the development of new designs for new applications (for instance at low or high powers) and the optimization of existing devices. Also, it blocks the development of reliable and predictive simulation tools, which are considered essential, not only for design purposes, but also for accelerating tests of lifetime and of operation at different conditions (e.g. high thrust and high specific impulse).

One of the main open problems in HET research is related to the plasma interaction with the thruster chamber walls and its effects on the electron velocity distribution function (VDF) and the subsequent energy losses and the plasma recombination at the walls. Due to the electric potential structure, the electrons are a confined population except for the small currents that flow to the walls or downstream forming the plasma jet. This confinement would facilitate the electron population thermalization, but the low collisionality of the discharge (at plasma densities of 10^{17}-10^{18} m^{-3}) causes the VDF tails of electrons collected by the walls are not fully replenished, and hence the VDF remains non-Maxwellian. A second issue, particularly acute for the ceramics used in HET chambers, is the large SEE caused by the impact of 'primary' electrons from the plasma bulk. This SEE generates counterstreaming flows of secondary electrons [98, 173, 174] making further non-Maxwellian the VDF.

Ahedo and Parra [175] considered a one-dimensional planar (1Dp) stationary fluid model to analyze the plausible case where the secondary electrons were partially trapped within the plasma bulk (and eventually thermalized) and partially recollected by the walls. They determined the effects of partial recollection on the potential fall in the sheaths (and its charge saturation) and on the energy flows to the walls. Later, Ahedo and de Pablo [119] extended the analysis to partial thermalization of both primary and secondary electrons with a 1Dp stationary kinetic model, describing the non-Maxwellian VDF and the SEE yields with phenomenological parameters. They obtained analytical expressions for the sheath potential fall and the energy losses to the walls, in terms of the model parameters.

Sydorenko, Kaganovich, and coworkers [28, 29] treated a similar time-dependent 1Dp problem with a particle-in-cell(PIC)/Monte-Carlo-Collision(MCC) formulation [22, 37]. Using a fixed background of neutrals, their steady-state solution confirmed the partial recollection of secondary electrons at the walls and, more importantly, determined the temperature anisotropy ratio of the VDF, in terms of the axial electric field, the collisional frequencies, and the SEE yields; interestingly, the near-wall conductivity effect [97] in the axial electron current was observed too. More recently, Wang et al. [176] investigated, with a similar 1Dp PIC/MCC model, the asymmetries in the electric potential profile and sheath potential falls caused by having different SEE yields at each wall (i.e. different materials).

Taccogna et al. [30–32] considered a 1D radial (1Dr) PIC/MCC model, much more suitable to simulate a HET annular chamber and where the asymmetry on the electric potential profile takes place naturally. The emphasis of these works is on the development of a strong asymmetry and a saturated stream instability propagating all along the radial domain, in conditions where a large axial electric field induces an azimuthal electron drift of the order of the electron thermal speed.

The present paper revisits the model and code of Taccogna [31] with two types of goals. The first one is to enrich the numerical consistency and the capabilities of the code and, at the same time, to analyze the intrinsic limitations of 1Dp and 1Dr models. In this respect and even assuming azimuthal symmetry (i.e. $\partial/\partial\theta = 0$) the restriction of an axisymmetric (r, z) discharge to a given radial section ($z =$ const) of the chamber implies that strong assumptions must be made on all terms related to the axial forces and plasma flows. As a consequence, there is a certain degree on arbitrariness on the 1D model and results that cannot be left aside when drawing conclusions. The second goal of the paper is to investigate further the steady-state solution (without stream instabilities) with the focus on assessing the temperature anisotropy ratio of the VDF of both primary and secondary electrons, combined with the asymmetries introduced by cylindrical geometry effects (which include the geometrical expansion, the centrifugal force, and the magnetic mirror). Finally, the influence of anisotropy and asymmetry in the macroscopic laws of interest is investigated.

The rest of the paper is organized as follows. The main physical aspects of the model are presented in Sec. 5.2, while Sec. 5.3 includes the numerical implementation and the validation of the new algorithms. A discussion of the main physical aspects of the plasma discharge is provided in Sec. 5.4. The conclusions are drawn in Sec. 5.5.

5.2 The 1D radial model

The model attempts to analyze the plasma radial structure at a given axial location within the acceleration region of a HET chamber, taking into consideration the weak plasma collisionality and the SEE from the walls due to the impacts of energetic primary electrons. Fig. 5.1 sketches the annular HET chamber with r_1 and r_2 as inner and outer radius, respectively; $A = \pi(r_2^2 - r_1^2)$ is the area of the radial section.

The 1Dr model considers electrons e, singly-charged ions i, and neutrals n. Neutrals are modeled just as a spatially-uniform population with a time-dependent density $n_n(t)$ and a constant temperature T_n. Electrons and ions are modeled as two populations of macroparticles of constant weight W (i.e. number of elementary particles per macroparticle) with densities and temperatures, n_j and T_j ($j = i, e$), evolving with (r, t). Let us define, as representative of the instantaneous plasma density, the radially-averaged electron density $\bar{n}_e(t) = WN_p/V$ where N_p/V is the number of macro-electrons per unit of volume.

We are interested here in simulating a quasi-stationary discharge with a certain mean plasma density, that is $\bar{n}_e(t) \approx$ const$= n_{e0}$. In a 1D model, this requires one to make some decisions on the behavior of the particle sources and sinks. In a 1D cylindrical geometry, the conservation equations for ions and electrons reduce to

$$\frac{\partial n_j}{\partial t} + \frac{1}{r}\frac{\partial}{\partial r}(r n_j u_{rj}) = S_{ioniz} + S_{axial,j}, \qquad j = i, e, \tag{5.1}$$

where: $n_j u_{rj}$ is the species radial flux; S_{ioniz} is the source term due to ionization, proportional to $n_n(t)$; and $S_{axial,j}$ is the source term due to the net axial contribution for

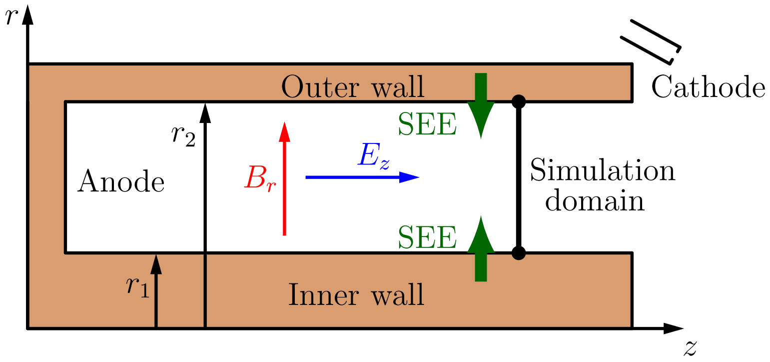

Figure 5.1: Sketch of a HET. The 1Dr simulation domain corresponds just to the thick black line.

species j. In a 2D (r,z) model one would have $S_{axial,j} = \partial(n_j u_{zj})/\partial z$, but, here $S_{axial,j}$ is as arbitrary as the HET radial section we are attempting to simulate. In the quasi-steady state, the integral of the continuity equation over the plasma volume (expressed in electric current units) yields

$$I_{wall,j} \approx I_{ioniz} + I_{axial,j}, \qquad j = i, e, \tag{5.2}$$

with $I_{wall,j}$ the species current lost into the wall, I_{ioniz} the (equivalent) current created through volumetric ionization (proportional to n_n and the same for electrons and singly-charged ions), and $I_{axial,j}$ the current injected (or extracted) through the axial flow. While $I_{wall,j}(t)$ is obtained directly from the dynamic plasma response, both I_{ioniz} and $I_{axial,j}$ depend on the particular model formulation.

If $n_n(t)$ is known, then the plasma variables determine completely $I_{ioniz}(t)$, and the simulation of a stationary discharge requires $I_{axial,j} \approx I_{wall,j} - I_{ioniz}$. This implies a continuous injection (or extraction) of plasma from the domain, requiring to define the properties of the injected macroparticles or the selection criteria for the extracted ones. We can distinguish between *axially-controlled* and *ionization-controlled* discharges depending on whether $I_{axial,j}$ is much larger or much smaller than I_{ioniz}, respectively. In an axially-controlled discharge, the plasma response is largely set by these conditions 'external' to the radial dynamics. Previous works seem to use $n_n(t) = n_{n0}$ and thus they would operate in a mixed regime.

The present work implements a model for a fully ionization-controlled discharge with $S_{axial,i} = S_{axial,e} = 0$ and $n_n(t)$ being adjusted in order that

$$I_{ioniz}(t) \approx I_{wall,j}(t), \tag{5.3}$$

at any time. It will be shown that adjusting $n_n(t)$ is simple and it assures that a stationary discharge is achieved. Besides, it corresponds reasonably to the physical situation in the HET chamber acceleration region, where ionization and wall recombination were found to compensate each other [98].

A 1Dr model needs also to prescribe the axial electric field E_z. This field accelerates over time the (nearly-unmagnetized) ions, which is an undesirable secular effect on the 1Dr simulation. Previous works have dealt with this issue by resetting or refreshing occasionally the ion population. Here, it is chosen to just ignore the effect of E_z on the ions, which can be interpreted as a continuous axial refreshing of ions. Therefore, macro-ions are inserted initially or created later with a mean axial velocity u_{zi}, and they are subjected only to the radial electric field (and the magnetic field). Thus E_z affects electrons only, primarily by forcing with the magnetic field the electron $\boldsymbol{E} \times \boldsymbol{B}$ azimuthal drift. In fact, a key validation of the model will be to check that there is not a secular increase of the macroscopic axial velocities of ions and electrons.

While E_z is taken constant and known, the radial electric field, $E_r = -d\phi/dr$, with $\phi(r,t)$ the electric potential, satisfies the Poisson equation

$$\frac{\varepsilon_0}{r}\frac{\partial}{\partial r}\left(r\frac{\partial \phi}{\partial r}\right) = \rho_{el}(r,t), \tag{5.4}$$

with ρ_{el} the net electric charge density of the plasma. The two boundary conditions for this equation are set here at the outer wall, $r = r_2$,

$$\phi_2 = 0, \qquad \varepsilon_0 E_{r2} = -\sigma_2(t). \tag{5.5}$$

Here: the first condition just sets a reference for the potential; ε_0 is the vacuum permittivity; σ_2 is the surface charge at the outer dielectric wall, to be defined in detail below; and, the radial electric displacement of the dielectric wall has been assumed negligible compared to $\varepsilon_0 E_{r2}$. A similar condition on E_{r1} is derived below in Eq.(5.9).

The magnetic field is assumed radial and, in order to be divergent-free, it satisfies

$$B_r(r) = B_{r1}\frac{r_1}{r}, \tag{5.6}$$

with B_{r1} known. Since $B_{r2}/B_{r1} = r_1/r_2 < 1$, magnetic mirror effects are possible.

Turning now to the plasma-wall interaction, ions and electrons reaching the walls are collected; however, ion recombination is not considered explicitly since neutrals are just modeled through $n_n(t)$. The SEE produced by the impacting electrons will follow the probabilistic model of Ref. [177]. In this model, the total SEE yield accounts for three different types of secondary electrons: the backscattered ones (elastically reflected by the wall), the rediffused ones (non-elastically reflected by the wall), and the true-secondary (TS) electrons (those extracted from the surface layers of the material). More details on the implementation of the SEE model are given in [31]. For the present purpose of understanding better the radial discharge and the electron VDF, backscattered and rediffused electrons are not considered, so that the SEE is limited to true secondary electrons. In the energy range of interest, the resulting SEE yield (i.e true-secondary-to-primary flux ratio) reduces to

$$\delta_{TS}(E) \simeq E/E_c \tag{5.7}$$

with E the impact electron energy, and E_c the crossover energy ($E_c = 51.1$ eV in simulations here [31]).

Simulations are generally started with a uniform electric potential profile. Thus, in the transient, the walls collect preferentially (highly mobile) electrons. These collected electrons build up the (negative) surface charge at the walls and create the plasma Debye sheaths around them. The accumulation over time of the surface charge is determined from integrating the current conservation equation across the wall surface *and* over time:

$$\sigma_l(t) = -\int dt \boldsymbol{j}_l(t) \cdot \mathbf{1}_l, \quad l = 1,2. \tag{5.8}$$

Type	Description	Symbol	Units	Value
Populations settings	Number of elementary particles per macroparticle	W	-	$3 \cdot 10^9$
	Initial r-averaged plasma density	$\bar{n}_{e0}$	$10^{17}\mathrm{m}^{-3}$	0.8
	Initial number of ion/electrons macroparticles*	N_{p0}	-	106814
	Initial electron temperature	T_{e0}	eV	10
	Initial ion temperature	T_{i0}	eV	1
	Ion axial mean velocity	u_{zi}	km/s	10
	Initial background neutral density	n_{n0}	10^{17} m^{-3}	40
	Neutral temperature	T_n	K	700
***E*, *B* fields**	Electric field axial component	E_z	V/cm	100
	Magnetic field radial component at inner radius	B_{r_1}	G	150
Simulation parameters	Inner radius	r_1	cm	3.5
	Outer radius	r_2	cm	5.0
	Number of nodes	N_r	-	1500
	Grid spacing*	Δr	μm	10
	timestep	Δt	ps	5
Physical parameters	Debye length*	λ_D	μm	83.1
	Electron Larmor radius*	r_l	μm	802.0
	Inverse of plasma frequency*	$1/\omega_{pe}$	ps	62.7
	Inverse of electron cyclotron frequency*	$1/\omega_{ce}$	ps	379.1

Table 5.1: Main input parameters including initial population settings, externally applied fields and grid definition. The magnitudes marked with an asterisk (*) are not input parameters of the model, but are derived from the other parameters instead. The variables named as physical parameters are estimated from the other input values given at initial conditions.

Here: l names the wall, $\boldsymbol{j}_l$ is the net electric current density at the plasma-wall boundary, and $\mathbf{1}_l$ is the wall normal pointing towards the plasma. At the steady state, $\boldsymbol{j}_l$ is zero for a dielectric and hence the surface charge remains constant.

As commented above, the integration of the Poisson equation across each of the wall surfaces yields

$$\varepsilon_0 E_{r2} = -\sigma_2(t), \qquad \varepsilon_0 E_{r1} = \sigma_1(t), \tag{5.9}$$

if the electric displacement field of the dielectric is negligible. The first condition was already imposed as a boundary condition in Eq. (5.5). Consistency requires that the second one be satisfied automatically. This is indeed the case since the radial integration of the current conservation and Poisson equations yield

$$\varepsilon_0 [rE_r]_{r_1}^{r_2} = -\int [rj_r]_{r_1}^{r_2} dt. \tag{5.10}$$

The collisional processes implemented in the code are the following: first, the electron-neutral collisions including elastic scattering, excitation, and single ionization, following the models of Refs. [178–180]; and second, the electron-ion, electron-electron, and ion-ion Coulomb collisions, according to the models of Refs. [181–184]. The ion-neutral collisions are found to be negligible for typical HET parameters.

In addition, secondary electrons are transferred to the main primary population when they undergo a collision with neutrals or a large-angle (higher than 90 degrees) Coulomb collision. Notice that, in a kinetic or particle formulation, the distinction between 'secondary' and 'primary' populations is just convenient for the analysis and understanding of the plasma response. On the contrary, that distinction acquires full sense in multi-fluid electron models.

5.3 Numerical implementation and validation

The main model input parameters and the resulting plasma magnitudes are listed on Tab. 5.1. A uniform radial mesh of $N_r + 1$ points from r_1 to r_2 is chosen, with a cell size Δr smaller than the plasma Debye length λ_D. The electron and ion macroparticles have the same constant weight W throughout the simulation, chosen so that the initial number of both electron and ion macroparticles is $N_{p0} \approx 10^5$, corresponding here to about 70 macroparticles per cell. It has been checked in an independent simulation that using double this number of particles per cell reduces only the PIC fluctuations, without changing the averaged trends.

Xenon is assumed as the propellant. The plasma macroscopic properties such as particle densities and fluxes are computed at the mesh nodes through an area weighting algorithm [36]. The nodal weighting volumes are corrected according to Ref. [69]. The higher moments of the VDF, such as the temperature, are obtained for each simulated species through a new extended volumetric weighting algorithm presented in Sec. 5.3.2. Additionally, surface weighting schemes [76, 185] are used for updating the particle fluxes to the walls.

In order to obtain the electric potential at the mesh nodes, second order finite difference schemes are used for discretizing the Poisson equation along the radial coordinate r. The Thomas tridiagonal algorithm [186] is applied as a direct solving technique. The electrons trajectories are propagated along time using both radial and axial components of the electric field, and the radial magnetic field. In contrast, only the radial electric field is used to update the ions' velocity and position. The Boris-Buneman leapfrog algorithm [36] is applied to move all macroparticles one timestep forward considering the corresponding electric and magnetic fields interpolated to the macroparticles position. The timestep is chosen so that $\Delta t < 0.3\omega_{pe}^{-1}$, where ω_{pe} is the plasma frequency. This condition ensures an accurate integration of the electron gyromotion since $\omega_{pe} > \omega_{ce}$, with ω_{ce} the electron gyrofrequency (see Tab. 5.1).

After advancing all macroparticles one timestep, the MCC module performs the electron-neutral elastic and inelastic collisions. The constant timestep method of Refs. [178, 179] for selecting the type of collision is implemented using the cross sections from Ref. [158]. The probability distribution function for the progeny electrons generated by ionization is taken from [180]. A mean axial velocity u_{zi} is added to any newborn ion. Regarding the emission of true-secondary electrons, a zero-drift semi-Maxwellian VDF with temperature $T_{eW} = 2$ eV is assumed.

5.3.1 The discharge control algorithm

An algorithm for an ionization-controlled discharge with no axial contributions of plasma is presented here. In principle, there would be two methods to proceed, both plotted in Fig. 5.2(a). The first one, used in previous works and represented by the dashed lines, fixes the neutral density, i.e. $n_n(t) = n_{n0}$ and lets the mean plasma density $\bar{n}_e(t)$ to evolve until a final state is reached after a few microseconds (i.e. a time related to the transit time of ions). The second method, represented by the solid lines of Fig. 5.2(a) and Fig. 5.2(b), fixes the mean plasma density in the domain, $\bar{n}_e(t) \simeq \bar{n}_{e0}$, and adjusts $n_n(t)$ in order to satisfy Eq. (5.3).

In the first method the final plasma density is unknown and it can be very different from the initial one. For instance, the case $n_n(t) = 4{\cdot}10^{18}$ m^{-3} starts with $\bar{n}_e \approx 8{\cdot}10^{16}$ m^{-3} and ends, after 25 μs, with $\bar{n}_e \approx 6 \cdot 10^{15}$ m^{-3}. This implies that starting with 80 macro-electrons per cell, we end with only 6 macro-electrons per cell, thus affecting the weighting accuracy. The advantage of the novel second method is that the number of macroparticles does not change practically along the simulation and thus it can be optimized. Besides, it seems preferable to fix from the beginning the mean plasma density we are targeting to, than the neutral density.

The second method is here implemented with the following ionization-controlled discharge (ICD) algorithm on neutrals. First, a tolerance is fixed for the variations of average plasma density,

$$\epsilon_{c1} = |\bar{n}_e(t)/\bar{n}_{e0} - 1|. \tag{5.11}$$

Then, every PIC-MCC timestep, both $\bar{n}_e(t)$ and its rate of change $\Delta\bar{n}_e$ are computed. The last one at the instant k is defined as

$$\Delta\bar{n}_e^{(k)} = \frac{1}{k_c}\left[n_e^{(k)} - n_e^{(k-1)} + (k_c - 1)\Delta\bar{n}_e^{(k-1)}\right] \tag{5.12}$$

where $(k-1)$ and (k) are two subsequent instants of PIC-time and k_c is a fixed number of time steps ($k_c = 100$ in the figures here).

The neutral density for instant $(k+1)$ is modified only if $|\bar{n}_e(t)/\bar{n}_{e0} - 1|$ is outside the above tolerance range, and

$$|\Delta\bar{n}_e^{(k)}| > \epsilon_{c2}, \tag{5.13}$$

with ϵ_{c2} fixed. The reason to include a condition on the rate of change, $\Delta\bar{n}_e$, is to filter the fast oscillations and the numerical noise inherent to the PIC calculations. Values of $\epsilon_{c1} = 10^{-3}$ and $\epsilon_{c2} = 10^{-2}$ have been found adequate to run smoothly the ICD algorithm here. The updated neutral density is defined as

$$n_n^{(k+1)} = n_n^{(k)}\frac{\bar{n}_{e0}}{\bar{n}_e^{(k)}}. \tag{5.14}$$

Fig. 5.2(b) shows that the stationary discharge with $\bar{n}_e \simeq 8 \cdot 10^{16}$ m^{-3} requires $n_n \approx 6.85 \cdot 10^{18}$ m^{-3}.

Fig. 5.2(c) plots the evolution of the surface charges (in absolute value). In fact, the ICD algorithm is not applied until the surface charges $\sigma_j(t)$ are practically constant. This takes about 1 μs ($\sim 2 \cdot 10^5$ PIC time steps) and corresponds to the formation time of the Debye sheaths (if the initial electric potential profile is flat). Fig. 5.2(d) plots the

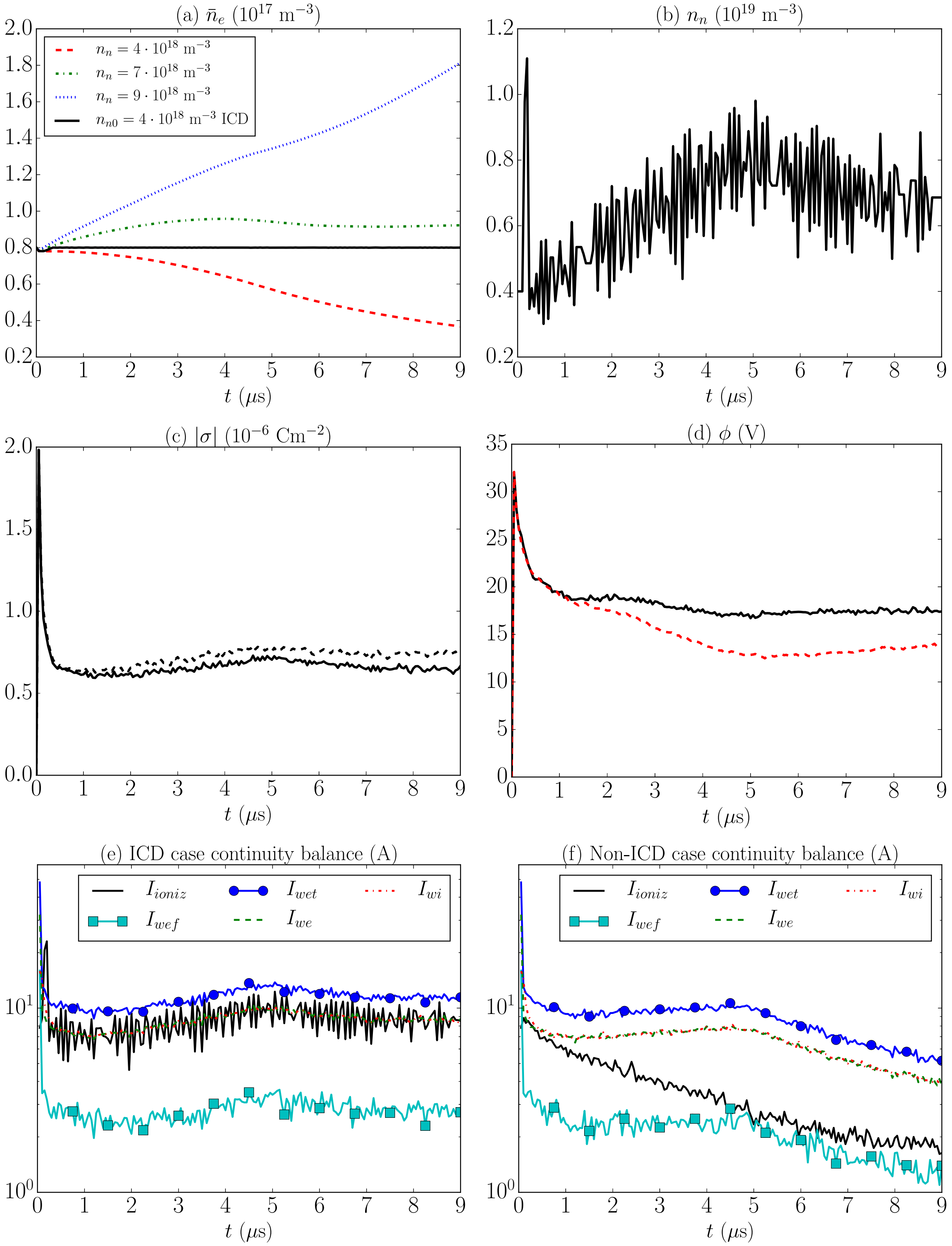

Figure 5.2: Time evolution of: (a) the average electron density in the simulation domain for non-ICD (dashed) and ICD (solid) cases; (b) the background neutral density in the ICD case of previous plot; (c) the absolute value of the surface charge densities at the inner (black solid) and outer (black dashed) walls in the ICD case; and (d) the electric potential at the central point M in the ICD (black solid) and the non-ICD case with $n_n(t) = n_{n0}$ (red dashed). Time evolution of the different electron sources and sinks on the current continuity balance of Eq. (5.15) for the ICD case (e) and the non-ICD case with $n_n(t) = n_{n0}$ (f). All plots represent time-averaged magnitudes over $N_k = 10^4$ time steps.

evolution of the electric potential at the central point M (i.e. $r_M = 42.5$ mm) for the ICD case and the non-ICD case with $n_n(t) = n_{n0}$.

Figs. 5.2(e) and 5.2(f) detail the time evolution of partial currents for the ICD and the non-ICD case, respectively. The net electric current to the two walls is there split into three populations: ions impacting the two walls (I_{wi}), electrons going *to* and impacting the walls (I_{wet}), and secondary electrons emitted *from* the walls (I_{wef}). The ICD case satisfies very well the steady-state and the dielectric conditions,

$$I_{ioniz} = I_{wi} = I_{we}, \qquad I_{we} \equiv I_{wet} - I_{wef}, \tag{5.15}$$

(I_{we} is the net electron current to the walls) thus validating the ICD algorithm. On the contrary, the non-ICD, satisfies well the dielectric condition but there is a deficit in ionization. As a consequence, $\bar{n}_e(t)$ and the currents to the walls decrease [see Figs. 5.2(a) and 5.2(f)]. As said before, the non-ICD simulation was run 25 μs without reaching a steady-state (or perhaps extinguishing), which anyway proves that a non-ICD procedure is not adequate.

5.3.2 The extended volumetric weighting algorithm

The PIC formulation operates with a constant macroparticle weight W for all the simulated species, which simplifies the treatment of collisional processes and saves computer memory. However, it also implies that, for each species, the number of macroparticles per cell is proportional to its density. The simulation parameters are optimized to reproduce well the response of the main species (ions and primary electrons) with similar densities (except inside the sheaths). But secondary electrons from the walls turn out to have a density 1-2 orders of magnitude lower. Thus, if there are 50-100 particles per cell for ions and primary electrons, there will be only 1-10 for secondary electrons. This leads to temporal oscillations on their density and, more importantly, to wrong estimates of their macroscopic velocity and temperature, as it will be shown below.

This issue can be solved by extending in time the conventional volumetric weighting of particles. The extended volumetric weighting (EVW) algorithm proposed here takes into consideration data from the last N_k time steps. Thus the particle density of species j in a given node satisfies

$$n_j = \frac{W}{N_k \Delta V} \sum_k \sum_p s_p, \tag{5.16}$$

where: ΔV is the weighting volume associated to the node, s_p is the weighting function assigning a weight to each macroparticle depending on its distance to the node, the sum in p is for all macroparticles with $s_p \neq 0$, and the sum in k is for the time steps.

Similarly, the particle flux vector at the same node and time is given by

$$\boldsymbol{g_j} = \frac{W}{N_k \Delta V} \sum_k \sum_p \boldsymbol{v}_p s_p, \tag{5.17}$$

with $\boldsymbol{v}_p$ the particle velocity. Then, the resultant fluid velocity is $\boldsymbol{u_j} = \boldsymbol{g_j}/n_j$. In the same way, the diagonal components of the pressure tensor at the same node and instant are computed as

$$p_{lj} = \frac{m_e W}{N_k \Delta V} \sum_k \sum_p (v_{lp} - u_{lj})^2 s_p, \qquad l = r, \theta, z, \tag{5.18}$$

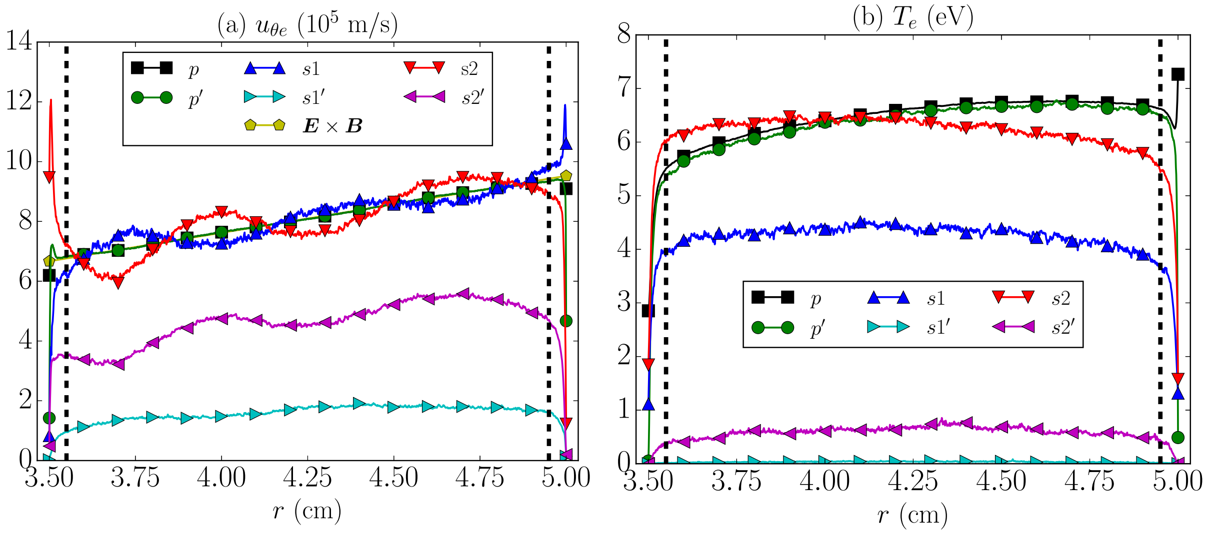

Figure 5.3: Steady-state radial profiles of (a) the macroscopic azimuthal velocities and (b) the mean temperatures of the different electron populations. Curves without (with) a prime correspond to extended (standard) volumetric weighting. Plot (a) also depicts the $\boldsymbol{E}\times\boldsymbol{B}$ velocity drift for comparison. Steady-state values have been averaged over the last $N_k = 2\cdot 10^5$ time steps (equivalent to the last microsecond of simulation time). In both plots the vertical dashed lines represent the approximate inner and outer sheath edges.

and the resultant temperatures are $T_{lj} = p_{lj}/n_j$.

Of course, the EVW is filtering oscillations of frequencies $(N_k\Delta t)^{-1}$ but this is not an issue when studying the steady-state discharge. For instance, in the simulations shown in this paper, values of $N_k = 10^4 - 10^5$ are taken, which correspond to 0.05-0.5 μs, so even oscillations of up to hundreds of kHz can be reproduced correctly.

Fig. 5.3 plots the macroscopic azimuthal velocity and the mean temperature of the three electron species considered hereafter: primary electrons p, and (true) secondary electrons emitted by the inner $s1$ and outer $s2$ walls (recall that secondary electrons become primary electrons after a large angle collision). In order to show the need and the good performance of the EVW algorithm, these two macroscopic variables are plotted in two ways. The plotted EVW variables correspond to

$$\boldsymbol{u}_e = \frac{\sum_k \sum_p \boldsymbol{v}_p s_p}{\sum_k \sum_p s_p}, \qquad T_e = \frac{m_e}{3}\frac{\sum_k \sum_p |\boldsymbol{v}_p - \boldsymbol{u}_e|^2 s_p}{\sum_k \sum_p s_p}. \tag{5.19}$$

The conventional volumetric weighting variables (averaged over N_k time steps, to make fairer the comparison) correspond to

$$\boldsymbol{u}'_e = \frac{1}{N_k}\sum_k \frac{\sum_p \boldsymbol{v}_p s_p}{\sum_p s_p}, \qquad T'_e = \frac{m_e}{3N_k}\sum_k \frac{\sum_p |\boldsymbol{v}_p - \boldsymbol{u}'_e|^2 s_p}{\sum_p s_p}. \tag{5.20}$$

Fig. 5.3(a) shows that applying the EVW, the azimuthal velocities of the three electron populations satisfy very well the $\boldsymbol{E}\times\boldsymbol{B}$ drift. In comparison, the conventional weighting yields incorrect (too low) values of $u_{\theta e}$ for secondary electrons. The reason of the discrepancies is that the instantaneous values used in Eq. (5.20) are weighted over a too small number of secondary macro-electrons per cell. The conventional weighting behaves well on $u_{\theta e}$ for p-electrons since enough number of macroparticles per cell are used at any time step. Only near the walls there is some discrepancy between the two weightings on p-electrons, due precisely to the decreasing density (and thus number of macroparticles per cell) there.

The differences between the extended and the conventional weightings are more pronounced when computing temperatures, since these variables measure velocity dispersion, so the double summation on particles-per-cell (both for $\boldsymbol{u}_j$ and for T_j) doubles the source of errors. In Fig. 5.3(b), the conventional weighting works fine for the primary electron temperature but it again underestimates much of the temperatures of secondary electrons; observe that it is practically zero for $s1$-electrons (and a zero temperature is the natural value when there is only one particle per cell).

The vertical dashed lines in Fig. 5.3 represent approximately the edges of the Debye sheaths. Notice that a 'sheath edge' is well and exactly defined only in the two-scale asymptotic model applicable to the zero-Debye-length limit. In the present one-scale (i.e. nonzero Debye length) model, the definition of sheath edges is just meant for a more detailed analysis of the results, in particular to point out the differences between the plasma response at the plasma bulk and near the walls. We have located sheath edges at 0.5 mm ($\sim 6\lambda_D$ from the wall, based on data from the knees of the electric potential profile, the relative charge density, and the radial ion Mach number [see Fig. 5.5(c) below].

Observe that secondary electrons are born at the wall from a semi-Maxwellian VDF with $T_{eW} = 2$ eV. Then, within the Debye sheath, they are preferentially accelerated by the large radial electric field E_r (~ 50000 V/m), and enter the plasma bulk as a quasi-monoenergetic beam. Their effective magnetization (a cycloidal combination of azimuthal drift and gyromotion) takes place once inside the plasma bulk, within one Larmor diameter (∼3 and ∼4 mm, at inner and outer sheath edges, respectively, based on local magnetic field and radial velocity). The reproduction of this well-known behavior in the simulations can be considered as an important validation step.

It is worth to point out that the EVW particle density defined in Eq. (5.16) is only used for macroscopic quantities calculation, while for solving Poisson equation [Eq. (5.4)] instantaneous conventional weighted electron and ion particle densities are considered so that any filtering effect due to the time-averaging process is avoided in the update of the ambipolar radial electric field.

5.4 Analysis of electron velocity distribution function and dynamics

The analysis here is focused on the stationary response for an ionization-controlled discharge defined in Tab. 5.1. Tab. 5.2 compiles relevant data of the discharge that will be commented along this section together with Figs. 5.4 to 5.6.

Fig. 5.4(a) plots the radial profile of the self-adjusted electric potential. Points W_1, W_2, Q_1, Q_2, and M correspond to walls, sheath edges, and channel mid-radius, respectively. The maximum potential is located just a bit inwards of point M and is only 0.03 V higher. The asymmetry of the potential profile due to cylindrical effects is evident at the sheath edges and the walls. The potential difference between the two sheath edges is $\Delta\phi_{Q_1Q_2} = 0.96$ V and between the two walls is $\Delta\phi_{W_1W_2} = 2.27$ V. This last one is a bit

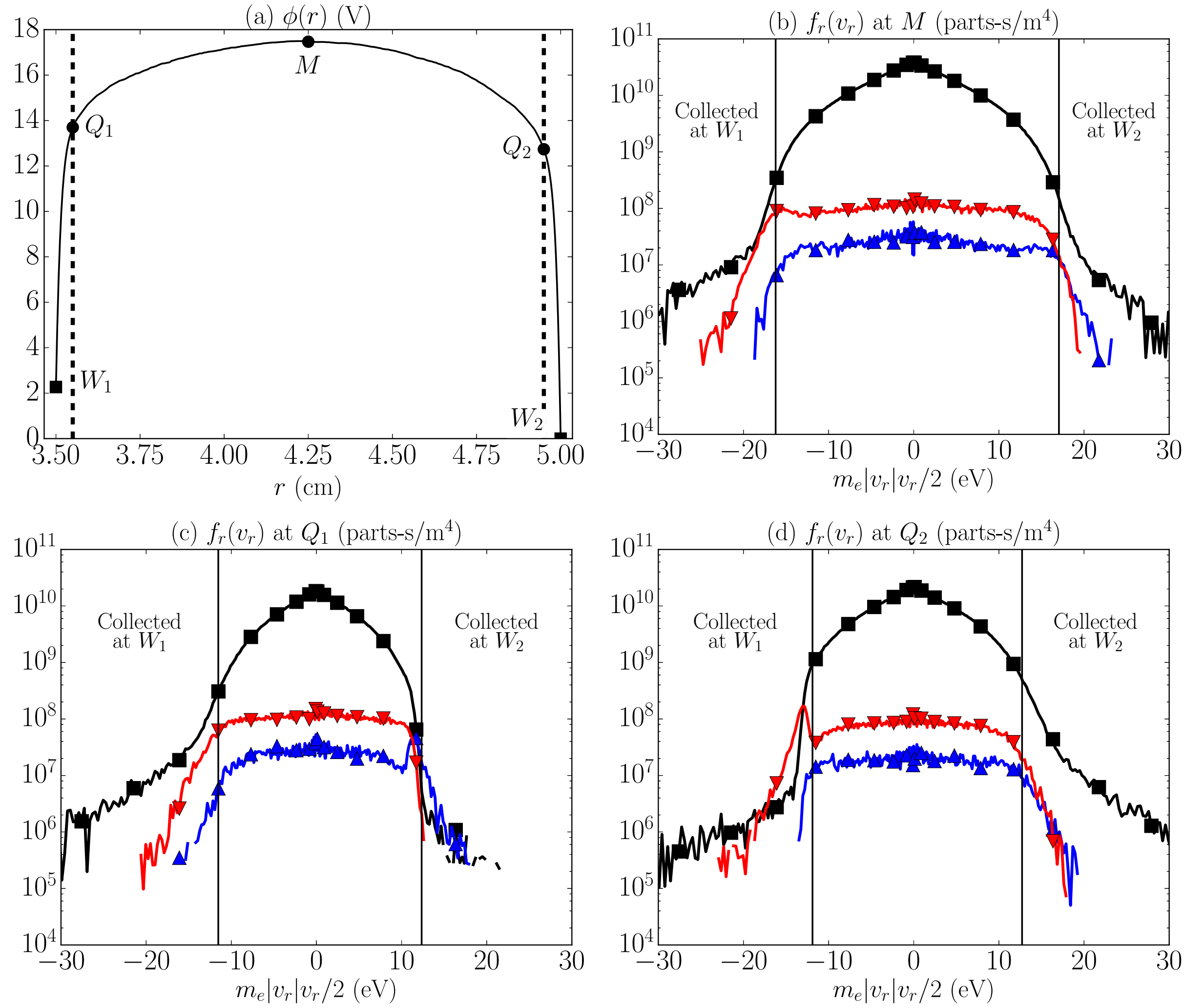

Figure 5.4: (a) Time-averaged (over last microsecond of simulation time) radial profile of the electric potential. Points M, Q_1, Q_2, W_1, W_2 correspond to channel mid-radius, sheath edges, and walls. (b)-(d) Radial VDF at nodes M, Q_1, and Q_2. Black, blue and red lines with square, up and down triangles correspond to the p, $s1$ and $s2$ populations, respectively. The VDFs have been accumulated over the last microsecond of simulation time.

higher than the typical emission energy of secondary electrons in our simulations, $T_{eW} = 2$ eV; nonetheless a simulation run with $T_{eW} = 0.2$ eV shows rather small differences in the steady-state response. The difference $\Delta\phi_{W_1W_2} > 0$ facilitates that electrons emitted from the wall W_2 be recollected at the wall W_1. However, there are two magnetic effects that change the perpendicular energy of an electron and therefore their radial energy and radial turning points (i.e. those with zero radial velocity, $v_r = 0$).

Neglecting collisions, the conserved total energy E of an electron satisfies

$$E = m_e \frac{v_r^2 + v_\perp^2}{2} - e\phi, \tag{5.21}$$

with $v_\perp$ the non-radial component of the electron velocity. In the small electron Larmor radius limit, the phase-averaged perpendicular energy, $m_e v_\perp^2/2$, is the sum of the one due to the gyromotion (which is proportional to the conserved magnetic moment μ) and the

Type and units	Description	Symbol	Value
Electric potentials (V)	At the mid radius M	ϕ_M	17.47
	At the inner sheath edge Q_1	ϕ_{Q_1}	13.70
	At the outer sheath edge Q_2	ϕ_{Q_2}	12.74
	At the inner wall W_1	ϕ_{W_1}	2.27
	At the outer wall W_2	ϕ_{W_2}	0.0
Collision frequencies (MHz)	e-n elastic collision	ν_{en}^{el}	3.680
	e-n excitation collision	ν_{en}^{ex}	0.209
	e-n ionization collision	ν_{en}^{ion}	0.168
	e-i Coulomb collision	ν_{ei}^{Coul}	0.076
	e-e Coulomb collision	ν_{ee}^{Coul}	0.017
	i-i Coulomb collision	ν_{ii}^{Coul}	0.119
Conversion to p and wall collection fractions (%)	$s1$ conversion to p	-	63.2
	$s1$ collection at the inner wall	-	7.5
	$s1$ collection at the outer wall	-	29.3
	$s2$ conversion to p	-	60.1
	$s2$ collection at the inner wall	-	28.7
	$s2$ collection at the outer wall	-	11.2
Current densities (A/m^2)	p to the inner wall	$\lvert j_{p,1-}\rvert$	12.80
	$s1$ to the inner wall	$\lvert j_{s1,1-}\rvert$	0.17
	$s1$ from the inner wall	$\lvert j_{s1,1+}\rvert$	2.36
	$s2$ to the inner wall	$\lvert j_{s2,1-}\rvert$	2.96
	p to the outer wall	$\lvert j_{p,2+}\rvert$	23.97
	$s1$ to the outer wall	$\lvert j_{s1,2+}\rvert$	0.48
	$s2$ to the outer wall	$\lvert j_{s2,2+}\rvert$	0.81
	$s2$ from the outer wall	$\lvert j_{s2,2-}\rvert$	7.23
Mean impact energies per elementary particle (eV)	$e \equiv p + s1 + s2$ at the inner wall	$E_{we,1}$	8.10
	p at the inner wall	$E_{wp,1}$	8.50
	$s1$ at the inner wall	$E_{ws1,1}$	4.06
	$s2$ at the inner wall	$E_{ws2,1}$	6.59
	$e \equiv p + s1 + s2$ at the outer wall	$E_{e,2}$	15.75
	p at the outer wall	$E_{wp,2}$	16.16
	$s1$ at the outer wall	$E_{ws1,2}$	6.24
	$s2$ at the outer wall	$E_{ws2,2}$	9.34
Electron energy balance source and sink terms (W)	Electric field work	P_{elec}	337.67
	SEE energy gain	$P_{wall,f}$	5.56
	Wall losses	$P_{wall,t}$	153.40
	Inelastic collisions losses	P_{inel}	194.30

Table 5.2: Main parameters characterizing the steady-state discharge. Values averaged over the last microsecond of simulation time have been used.

one due to the azimuthal $\boldsymbol{E}\times\boldsymbol{B}$ drift. Thus, here the radial kinetic energy satisfies

$$m_e\frac{v_r^2}{2}\simeq E+e\phi-\mu B-W_d=E+e\phi(r)-\mu B_1\frac{r_1}{r}-W_{d1}\frac{r^2}{r_1^2}, \tag{5.22}$$

where $W_d=m_eE_z^2/2B_r^2$ is the gyrocenter azimuthal energy, and the right-most side makes explicit the variation of B and W_d with r; in our simulations $W_{d1}=1.27$ eV and $W_{d2}=2.58$ eV at inner and outer walls, respectively. Therefore, the radial energy of an electron moving inwards is decreased by the magnetic mirror and is increased by the change on the $\boldsymbol{E}\times\boldsymbol{B}$ drift. For the plotted simulation, the change on W_d is mild, but not negligible, compared to the change of ϕ in the plasma bulk. Below it will be seen that this azimuthal energy plays a significant role on the electron macroscopic energy/momentum balance.

Figs. 5.4(b)-(d) show the VDFs, $f_r(v_r)$, (once integrated over v_θ and v_z) of primary and secondary electrons, p, $s1$ and $s2$, at points M, Q_1 and Q_2. Observe first that, in the plasma bulk, between Q_1 and Q_2, the densities of secondary electrons are much lower than that of the primary electrons, n_p, so this last determines almost exclusively the electric potential profile. In Figs. 5.4(b)-(d), the solid vertical lines separate approximately (and in the absence of collisions) the central region of confined electrons from the left and right regions of electrons to be collected by the inner and outer wall, respectively. These lines correspond to the radial turning points from Eq. (5.22) for electrons with an average gyroenergy value of $<\mu B>=9.2$ eV.

Tab. 5.2 shows that the Coulomb collisions are negligible compared to the collisions with neutrals, but even the elastic electron-neutral frequency, ~ 3.7 MHz, is low compared with the transit frequency, ~ 62 MHz. This explains that the VDFs at point M, Fig. 5.4(b), present a large depletion of the high-energy tails, filled with wall-collectable electrons. Figs. 5.4(c) and 5.4(d) show similar depletions of the VDF tails at points Q_1 and Q_2. In Fig. 5.4(c) the peak on the $s1$-VDF (blue line) corresponds to the electrons just emitted from W_1, which have acquired an electric potential energy $e\Delta\phi_{W_1Q_1}=11.43$ eV when crossing the sheath. An equivalent explanation applies to the peak of the $s2$-VDF (red line) in Fig. 5.4(d), with an energy $e\Delta\phi_{W_2Q_2}=12.74$ eV.

Beyond these peaks, the shape of the VDFs for secondary electrons at different locations is the consequence of their possible destinies. The most energetic ones are recollected after a single or double radial journey. The rest of them bounce radially, until collisions transfer them to the primary population. The SEE yield and the amounts of wall-recollection and conversion to p-electrons determine the density and other macroscopic properties of secondary electrons. Table 5.2 provides detailed data on these processes: 60% and 63% of $s1$ and $s2$ electrons, respectively, are converted to p-electrons due to electron-neutral or large angle Coulomb collisions, while the remaining fractions are re-collected at the walls.

Tab. 5.2 also provides the currents of the different electron species to and from the walls. Most of the current to the walls comes from the p-population, which has a much larger density, as illustrated in Fig. 5.5(a). The most prominent result is that large asymmetries are found between walls in, first, the current exchanged at each of them, with a ratio of $|j_{e,2+}|/|j_{e,1-}|\simeq 1.59$, and, second, the average true-secondary electron yields, defined as

$$<\delta_{TS,1}>=\frac{|j_{s1,1+}|}{|j_{e,1-}|}\approx 0.15,\qquad <\delta_{TS,2}>=\frac{|j_{s2,2-}|}{|j_{e,2+}|}\approx 0.29, \tag{5.23}$$

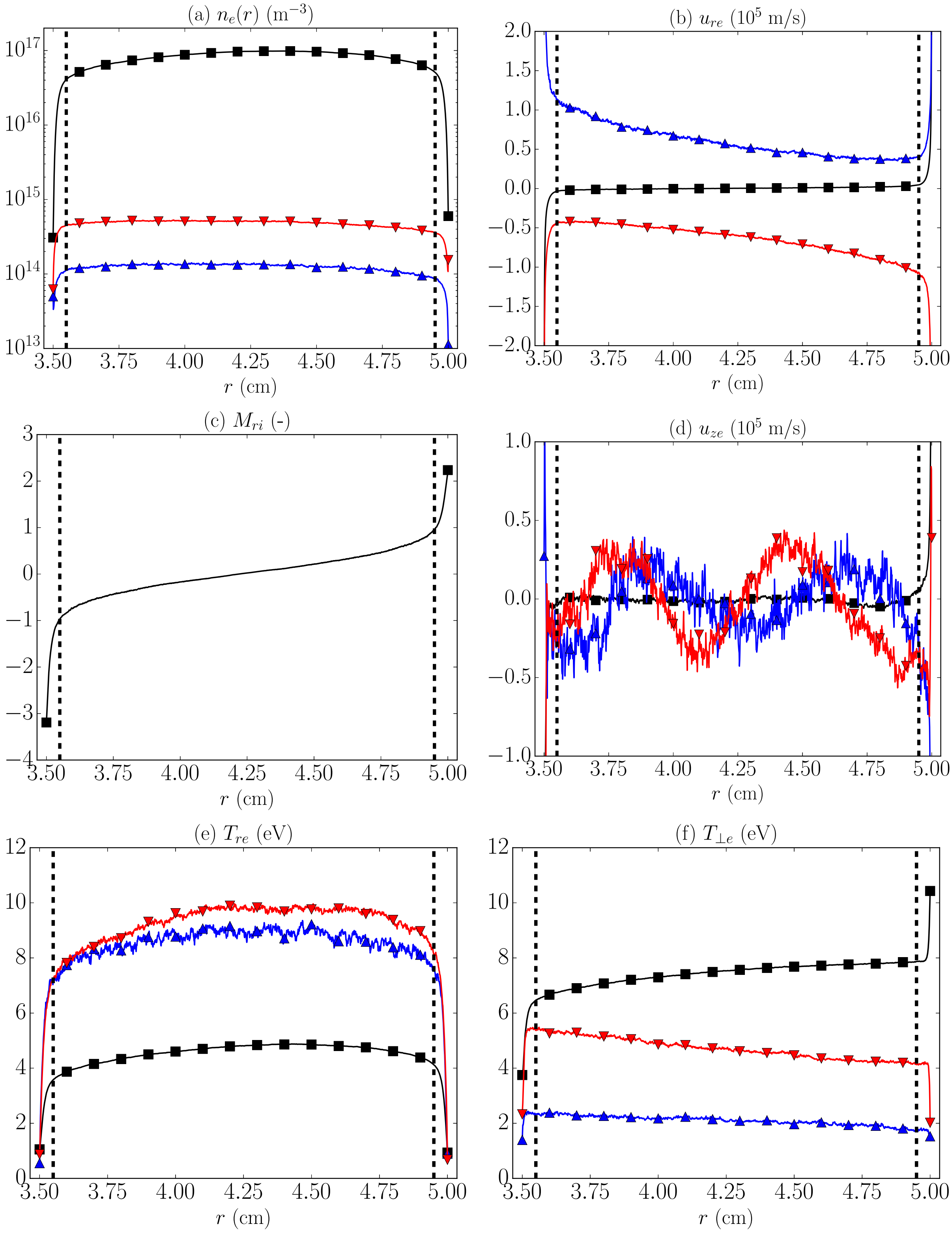

Figure 5.5: Steady-state radial profiles of macroscopic magnitudes for the different electron species and ions: (a) the electron particle density, (b) the electron radial velocity, (c) the ion radial Mach number, (d) the electron axial velocity, (e) the radial electron temperature, and (f) the perpendicular electron temperature. Black, blue and red lines with square, up and down triangles correspond to p, $s1$ and $s2$ electron populations, respectively. Dashed vertical lines mark the approximate sheath edges. Curves are computed using the EVW algorithm with the last $N_k = 2 \cdot 10^5$ time steps (equivalent to the last microsecond of simulation time).

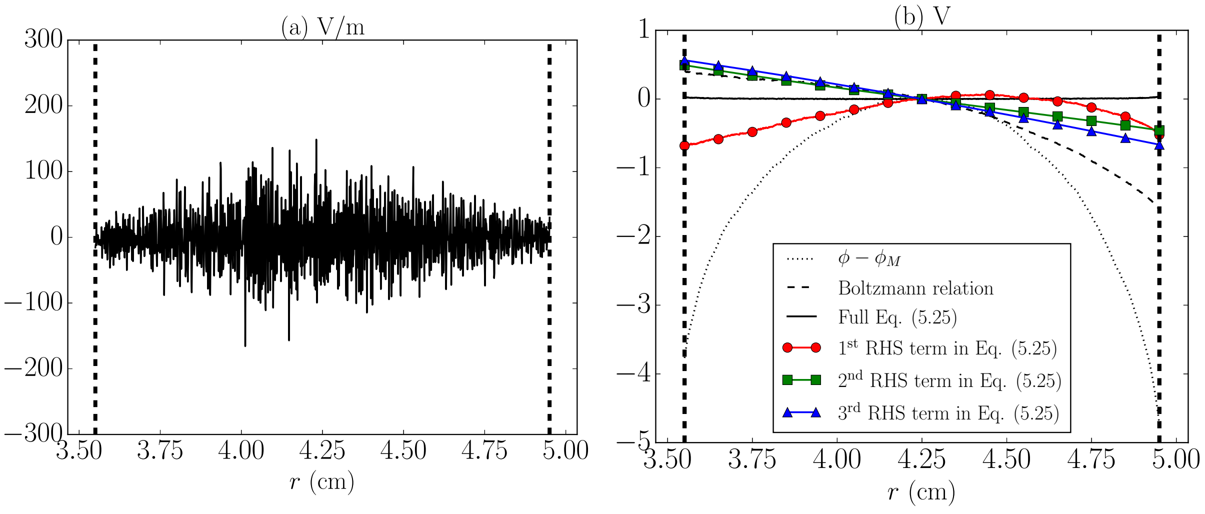

Figure 5.6: (a) Contribution of collisional and other minor effects to the local radial momentum balance of primary electrons, Eq. (5.24). (b) (dotted line) Electric potential profile relative to ϕ_M; (dashed line) Boltzmann relation, i.e. the left side of Eq. (5.25); (solid line) integrated radial momentum balance of primary electrons, i.e. the full Eq. (5.25); contributions to the right side of Eq. (5.25: red circles correspond to the radial temperature non-uniformity term; green squares represent the temperature anisotropy contribution; blue triangles stand for the centrifugal force. The macroscopic variables involved are computed through the EVW algorithm with the last $N_k = 2 \cdot 10^5$ time steps (equivalent to the last microsecond of simulation time).

for each wall. Here and in Tab. 5.2: subscripts 1 and 2 refer to each wall, and + and - to the direction of the radial velocity at the wall. Since the two wall materials are the same, the difference in the effective SEE yields is due to a difference in the mean impacting energy per particle, E_w. This energy is obtained dividing the net energy flux to a wall by the corresponding particle flux. Tab. 5.2 shows that $E_{wp,1} = 8.50$ eV and $E_{wp,2} = 16.16$ eV. In fact, these values are not far from twice the electron temperature, the mean impacting energy for a Maxwellian VDF.

Fig. 5.5 plots steady-state spatial profiles for the main macroscopic magnitudes. We focus the discussion here on the plasma bulk, since plasma magnitudes inside the steepened sheaths (such as the behavior of T_e) are generally not detailed in the conventional two-scale sheath analysis. Fig. 5.5(a) plots the density profiles of the different electron populations, confirming the much lower densities of secondary electrons. In addition, a large asymmetry between $s1$ and $s2$ population densities is observed. The lower $s1$-density is partially caused by the lower SEE yield from W_1.

Fig. 5.5(b) plots the macroscopic radial velocity u_r for the three electron populations. Primary electrons behave as usual with inward and outward fluxes from (around) the channel mid-line M. The velocity increase inside the sheaths is just the consequence of the decreasing density there. Indeed, the same behavior is observed in the radial velocity of ions, Fig. 5.5(c), where $M_{ri} = u_{ri}(T_e/m_i)^{-1/2}$ is the radial Mach number. Observe that the sheath edges were placed at the ion sonic points.

Back to Fig. 5.5(b), the $s1$-electrons present a net outwards radial velocity, indicating that their outwards flow is slightly larger than the inwards one, due to a larger recollection at W_2. The opposite situation happens to the $s2$-electrons. Notice that these radial velocities are just small drifts in the VDFs of the three populations: for instance, the energy corresponding to $u_r = 10^5$ ms^{-1} is ∼0.03 eV. The similar negative slope of du_r/dr for the $s1$ and $s2$ electrons is likely due to the net macroscopic effect of the magnetic mirror and the $\boldsymbol{E} \times \boldsymbol{B}$ contributions.

Fig. 5.5(d) plots the macroscopic axial velocity, u_z, of the three electron populations. These velocities are practically zero except for the oscillations shown in secondary electrons which correspond to the net axial residual of their gyromotion, which gives rise to the near-wall conductivity [97]. Although not shown here, ions present an average macroscopic velocity approximately equal to that assigned individually to their macroparticles when created. Very importantly, the simulations confirm that there are not secular effects on the axial flow of all populations and therefore there is no need to apply particle refreshing. (Nonetheless, in much longer simulations, collisional effects should yield a non-zero u_{ze}, of the order of $u_{\theta e}$ divided by the Hall parameter.)

Fig. 5.3(b) showed the mean temperatures of the three electron species. Now, Figs. 5.5(e) and 5.5(f), plot the radial (i.e. B-parallel) and perpendicular temperatures, unveiling a significant anisotropy. For the three populations, it is found $T_\theta \approx T_z \approx T_\perp$ and the anisotropy is the combined consequence of the electron magnetization and the depletion at the walls. Interestingly, and due to their very different dynamics, $T_r/T_\perp$ is lower than 1 for primary electrons and larger than 1 for secondary electrons. For instance, at point M one has $T_{rp,M}/T_{\perp p,M} \simeq 0.64$, $T_{rs1,M}/T_{\perp s1,M} \simeq 4.35$, and $T_{rs2,M}/T_{\perp s2,M} \simeq 2.08$. The temperature behavior of primary electrons is a direct consequence of the partial depletion of their radial VDF tail. The trend $T_r/T_\perp > 1$ for secondary electrons would be due to their preferential radial bouncing, further enhanced by the fact that when they collide strongly they are transferred to the primary population.

Because of the very low density of secondary electrons, the radial potential profile of Fig. 5.5(a), is shaped almost exclusively by the p-population. Indeed, the complete macroscopic radial equilibrium for the p-electrons reads

$$e\frac{\partial \phi}{\partial r} - T_{rp}\frac{\partial \ln n_p}{\partial r} - \frac{\partial T_{rp}}{\partial r} + \frac{T_{\perp p} - T_{rp}}{r} + \frac{m_e u_{\theta p}^2}{r} = F_r'. \tag{5.24}$$

The three first terms in the left side are well known. The fourth one, where $d\ln B/dr = -1/r$ has been applied, is the magnetic mirror, which in the macroscopic formulation requires *both* a parallel magnetic gradient and a temperature anisotropy. The fifth term is the radial centrifugal force, coming from the $\boldsymbol{E}\times\boldsymbol{B}$ drift. In the right side F_r', plotted in Fig. 5.6(a), groups the contributions of collisions and the convective term $m_e u_{re} \partial u_{re}/\partial r$. Since F_r' has been computed from the sum of all the terms in the left side, its large oscillations are due to inaccuracies when computing spatial derivatives from noisy PIC profiles. The two first terms of the left side are the dominant ones, with a typical value of $\mathcal{O}(1000$ Vm$^{-1})$. Therefore, we can conclude that F_r' and thus collisional and convection effects are marginal in the plasma response.

Neglecting F_r', the integration of Eq. (5.24) yields

$$\begin{aligned} e\phi - e\phi_M - T_{rpM}\ln\frac{n_p}{n_{pM}} &= \left[T_{rp} - T_{rpM} + \int_{r_M}^{r} dr\,(T_{rp} - T_{rpM})\,\frac{d\ln n_p}{dr}\right] + \\ &+ \int_{r_M}^{r} dr\frac{T_{rp} - T_{\perp p}}{r} - \int_{r_M}^{r} dr\frac{m_e u_{\theta p}^2}{r}. \end{aligned} \tag{5.25}$$

Here, the left side groups now the two terms of the isothermal Boltzmann relation, while the right side includes the effects of a non-uniform radial temperature, the magnetic mirror, and the centrifugal force. The different contributions are plotted in Fig. 5.6(b). This shows that: the whole radial equilibrium of Eq.(5.25) is satisfied excellently; the three contributions of the right side are of the same order (see symbols at the sheath edges); and the sum of these 3 contributions introduces a correction of up to 30% (relative to $e\phi - e\phi_M$) in the Boltzmann relation.

The potential fall in a sheath is closely related to the electron currents to and from the walls. In particular, the lower is the primary electron current because of its VDF tail depletion, the lower is the required potential fall to fulfill the zero electric current condition. Ahedo and de Pablo [119] treated this problem analytically assuming a functional form of the p-VDF which fits well with the present results. They modelled the partial depletion with a replenishment (via collisionality) parameter σ_t (not to be mistaken this symbol with a surface charge), which, in the end, measured the ratio between the actual potential fall and the one corresponding to a non-depleted Maxwellian population. For instance, for the inner wall W_1 it would be

$$\sigma_{t,1} = \frac{|j_{pW_1}|}{j_{ther,1}} \qquad \text{with} \qquad j_{ther,1} = en_{pQ_1} \exp\left(-e\frac{\phi_{W_1Q_1}}{T_{pQ_1}}\right)\sqrt{\frac{T_{pQ_1}}{2\pi m_e}}, \tag{5.26}$$

and a similar definition applies to the outer wall. In our simulation, the p-tail replenishment ratios are rather small, $\sigma_{t,1} \simeq 0.04$ and $\sigma_{t,2} \simeq 0.05$, which seems reasonable with the weak electron collisionality. If instead of the total temperature T_p, the radial temperature T_{rp} were used in the definition of j_{ther}, it would still be $\sigma_{t,1} \simeq 0.15$ and $\sigma_{t,2} \simeq 0.19$.

A final point to comment is that, in the present ionization-controlled model with no axial (i.e. external) injection of particles along the simulation, the mean steady-state electron temperature is totally intrinsic to the model and its parameters. Indeed, simulations started with different values of T_{e0} between 1 and 20 eV have led to the same final temperatures shown here. This final temperature comes out from the energy balance

$$P_{sinks} = P_{sources}, \qquad P_{sinks} \simeq P_{inel} + P_{wall,t}, \qquad P_{sources} \simeq P_{elec} + P_{wall,f}, \tag{5.27}$$

where: P_{inel} are the losses due to inelastic processes (ionization and excitation), $P_{wall,t}$ are the losses due to electron collection at the walls, $P_{wall,f}$ are the gains due to electron emission at the walls, and P_{elec} is the energy transmitted to electrons by the electric field. The values of these terms are in Tab. 5.2: $P_{wall,f}$ is negligible and P_{inel} and $P_{wall,t}$ are of the same order.

In the opposite case of an axially-controlled radial discharge, i.e. with $S_{axial,j} \gg S_{ioniz}$ in Eq. (5.1), the mean T_e would be dependent mainly on the temperature of the macro-electrons continuously injected through $S_{axial,j}$. Therefore, while the temperature anisotropy of the primary population and possibly the temperatures of the secondary populations are relevant results of a 1Dr model, the mean value of T_e is partially arbitrary. Indeed, in the complete HET discharge, T_e is determined basically by the axial dynamics, through the discharge voltage, the Joule heating, plus the ionization and wall losses.

5.5 Conclusions

The annular model and related PIC/MCC code of given radial section of the acceleration region of a HET has been built on a previous one by Taccogna [31]. The main numerical improvements and conclusions are the following. First, in an ionization-controlled discharge we cannot fix both the mean neutral density and the mean plasma density. Second, to fix the mean plasma density and adjust along the simulation the neutral density is a preferable method in terms of optimizing the PIC implementation. Third, the secular growth of ion axial energy and the subsequent refreshing of macro-ions has been avoided by canceling the ion axial acceleration. And fourth, a time-extended volumetric weighting algorithm is implemented, which improves very substantially the weighting of macroscopic magnitudes of the minor species (here the true-secondary electrons), while not affecting the major species (here the primary electrons and the ions).

On the physical side the main contributions are the following. First, because of the weak collisionality (dominated by elastic electron-neutral collisions), the VDF of primary electrons presents an important depletion of the high-radial-energy tails, leading to a radial-to-perpendicular temperature anisotropy ratio of about 2/3 in the simulation discussed here. Second, the true-secondary electrons are partially converted to primary electrons (after a strong collision) and partially recollected by the walls, in a proportion of about 60%-40%. The resulting density of the secondary electrons is very low, thus affecting little the shape of the electric potential profile. Besides, they keep a small radial drift velocity and a radial-to-perpendicular temperature ratio larger than one. Third, the replenishment ratio of the high radial-energy tail of primary electrons is small, which leads to a reduced sheath potential fall. Fourth, the electric potential profile in the (quasineutral) plasma bulk comes out from a radial momentum equilibrium which goes beyond the classical Boltzmann relation and incorporates non-negligible contributions of (*i*) the radial temperature gradients, (*ii*) the magnetic mirror, and (*iii*) the centrifugal force. This macroscopic magnetic mirror effect combines the temperature anisotropy and the cylindrical divergence of the magnetic field. The relevance of the centrifugal force stands out since it is disregarded in macroscopic models invoking the zero electron-inertia limit, but this assumption does not take into account the subtle detail that $m_e u_{\theta e}^2/r$ is in a HET plasma much larger than $m_e u_{re} \partial u_{re}/\partial r$. And fifth, the above cylindrical effects introduce a significant asymmetry in (*i*) the plasma profiles with respect to the mid-radius and (*ii*) the magnitudes related to plasma-wall interaction, such as the collected currents and the mean impact energies, and thus the resulting SEE yields.

While the present work has been devoted to the improvements of the 1Dr code and the capabilities it has to analyze the kinetic and macroscopic plasma responses, further work will deal with a parametric investigation on the trends and features found in the simulation analyzed here. This should yield scaling laws among input and output parameters, which will provide a solid characterization of the 1Dr discharge. Besides, some of these laws could be implemented as auxiliary models in HET hybrid codes, which use a macroscopic formulation of the electron population; one example is the replenishment ratio of the VDF for sheath calculations. A particularly interesting parametric investigation is the increase of the axial electric field in order to reach electron azimuthal velocities above the electron thermal velocity. This would allow to analyze the reported transition from a stable steady-state discharge to an instability-saturated one. A second prominent investigation is the plasma response in the presence of a non-fully-radial magnetic field, which is expected to largely modify the tails of the electron VDFs and the temperature anisotropy.

Chapter 6

A HET discharge 1D radial particle model: a parametric study

Chapter 5 presented the capabilities of an improved 1Dr PIC code for simulating the plasma physics in a HET discharge. Using said simulator, this Chapter focuses on a further investigation on the discharge exploring different scenarios of particular interest in order to both further validate the 1D radial particle model and get a deeper insight on the physics of the response. The contents of this Chapter are based on a conference paper [63], and have been submitted for their publication to the peer-reviewed journal Journal of Physics D: Applied Physics [64].

6.1 Introduction

A new 1D radial particle-in-cell model of the plasma discharge at an axial section within the acceleration region of an annular Hall effect thruster (HET) has been developed [35]. Chapter 5 showed a single simulation case for a relatively low value of the axial electric field, and with a fully radial magnetic field. The main goals were analyzing the combined effects of SEE and cylindrical asymmetry on (i) the velocity distribution function (VDF) of the different electron populations, and (ii) the macroscopic steady-state plasma response. The most valuable results of this work were:

- The radial profiles in both the plasma bulk and sheaths are asymmetric due to a combination of the geometric expansion, the magnetic mirror effect, and the centrifugal force (this last one emanating from the $\boldsymbol{E} \times \boldsymbol{B}$ drift).
- The collected electric currents, the mean impact energy, and the wall and sheath potentials present significant differences at the inner and outer walls;
- The two secondary electron populations are partially recollected by the walls and partially converted into primary electrons.
- The perpendicular and parallel temperatures to the magnetic field are different, and their ratios are different for primary and secondary electrons.
- The temperature anisotropy and non-uniformity, and the centrifugal force modify the classical Boltzmann relation on electrons along the magnetic lines.

Using the PIC code presented in Chapter 5, a further analysis of the plasma discharge structure in several scenarios of interest is carried out in this Chapter. In particular, different field values (keeping constant the ratio E_z/B_r), wall temperature and secondary electron emission are considered. Besides, a plane case (i.e. at larger radius) is explored. The present study allows for a further validation of the model and provides a deeper insight on the physics of the response.

6.2 Influence of relevant parameters

The stationary plasma discharge obtained for the 5 cases with main input parameters listed on Tab. 6.1 is analyzed in this section. The reference case, named here as case 1, corresponds to that analyzed in detail on Chapter 5. The changes from the case 1 defining the rest of the cases considered are indicated on Tab. 6.1. Regarding the SEE, the contrubution of the elastically and inelastically backscattered electrons is added only in case 3, so that the total SEE yield may be expressed as

$$\delta_{SEE}(E) = \delta_{BS}(E) + \delta_{TS}(E) \tag{6.1}$$

where $\delta_{BS}(E)$ and $\delta_{TS}(E)$ stand for the total (i.e. ellastic and inelastic) backscattering yield and the true secondary yield, respectively, with E the impacting electron energy. In all cases, the SEE follows the probabilistic model of Ref. [177], already implemented in Ref. [31].

Tab. 6.2 summarizes relevant data of the discharge for every case simulated. Average values over 1μs of simulation time are considered. Figs. 6.1-6.3 show the radial profiles of the main plasma macroscopic magnitudes obtained through the EVW algorithm with $N_k = 2 \cdot 10^5$ time steps (1 μs of simulation time). For the sake of clarity, the offset in the radial coordinate of the case 5 is eliminated for plotting purposes. The vertical dashed lines in Figs. 6.1-6.3 represent approximately the edges of the Debye sheaths, which, considering the data from the knees of the electric potential profile, the relative charge density and the radial ion Mach number, are located at 0.5 mm from the walls. The definition of 'sheath edges' in the present one-scale model is just meant for discussion purposes, since plasma response is known to change sharply when entering the thin Debye sheaths. The discussion here is focused on the plasma bulk.

Type	**Description, symbol and units**	**Case 1**	**Changes from case 1**
Populations settings	Number of elementary particles per macroparticle, W (-)	$3 \cdot 10^9$	-
	Initial average plasma density, n_{e0} (10^{17}m^{-3})	0.8	-
	Initial number of ions and electrons*, N_{p0} (-)	106814	-
	Initial electron temperature, T_{e0} (eV)	10	-
	Initial ion temperature, T_{i0} (eV)	1	-
	Ion axial mean velocity, u_{zi} (km/s)	10	-
	Initial background neutral density, n_{n0} (10^{17} m^{-3})	40	-
	Neutral temperature, T_n (K)	700	-
$\boldsymbol{E}$, $\boldsymbol{B}$ fields	Electric field axial component, E_z (V/cm)	100	Case 2: 200
	Magnetic field radial component at inner radius, B_{r_1} (G)	150	Case 2: 300
Simulation parameters	Backscattering SEE yield, $\delta_{BS}(E)$ (-)	OFF	Case 3: ON
	True secondary SEE yield, $\delta_{TS}(E)$ (-)	ON	-
	Walls temperature, T_{eW} (eV)	2	Case 4: 0.2
	Inner radius, r_1 (cm)	3.5	Case 5: 103.5
	Outer radius, r_2 (cm)	5.0	Case 5: 105.0
	Number of nodes, N_r (-)	1500	-
	Grid spacing*, Δr (μm)	10	-
	Time step, Δt, (ps)	5	-
Physical parameters	Debye length*, λ_D (μm)	83.1	-
	Electron Larmor radius*, r_l (μm)	802.0	Case 2: 401.0
	Inverse of plasma frequency*, $1/\omega_{pe}$ (ps)	62.7	-
	Inverse of electron cyclotron frequency*, $1/\omega_{ce}$, (ps)	379.1	Case 2: 189.5

Table 6.1: Main input parameters including initial population settings, externally applied fields and grid definition for the case 1 (reference case of Ref. [35]). The changes with respect to the case 1 defining the rest of the cases considered are indicated in the last column. The magnitudes marked with an asterisk (*) are not input parameters of the model, but are derived from the other parameters instead. The variables named as physical parameters are estimated from the other input values given at initial conditions.

The electric potential radial profiles are depicted on Fig. 6.1(a). Points W_1, W_2, Q_1, Q_2, and M correspond to walls, sheath edges, and channel mid radius, respectively. The electric potential values at those points is listed in Tab. 6.2. As already found on Ref. [35], the magnetic mirror effect and the centrifugal force in the cylindrical geometry lead to asymmetric radial profiles in the cases 1 to 4. The potential drop $\Delta\phi_{W_1W_2} > 0$ and the change on the $\boldsymbol{E} \times \boldsymbol{B}$ drift due to the radially varying magnetic field facilitate that

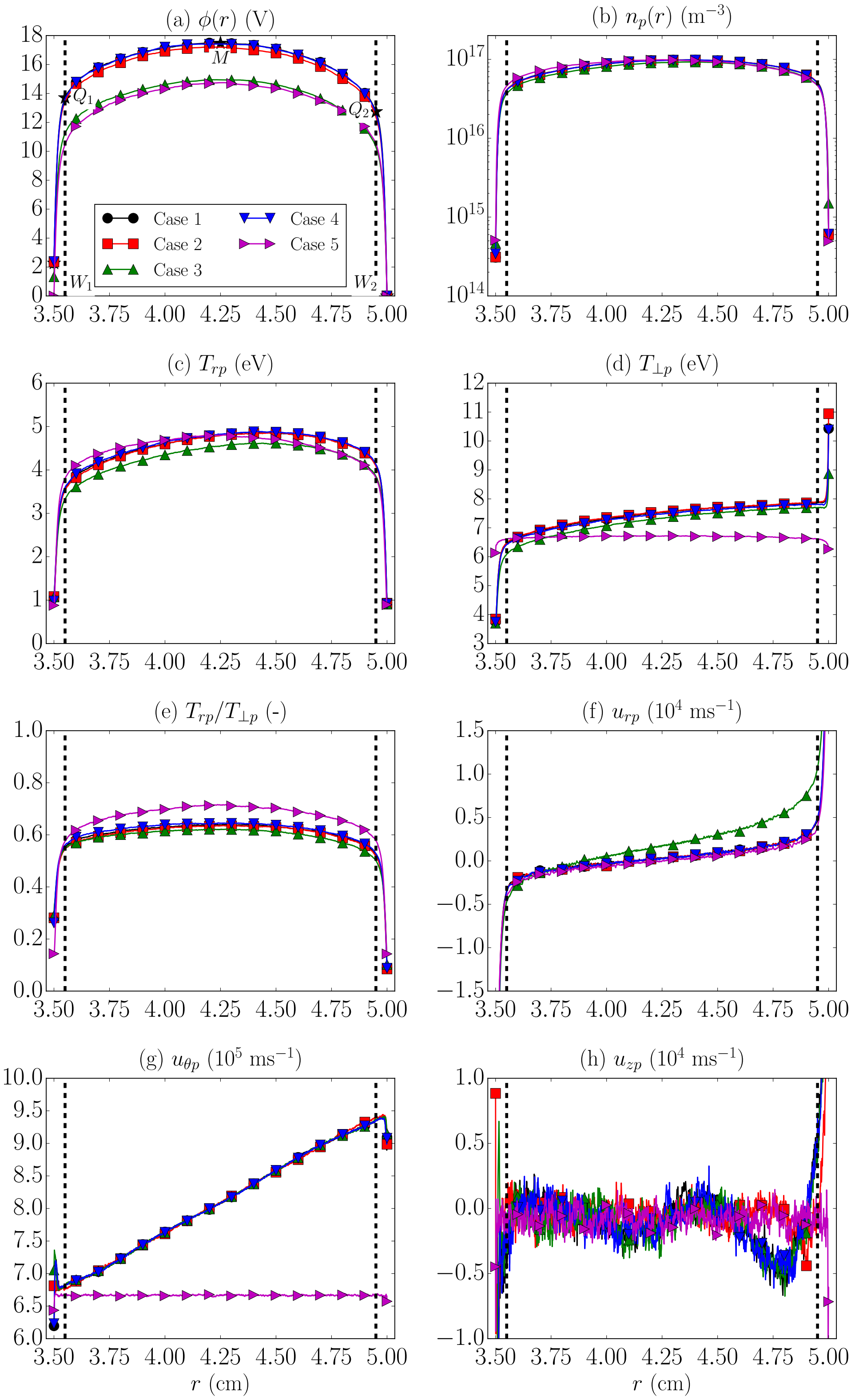

Figure 6.1: Steady-state radial profiles of different macroscopic magnitudes for primary electrons for the cases considered: (a) electric potential; (b) electron density; (c-e) electron parallel (radial) and perpendicular temperatures, and their ratio, respectively; (f-h) radial, azimuthal and axial electron mean velocities, respectively. Black stars on (a) indicates the points at the walls, sheath edges and channel mid radius. The weighted magnitudes are computed through the EVW algorithm with $N_k = 2 \cdot 10^5$ time steps (equivalent to 1μs of simulation time).

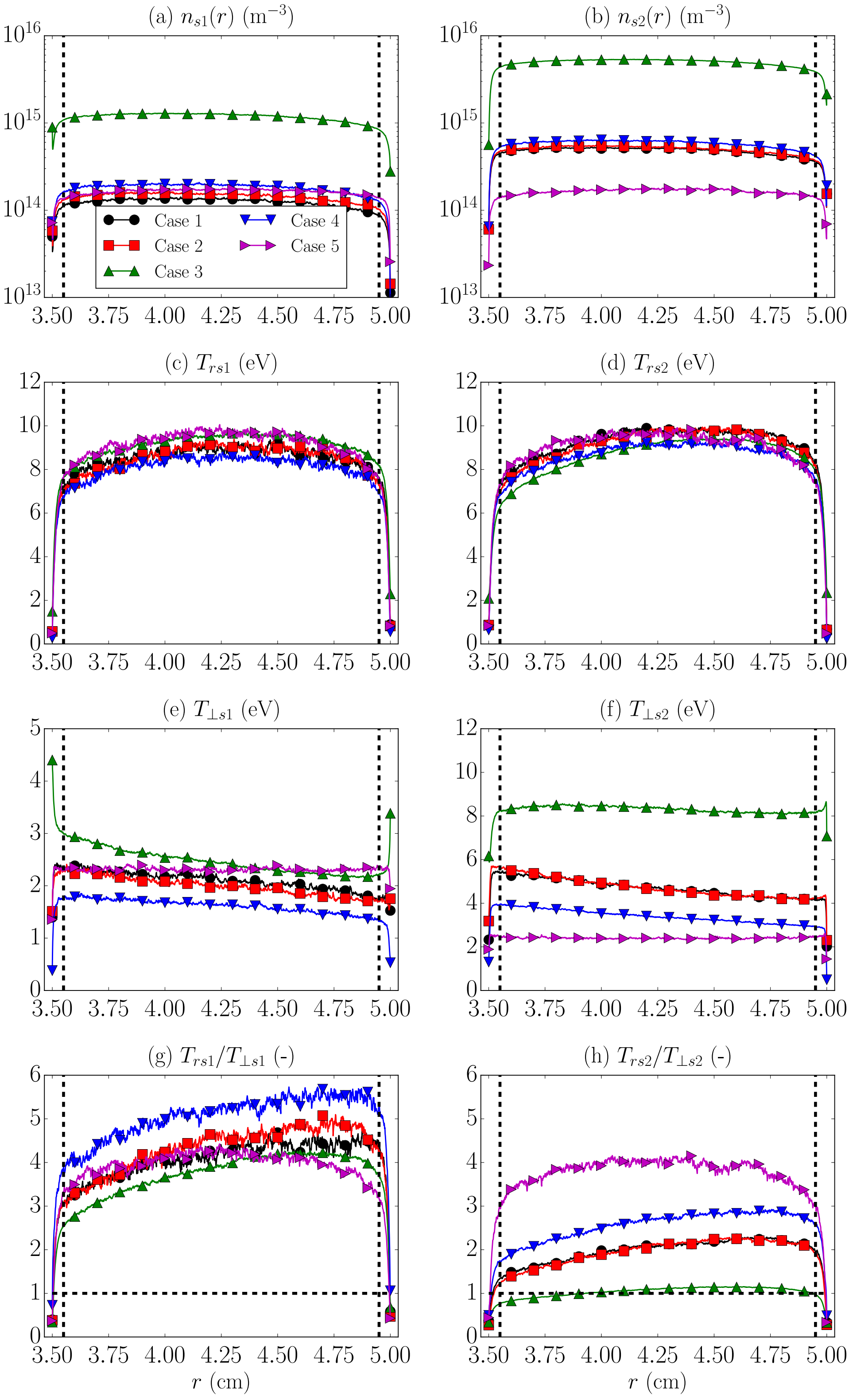

Figure 6.2: Steady-state radial profiles of different macroscopic magnitudes for secondary electrons for the cases considered: (a-b) electron density; (c-d) radial temperature; (e-f) perpendicular temperature; (g-h) temperature ratios, for $s1$ and $s2$ electron populations, respectively. The weighted magnitudes are computed through the EVW algorithm with $N_k = 2 \cdot 10^5$ time steps (equivalent to 1μs of simulation time).

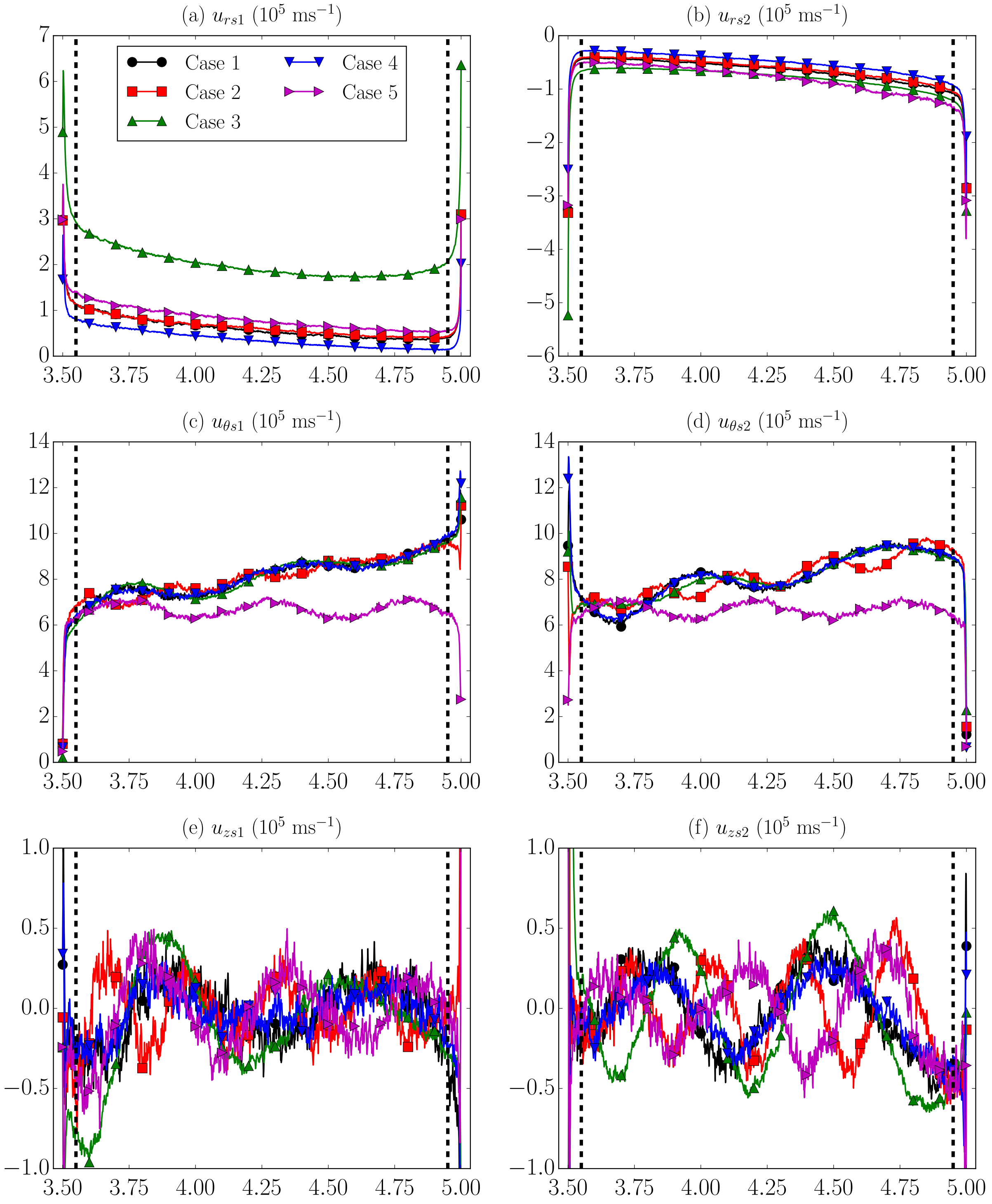

Figure 6.3: Steady-state radial profiles of macroscopic velocity components for secondary electrons for the cases considered: (a-b) radial velocity; (c-d) azimuthal velocity; (e-f) axial velocity, for $s1$ and $s2$ electron populations, respectively. The weighted magnitudes are computed through the EVW algorithm with $N_k = 2 \cdot 10^5$ time steps (equivalent to 1μs of simulation time).

Type and units	Description and symbol	Case 1	Case 2	Case 3	Case 4	Case 5
Electric potentials (V)	At the mid radius M, ϕ_M	17.47	17.19	14.94	17.41	14.75
	At the inner sheath edge Q_1, ϕ_{Q_1}	13.70	13.44	11.24	13.62	10.47
	At the outer sheath edge Q_2, ϕ_{Q_2}	12.74	12.38	10.30	12.61	10.53
	At the inner wall W_1, ϕ_{W_1}	2.27	2.35	1.33	2.39	0.00
	At the outer wall W_2, ϕ_{W_2}	0.00	0.00	0.00	0.00	0.00
Current densities (A/m^2)	p to the inner wall, $\lvert j_{p,1-}\rvert$	12.80	13.19	20.99	13.62	17.67
	$s1$ to the inner wall, $\lvert j_{s1,1-}\rvert$	0.17	0.21	1.81	0.29	0.20
	$s1$ from the inner wall, $\lvert j_{s1,1+}\rvert$	2.36	2.75	54.08	2.51	3.35
	$s2$ to the inner wall, $\lvert j_{s2,1-}\rvert$	2.96	2.93	44.90	2.26	1.07
	p to the outer wall, $\lvert j_{p,2+}\rvert$	23.97	23.71	67.86	23.98	17.54
	$s1$ to the outer wall, $\lvert j_{s1,2+}\rvert$	0.48	0.64	26.95	0.22	1.10
	$s2$ to the outer wall, $\lvert j_{s2,2+}\rvert$	0.81	0.71	29.17	0.54	0.16
	$s2$ from the outer wall, $\lvert j_{s2,2-}\rvert$	7.23	7.17	106.31	6.94	3.26
Mean impact energies per elementary particle (eV)	e at the inner wall, $E_{we,1}$	8.10	8.72	12.36	8.04	9.36
	p at the inner wall, $E_{wp,1}$	8.50	9.01	8.49	6.87	9.72
	$s1$ at the inner wall, $E_{ws1,1}$	4.06	4.08	3.78	3.86	3.39
	$s2$ at the inner wall, $E_{ws2,1}$	6.59	7.76	14.52	7.25	4.46
	e at the outer wall, $E_{e,2}$	15.75	15.99	14.99	15.74	9.29
	p at the outer wall, $E_{wp,2}$	16.16	16.36	13.90	16.07	9.63
	$s1$ at the outer wall, $E_{ws1,2}$	6.24	8.11	13.90	5.55	4.74
	$s2$ at the outer wall, $E_{ws2,2}$	9.34	10.94	18.54	5.13	3.77
SEE yields (-)	Backscattering at the inner wall, $\delta_{BS,1}$	0.00	0.00	0.57	0.00	0.00
	True secondary at the inner wall, $\delta_{TS,1}$	0.15	0.17	0.23	0.16	0.18
	Backscattering at the outer wall, $\delta_{BS,2}$	0.00	0.00	0.58	0.00	0.00
	True secondary at the outer wall, $\delta_{TS,2}$	0.29	0.29	0.27	0.28	0.17
Conversion to p and wall collection fractions (%)	$s1$ conversion to p	63.2	59.1	25.4	76.2	61.15
	$s1$ collection at the inner wall	7.5	7.8	3.4	11.5	6.07
	$s1$ collection at the outer wall	29.3	33.1	71.2	12.3	32.78
	$s2$ conversion to p	60.1	61.4	43.0	69.4	62.12
	$s2$ collection at the inner wall	28.7	28.6	29.6	22.8	32.97
	$s2$ collection at the outer wall	11.2	10.0	27.0	7.8	4.91
Electron temperatures at M (eV)	p radial, $T_{rp,M}$	4.81	4.80	4.55	4.83	4.80
	p perpendicular, $T_{\perp p,M}$	7.53	7.55	7.33	7.48	6.72
	$s1$ radial, $T_{rs1,M}$	8.97	9.07	9.55	8.45	9.80
	$s1$ perpendicular, $T_{\perp s1,M}$	2.06	2.01	2.45	1.64	2.26
	$s2$ radial, $T_{rs2,M}$	9.77	9.83	9.23	9.13	9.56
	$s2$ perpendicular, $T_{\perp s2,M}$	4.70	4.59	8.40	3.36	2.42

Table 6.2: Main parameters characterizing the steady-state discharge for the different cases considered. Time-averaged values over 1μs of simulation time are considered.

electrons emitted from the wall W_2 be recollected at the wall W_1. On the contrary, the magnetic mirror effect opposes the electron collection at W_1. This asymmetry becomes also evident in the collected electron currents at the walls, in the mean wall impact energy per particle and thus in the SEE yields. All these data is detailed in Tab. 6.2 for each case considered. As expected, the asymmetry vanishes in the planar case (case 5), in which the effect of the geometric cylindrical expansion (i.e. terms $\sim 1/r$) tends to zero. This case will be further analyzed below. Tab. 6.2 also provides the fractions of secondary electrons recollected at each wall and transferred to the primary population through collisional processes. A significant secondary electron recollection at walls is found due to the low collisionallity regime. For all cases Coulomb collisions are negligible compared to electron-neutral collisions, but even the elastic e-n collision frequency, ~ 3.7MHz, is low compared with the transit frequency, ~ 62MHz. The SEE yields and the amounts of wall-recollection and thermalization determine the density and other macroscopic properties of secondary electrons.

Figs. 6.1(b), 6.2(a) and 6.2(b) plot the density profiles for p, $s1$ and $s2$ electrons, respectively, confirming the much lower density of the secondary electrons and thus their minor role in shaping the electric potential. The lower $s1$-density is partially caused by the lower SEE yield at the inner wall in all cases.

Figs. 6.1(c) and 6.1(d) show the profiles of the radial (i.e. B-parallel) and the perpendicular temperature, respectively, for the primary electrons population, while their ratio is plotted in Fig. 6.1(e). Likewise, the profiles of the parallel and the perpendicular temperatures and their ratio are depicted in Figs. 6.2(c), 6.2(e) and 6.2(g) for the $s1$-electrons, and in Figs. 6.2(d), 6.2(f) and 6.2(h) for the $s2$-electrons, respectively. For the three populations, it is found $T_\theta \approx T_z \approx T_\perp$ and the anisotropy is the combined consequence of the electron magnetization and depletion at walls. The radial and perpendicular temperature values at point M are listed in Tab. 6.2 for each electron population. The ratio $T_r/T_\perp$ is lower than 1 for primary electrons and larger than 1 for secondary electrons in all cases considered but the case 3 for $s2$-electrons. This fact will be commented below. The temperature behavior of primary electrons is a direct consequence of the partial depletion of the radial VDF tail [35]. In general, p-electrons bounce radially between the sheaths several times before completing an azimuthal turn. The collisions (mainly with the neutral gas) introduce a larger dispersion (i.e. temperature) on the B-perpendicular direction and contribute to the replenishment of the primary electrons VDF tails. In contrast, the secondary electrons emitted from the walls are radially accelerated by the sheaths and act like two opposite radial beams before being quickly collected at the walls. The trend $T_r/T_\perp > 1$ is further enhanced by the fact that when they collide strongly (i.e electron-neutral or large angle Coulomb collisions) they are transferred to the primary population.

The macroscopic radial velocity profiles for the p, $s1$ and $s2$ electron populations are depicted in Figs. 6.1(f), 6.3(a) and 6.3(b), respectively. Primary electrons behave as usual with fluxes from the channel mid-point M to the walls. The velocity increase inside the sheaths is just the consequence of the decreasing density there. $s1$-electrons present a net outwards radial velocity, indicating that their outwards flow is slightly larger than the inwards one, due to a larger recollection at W_2. The opposite situation happens to $s2$-electrons.

The macroscopic azimuthal velocity of the three electron populations satisfy the $\boldsymbol{E}\times\boldsymbol{B}$ drift in all cases. The corresponding radial profiles for the p, $s1$ and $s2$ electrons are plotted in Figs. 6.1(g), 6.3(c) and 6.3(d), respectively. As it was already shown in Ref. [35], this result is particularly important to validate the simulation of the secondary electrons and reveals the excellent performance of the EVW algorithm in the computation of the weighted magnitudes for the low-populated species.

Figs. 6.1(h), 6.3(e) and 6.3(f) show the profiles of the macroscopic axial velocity for the p, $s1$ and $s2$ populations, respectively. These velocities are close to zero except for the oscillations shown in secondary electrons which correspond to the well known near-wall conductivity (NWC) phenomenon [97]. As proved in Ref. [35], the simulations confirm that there are not secular effects on the axial flow of all populations and therefore there is no need of performing particle refreshing.

After describing the general structure of the plasma discharge in all cases considered, in the following some particularities of the cases 2 to 5 are worth to be commented in comparison to the reference case 1.

Regarding the case 2, when both the axial electric field and the radial magnetic field are doubled, the number of peaks in the secondary electrons azimuthal and axial macroscopic velocity profiles is doubled (see Figs. 6.3(d) and 6.3(f) for the $s2$-electrons, for example) while the rest of plasma properties (including the electric potential and the electron temperatures) remain the same, as expected.

In the case 3 we have considerably larger total SEE yields: ~ 0.8 and ~ 0.85 at the inner and outer walls, respectively. As listed in Tab. 6.2, $\delta_{BS} > \delta_{TS}$, which is consistent with the SEE analysis performed in Ref. [31] for the impacting energy values obtained in this case. As a result, the sheaths potential drops decrease by a value of ~ 1.5 eV and of ~ 2.5 eV at the inner and outer walls, respectively, thus facilitating the electron collection at the walls both for primary and secondary electrons. Consequently, larger electron current densities to the walls are obtained and, since the collisional frequencies remain approximately the same, the secondary electrons wall collection fractions increase (see values in Tab. 6.2). This could explain the slightly lower primary electron temperatures obtained [see Figs. 6.1(c) and 6.1(d)], and the fact that the ratio $T_r/T_\perp$ becomes smaller than 1 for $s2$-electrons in the region from $r \approx 3.9$ cm to the inner wall [see Fig. 6.2(h)].

In the case 4 secondary electrons are emitted with 10 times less energy due to the lower wall temperature. As expected, they exhibit lower temperatures and lower absolute values of the macroscopic radial velocity. The influence of the wall temperature in the rest of plasma radial profiles is negligible. Due to their lower energy, secondary electrons spend a longer time bouncing radially between the sheaths where an eventual collision may turn them into the primary population. This explains the significantly larger thermalization fractions of both the $s1$ and $s2$ electrons (see Tab. 6.2).

Finally, special attention must be paid to the case 5. As mentioned above, the typical geometrical effects in cylindrical coordinates (i.e. terms $\sim 1/r$) become negligible when the simulation domain is displaced towards larger radii (e.g. 10^3 m displacement in the case 5). Therefore, the case 5 corresponds to a planar simulation in which the applied radial magnetic field is approximately constant (from Eq. (5.6): $B_{r_2}/B_{r_1} = r_1/r_2 = 9.9985 \cdot 10^{-1} \sim 1$). Hence, the $\boldsymbol{E} \times \boldsymbol{B}$ drift is approximately constant as well, and the magnetic mirror effect becomes negligible along the simulation domain. As a result, the asymmetries in the radial profiles and in the different magnitudes at the walls vanish. Interestingly, the different electron populations exhibit a similar temperature anisotropy in comparison to the other cases.

Recalling the macroscopic radial momentum equilibrium for p electrons of Eq. (5.25), neglecting collisions the left side groups the terms of the isothermal Boltzmann relation, while the right side includes the effects of a non-uniform radial temperature, the magnetic mirror (which in turn is a combination of temperature anisotropy and cylindrical expansion) and the centrifugal force. The results shown in Ref. [35] for the case 1 are here compared to those of the case 5 in Fig. (6.4). The whole radial equilibrium of Eq. (5.25) is excellently satisfied in both cases confirming the marginal role of the collisional processes and other convection effects. In the case 1, the three terms of the right side of Eq. (5.25) are of the same order and the sum of these 3 contributions introduces a correction of up to 30% (relative to $e\phi - e\phi_M$) in the Boltzmann relation. In the case 5 however, the terms $\sim 1/r$ vanish so that the correction above is reduced approximately to 15% and is mostly due to the non-uniform radial temperature.

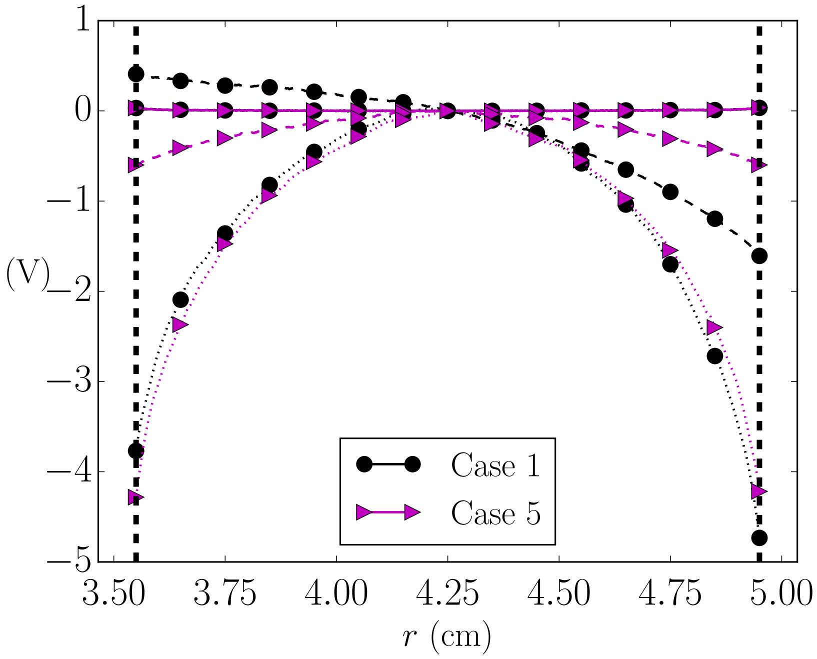

Figure 6.4: Fulfilment of the integrated radial momentum balance of primary electrons in Eq. (5.25) (solid lines); Boltzmann relation (dashed lines); electric potential profile relative to ϕ_M (dotted lines). Dashed vertical lines mark approximate sheath edges location. The macroscopic variables involved are computed through the EVW algorithm with $N_k = 2 \cdot 10^5$ time steps (equivalent to 1 μs of simulation time).

6.3 Conclusions

This work advances in the previous investigation carried out in Ref. [35] simulating a steady HET plasma discharge in different scenarios and analyzing the effect of different parameters in order to get a further insight of the discharge structure. The annular model and related PIC/MCC code of given axial section of the acceleration region of a HET was built on a previous one by Taccogna [31]. Important improvements have been recently added [35]. The main concluisions are the following. The case 2 allows the further code validation specially for what concerns the simulation of the dynamics of the secondary electron populations: the number of turns along the radial coordinate doubles when both the electric and the magnetic field are doubled while keeping the same electron temperature. The case 3 explores the influence of a complete SEE including backscattered electrons. The total SEE yields are found to be significantly larger with a predominance of the backscattering process. The enhanced SEE reduces the sheath potential drops, which facilitates the electron wall collection. This could explain the primary electron population temperature decrease in the bulk plasma. The influence of the wall temperature for the SEE has a negligible effect on the structure of the plasma discharge, as illustrated by the case 4. Finally, as expected, the cylindrical effects inducing asymmetries in the macroscopic profiles and in the different plasma magnitudes at the inner and outer walls vanish in the planar case 5. However, the electron temperature anisotropy induced by the magnetic field and the wall losses in the low collisionality regime follows the same trend as in the reference case 1. From the analysis of the radial momentum equilibrium for the primary electron population, a smaller deviation from the Boltzmann relation is found in this case since the influence of the magnetic mirror effect (which is a combination of temperature anisotropy and cylindrical divergence) and the centrifugal force tends to zero as $1/r$.

Further work will focus on the effect of a higher axial electric field in the reported transition from a stationary solution to an instability-saturated one. In addition, a non-purely radial magnetic field should change substantially the plasma discharge structure and thus have important consequences on the electron VDFs.

Chapter 7

Conclusions

This final Chapter summarizes the main contributions of this Thesis and proposes a number of activities and relevant research lines for future work.

7.1 Main Thesis contributions

The major contributions of this Thesis may be divided into two complementary groups. The former refers to (*i*) the development and testing of a new 2D axisymmetric PIC model for heavy species (i.e. ions and neutrals), (*ii*) its integration with an improved electron-fluid model for HET discharges, thus establishing the basis of HYPHEN, the new versatile hybrid PIC-fluid multi-thruster simulation platform under development by the EP2 research group at UC3M, and (*iii*) the application of HYPHEN to the simulation of different simulation scenarios of interest, including HET discharges and plasma plumes. On the other hand, the latter corresponds to a new improved version of a 1D radial PIC model for the simulation of a HET discharge originally developed by Taccogna [30–32], with the main goal of analyzing the radial dynamics of both the primary and secondary electron populations obtaining valuable information from their respective VDFs, which will enable a future improvement of the plasma-wall interaction models implemented in HYPHEN.

Regarding HYPHEN, its modular architecture makes it potentially extensible to the simulation of different plasma discharge scenarios, including HPT, ECRA or HEMPT, as well as HET and 2D axisymmetric plasma thruster plumes. One of the main contributions of this Thesis corresponds to the development and testing of its versatile PIC module, which is applicable to all simulation scenarios above, and includes up-to-date optimized algorithms for the heavy species treatment. The main modeling novelties on the PIC module, oriented toward the improvement of the heavy species PIC-related statistics and the extension of the code capabilities, are:

- The subdivision of the different ion and neutral species into different populations (or particle lists) based on their atomic mass, charge or energy content. This strategy allows for an independent treatment and monitoring of heavy species featuring very different dynamics (such as those coming from a CEX collision), thus facilitating its population control and reducing the numerical noise in the PIC related statistics.

- The development of a new versatile PIC mesh generator providing *ad hoc* structured non-uniform meshes of typical simulation domains of interest, including HETs, HPTs and ECRAs. It enables the simulation of the symmetry axis in HET-like, HPT-like and cylindrical domains, producing optimized meshes with exponential node distribution and reduced cell deformation, thus improving PIC derived statistics while limiting the computational cost. Moreover, it supports the inclusion of active inner surfaces in the simulation domain.

- The use of the 3D Cartesian leap-frog algorithm implemented in EP2PLUS [52] for integrating the macroparticles trajectory, which avoids the singularity problem at $r = 0$ of a 2D cylindrical particle mover [36].

- The development of an *ad hoc* particle crossing check algorithm which enables the simulation of active inner surfaces in the simulation domain, which can inject a propellant mass flow with given properties into the domain, recombine collected ions into neutrals reinjected into the simulation domain, or reflect neutrals impinging on them.

- The extension of the neutral-wall interaction algorithm for supporting mixed specular-diffuse neutral wall reflections through a constant specified probability of neutral-wall specular reflection.

- The incorporation of a new algorithm for the heavy species CEX collisions, which presents important improvements with respect to that of previous legacy codes such as HPHall-2 [45], and which has been developed in parallel with that of EP2PLUS [52]. Taking advantage of the heavy species subdivision into dedicated computational lists, the new algorithm allows for a more accurate simulation of the CEX collisions effects on the heavy species macroscopic magnitudes not only in the thruster chamber, but also in its near plume. Moreover, it extends the code capabilities enabling HYPHEN to simulate plasma plumes, in which CEX collisions are essential for determining the backscattering ion flux impinging sensitive S/C surfaces [85, 86].

- The development of a dedicated population control algorithm which, acting through all those processes generating new macroparticles in the domain (i.e. injection, collisions or wall recombination), maintains the number of macroparticles per cell of each simulated particle population within a specified range while limiting both the macroparticle weights dispersion and the computational time (when compared to particle resampling or merging/splitting approaches [133, 134]).

Still in the context of HYPHEN, for what concerns NOMADS, the electron-fluid module for HET discharges originally developed by Pérez-Grande [60], an improved version for the isotropic electron pressure case has been presented. The following improvements have been implemented in the frame of this Thesis:

- A preliminary treatment of electron inertial effects through an electron drift velocity limiter.

- The incorporation to the electron internal energy equation of the equivalent Joule heating term corresponding to the anomalous electron transport, according to the collisional version of turbulent effects.

- The improved treatment of the volumetric cathode source term in the electron conservation equations, which eliminates unphisical effects present in the original version of the code when changing the location of the MFAM cell corresponding to the volumetric cathode in the simulation domain.

With the purpose of validating and showing its capabilities, in this Thesis HYPHEN has been applied to the simulation of three different scenarios of interest. First, the simulation of a typical plasma plume expansion scenario based on an ion thruster has been considered to compare and benchmark HYPHEN against EP2PLUS. The non-trivial difficulties in the particle modeling inherent to the 2D cylindrical geometry have been satisfactorily overcome, and an excellent agreement has been found between the two codes, which are both capable of reproducing, with an acceptable noise level, the properties of heavy particle populations with densities differing by several orders of magnitude (i.e. the injected and CEX ions populations). It has been found that the optimal population control approach depends on the dynamics of the simulated macroparticle population, and it becomes essential to limit the noise level at the symmetry axis. As expected, the simulation of an axisymmetric plasma plume expansion into vacuum greatly benefits from a 2D formulation, which allows for a significant reduction of the computational time (a factor of 10) while keeping a similar PIC statistics noise level.

Second, the simulation of a simple scenario consisting of an unmagnetized plasma discharge in a surface-dominated cylindrical channel with isothermal electrons has permitted to further assess the performance of the HYPHEN hybrid code and to show the effect of the neutral-wall interaction on the plasma discharge considering the limit cases corresponding to pure diffuse and pure specular neutral-wall reflection. The main conclusions are: (*i*) the minimum propellant injection mass flow for which a steady and self-sustained plasma discharge is obtained greatly depends on the neutral-wall reflection process for the surface-dominated simulation domain considered; (*ii*) the diffuse neutral-wall reflection leads to a significant increase of the neutral residence time with respect to that of the specular reflection cases, thus enhancing the neutral ionization in the channel and explaining the existence of different neutral injection mass flow thresholds for the discharge ignition depending on the neutral-wall reflection type; and (*iii*) once the plasma discharge ignition takes place, it becomes dominated by the ion population, which is mostly generated through the ionization of the recombined neutrals, and the neutral-wall reflection type has been found to have a marginal effect on the discharge structure and performance.

Finally, a typical SPT-100 HET simulation scenario has allowed for a preliminary evaluation of the performance of an improved version of NOMADS for the isotropic electron pressure case, showing its capabilities and limitations. The simulations reproduce the typical HET breathing mode, although several numerical issues have been identified, which are related to (*i*) the large oscillations of the discharge current induced by the low frequency ionization instability, (*ii*) the determination of plasma properties such as the electric potential and the electron pressure (or temperature) at the simulation boundary through GR techniques, and (*iii*) the MFAM quality and the relative size of both the PIC and the MFAM cells, which may yield important interpolation errors. The neutral-wall specular reflection type has been found to increase up to a 7% the breathing mode frequency with respect to the diffuse neutral-wall reflection case. The reciprocal of the neutral gas average residence time in the thruster chamber turned out to closely approximate the resulting breathing mode frequency. Moreover, preliminary results for different electron turbulent parameter α_t values featuring step-out profiles have shown that the breathing mode frequency slightly increases when considering both increasing α_t in the near plume region and decreasing α_t in the thruster chamber. The electric potential flattens in the first part of the thruster chamber for higher α_t values, while a larger potential fall is found for all the step-out profiles in the last part of the chamber. The peak in the axial component of the electric field increases accordingly, and moves upstream into the thruster chamber in those cases. Larger thrust efficiency values, favored by the lower average discharge current values (closer to experimental ones) have been obtained for lower electron turbulent contribution inside the thruster chamber. On the other hand, a local perturbation of the plasma solution due to the concentrated electron injection performed through the volumetric cathode has been reported. The cathode magnetic line is far from being isothermal, specially near the cathode position. Similar plasma profiles inside the thruster chamber and thruster performances have been obtained when moving the cathode position along the same magnetic field streamline in the near plume region. In contrast, larger discrepancies have been found when the cathode magnetic streamline crosses the simulation domain further downstream.

The second major contribution of this Thesis corresponds to the improvement of the radial particle-in-cell model for the simulation of an annular Hall effect thruster discharge developed by Taccogna. The model features secondary electron emission from the walls and a non-uniform radial magnetic field. With the main goals of (*i*) assessing the temperature anisotropy ratio of the VDF of both primary and secondary electrons combined with the asymmetries introduced by cylindrical geometry effects (which include the geometrical expansion, the centrifugal force, and the magnetic mirror), and (*ii*) analyzing the influence of this anisotropy and asymmetry in the macroscopic laws of interest in the steady-state discharge, the following improvements have been incorporated to the model, increasing its numerical consistency and extending its capabilities:

- An ionization-controlled discharge (ICD) algorithm, which ensures a stationary discharge by compensating the wall losses through the ionization collisions in the HET acceleration region. It has been shown that acting through the background neutral density is simple, and allows keeping the average plasma density in the domain without the need of an axial contribution (axial particle refreshing) of plasma. Moreover, since the number of macroparticles in the domain does not practically change throughout the simulation, it can be optimized to reduce the PIC-related statistics noise while limiting the computational time.

- The secular growth of ion axial energy and the subsequent refreshing of ion macroparticles have been avoided by canceling the ion axial acceleration, and generating them with a prescribed mean axial velocity instead. This strategy can be interpreted as a continuous axial refreshing of ions.

- An extended volumetric weighting (EVW) algorithm, which, considering the information of the simulated particles during a given number of steps, allows to obtain much more reliable estimates of the relevant macroscopic magnitudes characterizing the low populated species, such as the secondary electrons emitted from the walls.

Two different studies have been conducted using the improved radial PIC model. First, a reference simulation case has permitted to validate the model and analyze in detail the physics of the steady-state plasma discharge, with special focus on the radial dynamics and the VDF of the different electron populations. This study has permitted to draw the following major conclusions:

- The weak collisionality regime typical of a HET discharge yields an important depletion of the high-radial-energy tails of the primary electrons VDF.
- The replenishment ratio of the high radial-energy tail of primary electrons is small, which leads to a reduced sheath potential fall.
- The parallel-to-perpendicular temperature anisotropy ratio is lower (greater) than one for the primary (secondary) electrons.
- The two secondary electron populations are partially recollected by the walls and partially converted into primary electrons (after a strong collision) in a proportion of about 60%-40%, respectively.
- The resulting density of the secondary electrons is very low, thus being the radial electric potential profile almost exclusively shaped by the primary electrons.
- The radial profiles in both the plasma bulk and sheaths are asymmetric with respect to the mid-radius due to the magnetic mirror effect, which combines the temperature anisotropy and the geometric cylindrical expansion induced by the non-uniform (divergence-free) radial magnetic field, and the centrifugal force (this last one emanating from the $\boldsymbol{E} \times \boldsymbol{B}$ drift).
- The above cylindrical effects introduce significant differences between those magnitudes related to the plasma-wall interaction at the inner and outer walls, such as the collected electric currents, the mean impact energy (and thus the resulting SEE yields), and the wall and sheath electric potentials.
- The temperature anisotropy and non-uniformity, and the centrifugal force modify the classical Boltzmann relation on electrons along the magnetic lines. Therefore, the electric potential profile in the (quasineutral) plasma bulk comes out from a radial momentum equilibrium which goes beyond the classical Boltzmann relation and incorporates non-negligible contributions of (*i*) the radial temperature gradients, (*ii*) the magnetic mirror, and (*iii*) the centrifugal force.

Finally, a parametric study for different field values (keeping constant the ratio E_z/B_r), wall temperature and secondary electron emission, as well as the simulation of a plane case (i.e. at larger radius) have been carried out to further validate the 1D radial particle model and provide a deeper insight on the physics of the response. The main conclusions of this analysis are:

- Significantly larger SEE yields have been found in both walls when the dominant electron backscattering process is included in the model.

- The enhanced SEE reduces the sheath potential drops, which facilitates the electron wall collection. This fact could explain the decrease of the primary electron population temperature in the bulk plasma.
- The influence of the wall temperature for the SEE has a negligible effect on the structure of the plasma discharge.
- The cylindrical effects inducing asymmetries in the macroscopic profiles and in the different plasma magnitudes at the inner and outer walls turned out to vanish in the planar case analyzed, although the electron temperature anisotropy induced by the magnetic field and the wall losses in the low collisionality regime has been found to follow the same trend as in the cylindrical reference case.
- A smaller deviation from the Boltzmann relation has been reported for the primary electrons in the planar case, since the influence of the magnetic mirror effect and the centrifugal force tends to zero as $1/r$.

7.2 Future work

Concerning HYPHEN continuous development and improvement, various actions are here proposed as future work. First, regarding NOMADS module for HET simulations, the following main tasks are foreseen:

- The implementation of effective damping strategies for the discharge current large oscillations, such as resistor-inductor-capacitor (RLC) networks or proportional-integral-derivative (PID) control algorithms [166, 167], which will allow to obtain less fluctuating solutions, thus more amenable to analysis, and will facilitate the tuning of the electron turbulence parameters aiming to better reproduce the reported experimental results in future simulations.
- The incorporation of a data base with values for the thermalization or replenishment parameter σ_t used in the sheath models included in HYPHEN provided by the 1D radial particle model presented in Chapters 5 and 6.
- The definition of the heavy species equivalent collisional current density $\boldsymbol{j}_c$ in Eq. (2.67), which treats separately every collision process between the electron population and a given heavy species s with known properties (see Secs. 2.3.3 and 2.3.8).
- The incorporation of the advanced GR schemes based on arc lengths along the magnetic lines proposed in Ref. [93], which permits to obtain more accurate results near magnetic singular points.
- The determination the electric potential and the electron temperature at the simulation domain boundary from the corresponding boundary conditions so as to avoid current extrapolation errors.
- The improvement of the MFAM generator so as to provide simulation domain MFAMs featuring a smoother and progressive evolution of the cells size, with special attention on the PIC-mesh-to-MFAM cell size ratio in order to limit mesh interpolation errors.

- The extension of the volumetric cathode to several MFAM cells in order to limit the local perturbation induced on the plasma solution. In this line, the implementation of the wall cathode model presented in Ref. [147] could provide more realistic results in the near cathode region.

- The simulation of domains featuring an extended plume region so as to assess the effects on the plasma discharge of the boundary conditions downstream, and analyze the evolution of the plasma properties when the magnetic field becomes residual.

- A dedicated parametric study of the discharge response for a wide range and combination of three different turbulent parameters introduced in Chapter 2, including the analysis of the plasma discharge with α_{te}/α_{tm} much larger and much smaller than one.

- A devoted study of the electron inertial contribution in regions of low electron magnetization (e.g. the anode and the near plume) and the possible implementation of the dominant inertial terms in the electron momentum equation.

- A deeper investigation about the effects on the simulation results of different NOMADS time discretization schemes.

Second, several proposed improvements in the PIC model include:

- The development of a more effective population control based on a particle rezoning or renormalization algorithm which would allow for a better noise control in those regions not dominated by a particle generation processes.

- The incorporation of a more consistent model for the neutral-wall reflection process accounting for the impacting particle energy and angle relative to the surface.

- The modeling of the material wall sputtering phenomena following the approach of Ref. [128], which would permit to evaluate the thruster walls erosion, and thus to better assess its operational lifetime.

- The extension of the particle injection algorithm to enable time-varying injection conditions.

- The incorporation of additional heavy species collisions, such as MEX, or neutral gas elastic collisions.

Additionally, various proposed research directives aiming at extending HYPHEN capabilities are:

- The modeling of active surfaces such as metallic walls admitting net current exchanges. This would enable HYPHEN to simulate multistage thrusters and those belonging to the thruster-with-anode-layer (TAL) family.

- The incorporation of dedicated plasma-wave interaction modules devoted to the simulation of HPTs and ECRAs, which are currently under development by EP2 researchers [67, 68].

- The PIC module adaptation to the particle simulation of the electron population, thus enabling HYPHEN as a full-PIC code suitable, for example, for the study of the collisionless electron cooling phenomena along an axisymmetric plasma plume expansion in vacuum [23–27].

Finally, regarding the 1D radial particle model presented in Chapters 5 and 6, future work will deal with:

- A further parametric investigation for obtaining scaling laws among input and output parameters, which will provide a solid characterization of the 1Dr discharge, and valuable data for the improvement of HYPHEN auxiliary models; one example is the replenishment ratio of the electron VDF for sheath calculations.

- The implementation of an axially-controlled discharge (ACD) algorithm in a similar fashion to the ICD, which will represent the axial source of primary electrons coming from the thruster cathode and which, along with the ionization collisions, will balance out the wall losses in a steady-state discharge. This strategy will enrich the radial model incorporating important information about the primary electron population which is external to the radial dynamics simulated, and which play an essential role in determining the plasma discharge structure and characteristics.

- The investigation of the discharge response in the presence of a non-fully-radial magnetic field, which is expected to largely modify the tails of the electron VDFs and the temperature anisotropy. Preliminary results in this line have already been obtained and presented at the Princeton ExB Plasma Workshop [187].

- The analysis of the effect of a higher axial electric field in the reported transition from a stationary solution to an instability-saturated one.

Conclusiones

Este Capítulo final resume las contribuciones principales de la presente Tesis y propone una serie de actividades y líneas de trabajo futuras relevantes.

Principales contribuciones de la Tesis

Las contribuciones principales de la presente Tesis pueden dividirse en dos grupos complementarios. El primero de ellos hace referencia (*i*) al desarrollo y validación de un nuevo modelo PIC bidimensional y axisimétrico para especies pesadas (es decir, iones y neutros), (*ii*) a su integración con un modelo fluido de electrones mejorado para descargas HET, estableciendo por tanto las bases de HYPHEN, la nueva y versátil plataforma de simulación multi-propulsor, híbrida PIC-fluida desarrollada por el Equipo de Propulsión Espacial y Plasmas (EP2) de la Universidad Carlos III de Madrid (UC3M), y (*iii*) a la aplicación de HYPHEN a la simulación de diferentes escenarios de interés, incluyendo descargas HET y plumas de plasma. Por otro lado, el segundo grupo se corresponde con la nueva versión mejorada del modelo PIC radial para la simulación de una descarga HET desarrollado originalmente por Taccogna [30–32] con el objetivo principal de analizar la dinámica radial de los electrones primarios y secundarios para obtener información valiosa acerca de sus respectivas funciones de distribución de velocidad, lo que permitirá una futura mejora de los modelos de interacción plasma-pared implementados en HYPHEN.

Respecto a HYPHEN, su arquitectura modular lo hace potencialmente extensible a la simulación de diferentes descargas de plasma, incluyendo las de motores HPT, ECRA o HEMPT, además de HET y sus correspondientes plumas de plasma axisimétricas. Una de las contribuciones principales de esta Tesis es el desarrollo y validación de su versátil módulo PIC, aplicable a todos los escenarios anteriores, y que incorpora algoritmos optimizados para el tratamiento de las especies pesadas.

Las principales novedades en el modelado del módulo PIC, orientadas a la mejora de las estadísticas PIC de las especies pesadas y a la extensión de las capacidades del código, son:

- La subdivisón de las varias especies ion y neutro en diferentes poblaciones (o listas de partículas) en base a su diferente masa atómica, carga o energía. Esta estrategia permite tratar y monitorizar por separado a especies pesadas que presentan dinámicas diferentes (como aquellas provenientes de colisiones de tipo CEX), facilitando por tanto el control de su población y reduciendo el ruido estadístico asociado al modelado PIC.

- El desarrollo de un nuevo y versátil generador de mallas PIC que proporciona mallas estructuradas y no uniformes *ad hoc* de los dominios de simulación de interés, incluyendo los correspondientes a motores de tipo HET, HPT y ECRA. El mallador permite incluir el eje de simetría en dichos dominios cilíndricos, y proporciona mallas optimizadas con distribución nodal exponencial y celdas de baja deformación, contribuyendo por tanto a la mejora de las estadísticas PIC y limitando el coste computacional. Además, hace posible la simulación de superficies activas inmersas en el plasma.

- El uso del algoritmo 3D Cartesiano de tipo *leap-frog* implementado en el código EP2PLUS [52] para propagar las macropartículas obteniendo sus trayectorias, evitando así la singularidad presente en las ecuaciones de movimiento en coordenadas cilíndricas en el eje de simetría $r = 0$ [36].

- El desarrollo de un algoritmo *ad hoc* de detección de cruce de partículas con los límites del dominio computacional, que permite la simulación de superficies activas inmersas en el plasma capaces, por ejemplo, de inyectar propulsante en el dominio, emitir neutros procedentes de la recombinación de iones colectados en las mismas, o reflejar las partículas neutro que impactan en ellas.

- La ampliación del algoritmo de interacción del gas neutro con la pared del propulsor para simular reflexiones de tipo mixto especular-difuso de partículas neutras en pared a través de una probabilidad de reflexión especular.

- La incorporación de un nuevo algoritmo para las colisiones de tipo CEX entre especies pesadas que presenta mejoras importantes con respecto al de códigos previos como HPHall-2 [45], y que ha sido desarrollado en paralelo con el incluido en el código EP2PLUS [52]. El nuevo algoritmo explota la subdivisión de las especies pesadas en diferentes listas computacionales permitiendo una simulación más precisa de los efectos producidos por las colisiones CEX sobre las magnitudes macroscópicas de las mismas tanto en la cámara del propulsor como a lo largo de la región de pluma cercana. Además, extiende las capacidades de HYPHEN, habilitándolo para la simulación de plumas de plasma, en las que dichas colisiones juegan un papel fundamental en la determinación del flujo de iones que impacta sobre las superficies sensibles del satélite [85, 86].

- El desarrollo de un algoritmo específico de control de población que, actuando a través de los procesos de generación de nuevas macropartículas en el dominio (como por ejemplo la inyección, las colisiones o la recombinación en pared), mantiene el número de macropartículas por celda de cada especie dentro del rango requerido, limitando así la dispersión en los pesos de las macropartículas y el tiempo computacional (en comparación con técnicas de repoblación o renormalización basadas en la fusión o división de macropartículas [133, 134]).

Dentro de HYPHEN, en relación a NOMADS, el módulo fluido-electrónico para descargas de motores de tipo HET desarrollado originalmente por Pérez-Grande [60], se ha presentado una versión mejorada para el caso de presión isótropa de electrones. Las mejoras implementadas en el marco de la presente Tesis son:

- El tratamiento preliminar de los efectos de inercia de electrones mediante un limitador de la velocidad de deriva de los mismos.
- La incorporación del término anómalo equivalente de calentamiento de Joule en la ecuación de la energía interna de los electrones, de acuerdo con el modelado colisional de los efectos turbulentos.
- La mejora del tratamiento del término fuente correspondiente al cátodo volumétrico en las ecuaciones de conservación de electrones, lo que ha permitido corregir efectos no físicos que aparecían en la versión original del código al cambiar la posición del elemento de la malla magnética correspondiente al cátodo volumétrico.

Empleando HYPHEN, se han simulado tres escenarios de interés con el objetivo de validar sus resultados y mostrar sus capacidades. En primer lugar, se ha considerado la simulación de un escenario típico de expansión de una pluma de plasma axisimétrica de un motor iónico para comparar y validar HYPHEN con EP2PLUS. Las dificultades no triviales inherentes al modelado de partículas en una geometría 2D cilíndrica se han superado satisfactoriamente, y se ha encontrando un acuerdo excelente entre los resultados de dichos códigos, siendo ambos capaces de reproducir con un nivel de ruido aceptable las propedades de especies pesadas cuyas densidades difieren en varios órdenes de magnitud (como por ejemplo las especies de iones inyectadas y las provenientes de colisiones CEX). Se ha encontrado que la estrategia de control de población óptima depende de la dinámica de la población simulada, y resulta esencial para limitar el nivel de ruido en el eje de simetría. Como era de esperar, la formulación 2D presenta grandes ventajas para la simulación de la expansión en el vacío de una pluma de plasma axisimétrica, permitiendo una reducción imporntante del tiempo computacional (alrededor de un factor 10) para un nivel similar de ruido PIC asociado.

En segundo lugar, la simulación de una descarga de plasma no magnetizada con electrones isotermos en un canal cilíndrico esbelto ha permitido mostrar el efecto sobre la descarga de la interacción del gas neutro con la pared en los casos límite de reflexión especular y difusa de neutros en pared, además de proporcionar una evaluación adicional del código híbrido HYPHEN. Las conclusiones principales son: (*i*) el mínimo gasto másico de propulsante a inyectar necesario para obtener una descarga sostenida y estacionaria depende del tipo de reflexión de neutros en pared en el dominio esbelto considerado; (*ii*) la reflexión difusa de neutros aumenta notablemente el tiempo de residencia de los neutros en el canal en relación al caso especular, favoreciendo por tanto la ionización del gas neutro en el canal, y explicando la existencia de diferentes gastos másicos de inyección mínimos para encender la descarga en función del tipo de reflexión de neutros en pared; y (*iii*) una vez encendida la descarga de plasma, esta queda dominada por la población de iones, en su mayoría generados a partir de la ionización de los neutros provenientes de la recombinación de iones en pared, jugando entonces el tipo de reflexión de neutros en pared un papel marginal en la estructura de la descarga.

Finalmente, la simulación de un escenario tipo SPT-100 HET ha permitido una primera evaluación de la versión mejorada de NOMADS para el caso de presión isótropa de electrones, revelando sus capacidades y limitaciones. Las simulaciones reproducen el conocido como *breathing mode*, típico de los motores de tipo HET, aunque se han identificado varios problemas de carácter numérico relacionados con (*i*) las grandes oscilaciones que presenta la corriente de descarga, inducidas por una inestabilidad de ionización de baja frecuencia, (*ii*) la determinación en los bordes del dominio de simulación de propiedades del plasma como el potencial eléctrico o la presión de electrones (o su temperatura) mediante técnicas de reconstrucción de gradientes, y (*iii*) la calidad de la malla magnética y el tamaño de celda relativo entre esta última y la malla PIC, que puede acarrear errores de interpolación importantes. La frecuencia característica del *breathing mode* aumenta en hasta un 7% en el caso de reflexión especular de neutros en pared en relación al caso de reflexión difusa, tomando la inversa del tiempo medio de residencia del gas neutro en la cámara del propulsor valores próximos a dicha frecuencia. Además, resultados preliminares para varios perfiles de tipo *step-out* del parámetro de turbulencia de electrones α_t han mostrado que la frecuencia anterior aumenta ligeramente cuando se incrementa α_t en la región de la pluma cercana, y cuando se disminuye α_t en la cámara del propulsor. El perfil axial de potencial eléctrico se hace más plano en la primera parte de la cámara del propulsor para valores mayores de α_t, encontrándose una mayor caída de potencial en la parte final de la cámara para todos los casos con perfiles de tipo *step-out*. En dichos casos, el valor pico de la componente axial del campo eléctrico aumenta acordemente y se desplaza aguas arriba hacia dentro de la cámara del propulsor. Se han obtenido mayores valores de empuje y eficiencia en los casos con menor contribución turbulenta de electrones en la cámara, favorecidos por la menor corriente de descarga promedio propia de dichos casos. Por otro lado, se ha encontrado una perturbación local en la solución del plasma debida a la inyección concentrada de electrones a través del cátodo volumétrico. La línea magnética correspondiente al cátodo no es isoterma, especialmente en la región cercana al cátodo. Se han obtenido actuaciones del motor y perfiles de plasma similares dentro de la cámara del propulsor para diferentes posiciones del cátodo a lo largo de la misma línea magnética en la región de la pluma cercana, encontrándose sin embargo mayores discrepancias cuando la línea magnética que pasa por el cátodo cruza el dominio de simulación más lejos aguas abajo.

La segunda contribución principal de la presente Tesis se corresponde con la mejora del modelo radial de partículas desarrollado por Taccogna para la simulación de una descarga de un propulsor de tipo Hall. El modelo incluye la emisión de electrones secundarios desde las paredes del propulsor y un campo magnético radial no uniforme. Con los objetivos principales de (*i*) evaluar la anisotropía de temperaturas de las funciones de distribución de velocidad de electrones primarios y secundarios, junto con las asimetrías debidas a efectos propios de la geometría cilíndrica (incluyendo la expansión geométrica, la fuerza centrífuga y el espejo magnético), y (*ii*) analizar la influencia de dicha anisotropía y asimetría en las leyes macroscópicas de interés que gobiernan la descarga estacionaria, se han incorporado las siguientes mejoras al modelo, las cuales incrementan su consistencia numérica y sus capacidades:

- Un algoritmo de control de descarga a través en la ionización (ICD), que permite obtener una descarga estacionaria compensando las pérdidas en pared mediante las colisiones de ionización en la zona de aceleración de un motor de tipo HET. Se ha demostrado que, actuando a través de la densidad de neutros de fondo, es posible mantener la densidad de plasma promedio deseada en la descarga de manera simple y sin necesidad una contribución axial de plasma. Es más, puesto que el número de macropartículas resultante en el dominio se mantiene prácticamente constante durante la simulación, dicho algoritmo representa una solución óptima que permite reducir el ruido estadístico propio del modelado PIC con bajo coste computacional.

- Se ha evitado el crecimiento secular de la energía axial de la población de iones y, en consecuencia, el necesario *refresco* axial de partículas ion ignorando la aceleración axial de los mismos y generándolos, en su lugar, con una velocidad de deriva dada. Esta estrategia puede interpretarse como un continuo refresco axial de iones.
- Un algoritmo de pesado volumétrico extendido (EVW) que, empleando la información de todas las partículas simuladas a lo largo de un número dado de pasos de tiempo, permite obtener estimaciones mucho más precisas de las magnitudes macroscópicas relevantes que caracterizan a las especies poco pobladas, como por ejemplo los electrones secundarios emitidos desde las paredes del motor.

Se han realizado dos estudios diferentes empleando dicho modelo PIC radial mejorado. En primer lugar, se ha validado el modelo mediante una simulación de referencia, que ha permitido el análisis detallado de la física de la descarga estacionaria, poniendo especial interés en la dinámica radial y en las funciones de distribución de velocidad de las diferentes poblaciones de electrones. Las principales conclusiones de dicho estudio son:

- La baja colisionalidad que caracteriza la descarga de tipo HET propicia un vaciado importante de las colas de alta energía de la función de distribución de velocidad de los electrones primarios.
- La tasa de reposición de dichas colas de alta energía es pequeña, lo que se traduce en saltos de potencial reducidos en las vainas de plasma.
- La relación de anisotropía de temperaturas definida como el cociente entre la temperatura paralela y la perpendicular al campo magnético es menor (mayor) que uno para los electrones primarios (secundarios).
- Las dos poblaciones de electrones secundarios son en parte recolectados en las paredes y en parte convertidos a electrones primarios (tras una colisión fuerte) en una proporción de alrededor del 60%-40%, respectivamente.
- La densidad de electrones secundarios es muy baja en comparación con la de electrones primarios, de manera los últimos determinan casi exclusivamente el perfil radial de potencial eléctrico en la descarga.
- Los perfiles radiales de las diferentes magnitudes tanto en el seno del plasma como en las vainas cercanas a las paredes son asimétricos respecto del radio medio del dominio. Este hecho se debe, por un lado, al efecto de espejo magnético, que combina la anisotropía de temperaturas y la expansión propia de la geometría cilíndrica, y que es inducido por el campo magnético radial no uniforme (solenoidal, es decir, con divergencia nula), y, por otro, a la fuerza centrífuga (proveniente de la deriva azimutal de tipo $\boldsymbol{E} \times \boldsymbol{B}$).
- Los efectos cilíndricos anteriores inducen diferencias notables entre las magnitudes relacionadas con la interacción plasma-pared correspondientes a las paredes superior e inferior del propulsor, tales como las corrientes eléctricas colectadas, la energía de impacto medio de las partículas (y por tanto los coeficientes de emisión de electrones secundarios asociados), y los potenciales eléctricos de pared y de entrada de vaina.

- Las contribuciones debidas a la variación y anisotropía de temperaturas y a la fuerza centrífuga modifican la relación de Bolztmann clásica para electrones a lo largo de las líneas magnéticas. Por tanto, el perfil radial de potencial eléctrico que se desarrolla en el seno del plasma responde a un equilibrio radial de cantidad de movimiento más complejo que dicha relación de Boltzmann, incorporando contribuciones relevantes debidas a (*i*) los gradientes radiales de temperatura, (*ii*) el espejo magnético, y (*iii*) la fuerza centrífuga.

Finalmente, un estudio paramétrico para diferentes valores de los campos eléctrico y magnético (manteniendo constante la relación E_z/B_r) y de la temperatura de pared, así como la simulación de diferentes modelos de emisión de electrones secundarios y de un caso con geometría plana (es decir, a alto radio) ha permitido profundizar en la física de la descarga y validar adicionalmente el modelo. Las conclusiones más relevantes de dicho estudio son:

- La emisión de electrones secundarios desde ambas paredes del motor aumenta notablemente al incluir el proceso dominante de reflexión de electrones en la vaina.
- La mayor emisión secundaria reduce los saltos de potencial en las vainas, lo que facilita la recolección de electrones en la pared. Este hecho podría explicar la disminución de la temperatura de electrones primarios en el seno del plasma.
- La temperatura de pared empleada en el modelo de emisión secundaria de electrones presenta un efecto despreciable en la estructura de la descarga.
- Los efectos cilíndricos responsables de las asimetrías presentes tanto en los perfiles radiales como en las diferentes propiedades del plasma entre las paredes interior y exterior del propulsor desaparecen en el caso con geometría plana analizado, aunque la anisotropía de temperatura de electrones, inducida por el campo magnético y las pérdidas a pared dada la baja colisionalidad, presenta la misma tendencia que en el caso cilíndrico de referencia.
- El caso plano presenta una menor desviación con respecto a la relación de Boltzmann puesto que la influencia del efecto de espejo magnético y de la fuerza centrífuga tiende a cero a altos radios conforme a $1/r$.

Trabajo futuro

En esta sección se proponen varias acciones como trabajo futuro en el marco del proceso continuo de desarrollo y mejora de HYPHEN. En primer lugar, en relación a NOMADS, el módulo fluido-electrónico para simulaciones de motores de tipo HET, se prevén las siguientes tareas principales:

- La implementación de estrategias efectivas como circuitos RLC o esquemas de control PID para reducir las grandes oscilaciones de la corriente de descarga [166, 167], lo que permitirá obtener soluciones menos oscilantes y por tanto más adecuadas para su análisis, y facilitará el ajuste de los parámetros de turbulencia de electrones con el objeto de reproducir resultados experimentales en futuras simulaciones.

- La incorporación en el modelo de vaina incluido en HYPHEN de una base de datos con valores del coeficiente de termalización o tasa de reposición σ_t proporcionados por el modelo radial 1D de partículas presentado en los Capítulos 5 y 6.

- La definición de la corriente equivalente colisional de especies pesadas $\boldsymbol{j}_c$ presentada en Eq. (2.67), que trata de manera independiente cada proceso de colisión entre la población de electrones y una especie pesada dada s con propiedades conocidas (ver Secs. 2.3.3 and 2.3.8).

- La incorporación de los esquemas avanzados de reconstrucción de gradientes propuestos en Ref. [93] basados en longitudes arco a lo largo de las líneas magnéticas, que permiten obtener resultados más precisos cerca de los puntos magnéticos singulares.

- La determinación del potencial eléctrico y de la temperatura de electrones en el borde del dominio computacional mediante la aplicación directa de las condiciones de contorno correspondientes, con tal de evitar los errores de extrapolación actualmente presentes.

- La mejora del generador de mallas magnéticas MFAM para proporcionar mallas del dominio computacional con una evolución más suave y progresiva del tamaño de las celdas, prestando especial atención a la relación de tamaños de celda entre las mallas PIC y MFAM con el objeto de reducir errores de interpolación.

- La extensión del cátodo volumétrico a varias celdas de la malla magnética MFAM con el objetivo de limitar la perturbación inducida en el plasma. En este sentido, la implementación del modelo de cátodo de pared presentado en Ref. [147] podría proporcionar resultados más realistas en la región cercana al cátodo.

- La simulación de dominios con una región de pluma extendida para evaluar los efectos de las condiciones de contorno impuestas aguas abajo en la descarga de plasma y analizar la evolución de las propiedades del plasma en zonas de bajo campo magnético.

- Un estudio paramétrico de la respuesta de la descarga para un amplio rango y combinación de los tres parámetros diferentes de turbulencia de electrones presentados en el Capítulo 2, incluyendo el análisis de los casos con α_{te}/α_{tm} mucho mayor y mucho menor que la unidad.

- Un estudio de la contribución de la inercia de electrones en regiones de baja magnetización (como por ejemplo el ánodo y la pluma cercana), y la posible implementación de los términos de inercia dominantes en la ecuación de cantidad de movimiento de electrones.

- Una investigación más profunda sobre los efectos en los resultados de simulación de diferentes esquemas de discretización temporal del módulo NOMADS.

En segundo lugar, las mejoras propuestas para el módulo PIC incluyen:

- El desarrollo de un control de población más efectivo basado en un algoritmo de renormalización de la población de partículas, que permitiría un mejor control del ruido PIC en aquellas regiones no dominadas por un proceso de generación de partículas.
- La incorporación de un modelo de reflexión de neutros en pared más consistente que tenga en cuenta la energía y el ángulo de impacto relativo a la superficie.
- El modelado de los fenómenos de erosión de las paredes del motor siguiendo la estrategia presentada en Ref. [128], lo que permitiría evaluar la vida operativa del motor.
- La ampliación del algoritmo de inyección para permitir la inyección no estacionaria de propulsante con condiciones variables en el tiempo.
- La incorporación de nuevos tipos de colisiones entre especies pesadas, como por ejemplo colisiones de tipo MEX o colisiones elásticas en el gas neutro.

Asimismo, con el objeto de ampliar las capacidades de HYPHEN, se proponen las siguientes líneas de actuación:

- El modelado de superficies activas inmersas en el plasma, como por ejemplo paredes metálicas que admitan un intercambio neto de corriente con el plasma. Esto permitiría simular con HYPHEN motores de varias etapas y motores TAL (del inglés, *thruster-with-anode-layer*).
- La incorporación de módulos específicos de interacción onda-plasma actualmente en desarrollo por los investigadores del grupo EP2 [67, 68] para la simulación de motores de tipo HPT y ECRA.
- La adaptación del módulo PIC para la simulación de la población de electrones mediante un modelo de partículas, lo que habilitaría a HYPHEN como código *full*-PIC aplicable, por ejemplo, al estudio del fenómeno de enfriamiento de electrones a lo largo de la expansión de una pluma de plasma axisimétrica en el vacío [23–27].

Finalmente, en relación al modelo 1D radial de partículas presentado en los Capítulos 5 y 6, se propone como trabajo futuro:

- Una estudio paramétrico adicional para obtener leyes de escalado que relacionen parámetros de entrada y salida y que proporcionen una caracterización sólida de la descarga radial e información valiosa para la mejora de los modelos auxiliares de HYPHEN; un ejemplo es la tasa de reposición de la función de distribución de velocidad empleada en el modelo de vaina.
- La implementación de un algoritmo similar al ICD para el control de la descarga mediante el aporte axial de partículas (ACD), que representará la fuente axial de electrones primarios provenientes del cátodo del motor y que, junto con las colisiones de ionización, compensará las pérdidas en pared estableciendo una descarga estacionaria. Esta estrategia enriquecerá el modelo incorporando una información sobre la población de electrones primarios que es externa a la dinámica radial simulada, y que juega un papel esencial en la determinación de la estructura y características de la descarga de plasma.

- La investigación de la respuesta de la descarga en presencia de un campo magnético oblícuo (es decir, con una cierta componente axial), que se espera modifique sustancialmente la anisotropía de temperaturas y las colas de alta energía de las funciones de distribución de velocidad de las diferentes poblaciones de electrones. En este sentido, se han obtenido ya resultados preliminares, que han sido presentados en el Princeton ExB Plasma Workshop [187].

- El análisis de la transición de una solución estacionaria a una inestable saturada mediante el incremento del campo eléctrico axial.

Appendix A

HYPHEN PIC module validation tests

HYPHEN is distributed with a complete suit of individual and integrated tests of the different algorithms implemented that can be completely run in a few minutes in a usual personal computer. The individual tests are devoted to assess the performance of a particular functionality of the code and reveal possible algorithm errors in the simplest scenarios. On the other hand, the integrated tests evaluate the correct functioning of different algorithms involving several modules in a particular simulation setup. The following sections detail the complete set of individual and integrated tests developed during this Thesis, which are mainly related to the algorithms included in the HYPHEN PIC module, already described in Chapter 2. Tab. A.1 summarizes said tests.

Test name	**Test type**	**Success criteria**
Field computation	Individual	Reconstructed electric field error with respect to the exact one for a known electric potential field below a given tolerance.
Particle mover	Individual	Particle trajectory error with respect to the exact solution below a threshold.
Particle-surface crossing	Individual	Detection of particles crossing boundary surfaces and identification of the crossing points.
Volume weighting	Individual	Error on the volumetric weighted particle density at the PIC mesh nodes with respect to the known values for various given populations with different number of particles per cell below a tolerance.
Particle injection	Individual	Density and temperature errors of the injected species with respect to their known values below a given threshold.
Surface weighting	Individual	Error on the surface weighted density and fluid velocity at a PIC mesh surface with respect to their known values for a given population below a tolerance.
Surface interaction	Individual	Mass conservation on a closed cylinder.
Ionization collisions	Individual	Error on the density of the ionized neutrals with respect to their expected values below a threeshold.
CEX collisions	Individual	Error on the density of the colliding fast ions with respect to their expected values below a tolerance.
Population control	Individual	Number of macroparticles per cell within the prescribed range
Collisionless plasma plume expansion	Integrated	Error on plasma density with respect to the SSM fluid solution within a given tolerance.
Bohm condition	Integrated	Fulfillment of the KBC at the material wall surface elements for the ion species.

Table A.1: HYPHEN PIC module validation tests description.

A.1 Field computation

As commented in Sec. 2.2.2, two different approaches have been considered for the electric field reconstruction from a given electric potential field at the PIC mesh. The electric field reconstruction based on the computational coordinates corresponds to Eq. (2.11) and is here referred to as approach A. On the other hand, the approach B uses the arc parameter variables, as indicated in Eq. (2.10). In the field computation test, the performance of the two approaches below are compared when obtaining the electric field in a different HET-like PIC mesh from the electric potential field

$$\phi = V_d \exp\left(-\frac{1}{2}\left(\frac{z}{z_{exit}}\right)^2\right)\left(\frac{5}{4}\cos\left(\frac{2(r-r_m)}{3\Delta r}\right)-\frac{1}{4}\right), \tag{A.1}$$

where $V_d = 300$V is the discharge voltage, z_{exit} is the axial coordinate of the thruster exit section, r_m is the thruster chamber mean radius and $\Delta r = r_{out} - r_{in}$, being r_{out} and r_{in} the outer and inner thruster chamber radius, respectively. This electric potential field is symmetric with respect to the chamber mean radius along the axial coordinate.

Fig. A.1(a) shows the PIC mesh considered, while Fig. A.1(b) depicts the corresponding electric potential field given in Eq. (A.1). The PIC mesh has been obtained with the new PIC mesh generator (see Sec. 2.2.1), and contains a line of nodes along the axial coordinate exactly at the chamber mean radius $r_m = 4.25$ cm [red line in Fig. A.1(a)]. Near the chamber exit, two erosion chamfers have been added so that inside the chamber the nodes are symmetric with respect to the chamber mean line until the chamfers begin. Since the electric potential field is symmetric with respect to this line, the radial component of the electric field along this line must be zero.

The relative error on the reconstructed electric field with respect to the exact one considering Eq. (A.1) is shown in Figs. A.1(c) and A.1(d) when using approach A and B, respectively. The approach A gives larger field reconstruction errors, with a maximum of 15.76% at $z = 2$ cm at the chamber mean line, coinciding with the point at which the inner wall chamfer begins, thus generating the largest radial asymmetry between the chamber mean line neighbors nodes.

According to Eqs. (2.10) and (2.11), it is worth noting that, in both approaches, the electric field components are given by two contributions:

1. The Jacobian matrix terms, whose error depends on the mesh characteristics and on the numerical schemes used for computing the derivatives.
2. The partial derivatives $\partial\phi/\partial k$, with respect to the computational coordinates ($k = \xi, \eta$) in approach A, or with respect to the arc parameter variables ($k = l_\eta, l_\xi$) in approach B.

In this test the same mesh is used for both approaches and second order schemes are applied for computing the Jacobian matrices in Eqs. (2.10) and (2.11). Therefore, the key point here is the second contribution. In particular, the larger error observed in the approach A comes from the radial component of the reconstructed field E_r, and is induced by the term $\partial\phi/\partial\eta$, computed with a second order central difference scheme for uniform meshes (computational mesh), as

$$\left.\frac{\partial\phi}{\partial\eta}\right|_{ij} = \frac{\phi_{i+1j} - \phi_{i-1j}}{2}, \tag{A.2}$$

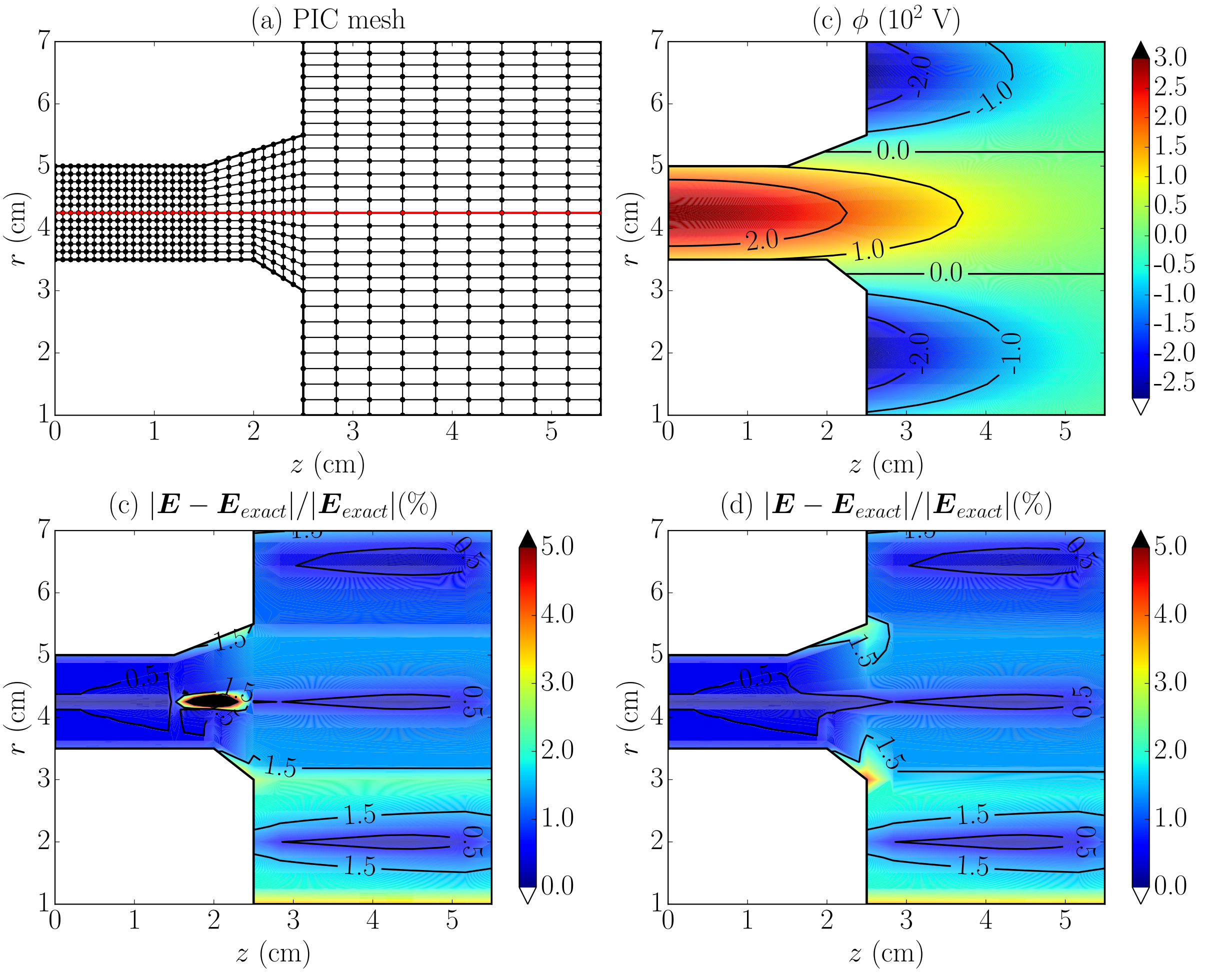

Figure A.1: Field computation test results. (a) PIC mesh for a HET domain with symmetric node distribution in chamber before erosion chamfers. The red line indicates the mean chamber line at $r = r_m$. (b) Electric potential field given in Eq. (A.1). Computed electric field relative error with respect to the exact electric field using approach A (c) and B (d).

where (i, j) are the indices of a node located at the mean chamber line in the chamfers zone, being i the index along r direction and j the index along z direction. This scheme does not take into account the real physical distance between nodes. Since $\phi_{i+1j} \neq \phi_{i-1j}$, the result for E_r at this node is quite different from zero, which is the exact value. In contrast, the physical radial distance between nodes is considered in the general second order finite difference schemes for the corresponding derivative $\partial\phi/\partial l_\xi$ in the approach B, so that the error commited is significantly lower.

As already commented in Sec. 2.2.2, both approaches are equivalent for uniform meshes. As depicted in Figs. A.1(c) and A.1(d), the same relative error is obtained in those zones where the mesh is uniform (inside the chamber before the chamfers and in the near plume region).

A.2 Particle mover

In this test, the trajectory of an ion macroparticle is integrated using the HYPHEN particle mover algorithm and considering constant electromagnetic fields. The results are compared with the corresponding exact analytical solution for the same fields. The macroparticle trajectory in the $\boldsymbol{E} \times \boldsymbol{B}$ plane is shown in Fig. A.2(a), while the position and velocity relative errors, $\epsilon_p = |\boldsymbol{x} - \boldsymbol{x}_{ex}|/|\boldsymbol{x}_{ex}|$ and $\epsilon_v = |\boldsymbol{v} - \boldsymbol{v}_{ex}|/|\boldsymbol{v}_{ex}|$, respectively, are depicted in Fig. A.2(b).

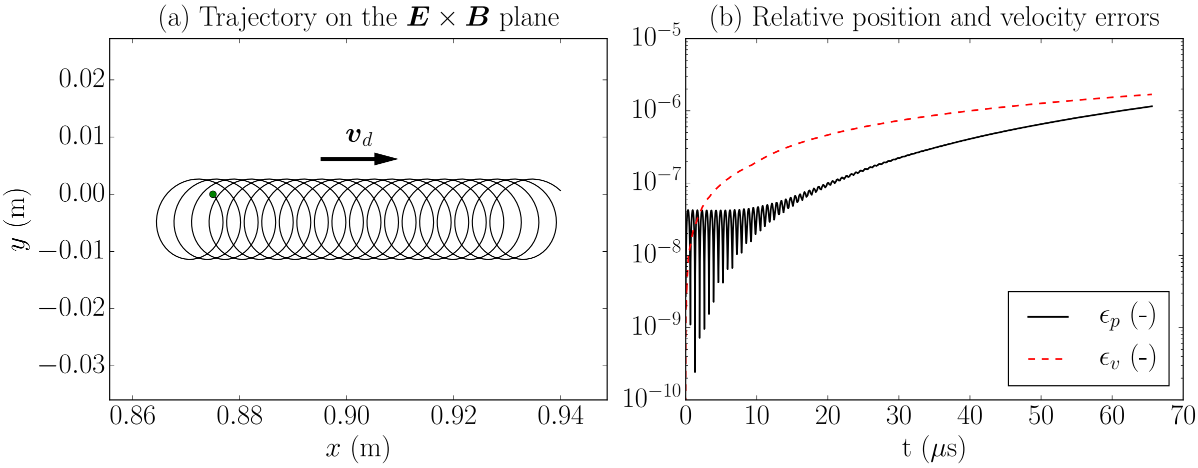

Figure A.2: Particle mover test results. (a) Particle trajectory in the $\boldsymbol{E} \times \boldsymbol{B}$ plane. The green dot indicates the particle initial position and $\boldsymbol{v}_d = \boldsymbol{E} \times \boldsymbol{B}/|\boldsymbol{B}|$ is the $\boldsymbol{E} \times \boldsymbol{B}$ drift velocity. (b) Position and velocity relative errors.

A.3 Particle-surface crossing

In the particle-surface crossing test, a particle population with random velocities is generated inside a HET-like PIC mesh as that shown in Fig. A.1(a). The test confirms that every particle crossing the mesh boundaries is collected and removed from the domain.

A.4 Volumetric weighting

In the volumetric weighting algorithm test, ten random particle populations representing a particle density n_{ex} with increasing number of particles per cell are weighted to the nodes of the HET-like PIC mesh depicted in Fig. A.1(a). For every population, and at each mesh cell, a number N_{cell} of particles is distributed uniformly in the cell with a corrected macroparticle weight to cancel out cylindrical effects (see Sec. 2.2.5.1.1).

Figs. A.3(a) and A.3(b) show the evolution with the number of particles per cell of the normalized average weighted particle density and of the weighted particle density normalized standard deviation, $\tilde{\sigma}$ respectively. The expected normalized standard deviation is defined as

$$\tilde{\sigma}_{ex} = \frac{1}{\sqrt{N_{cell}}}, \tag{A.3}$$

and, considering a 1% tolerance, it corresponds to the black line with square markers in Fig. A.3(b).

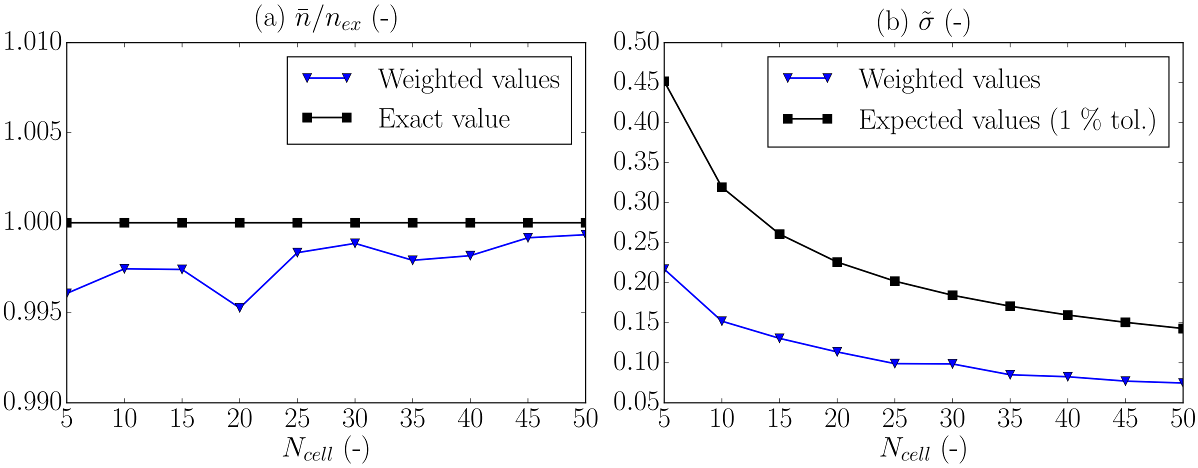

Figure A.3: Volumetric weighting test results. Evolution with the number of particles per cell of (a) the normalized average weighted particle density and (b) the weighted particle density normalized standard deviation.

A.5 Particle injection

Two different tests are carried out considering the following injected populations:

1. Drifting Maxwellian population injected from an annular injection surface located at the axial coordinate origin, with $n_{inj} = 10^{16}$ m^{-3}, $\boldsymbol{u}_{inj} = (0, 0, 3 \cdot 10^4)$ ms^{-1} and $T_{inj} = 0.05$ eV.
2. Thermal Maxwellian population injected from the surfaces of a cylinder towards its center, with $n_{inj} = 10^{16}$ m^{-3} and $T_{inj} = 50$ eV.

Figs. A.4(a) and A.4(b) shows, respectively, the weighted density and temperature of the first injected population. Similarly, the results for the weighted density and temperature for the second injected population are depicted in Figs. A.4(c) and A.4(d). An excellent agreement with the corresponding injection values is found. Furthermore, the normalized velocity distribution functions $\tilde{f}(v_r)$ and $\tilde{f}(v_z)$ are shown in Figs. A.5(a) and A.5(b), respectively, both fitting successfully the expected Maxwellian distribution.

A.6 Surface weighting

The test configuration is shown in Fig. A.6. A particle population is axially injected with known properties (the injection temperature is set to zero) from a circular injection surface at the axial coordinate origin. This population is surface weighted at a circular test surface parallel to the injection one and located downstream. The relative error of the weighted particle density and flux with respect to the know values at the injection surface is lower than 0.5 %, so that the surface weighting algorithms are validated.

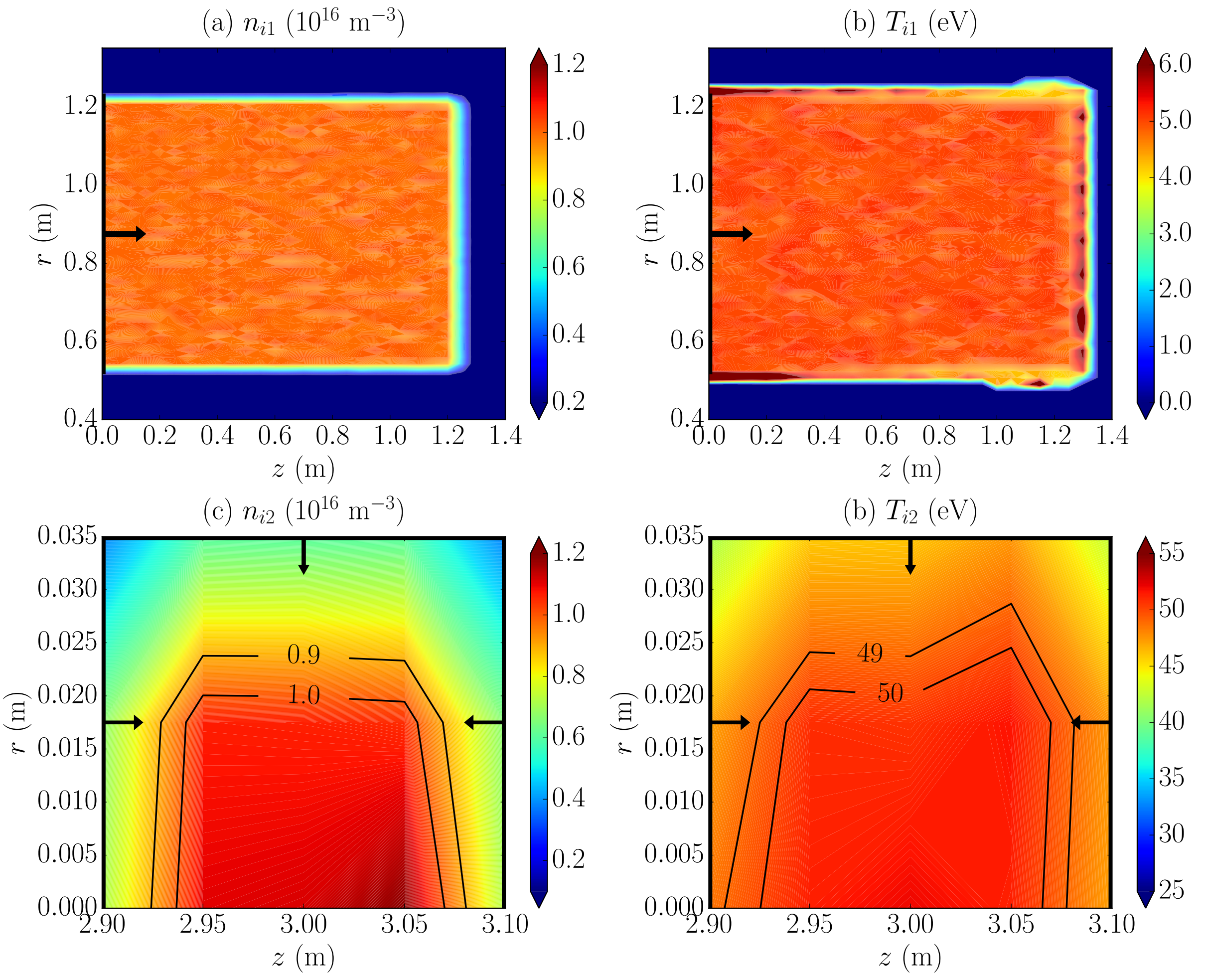

Figure A.4: Particle injection test results. (a) Weighted particle density and (b) weighted temperature for the first injected population. (c) Weighted particle density and (d) weighted temperature for the second injected population. The black lines indicate the injection surfaces and the black arrows their corresponding injection direction..

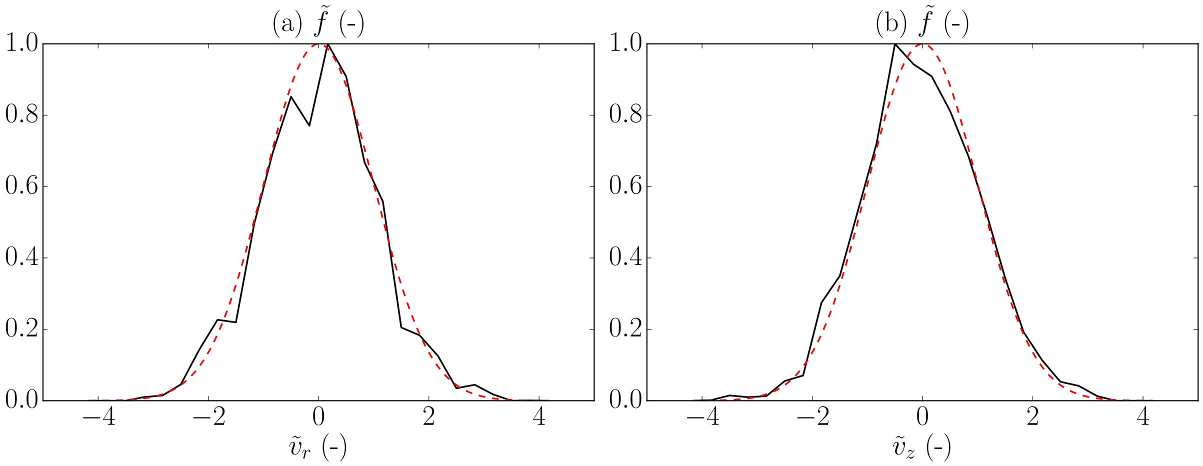

Figure A.5: Particle injection test results. Normalized VDFs for (a) the radial and (b) the axial particle velocities, both normalized with the population thermal velocity $c = \sqrt{T/m}$, with T in energy units. The red dashed lines correspond to the expected Maxwellian distributions of the injected population.

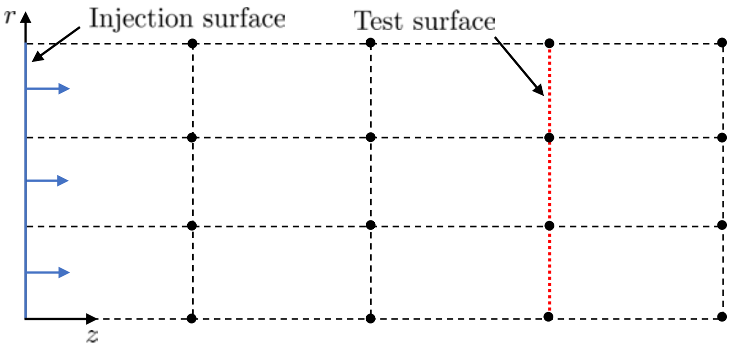

Figure A.6: Surface weighting test configuration. The vertical blue line represents the injection surface at $z = 0$, while the test surface at which the injected population is surface weighted corresponds to the red dashed vertical line located downstream.

A.7 Surface interaction

In this test an ion and a neutral population with given initial velocities is generated inside a cylinder with material walls. When the ions hit the material walls, they are recombined into neutrals which are diffusely reinjected into the simulation domain. In addition, both the recombined neutrals and those from the initial population are reflected either specularly or diffusely by the material walls. The mass conservation in the cylinder and the expected distribution function of the reinjected and reflected neutrals is achieved, so that the ion recombination and neutral reflection algorithms are successfully validated.

A.8 Ionization collisions

The ionization test configuration is depicted in Fig. A.7(a). Considering a cylindrical domain, a plasma background is generated with a still ion population which ionize the axially injected neutrals through the circular injection surface at $z = 0$. Since the plasma background density is much higher than that of the ionization products, the expected steady axial evolution of the neutral density is

$$n_n(z) = n_{n0} \exp\left(\frac{-n_e R_i z}{u_{zn}}\right), \tag{A.4}$$

where $n_{n0} \equiv n_n(z = 0)$ is the neutral density at the injection surface, n_e is the plasma background density, u_{zn} is the neutrals axial velocity and R_i is the ionization rate at a given constant electron temperature.

Fig. A.7(c) compares the obtained axial evolution of the neutral density along the symmetry axis with that of Eq. (A.4) showing an excellent agreement.

A.9 CEX collisions

The configuration of the CEX collisions tests is similar to that for the ionization test and it is shown in Fig. A.7(b). Two different ion populations, $i1$ and $i2$, are injected axial

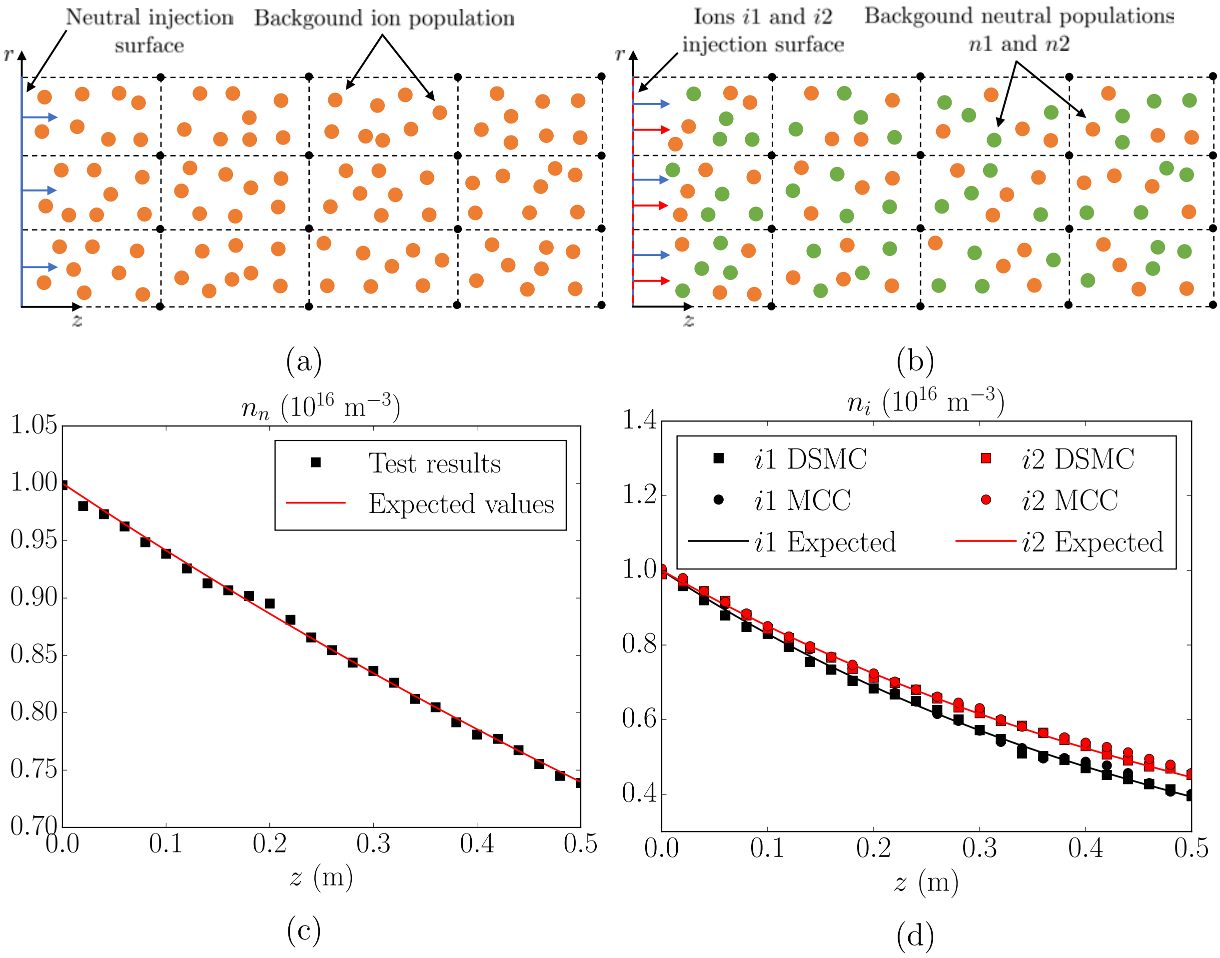

(a) (b) (c) (d)

Figure A.7: (a) Ionization collisions test configuration. Cylindrical domain with a still background ion population represented by the orange dots. The neutral axial injection is performed through the injection surface at $z = 0$, represented by the blue vertical line. (b) CEX collisions test configuration. Cylindrical domain with two still background neutral populations, $n1$ and $n2$, represented by the orange and green dots, respectively. The two ion populations $i1$ and $i2$ are injected through the injection surface at $z = 0$, represented by the blue and red vertical line. (c) Axial evolution of the injected neutrals density along the symmetry axis at stationary conditions in the ionization collisions test. (d) Axial evolution of the injected ions density along the symmetry axis at stationary conditions in the CEX collisions test.

velocity of 10 and 20 kms^{-1}, respectively. On the other hand, two still neutral populations $n1$ and $n2$ are distributed in the domain with the same density. The test checks the results of four CEX collisions using both DSMC and MCC sampling of the input species::

1. CEX collision $i1$-$n1$ with DSMC and MCC sampling.

2. CEX collision $i2$-$n2$ with DSMC and MCC sampling.

For each collision, the expected steady axial evolution of the corresponding injected ions density is

$$n_i(z) = n_{i0} \exp\left(\frac{-z}{\lambda_c}\right), \tag{A.5}$$

where $n_{i0} \equiv n_i(z=0)$ is the ion density at the injection surface, n_n is the corresponding neutral background density, and λ_c is the mean free path for the CEX collision, which depends on the relative ion-neutral velocity and thus is different for each injected ion population. Fig. A.7(d) compares, for each collision above, the obtained axial evolution of the ion density along the symmetry axis with that of Eq. (A.5). An excellent agreement is found when using both DSMC and MCC sampling algorithms.

A.10 Population control

The population control described in Sec. 2.2.5.6 is applied to any process involving the generation of new particles in the domain. Those include the particle injection, the neutral reinjection due to the ion recombination at the material walls and the particle collisions (see Secs. 2.2.5.1.1, 2.2.5.1.2.4 and 2.2.5.3, respectively). In this test, an scenario involving the second process mentioned above is considered to assess the performance of the new population control (here referred to as approach A) and compare its results to those of the population control implemented in HallMA [72] (named hereafter as approach B).

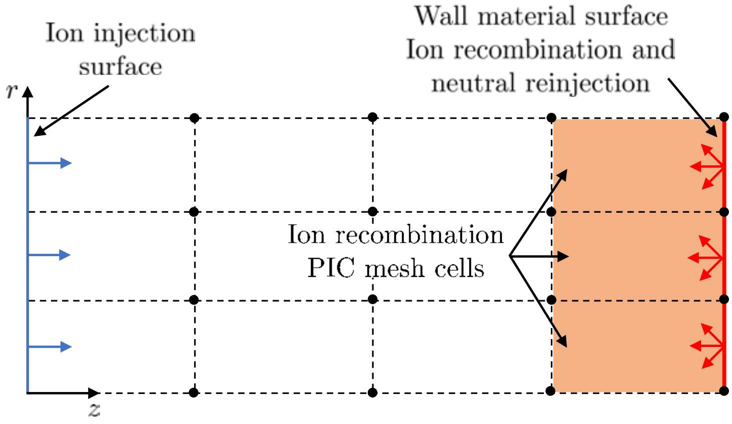

Figure A.8: Population control test configuration. The vertical blue line represents the ion injection surface at $z = 0$, while the material wall surface characterized by the ion recombination and neutral reinjection process corresponds to the red vertical line located downstream.

The test configuration is shown in Fig. A.8. An ion population is injected according to a generalized Parks-Katz radial plume profile [39,137,138] through a circular injection surface defined at $z = 0$, and is recombined into neutrals at a circular material wall parallel to the injection one and located downstream. At the ion recombination cells, the target number of particles per cell for the recombined neutrals is $N_{tg} = 300$, while the maximum and minimum number of particles per cell are $N_{min} = 250$ and $N_{max} = 350$, respectively. The injected ions density at steady conditions is shown in Fig. A.9(a), while the radial profile of the recombined neutrals density at the ion recombination cells obtained with both approaches A and B is depicted in Fig. A.9(b). The time evolution of the average number of particles per cell at the ion recombination cells is shown in

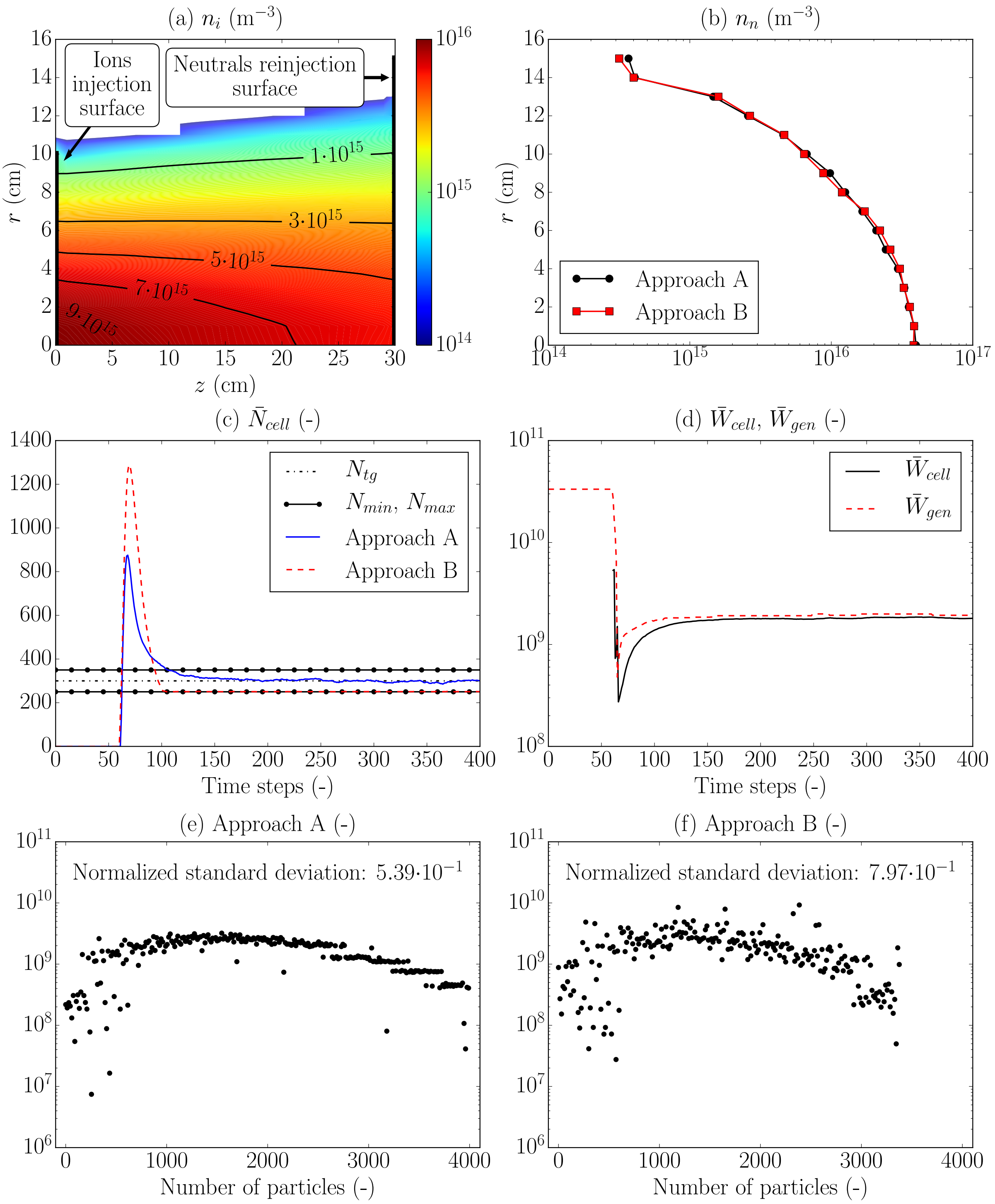

Figure A.9: Population control test results. (a) Injected ions density, (b) recombined neutrals radial density profile at the ion recombination cells, time evolution of (c) the average number of particles per cell and (d) generation and average macroparticle weights for the recombined neutrals at the ion recombination cells, and, (e) and (f) recombined neutrals macroparticle weight distribution at the ion recombination cells at the last simulation step.

Fig. A.9(c) for both approaches. Fig A.9(d) plots the time evolution of the average generation and macroparticle weight per cell in the ion recombination cells, $\overline{W}_{gen}$ and $\overline{W}_{cell}$, respectively. Finally, the weights of the neutral macroparticles within those cells at the last simulation step are shown in Figs. A.9(e) and A.9(f) for the approach A and B, respectively. The progressive self-adjusting of the generation macroparticle weight in the approach A reduces significantly the initial overshoot in the average number of particle per cell with respect to that found when the approach B is applied. Moreover, the approach A permits to maintain the target number of particles per cell with a lower macroparticle weight dispersion, while the approach B keeps only the minimum number of particles per cell with a higher weight dispersion. Finally, as expected, in the approach A both the generation weight and the average macroparticle weight per cell tend to the same value at steady conditions, when the number of macroparticles per cell is kept within the control range.

A.11 Collisionless plasma plume expansion

In this integrated test, the results of a collisionless plasma plume simulation are compared with the corresponding Parks-Katz plume solution for polytropic electrons. The injected ions follow the generalized Parks-Katz plume profile of Eq. (3.8) with $\gamma = 1.05$, $R_0 = 0.1$ m, $n_0 = 10^{16}$ m^{-3}, $u_{z0} = 4 \cdot 10^4$ ms^{-1} and $\alpha_0 = 5°$. Two different scenarios are evaluated:

a) The electric field is constant during the simulation and given by the Parks-Katz solution.

b) The electric field is computed self-consistently during the simulation applying the electron polytropic closure in Eq. (3.2).

Fig. A.10 shows the axial evolution of the plasma density along the axis in both cases showing a good agreement. As expected, when a self-consistent electric field is considered the match with the expected solution is even better.

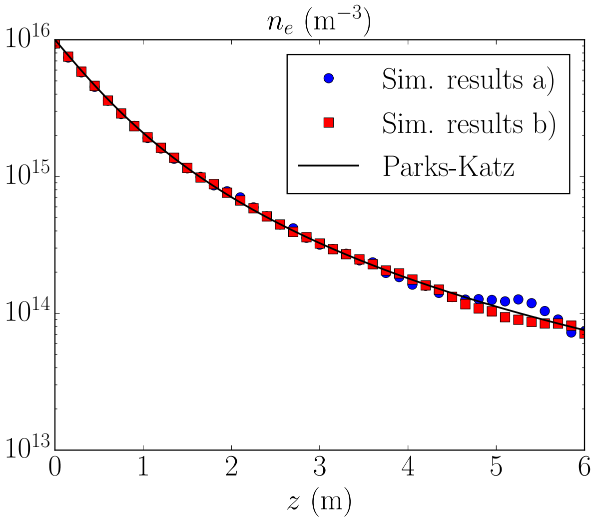

Figure A.10: Collisionless plasma plume expansion test results.

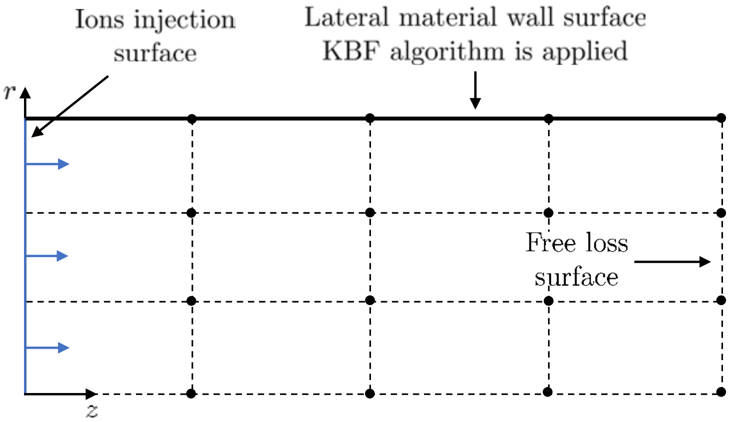

Figure A.11: Bohm condition test configuration. The vertical blue line represents the ions injection surface at $z = 0$, while the lateral material wall surface where the KBF algorithm is applied coincides with the solid horizontal black line in the top boundary. A free loss surface is located downstream at the end of the cylindrical domain.

A.12 Bohm condition

The KBF algorithm included in HYPHEN is tested in the simulation scenario shown in Fig. A.11, which represents a cylindrical domain with lateral material walls, a free loss circular surface at the end, and an injection surface at $z = 0$ through which singly and doubly charged ions are axially injected with sonic axial velocity $c_s = \sqrt{eZT_e/m_i}$ and $T_i = 0.05$ eV. The isothermal closure ($\gamma = 1$) in Eq. (3.2) is considered for the electrons, with $T_e = 3$ eV.

The steady electric potential in the domain is shown in Fig. A.12(a). The KBF algorithm induces the development of a pre-sheath region in the bulk plasma that accelerates radially the injected ions, so that they reach the lateral material walls with sonic conditions downstream. In fact, the total potential drop in the pre-sheath is of the order of $T_e/2$, as expected for cold ion populations ($T_i \ll T_e$). Fig. A.12(b) depicts the Bohm condition potential drop normalized with the electron temperature along the lateral material wall, while the corresponding correction on the plasma density is shown in Fig. A.12(c). Finally, the value of the Mach-Bohm number defined in Ref. [76] along the lateral material wall is plotted in Fig. A.12(d), showing sonic conditions for the ions in most of the material wall, except for an initial region where the electric potential profile is dominated by the ion injection.

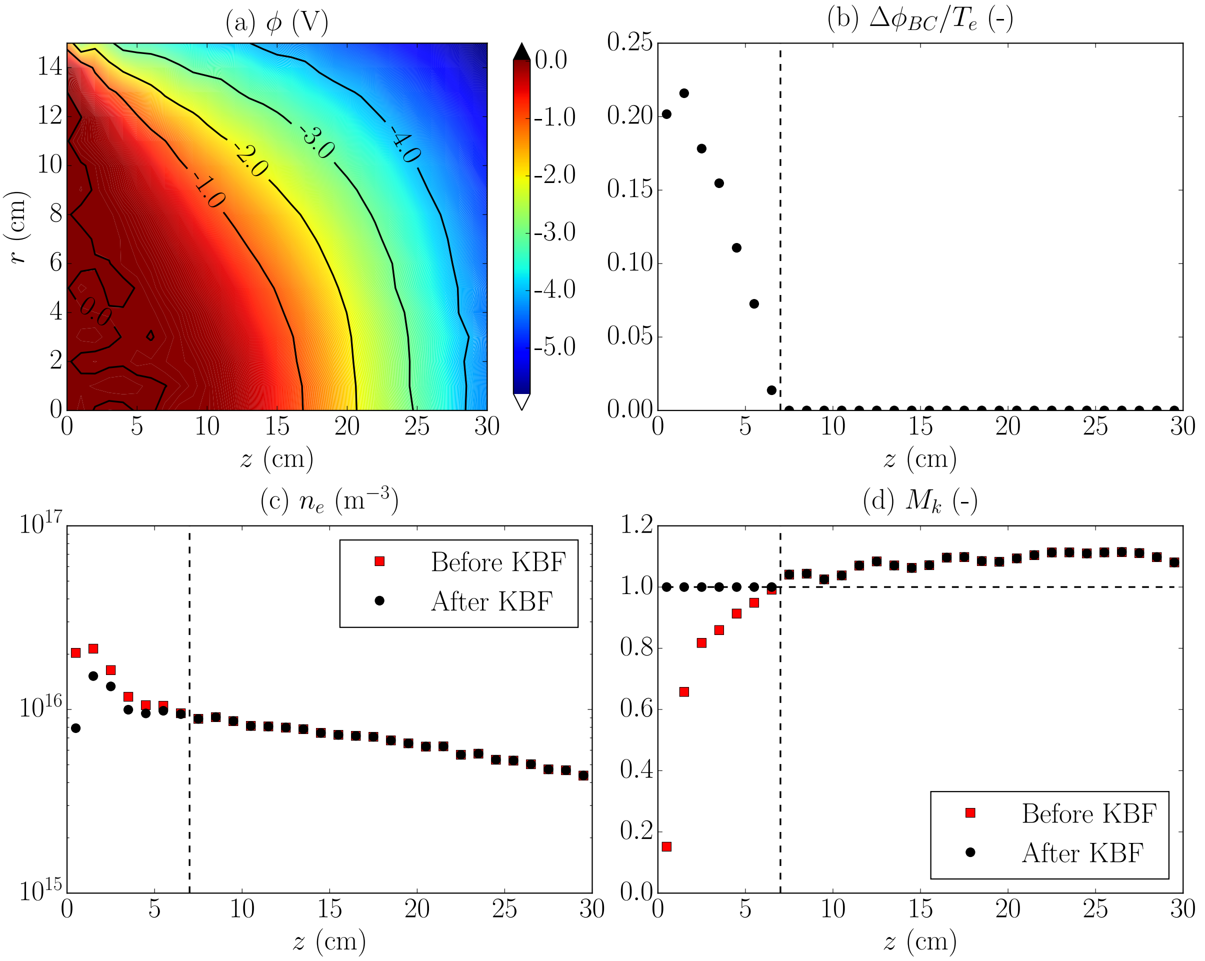

Figure A.12: Bohm condition test results. (a) Electric potential, axial evolution along the lateral material wall of (b) the non-dimensional Bohm condition potential drop $\Delta\phi_{BC}/T_e$, (c) the plasma density and (d) the Mach-Bohm number before and after the KBF algorithm.

Appendix B

HYPHEN SPT-100 HET simulations data

This appendix contains additional data corresponding to the different SPT-100 HET simulation cases analyzed in Chapter 4. Sec. B.1 refers to the cases with different volumetric cathode locations presented in Sec. 4.2.2.4, while Sec. B.2 is devoted to those simulation cases featuring different electron turbulent parameter α_t profiles detailed in Sec. 4.2.2.5.

B.1 HET simulation cases featuring different cathode locations

Tabs. B.1-B.3 contains the relevant simulation results for the SPT-100 HET cases C2-C4 analyzed in Sec. 4.2.2.4. In addition, Figs B.1-B.7 complete the results for the cases C1-C4 shown in Sec. 4.2.2.4 and have been included here for further analysis and discussion.

Variable	**Units**	**Value**
$\bar{n}_e$ min., max., mean	m^{-3}	$8.87 \cdot 10^{15}$, $6.63 \cdot 10^{17}$, $1.51 \cdot 10^{17}$
$\bar{n}_n$ min., max., mean	m^{-3}	$2.41 \cdot 10^{17}$, $9.23 \cdot 10^{17}$, $7.17 \cdot 10^{17}$
$\bar{n}_e$, $\bar{n}_n$ frequency, phase shift	kHz, deg	11.26, 71.38
I_d min., max., mean	A	$6.36 \cdot 10^{-2}$, $4.67 \cdot 10^{1}$, $6.78 \cdot 10^{0}$
$I_{i\infty}$ min., max., mean	A	$8.26 \cdot 10^{-2}$, $3.74 \cdot 10^{1}$, $4.98 \cdot 10^{0}$
I_d, $I_{i\infty}$ frequency, phase shift	kHz, deg	11.26, 18.89
I_{wi}, I_{prod}	A	3.02, 8.00
I_{sp}, F	s, mN	1646, 80.74
$P_{zi\infty}$, $P_{i\infty}$	W	766, 899
P_d, $\varepsilon_E^{P_d}$	W, -	2028, 0.51
P_{use}, $\varepsilon_E^{P_{use}}$	W, -	766, 0.19
P_{loss}, $\varepsilon_E^{P_{loss}}$	W, -	1200, 0.30
P_{walls}, $\varepsilon_E^{P_{walls}}$	W, -	1028, 0.26
$P_{ion,ex}$, $\varepsilon_E^{P_{ion,ex}}$	W, -	172, 0.04
η_{thr}, η_u, η_{cur}, η_{div}, η_{prod}	-	0.32, 0.97, 0.73, 0.85, 0.62
ν_{cat}, P_{cat}	MHz, W	154, 30

Table B.1: Main results for the SPT-100 HET C2 simulation case. Mean values represent time-averaged values over the number of complete cycles within the last 450 μs of simulation time. The maximum and minimum values represent the average of the peak and trough values within that period. Please note that the value of $P_{zi\infty}$ does not contain the contribution of the neutral species. However, since this contribution is negligible compared to that of the ions, $P_{zi\infty}$ takes the value of P_{use} after truncation and approximation.

Variable	**Units**	**Value**
$\bar{n}_e$ min., max., mean	m^{-3}	$8.47 \cdot 10^{15}$, $6.38 \cdot 10^{17}$, $1.53 \cdot 10^{17}$
$\bar{n}_n$ min., max., mean	m^{-3}	$2.66 \cdot 10^{17}$, $8.67 \cdot 10^{17}$, $7.26 \cdot 10^{17}$
$\bar{n}_e$, $\bar{n}_n$ frequency, phase shift	kHz, deg	11.30, 72.28
I_d min., max., mean	A	$6.71 \cdot 10^{-2}$, $4.25 \cdot 10^{1}$, $6.62 \cdot 10^{0}$
$I_{i\infty}$ min., max., mean	A	$8.01 \cdot 10^{-2}$, $3.30 \cdot 10^{1}$, $4.89 \cdot 10^{0}$
I_d, $I_{i\infty}$ frequency, phase shift	kHz, deg	11.30, 20.24
I_{wi}, I_{prod}	A	3.16, 8.05
I_{sp}, F	s, mN	1578, 77.39
$P_{zi\infty}$, $P_{i\infty}$	W	717, 858
P_d, $\varepsilon_E^{P_d}$	W, -	1986, 0.51
P_{use}, $\varepsilon_E^{P_{use}}$	W, -	717, 0.18
P_{loss}, $\varepsilon_E^{P_{loss}}$	W, -	1226, 0.31
P_{walls}, $\varepsilon_E^{P_{walls}}$	W, -	1055, 0.27
$P_{ion,ex}$, $\varepsilon_E^{P_{ion,ex}}$	W, -	171, 0.04
η_{thr}, η_u, η_{cur}, η_{div}, η_{prod}	-	0.30, 0.95, 0.74, 0.84, 0.61
ν_{cat}, P_{cat}	MHz, W	16354, 30

Table B.2: Main results for the SPT-100 HET C3 simulation case. Mean values represent time-averaged values over the number of complete cycles within the last 450 μs of simulation time. The maximum and minimum values represent the average of the peak and trough values within that period. Please note that the value of $P_{zi\infty}$ does not contain the contribution of the neutral species. However, since this contribution is negligible compared to that of the ions, $P_{zi\infty}$ takes the value of P_{use} after truncation and approximation.

Variable	**Units**	**Value**
$\bar{n}_e$ min., max., mean	m^{-3}	$2.55 \cdot 10^{15}$, $8.60 \cdot 10^{17}$, $1.40 \cdot 10^{17}$
$\bar{n}_n$ min., max., mean	m^{-3}	$2.58 \cdot 10^{17}$, $1.22 \cdot 10^{18}$, $8.03 \cdot 10^{17}$
$\bar{n}_e$, $\bar{n}_n$ frequency, phase shift	kHz, deg	9.66, 69.28
I_d min., max., mean	A	$1.88 \cdot 10^{-2}$, $4.21 \cdot 10^{1}$, $6.01 \cdot 10^{0}$
$I_{i\infty}$ min., max., mean	A	$3.30 \cdot 10^{-2}$, $3.49 \cdot 10^{1}$, $4.74 \cdot 10^{0}$
I_d, $I_{i\infty}$ frequency, phase shift	kHz, deg	9.66, 17.22
I_{wi}, I_{prod}	A	2.67, 7.41
I_{sp}, F	s, mN	1667, 81.47
$P_{zi\infty}$, $P_{i\infty}$	W	780, 960
P_d, $\varepsilon_E^{P_d}$	W, -	1803, 0.51
P_{use}, $\varepsilon_E^{P_{use}}$	W, -	780, 0.22
P_{loss}, $\varepsilon_E^{P_{loss}}$	W, -	958, 0.27
P_{walls}, $\varepsilon_E^{P_{walls}}$	W, -	801, 0.23
$P_{ion,ex}$, $\varepsilon_E^{P_{ion,ex}}$	W, -	157, 0.04
η_{thr}, η_u, η_{cur}, η_{div}, η_{prod}	-	0.37, 0.95, 0.79, 0.81, 0.64
ν_{cat}, P_{cat}	MHz, W	16354, 27

Table B.3: Main results for the SPT-100 HET C4 simulation case. Mean values represent time-averaged values over the number of complete cycles within the last 450 μs of simulation time. The maximum and minimum values represent the average of the peak and trough values within that period. Please note that the value of $P_{zi\infty}$ does not contain the contribution of the neutral species. However, since this contribution is negligible compared to that of the ions, $P_{zi\infty}$ takes the value of P_{use} after truncation and approximation.

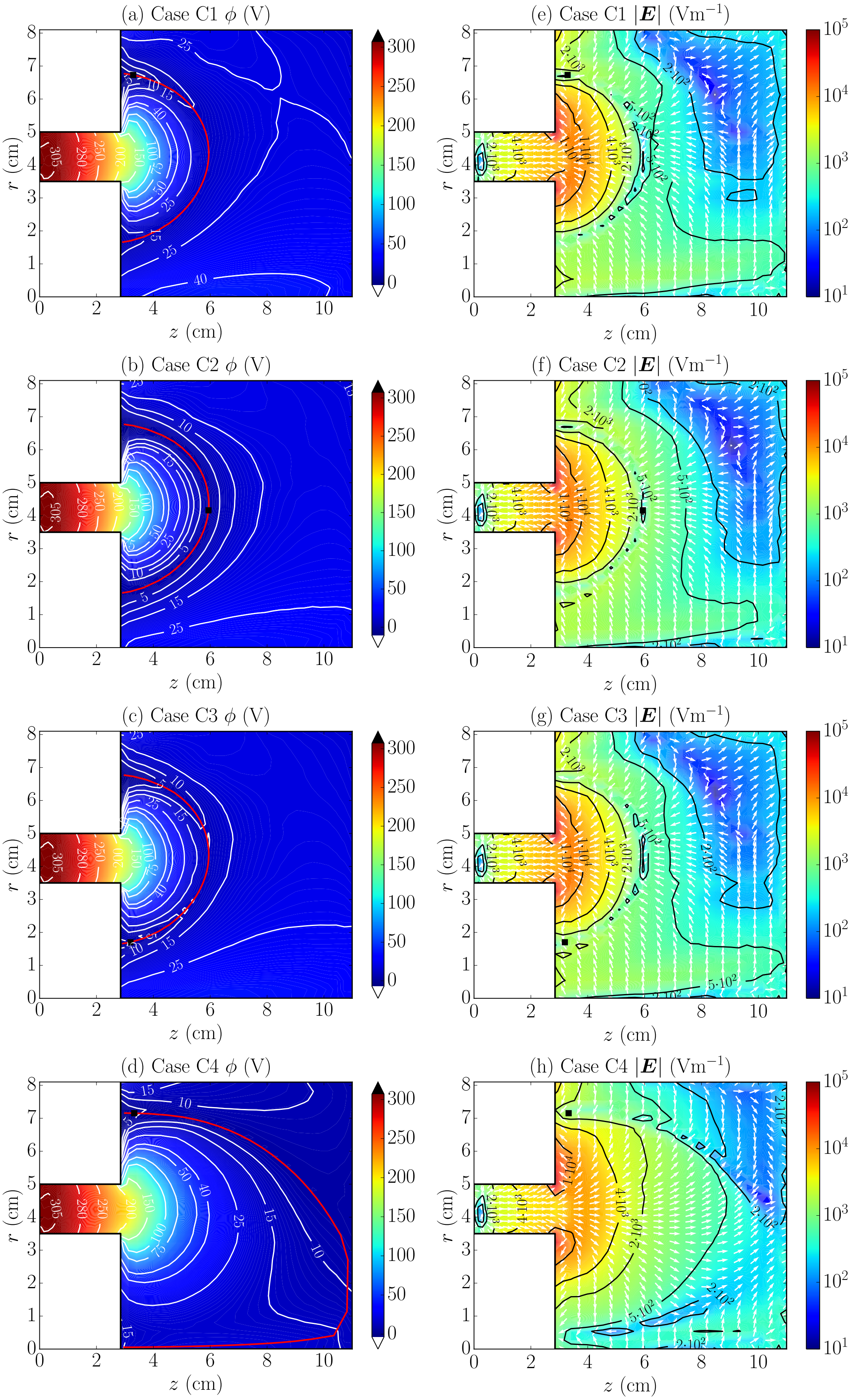

Figure B.1: Time-averaged electric potential (a)-(d) and electric field (e)-(h) 2D contour plots for the simulation cases C1-C4, respectively. The black square marker indicates the cathode position for each case.

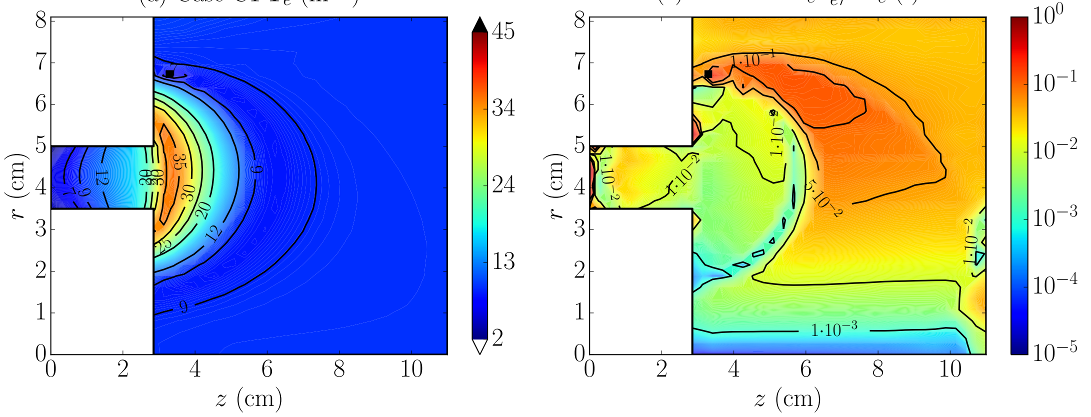
(a) Case C1 T_e (m^{-3}) (e) Case C1 $m_e u_e^2/2T_e$ (-)

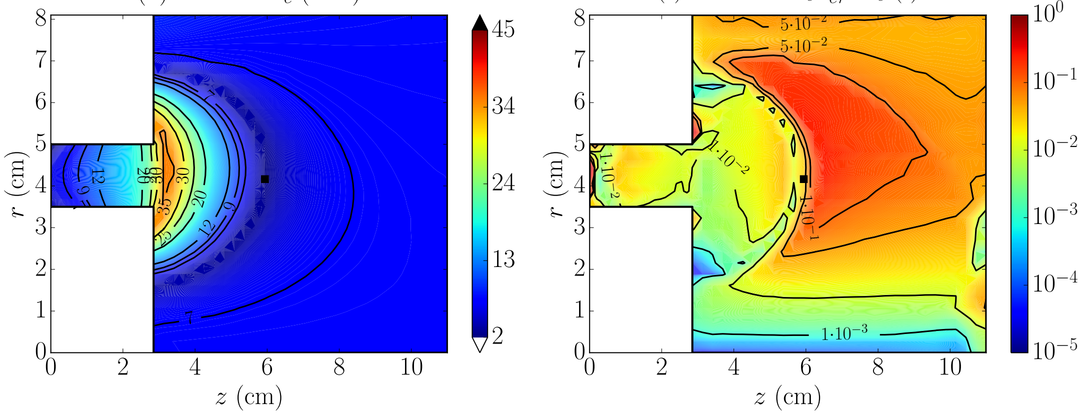
(b) Case C2 T_e (m^{-3}) (f) Case C2 $m_e u_e^2/2T_e$ (-)

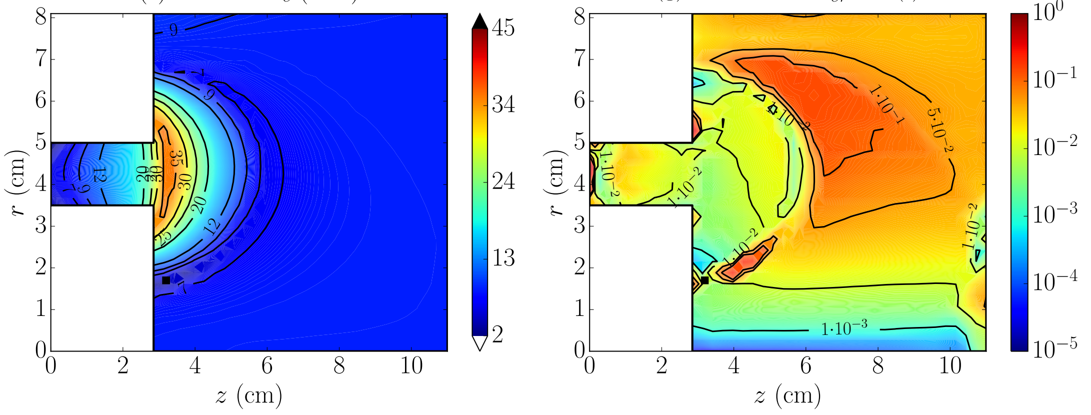
(c) Case C3 T_e (m^{-3}) (g) Case C3 $m_e u_e^2/2T_e$ (-)

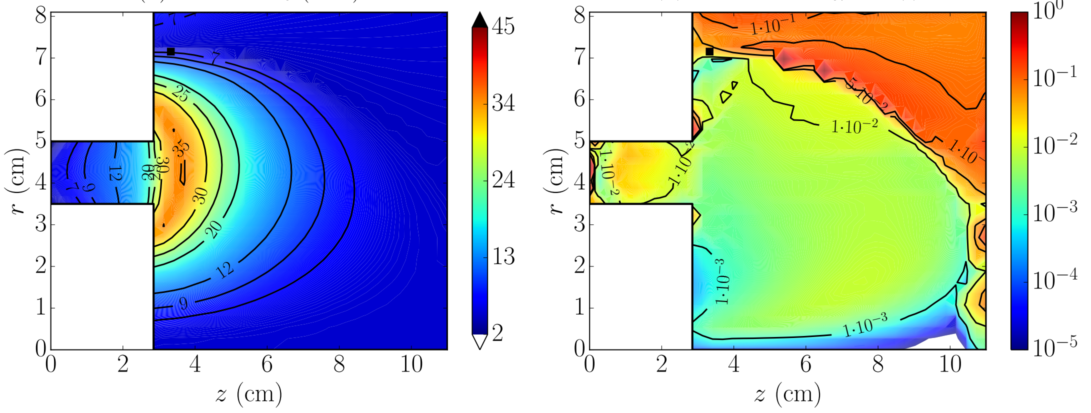
(d) Case C4 T_e (m^{-3}) (h) Case C4 $m_e u_e^2/2T_e$ (-)

Figure B.2: Time-averaged electron temperature (a)-(d) and electron drift-to-internal energy ratio (e)-(h) 2D contour plots for the simulation cases C1-C4, respectively. The black square marker indicates the cathode position for each case.

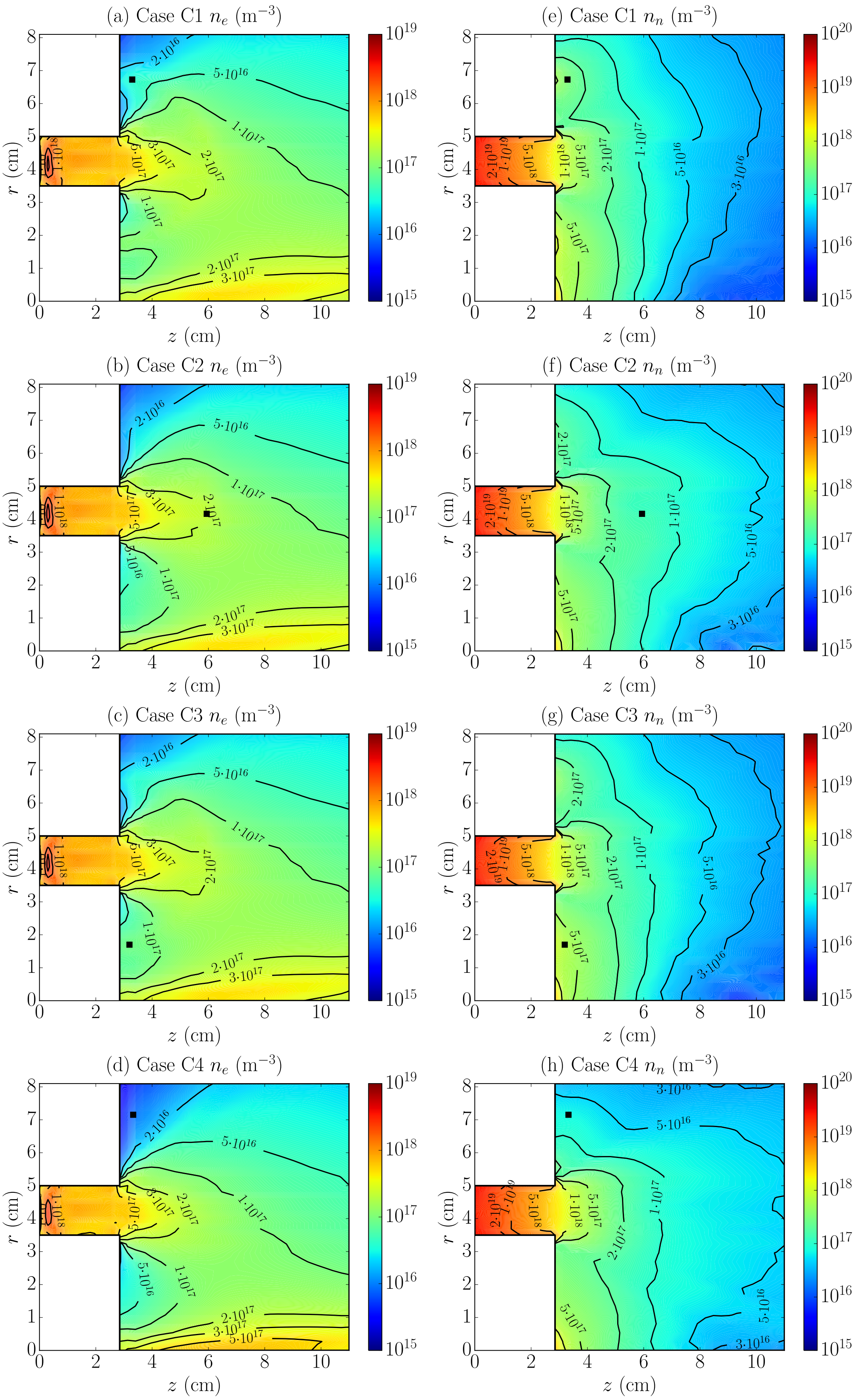

Figure B.3: Time-averaged plasma density (a)-(d) and neutrals particle density (e)-(h) 2D contour plots for the simulation cases C1-C4, respectively. The black square marker indicates the cathode position for each case.

(a) Case C1 n_{i1} ($\mathrm{m^{-3}}$) (e) Case C1 n_{i2}/n_{i1} (-)

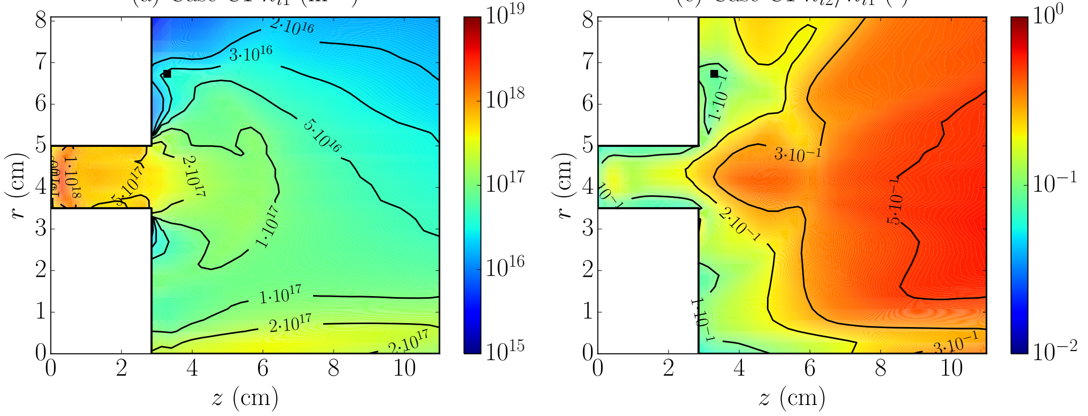

(b) Case C2 n_{i1} ($\mathrm{m^{-3}}$) (f) Case C2 n_{i2}/n_{i1} (-)

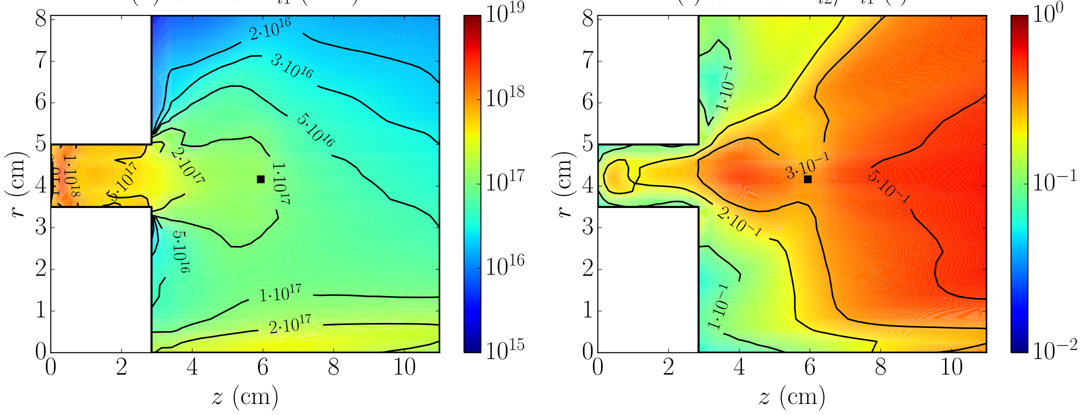

(c) Case C3 n_{i1} ($\mathrm{m^{-3}}$) (g) Case C3 n_{i2}/n_{i1} (-)

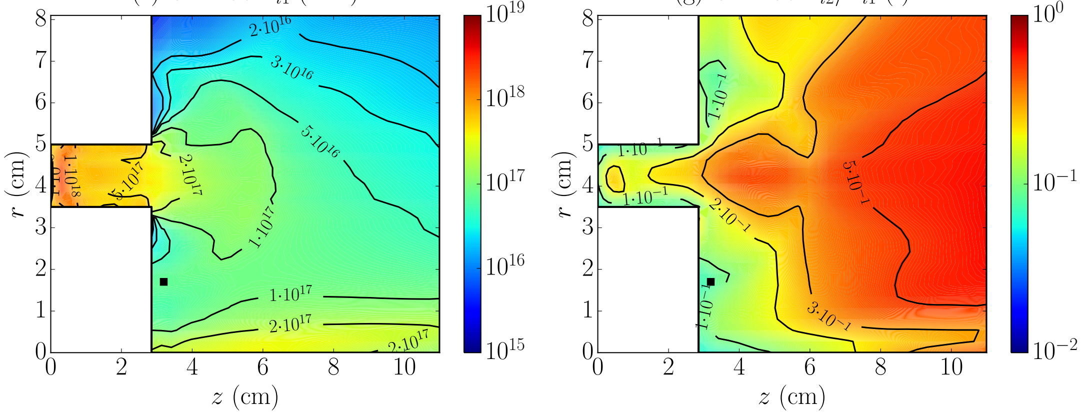

(d) Case C4 n_{i1} ($\mathrm{m^{-3}}$) (h) Case C4 n_{i2}/n_{i1} (-)

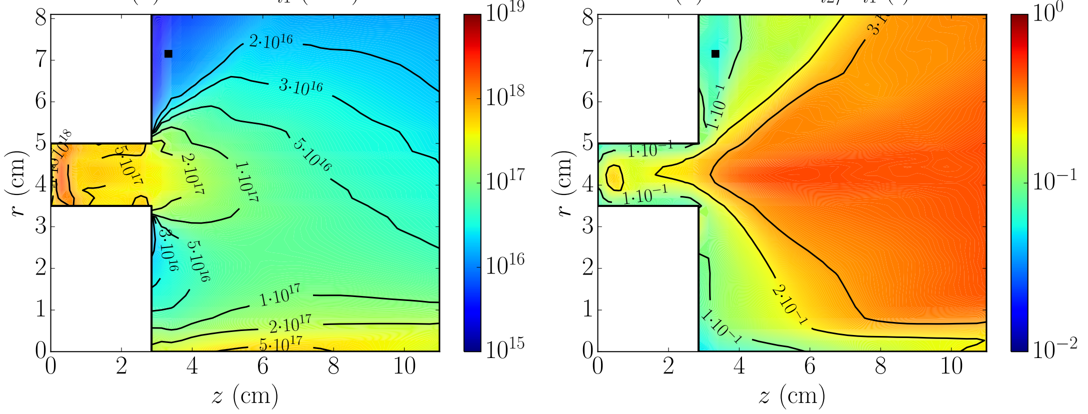

Figure B.4: Time-averaged singly charged ions particle density (a)-(d) and doubly-to-singly charged ions particle density ration (e)-(h) 2D contour plots for the simulation cases C1-C4, respectively. The black square marker indicates the cathode position for each case.

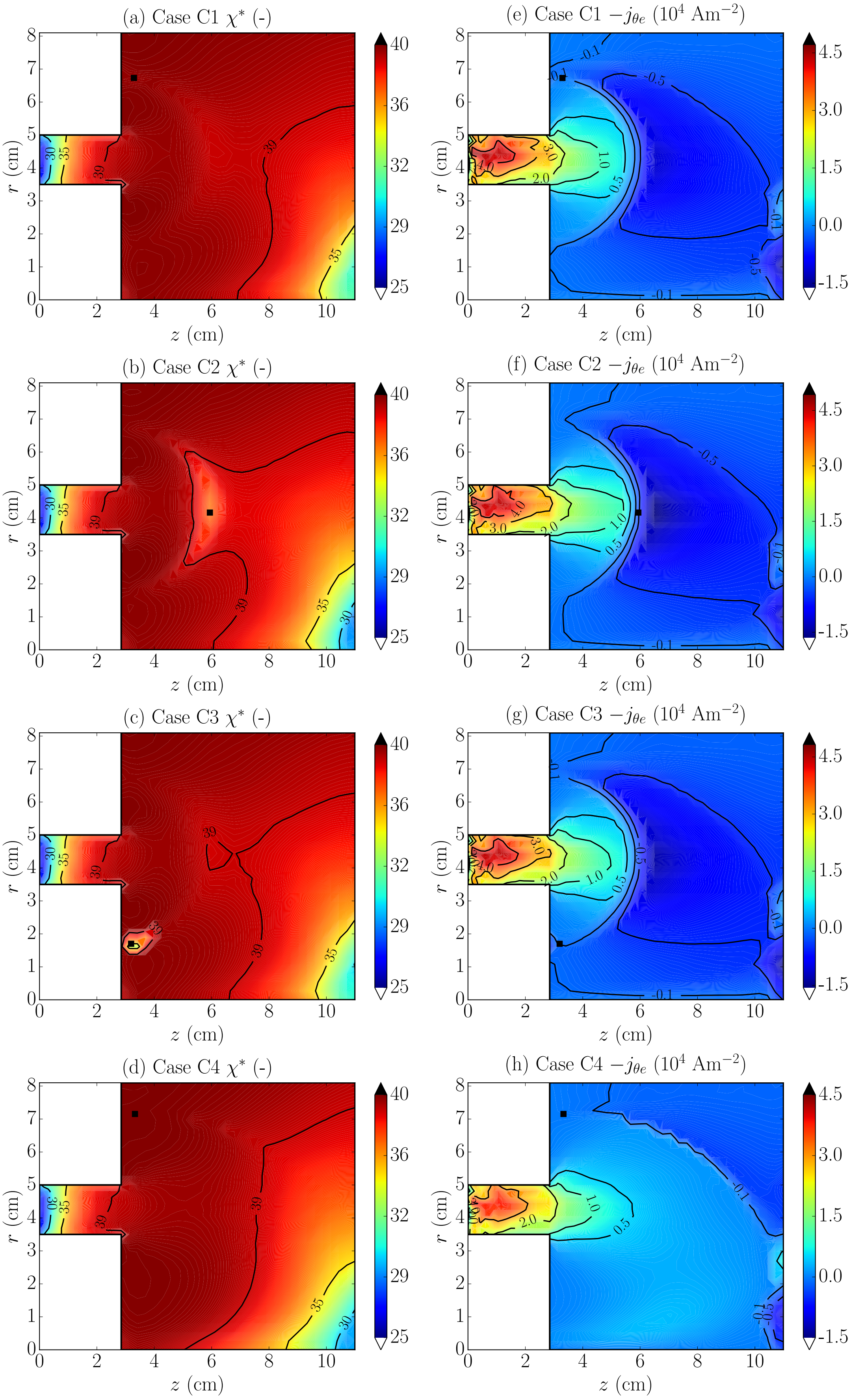

Figure B.5: Time-averaged effective Hall parameter (a)-(d) and electron azimuthal current density component (e)-(h) 2D contour plots for the simulation cases C1-C4, respectively. The black square marker indicates the cathode position for each case.

(a) Case C1 $-j_{\top e}$ (10^4 Am^{-2}) (e) Case C1 $-j_{\parallel e}$ (10^4 Am^{-2})

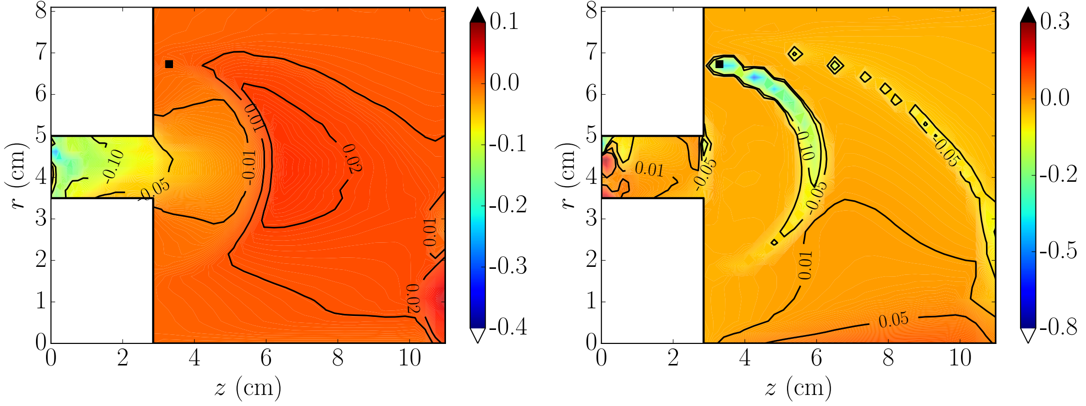

(b) Case C2 $-j_{\top e}$ (10^4 Am^{-2}) (f) Case C2 $-j_{\parallel e}$ (10^4 Am^{-2})

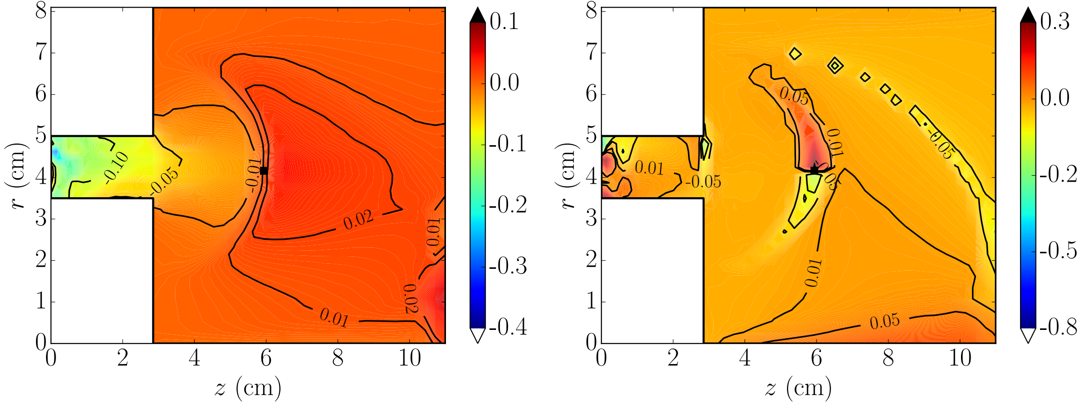

(c) Case C3 $-j_{\top e}$ (10^4 Am^{-2}) (g) Case C3 $-j_{\parallel e}$ (10^4 Am^{-2})

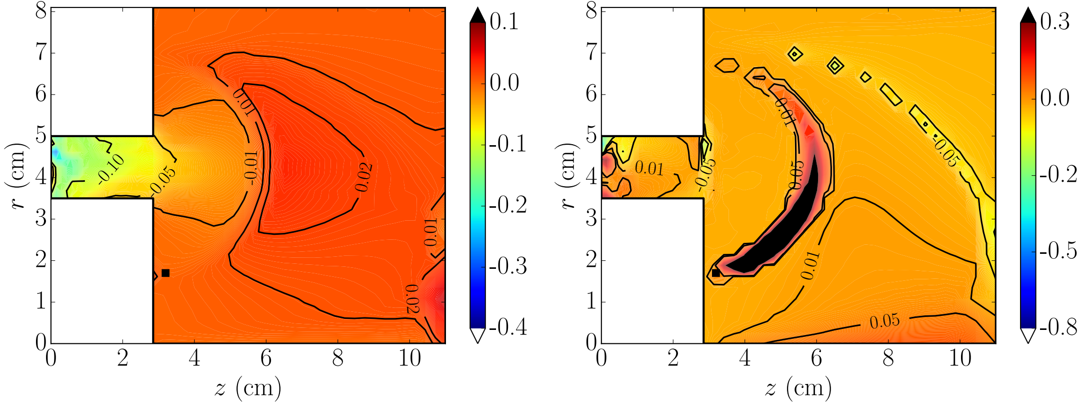

(d) Case C4 $-j_{\top e}$ (10^4 Am^{-2}) (h) Case C4 $-j_{\parallel e}$ (10^4 Am^{-2})

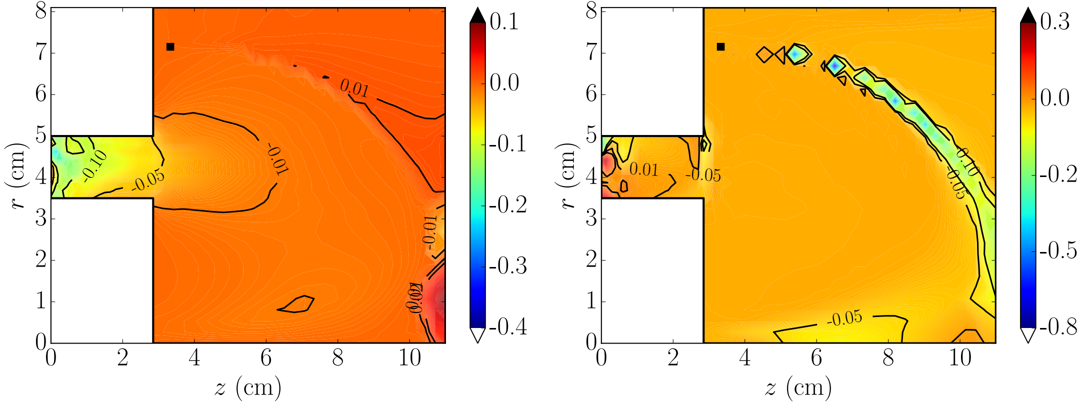

Figure B.6: Time-averaged electron perpendicular (a)-(d) and parallel (e)-(h) current density components 2D contour plots for the simulation cases C1-C4, respectively. The black square marker indicates the cathode position for each case.

(a) Case C1 $|\tilde{\boldsymbol{j}}_e|$ (Am^{-2}) (e) Case C1 $|\tilde{\boldsymbol{j}}_i|$ (Am^{-2})

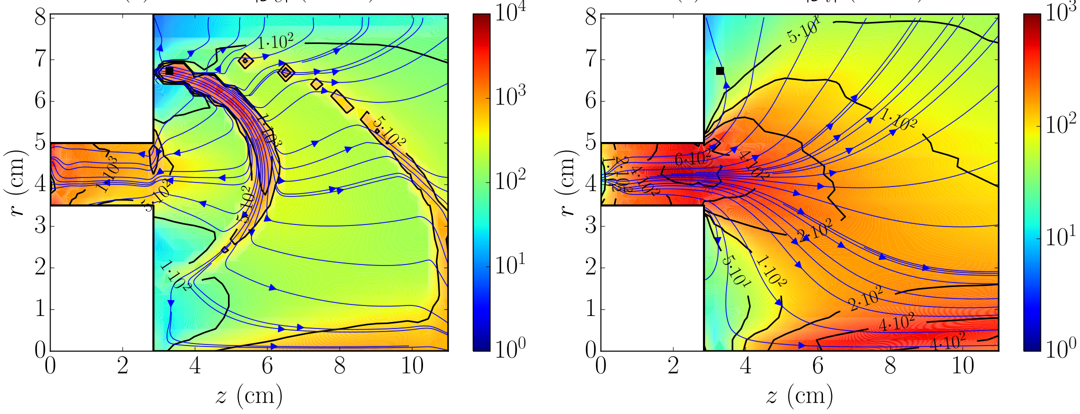

(b) Case C2 $|\tilde{\boldsymbol{j}}_e|$ (Am^{-2}) (f) Case C2 $|\tilde{\boldsymbol{j}}_i|$ (Am^{-2})

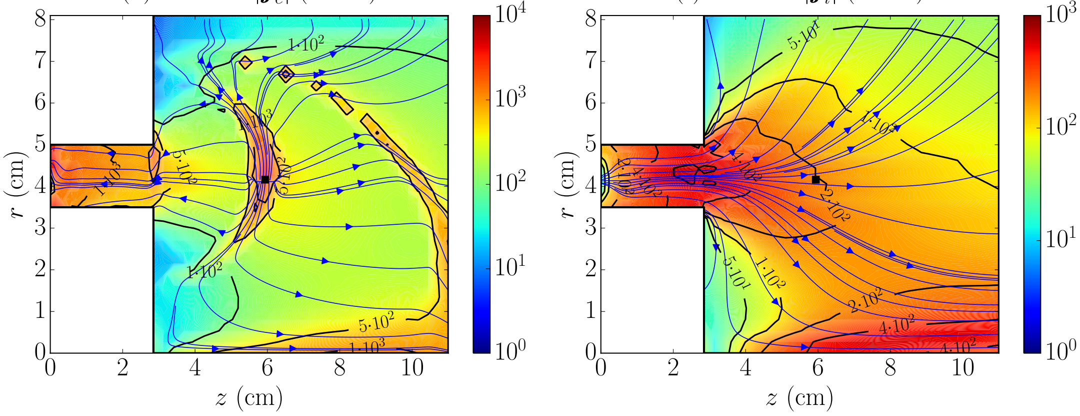

(c) Case C3 $|\tilde{\boldsymbol{j}}_e|$ (Am^{-2}) (g) Case C3 $|\tilde{\boldsymbol{j}}_i|$ (Am^{-2})

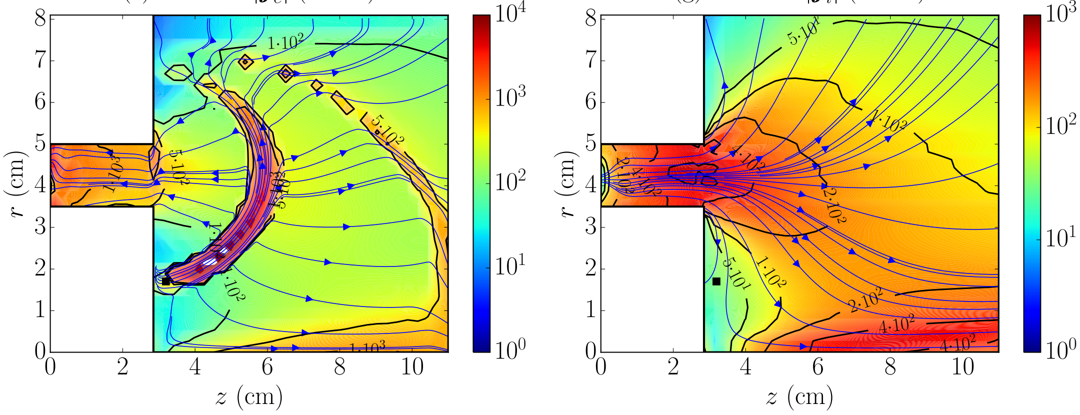

(d) Case C4 $|\tilde{\boldsymbol{j}}_e|$ (Am^{-2}) (h) Case C4 $|\tilde{\boldsymbol{j}}_i|$ (Am^{-2})

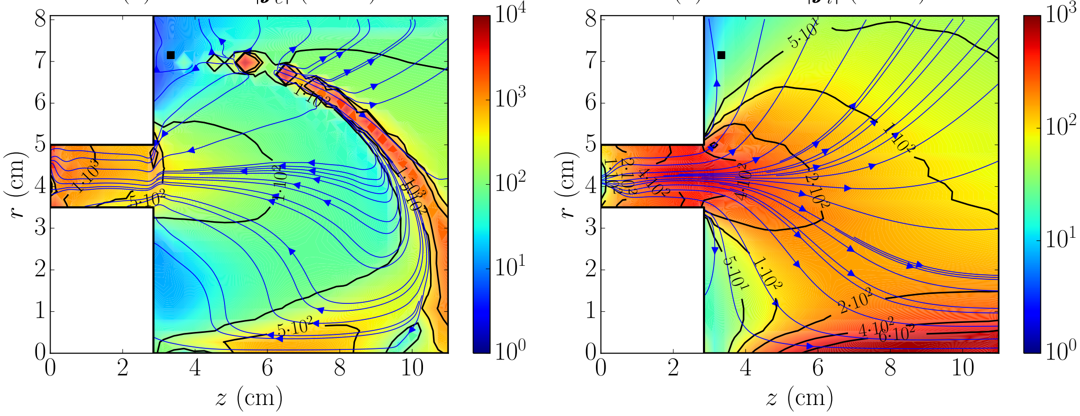

Figure B.7: 2D magnitude contour plots and streamlines of the time-averaged electron (a)-(d) and ion (e)-(h) 2D (z, r) current density vectors $-\tilde{\boldsymbol{j}}_e$ and $\tilde{\boldsymbol{j}}_i$, respectively, for the SPT-100 HET simulation cases C1-C4. The black square marker indicates the cathode position for each case.

B.2 HET simulation cases featuring different turbulent parameter profiles

Tabs. B.4-B.9 contains the relevant simulation results for the SPT-100 HET cases T2-T7 defined in Tab. 4.9 and analyzed in Sec. 4.2.2.5. In addition, Figs B.8-B.21 complete the results for the cases T2-T7 shown in Sec. 4.2.2.5 and have been included here for further analysis and discussion.

Variable	**Units**	**Value**
$\bar{n}_e$ min., max., mean	m^{-3}	$2.66 \cdot 10^{15}$, $7.40 \cdot 10^{17}$, $1.70 \cdot 10^{17}$
$\bar{n}_n$ min., max., mean	m^{-3}	$1.89 \cdot 10^{17}$, $1.13 \cdot 10^{18}$, $7.13 \cdot 10^{17}$
$\bar{n}_e$, $\bar{n}_n$ frequency, phase shift	kHz, deg	10.65, 64.14
I_d min., max., mean	A	$4.50 \cdot 10^{-2}$, $6.49 \cdot 10^{1}$, $9.40 \cdot 10^{0}$
$I_{i\infty}$ min., max., mean	A	$4.21 \cdot 10^{-2}$, $3.57 \cdot 10^{1}$, $5.41 \cdot 10^{0}$
I_d, $I_{i\infty}$ frequency, phase shift	kHz, deg	10.65, 15.78
I_{wi}, I_{prod}	A	4.26, 9.67
I_{sp}, F	s, mN	1636, 80.24
$P_{zi\infty}$, $P_{i\infty}$	W	774, 1034
P_d, $\varepsilon_E^{P_d}$	W, -	2821, 0.51
P_{use}, $\varepsilon_E^{P_{use}}$	W, -	774, 0.14
P_{loss}, $\varepsilon_E^{P_{loss}}$	W, -	1888, 0.35
P_{walls}, $\varepsilon_E^{P_{walls}}$	W, -	1663, 0.30
$P_{ion,ex}$, $\varepsilon_E^{P_{ion,ex}}$	W, -	225, 0.04
η_{thr}, η_u, η_{cur}, η_{div}, η_{prod}	-	0.23, 0.97, 0.58, 0.75, 0.56
ν_{cat}, P_{cat}	MHz, W	873, 42

Table B.4: Main results for the SPT-100 HET T2 simulation case. Mean values represent time-averaged values over the number of complete cycles within the last 450 μs of simulation time. The maximum and minimum values represent the average of the peak and trough values within that period. Please note that the value of $P_{zi\infty}$ does not contain the contribution of the neutral species. However, since this contribution is negligible compared to that of the ions, $P_{zi\infty}$ takes the value of P_{use} after truncation and approximation.

Variable	**Units**	**Value**
$\bar{n}_e$ min., max., mean	m^{-3}	$4.40 \cdot 10^{15}$, $8.40 \cdot 10^{17}$, $1.59 \cdot 10^{17}$
$\bar{n}_n$ min., max., mean	m^{-3}	$1.96 \cdot 10^{17}$, $1.00 \cdot 10^{18}$, $6.46 \cdot 10^{17}$
$\bar{n}_e$, $\bar{n}_n$ frequency, phase shift	kHz, deg	12.12, 68.09
I_d min., max., mean	A	$9.36 \cdot 10^{-2}$, $5.29 \cdot 10^{1}$, $7.35 \cdot 10^{0}$
$I_{i\infty}$ min., max., mean	A	$8.24 \cdot 10^{-2}$, $3.95 \cdot 10^{1}$, $5.20 \cdot 10^{0}$
I_d, $I_{i\infty}$ frequency, phase shift	kHz, deg	12.12, 21.27
I_{wi}, I_{prod}	A	3.47, 8.66
I_{sp}, F	s, mN	1597, 78.09
$P_{zi\infty}$, $P_{i\infty}$	W	731, 880
P_d, $\varepsilon_E^{P_d}$	W, -	2205, 0.51
P_{use}, $\varepsilon_E^{P_{use}}$	W, -	728, 0.17
P_{loss}, $\varepsilon_E^{P_{loss}}$	W, -	1385, 0.32
P_{walls}, $\varepsilon_E^{P_{walls}}$	W, -	1197, 0.28
$P_{ion,ex}$, $\varepsilon_E^{P_{ion,ex}}$	W, -	188, 0.04
η_{thr}, η_u, η_{cur}, η_{div}, η_{prod}	-	0.28, 0.98, 0.71, 0.83, 0.60
ν_{cat}, P_{cat}	MHz, W	906, 33

Table B.5: Main results for the SPT-100 HET T3 simulation case. Mean values represent time-averaged values over the number of complete cycles within the last 450 μs of simulation time. The maximum and minimum values represent the average of the peak and trough values within that period. Please note that the value of $P_{zi\infty}$ does not contain the contribution of the neutral species. However, since this contribution is negligible compared to that of the ions, $P_{zi\infty}$ takes the value of P_{use} after truncation and approximation.

Variable	**Units**	**Value**
$\bar{n}_e$ min., max., mean	m^{-3}	$4.41 \cdot 10^{15}$, $7.48 \cdot 10^{17}$, $1.64 \cdot 10^{17}$
$\bar{n}_n$ min., max., mean	m^{-3}	$1.66 \cdot 10^{17}$, $9.46 \cdot 10^{17}$, $6.09 \cdot 10^{17}$
$\bar{n}_e$, $\bar{n}_n$ frequency, phase shift	kHz, deg	12.74, 67.39
I_d min., max., mean	A	$1.29 \cdot 10^{-1}$, $5.72 \cdot 10^{1}$, $7.79 \cdot 10^{0}$
$I_{i\infty}$ min., max., mean	A	$1.04 \cdot 10^{-1}$, $4.10 \cdot 10^{1}$, $5.33 \cdot 10^{0}$
I_d, $I_{i\infty}$ frequency, phase shift	kHz, deg	12.74, 21.94
I_{wi}, I_{prod}	A	3.61, 8.95
I_{sp}, F	s, mN	1615, 79.16
$P_{zi\infty}$, $P_{i\infty}$	W	754, 923
P_d, $\varepsilon_E^{P_d}$	W, -	2337, 0.50
P_{use}, $\varepsilon_E^{P_{use}}$	W, -	754, 0.16
P_{loss}, $\varepsilon_E^{P_{loss}}$	W, -	1544, 0.34
P_{walls}, $\varepsilon_E^{P_{walls}}$	W, -	1347, 0.30
$P_{ion,ex}$, $\varepsilon_E^{P_{ion,ex}}$	W, -	197, 0.04
η_{thr}, η_u, η_{cur}, η_{div}, η_{prod}	-	0.27, 0.99, 0.68, 0.82, 0.60
ν_{cat}, P_{cat}	MHz, W	2396, 35

Table B.6: Main results for the SPT-100 HET T4 simulation case. Mean values represent time-averaged values over the number of complete cycles within the last 450 μs of simulation time. The maximum and minimum values represent the average of the peak and trough values within that period. Please note that the value of $P_{zi\infty}$ does not contain the contribution of the neutral species. However, since this contribution is negligible compared to that of the ions, $P_{zi\infty}$ takes the value of P_{use} after truncation and approximation.

Variable	**Units**	**Value**
$\bar{n}_e$ min., max., mean	m^{-3}	$5.08 \cdot 10^{15}$, $5.92 \cdot 10^{17}$, $1.63 \cdot 10^{17}$
$\bar{n}_n$ min., max., mean	m^{-3}	$1.64 \cdot 10^{17}$, $9.04 \cdot 10^{17}$, $5.80 \cdot 10^{17}$
$\bar{n}_e$, $\bar{n}_n$ frequency, phase shift	kHz, deg	13.20, 68.05
I_d min., max., mean	A	$1.62 \cdot 10^{-1}$, $5.77 \cdot 10^{1}$, $8.08 \cdot 10^{0}$
$I_{i\infty}$ min., max., mean	A	$1.18 \cdot 10^{-1}$, $4.06 \cdot 10^{1}$, $5.28 \cdot 10^{0}$
I_d, $I_{i\infty}$ frequency, phase shift	kHz, deg	13.20, 22.61
I_{wi}, I_{prod}	A	3.92, 9.21
I_{sp}, F	s, mN	1658, 81.07
$P_{zi\infty}$, $P_{i\infty}$	W	792, 949
P_d, $\varepsilon_E^{P_d}$	W, -	2425, 0.50
P_{use}, $\varepsilon_E^{P_{use}}$	W, -	792, 0.16
P_{loss}, $\varepsilon_E^{P_{loss}}$	W, -	1615, 0.34
P_{walls}, $\varepsilon_E^{P_{walls}}$	W, -	1430, 0.30
$P_{ion,ex}$, $\varepsilon_E^{P_{ion,ex}}$	W, -	185, 0.04
η_{thr}, η_u, η_{cur}, η_{div}, η_{prod}	-	0.27, 0.98, 0.65, 0.83, 0.57
ν_{cat}, P_{cat}	MHz, W	3857, 30

Table B.7: Main results for the SPT-100 HET T5 simulation case. Mean values represent time-averaged values over the number of complete cycles within the last 450 μs of simulation time. The maximum and minimum values represent the average of the peak and trough values within that period. Please note that the value of $P_{zi\infty}$ does not contain the contribution of the neutral species. However, since this contribution is negligible compared to that of the ions, $P_{zi\infty}$ takes the value of P_{use} after truncation and approximation.

Variable	**Units**	**Value**
$\bar{n}_e$ min., max., mean	m^{-3}	$6.00 \cdot 10^{15}$, $9.21 \cdot 10^{17}$, $1.59 \cdot 10^{17}$
$\bar{n}_n$ min., max., mean	m^{-3}	$1.82 \cdot 10^{17}$, $8.94 \cdot 10^{17}$, $5.85 \cdot 10^{17}$
$\bar{n}_e$, $\bar{n}_n$ frequency, phase shift	kHz, deg	13.61, 69.16
I_d min., max., mean	A	$1.81 \cdot 10^{-1}$, $4.93 \cdot 10^{1}$, $7.24 \cdot 10^{0}$
$I_{i\infty}$ min., max., mean	A	$1.40 \cdot 10^{-1}$, $3.72 \cdot 10^{1}$, $5.14 \cdot 10^{0}$
I_d, $I_{i\infty}$ frequency, phase shift	kHz, deg	13.61, 22.57
I_{wi}, I_{prod}	A	3.55, 8.69
I_{sp}, F	s, mN	1626, 79.18
$P_{zi\infty}$, $P_{i\infty}$	W	752, 919
P_d, $\varepsilon_E^{P_d}$	W, -	2172, 0.50
P_{use}, $\varepsilon_E^{P_{use}}$	W, -	752, 0.17
P_{loss}, $\varepsilon_E^{P_{loss}}$	W, -	1459, 0.33
P_{walls}, $\varepsilon_E^{P_{walls}}$	W, -	1256, 0.29
$P_{ion,ex}$, $\varepsilon_E^{P_{ion,ex}}$	W, -	163, 0.04
η_{thr}, η_u, η_{cur}, η_{div}, η_{prod}	-	0.29, 0.98, 0.71, 0.82, 0.59
ν_{cat}, P_{cat}	MHz, W	3598, 33

Table B.8: Main results for the SPT-100 HET T6 simulation case. Mean values represent time-averaged values over the number of complete cycles within the last 450 μs of simulation time. The maximum and minimum values represent the average of the peak and trough values within that period. Please note that the value of $P_{zi\infty}$ does not contain the contribution of the neutral species. However, since this contribution is negligible compared to that of the ions, $P_{zi\infty}$ takes the value of P_{use} after truncation and approximation.

Variable	**Units**	**Value**
$\bar{n}_e$ min., max., mean	m^{-3}	$8.39 \cdot 10^{15}$, $4.55 \cdot 10^{17}$, $1.50 \cdot 10^{17}$
$\bar{n}_n$ min., max., mean	m^{-3}	$2.29 \cdot 10^{17}$, $7.89 \cdot 10^{17}$, $5.97 \cdot 10^{17}$
$\bar{n}_e$, $\bar{n}_n$ frequency, phase shift	kHz, deg	14.04, 74.22
I_d min., max., mean	A	$2.26 \cdot 10^{-1}$, $3.58 \cdot 10^{1}$, $6.33 \cdot 10^{0}$
$I_{i\infty}$ min., max., mean	A	$2.31 \cdot 10^{-1}$, $3.04 \cdot 10^{1}$, $4.91 \cdot 10^{0}$
I_d, $I_{i\infty}$ frequency, phase shift	kHz, deg	14.04, 25.15
I_{wi}, I_{prod}	A	3.13, 8.03
I_{sp}, F	s, mN	1609, 78.84
$P_{zi\infty}$, $P_{i\infty}$	W	745, 875
P_d, $\varepsilon_E^{P_d}$	W, -	1899, 0.50
P_{use}, $\varepsilon_E^{P_{use}}$	W, -	745, 0.20
P_{loss}, $\varepsilon_E^{P_{loss}}$	W, -	1153, 0.30
P_{walls}, $\varepsilon_E^{P_{walls}}$	W, -	1002, 0.26
$P_{ion,ex}$, $\varepsilon_E^{P_{ion,ex}}$	W, -	151, 0.04
η_{thr}, η_u, η_{cur}, η_{div}, η_{prod}	-	0.33, 0.98, 0.78, 0.85, 0.61
ν_{cat}, P_{cat}	MHz, W	2908, 28

Table B.9: Main results for the SPT-100 HET T7 simulation case. Mean values represent time-averaged values over the number of complete cycles within the last 450 μs of simulation time. The maximum and minimum values represent the average of the peak and trough values within that period. Please note that the value of $P_{zi\infty}$ does not contain the contribution of the neutral species. However, since this contribution is negligible compared to that of the ions, $P_{zi\infty}$ takes the value of P_{use} after truncation and approximation.

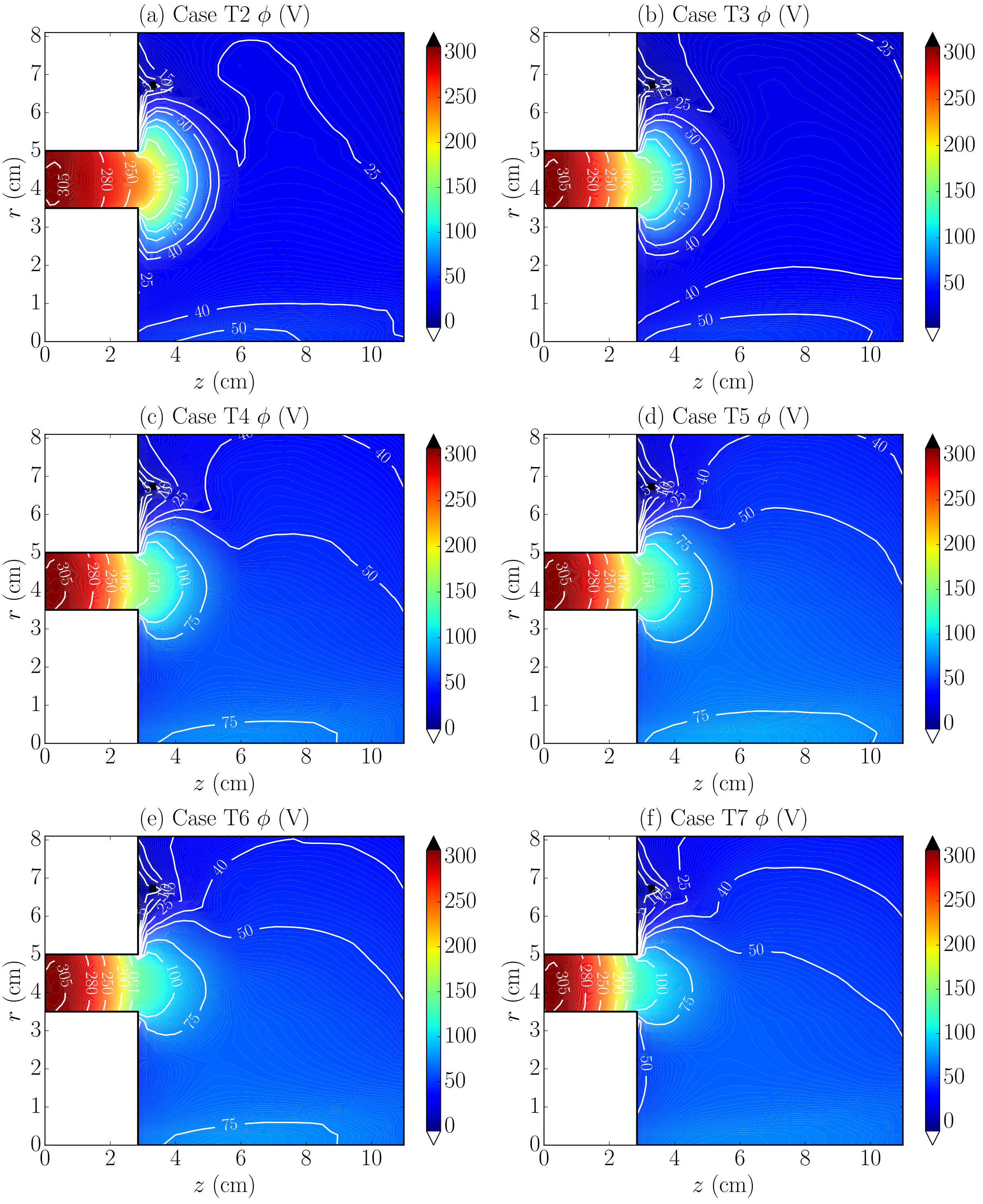
(a) Case T2 ϕ (V)

(b) Case T3 ϕ (V)

(c) Case T4 ϕ (V)

(d) Case T5 ϕ (V)

(e) Case T6 ϕ (V)

(f) Case T7 ϕ (V)

Figure B.8: Time-averaged electric potential 2D contour plot for the simulation cases (a) T2, (b) T3, (c) T4, (d) T5, (e) T6 and (f) T7. The black square marker indicates the cathode position at C1 [see Fig. 4.6(b)].

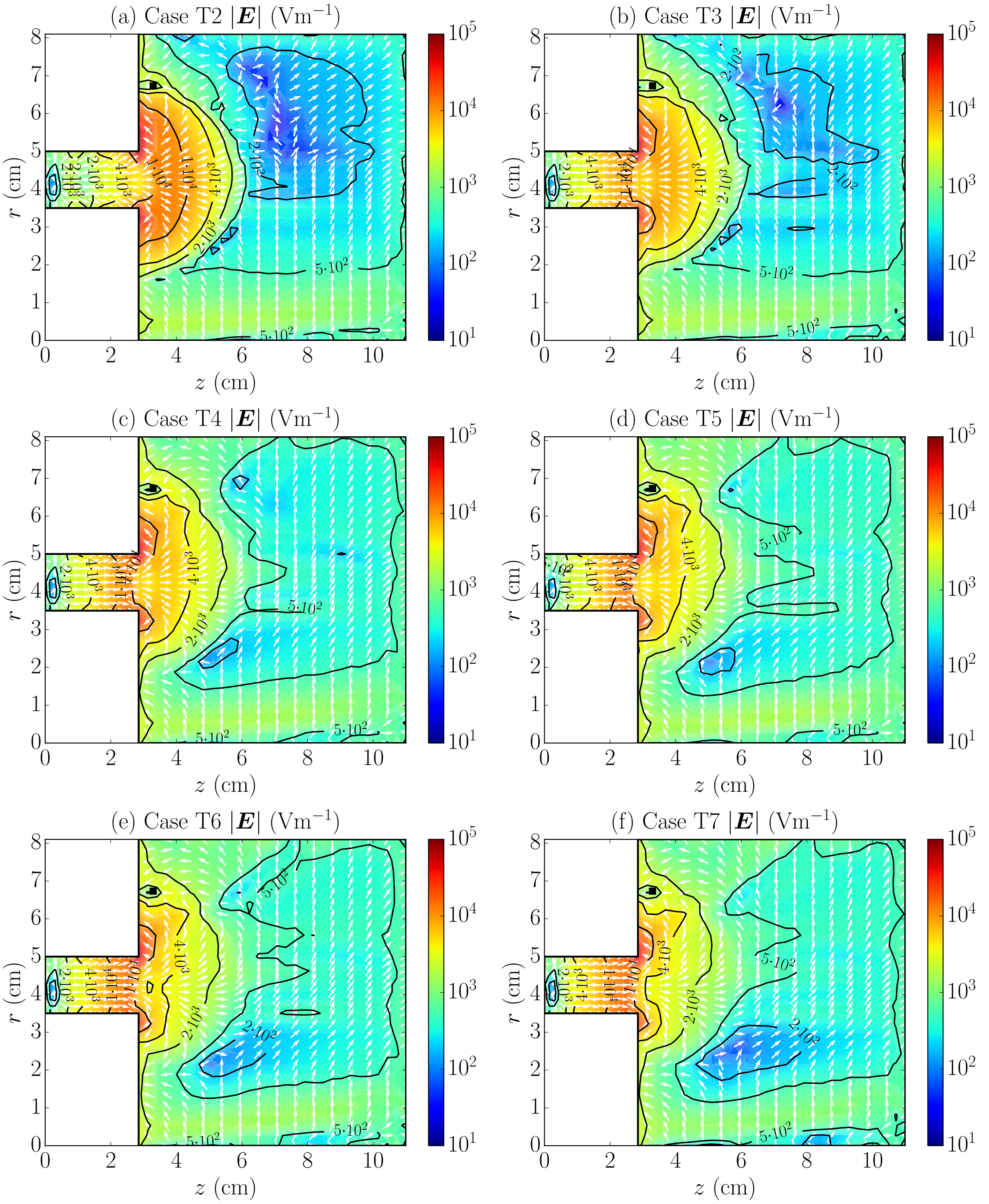

Figure B.9: Time-averaged electric potential 2D contour plot for the simulation cases (a) T2, (b) T3, (c) T4, (d) T5, (e) T6 and (f) T7. The black square marker indicates the cathode position at C1 [see Fig. 4.6(b)].

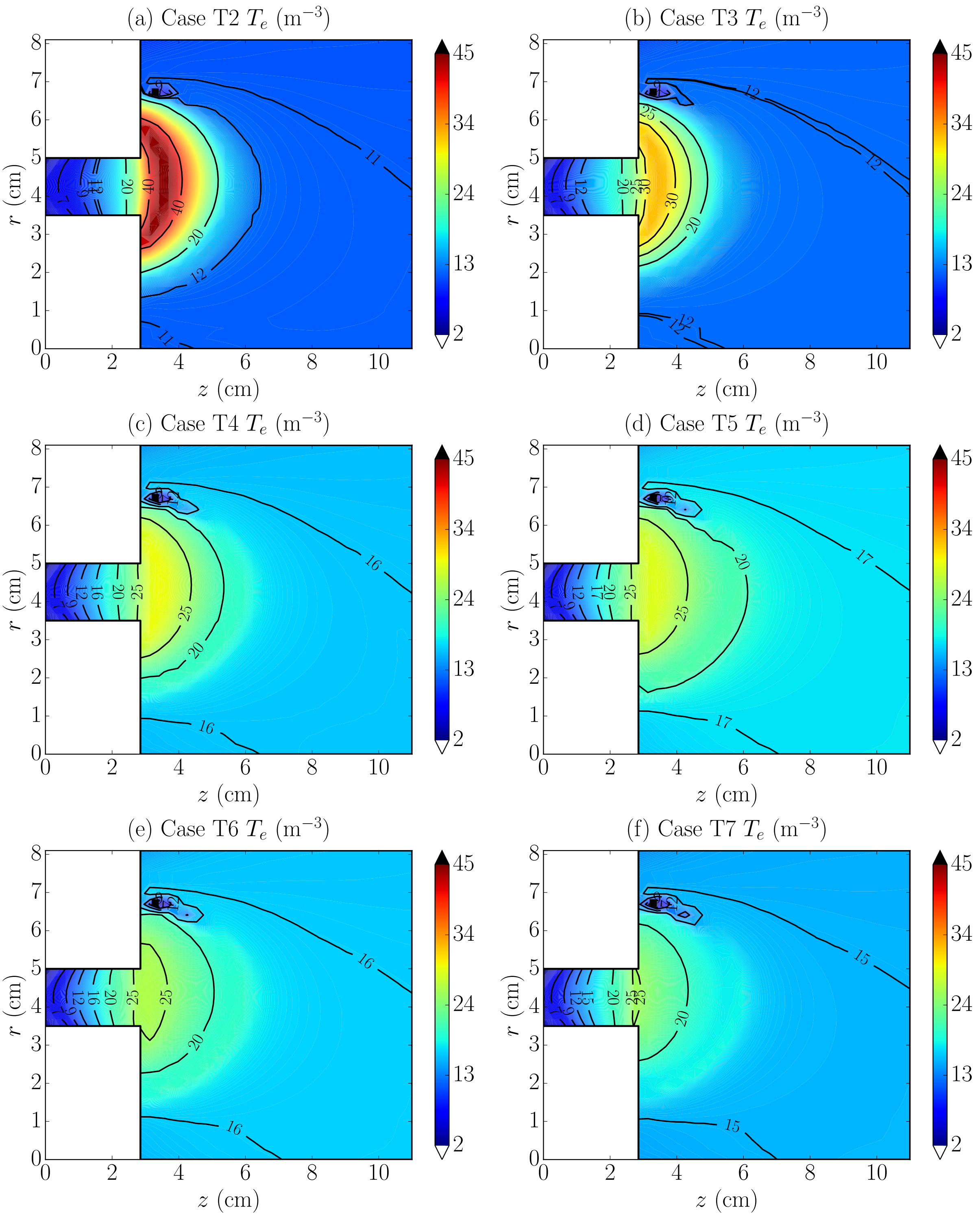

Figure B.10: Time-averaged electron temperature 2D contour plot for the simulation cases (a) T2, (b) T3, (c) T4, (d) T5, (e) T6 and (f) T7. The black square marker indicates the cathode position at C1 [see Fig. 4.6(b)].

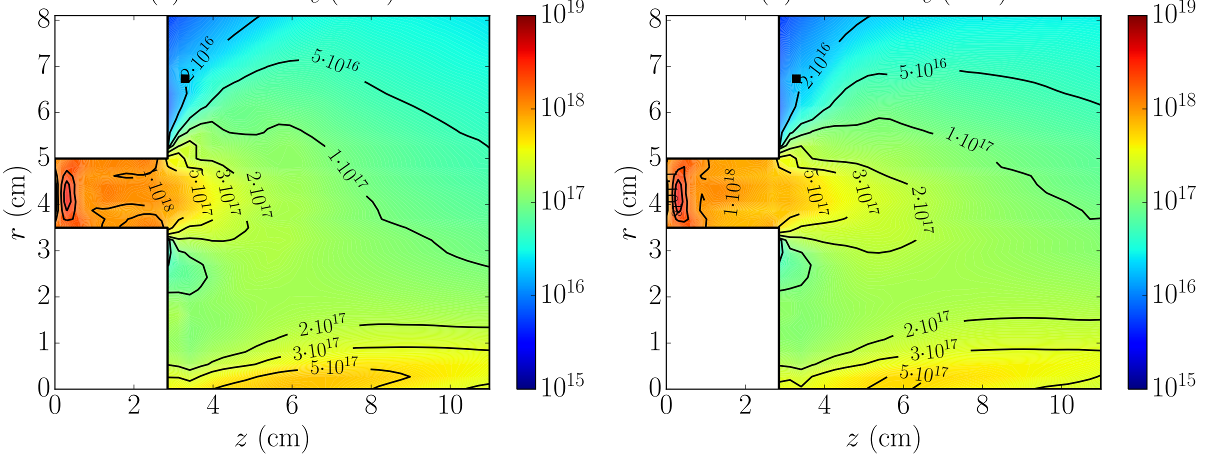
(a) Case T2 n_e (m^{-3})

(b) Case T3 n_e (m^{-3})

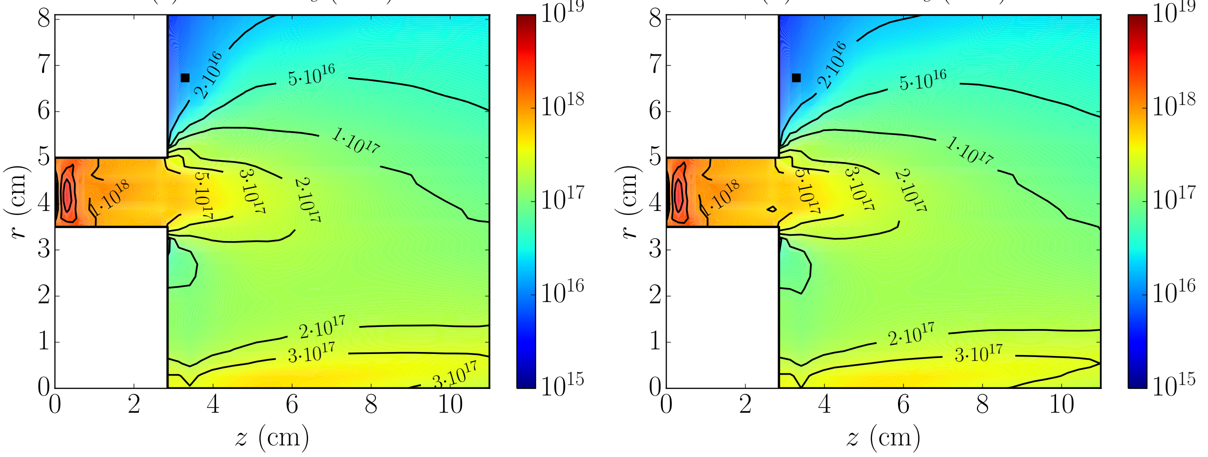
(c) Case T4 n_e (m^{-3})

(d) Case T5 n_e (m^{-3})

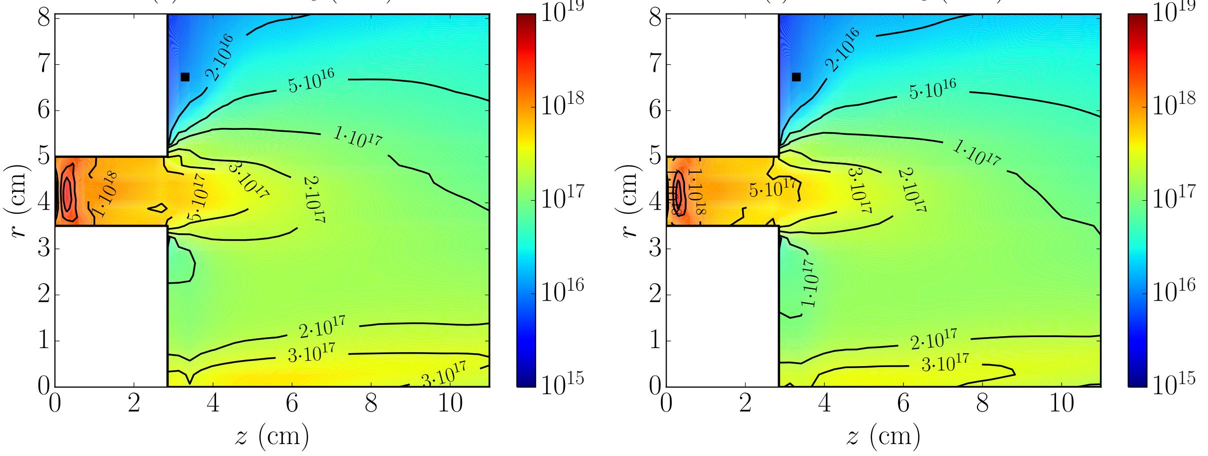
(e) Case T6 n_e (m^{-3})

(f) Case T7 n_e (m^{-3})

Figure B.11: Time-averaged plasma density 2D contour plot for the simulation cases (a) T2, (b) T3, (c) T4, (d) T5, (e) T6 and (f) T7. The black square marker indicates the cathode position at C1 [see Fig. 4.6(b)].

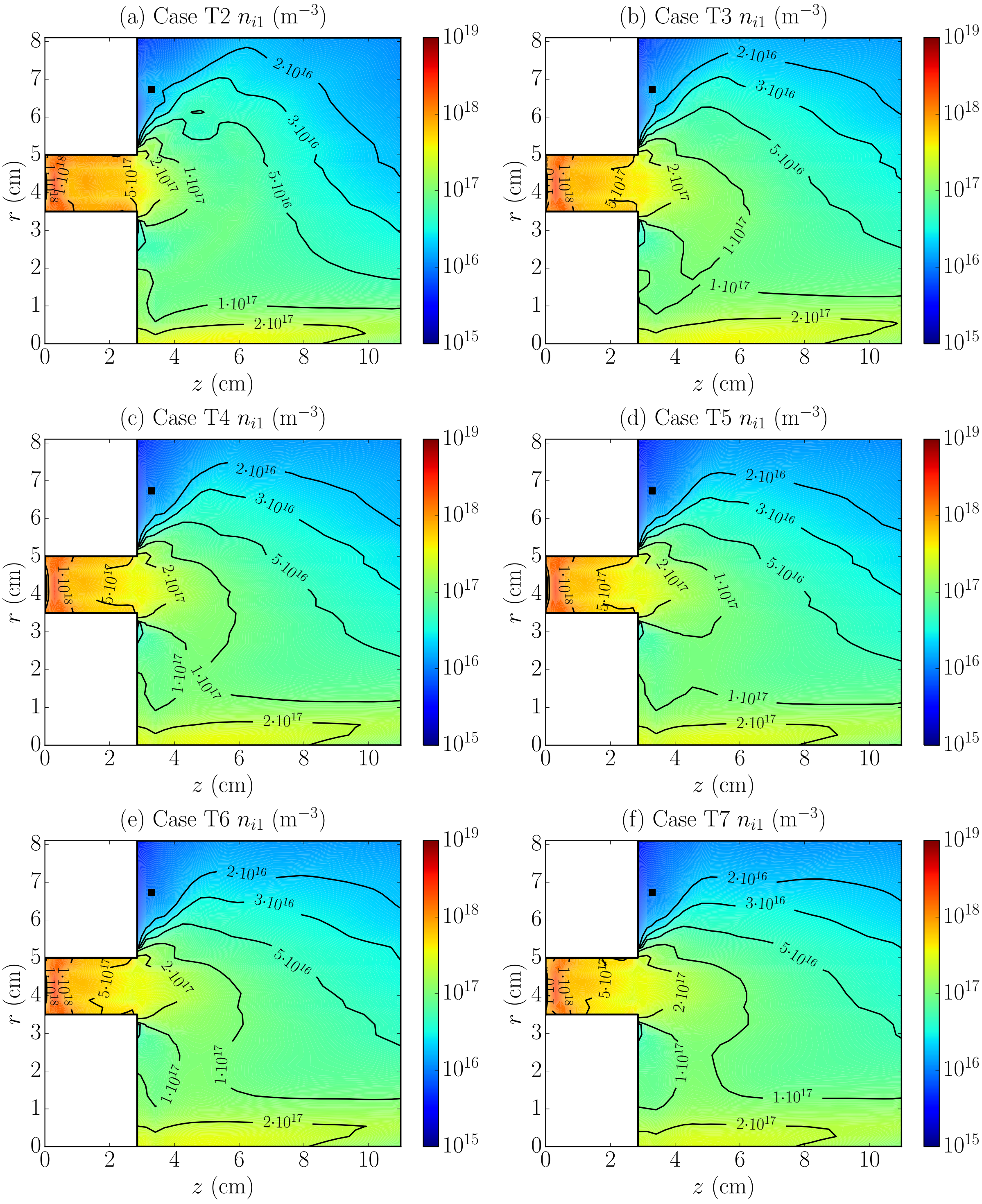
(a) Case T2 n_{i1} (m^{-3})

(b) Case T3 n_{i1} (m^{-3})

(c) Case T4 n_{i1} (m^{-3})

(d) Case T5 n_{i1} (m^{-3})

(e) Case T6 n_{i1} (m^{-3})

(f) Case T7 n_{i1} (m^{-3})

Figure B.12: Time-averaged singly charged ions particle density 2D contour plot for the simulation cases (a) T2, (b) T3, (c) T4, (d) T5, (e) T6 and (f) T7. The black square marker indicates the cathode position at C1 [see Fig. 4.6(b)].

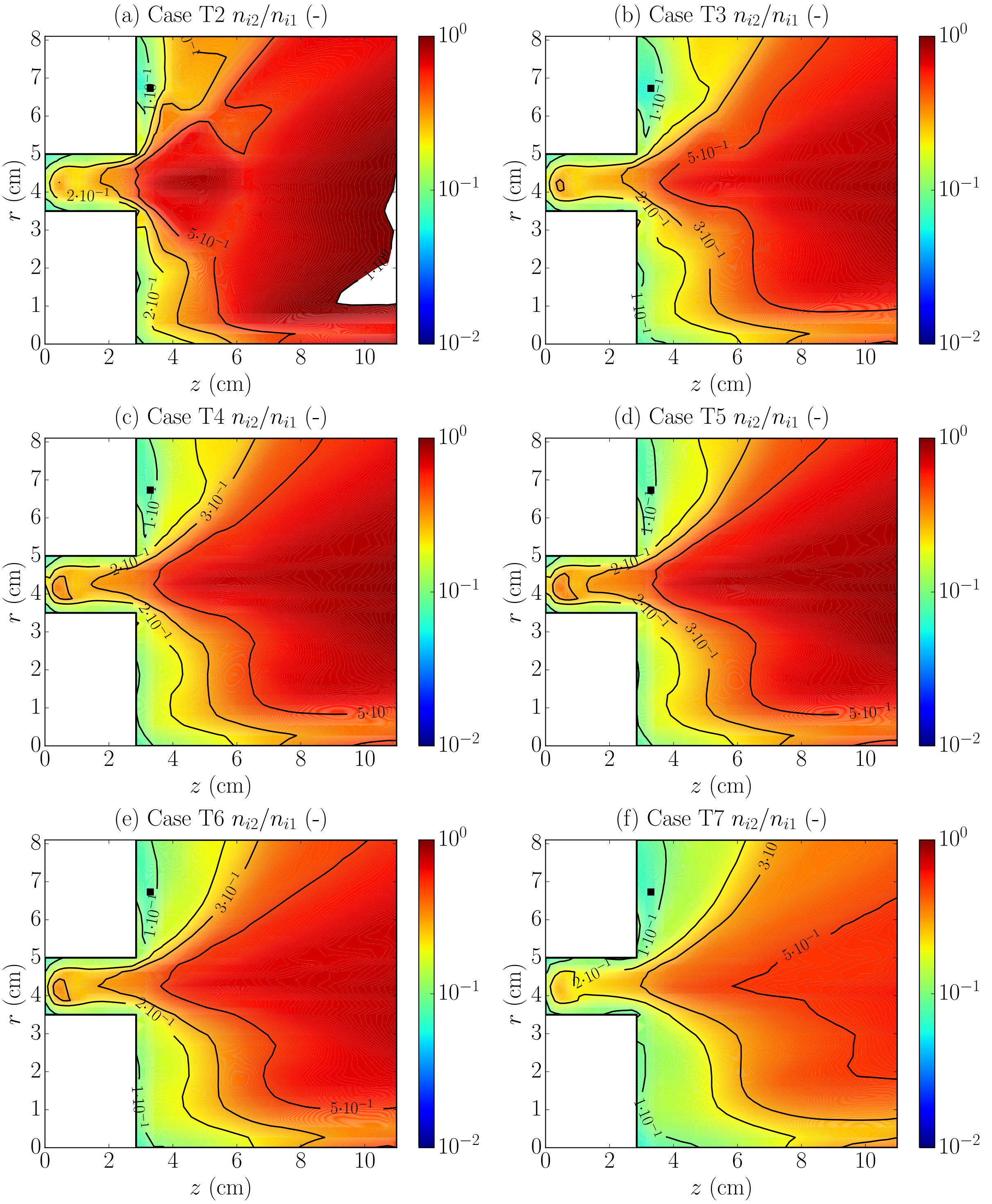

Figure B.13: Time-averaged doubly-to-singly charged ions particle density ratio 2D contour plot for the simulation cases (a) T2, (b) T3, (c) T4, (d) T5, (e) T6 and (f) T7. The black square marker indicates the cathode position at C1 [see Fig. 4.6(b)].

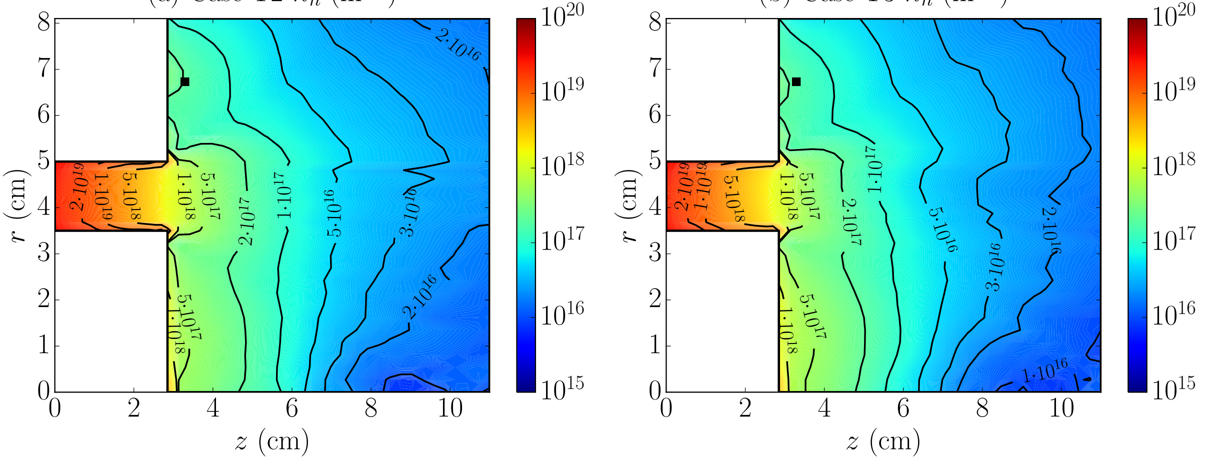
(a) Case T2 n_n (m^{-3})

(b) Case T3 n_n (m^{-3})

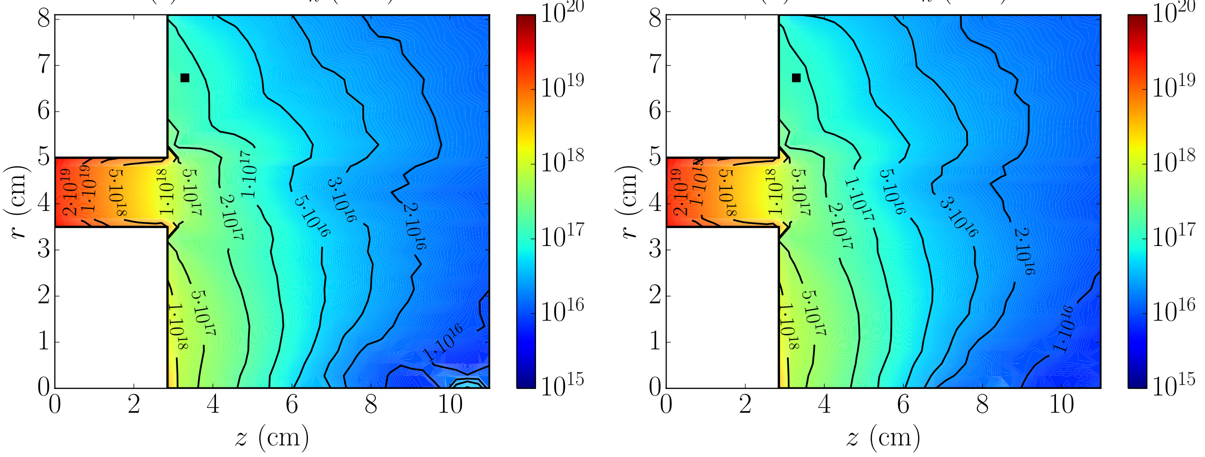
(c) Case T4 n_n (m^{-3})

(d) Case T5 n_n (m^{-3})

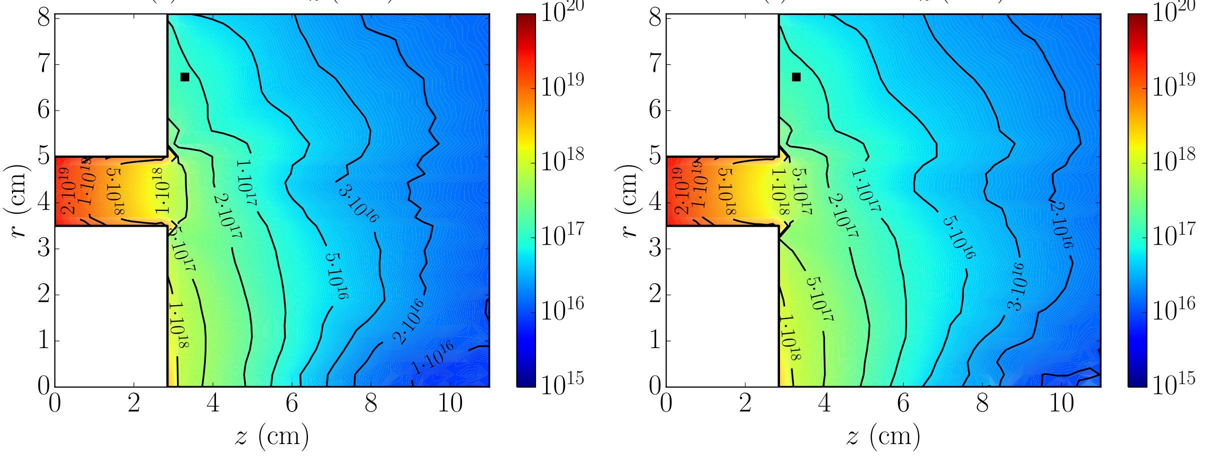
(e) Case T6 n_n (m^{-3})

(f) Case T7 n_n (m^{-3})

Figure B.14: Time-averaged neutrals particle density 2D contour plot for the simulation cases (a) T2, (b) T3, (c) T4, (d) T5, (e) T6 and (f) T7. The black square marker indicates the cathode position at C1 [see Fig. 4.6(b)].

(a) Case T2 ν_e^* (Hz) (b) Case T3 ν_e^* (Hz)

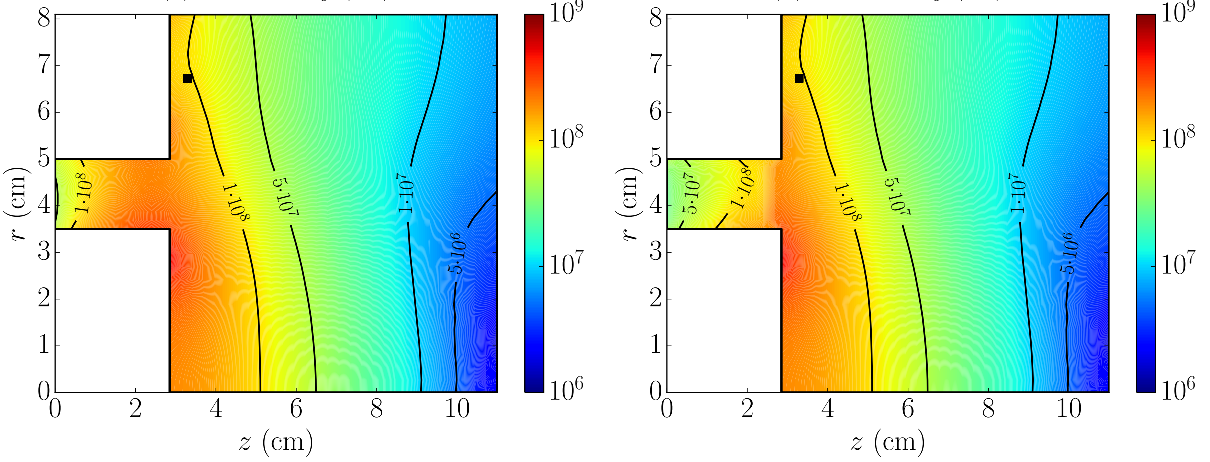

(c) Case T4 ν_e^* (Hz) (d) Case T5 ν_e^* (Hz)

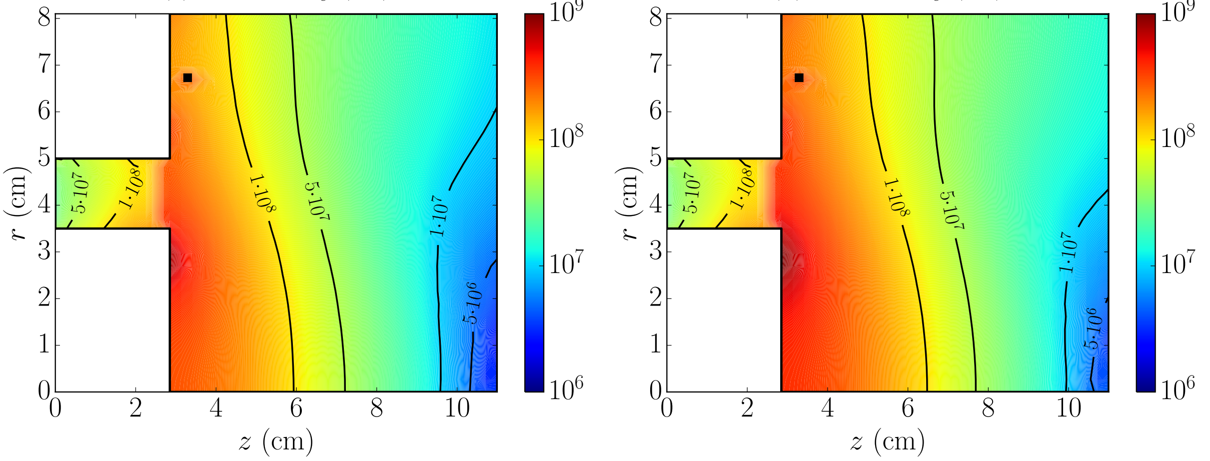

(e) Case T6 ν_e^* (Hz) (f) Case T7 ν_e^* (Hz)

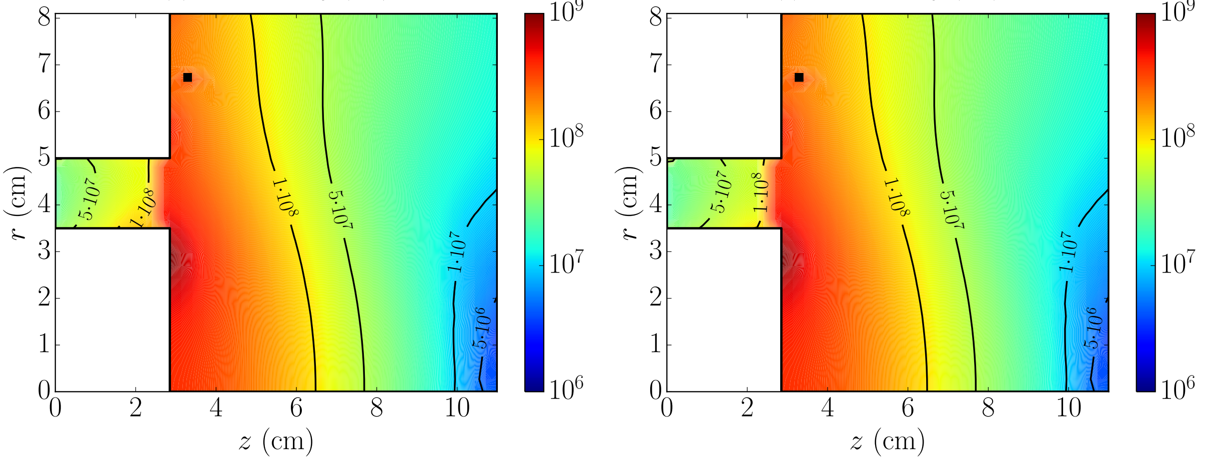

Figure B.15: Time-averaged electron effective collision frequency 2D contour plot for the simulation cases (a) T2, (b) T3, (c) T4, (d) T5, (e) T6 and (f) T7. The black square marker indicates the cathode position at C1 [see Fig. 4.6(b)].

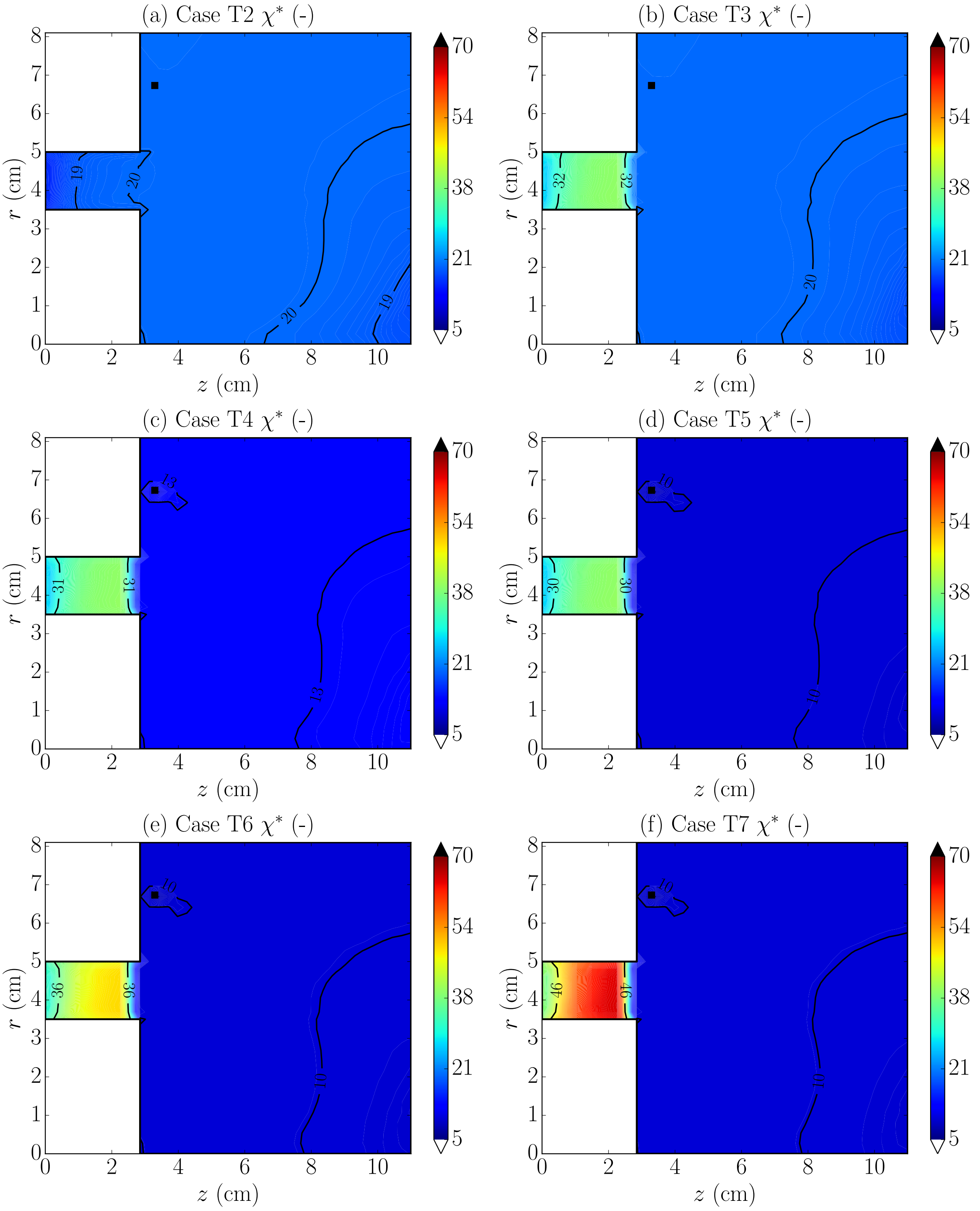

Figure B.16: Time-averaged effective Hall parameter 2D contour plot for the simulation cases (a) T2, (b) T3, (c) T4, (d) T5, (e) T6 and (f) T7. The black square marker indicates the cathode position at C1 [see Fig. 4.6(b)].

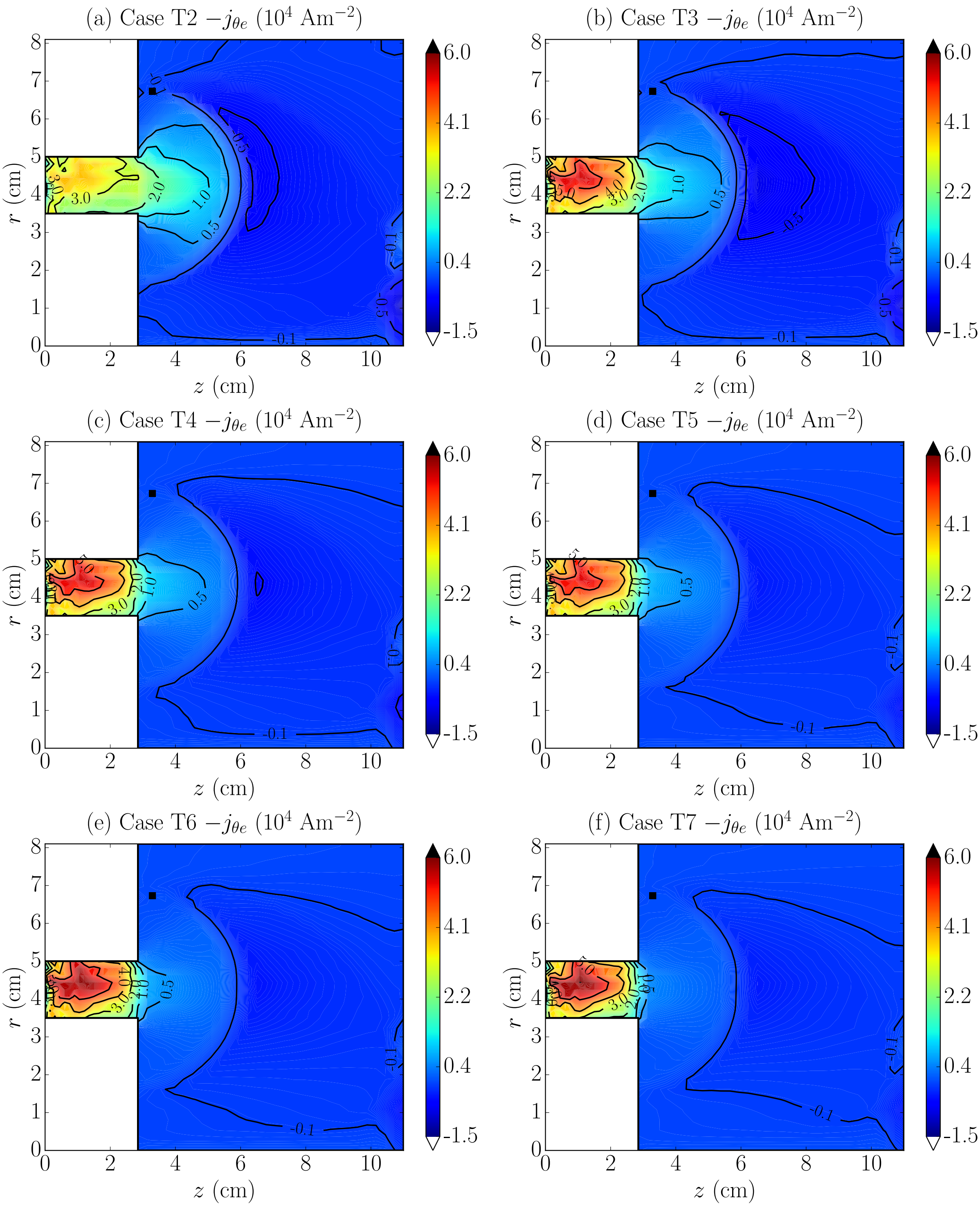
(a) Case T2 $-j_{\theta e}$ (10^4 Am^{-2})

(b) Case T3 $-j_{\theta e}$ (10^4 Am^{-2})

(c) Case T4 $-j_{\theta e}$ (10^4 Am^{-2})

(d) Case T5 $-j_{\theta e}$ (10^4 Am^{-2})

(e) Case T6 $-j_{\theta e}$ (10^4 Am^{-2})

(f) Case T7 $-j_{\theta e}$ (10^4 Am^{-2})

Figure B.17: Time-averaged electron azimuthal current density component 2D contour plot for the simulation cases (a) T2, (b) T3, (c) T4, (d) T5, (e) T6 and (f) T7. The black square marker indicates the cathode position at C1 [see Fig. 4.6(b)].

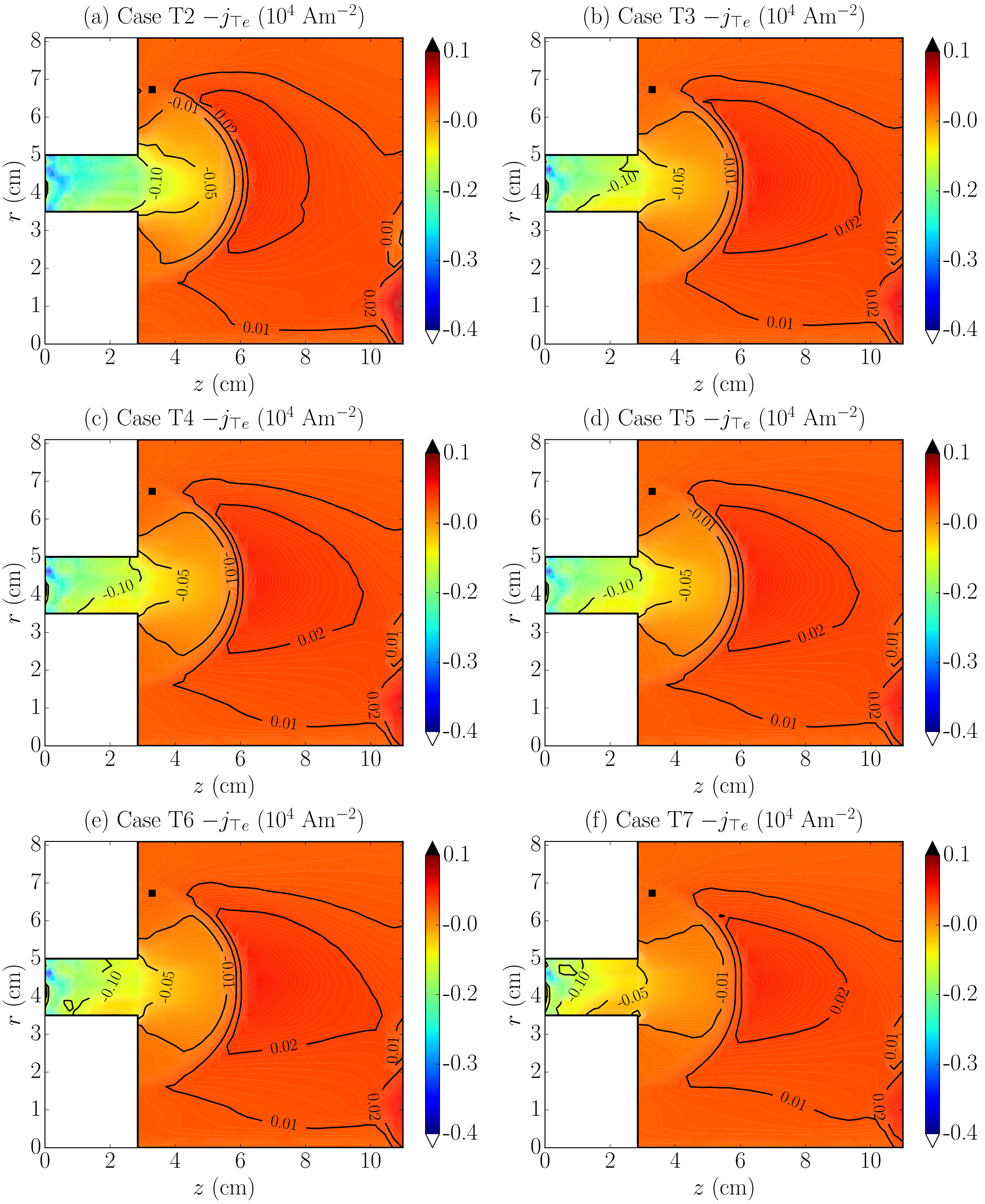

Figure B.18: Time-averaged electron perpendicular current density component 2D contour plot for the simulation cases (a) T2, (b) T3, (c) T4, (d) T5, (e) T6 and (f) T7. The black square marker indicates the cathode position at C1 [see Fig. 4.6(b)].

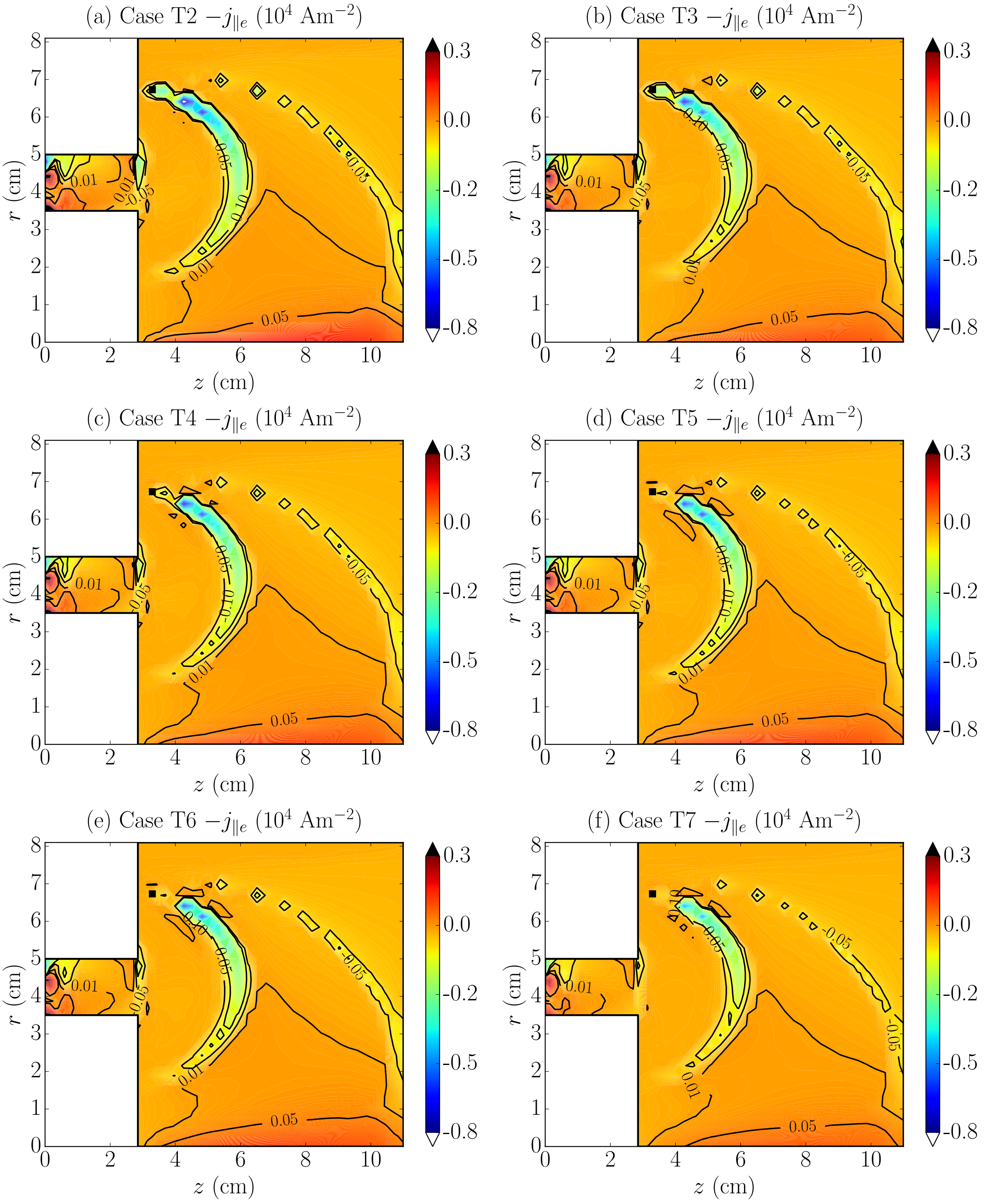

Figure B.19: Time-averaged electron parallel current density component 2D contour plot for the simulation cases (a) T2, (b) T3, (c) T4, (d) T5, (e) T6 and (f) T7. The black square marker indicates the cathode position at C1 [see Fig. 4.6(b)].

(a) Case T2 $|\tilde{\boldsymbol{j}}_e|$ (Am^{-2}) (b) Case T3 $|\tilde{\boldsymbol{j}}_e|$ (Am^{-2})

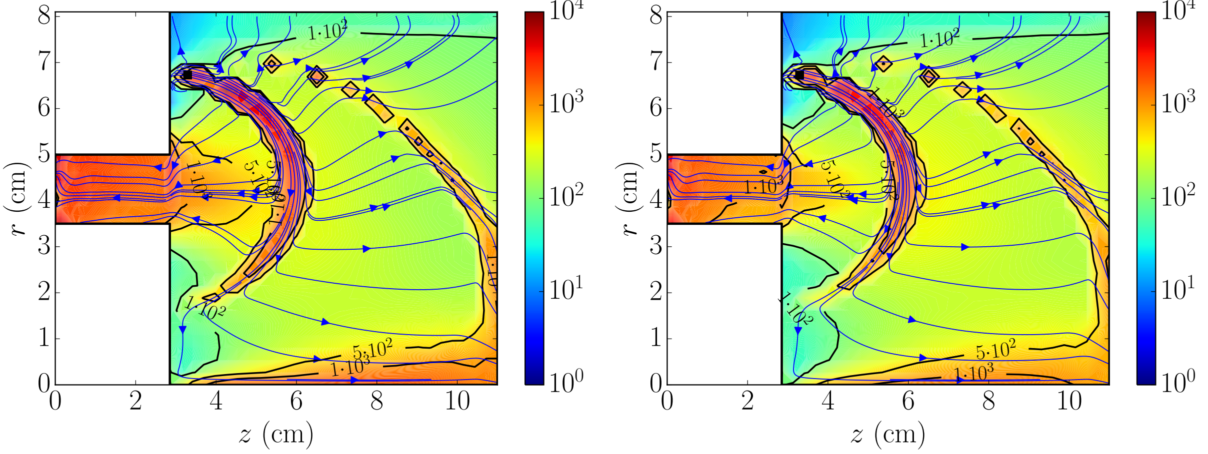

(c) Case T4 $|\tilde{\boldsymbol{j}}_e|$ (Am^{-2}) (d) Case T5 $|\tilde{\boldsymbol{j}}_e|$ (Am^{-2})

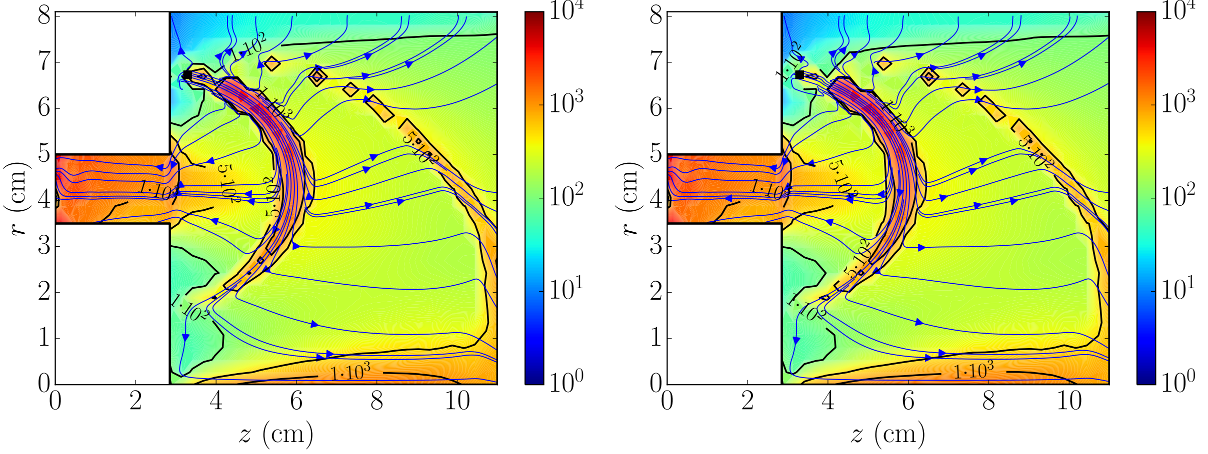

(e) Case T6 $|\tilde{\boldsymbol{j}}_e|$ (Am^{-2}) (f) Case T7 $|\tilde{\boldsymbol{j}}_e|$ (Am^{-2})

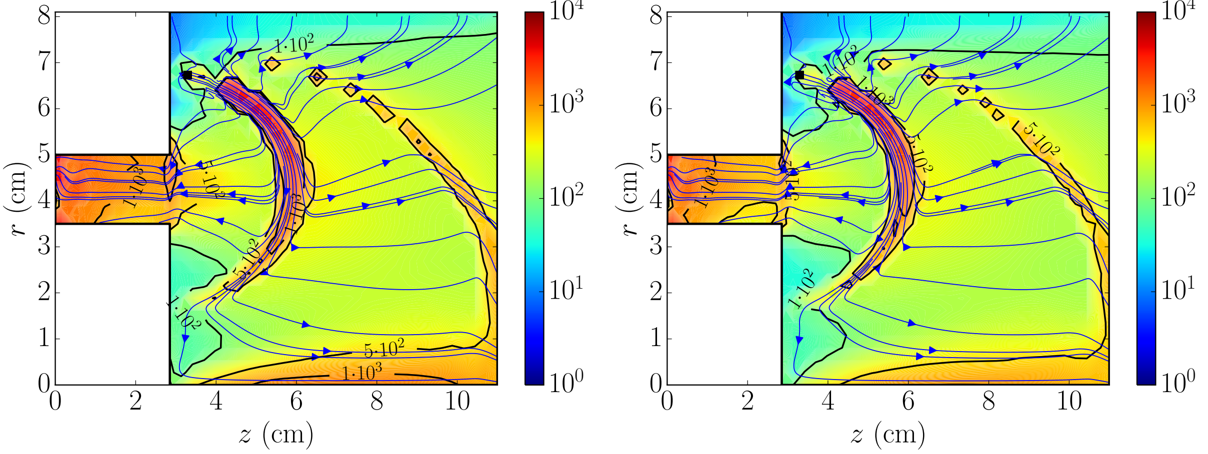

Figure B.20: 2D magnitude contour plot and streamlines of the time-averaged electron 2D (z, r) current density vector $-\tilde{\boldsymbol{j}}_e$ for the simulation cases (a) T2, (b) T3, (c) T4, (d) T5, (e) T6 and (f) T7. The black square marker indicates the cathode position at C1 [see Fig. 4.6(b)].

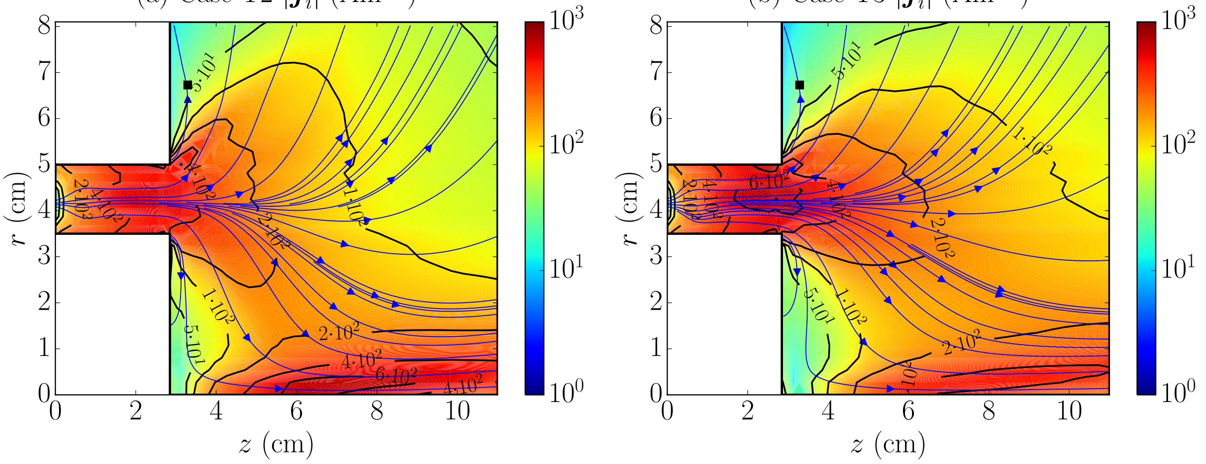

(a) Case T2 $|\tilde{\boldsymbol{j}}_i|$ (Am^{-2})

(b) Case T3 $|\tilde{\boldsymbol{j}}_i|$ (Am^{-2})

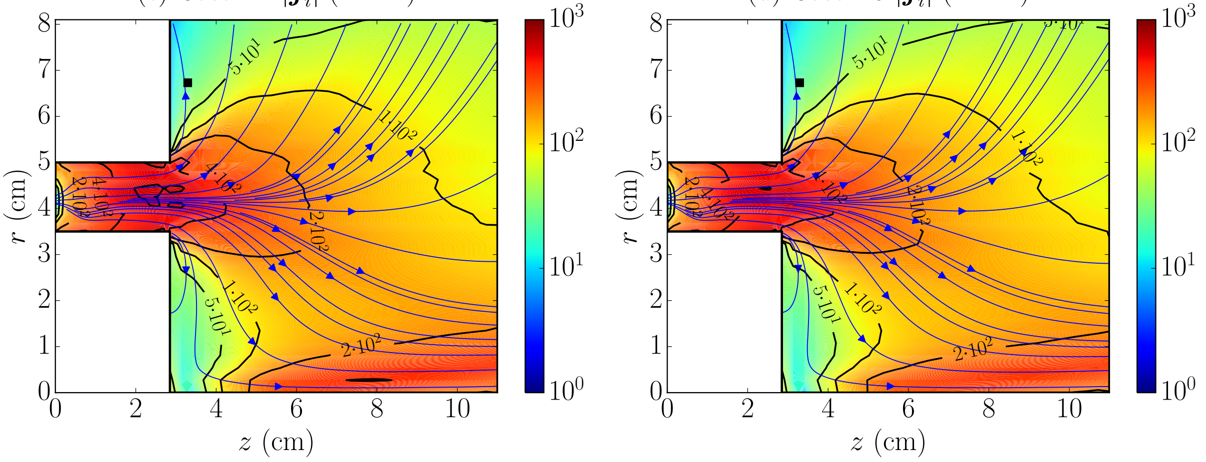

(c) Case T4 $|\tilde{\boldsymbol{j}}_i|$ (Am^{-2})

(d) Case T5 $|\tilde{\boldsymbol{j}}_i|$ (Am^{-2})

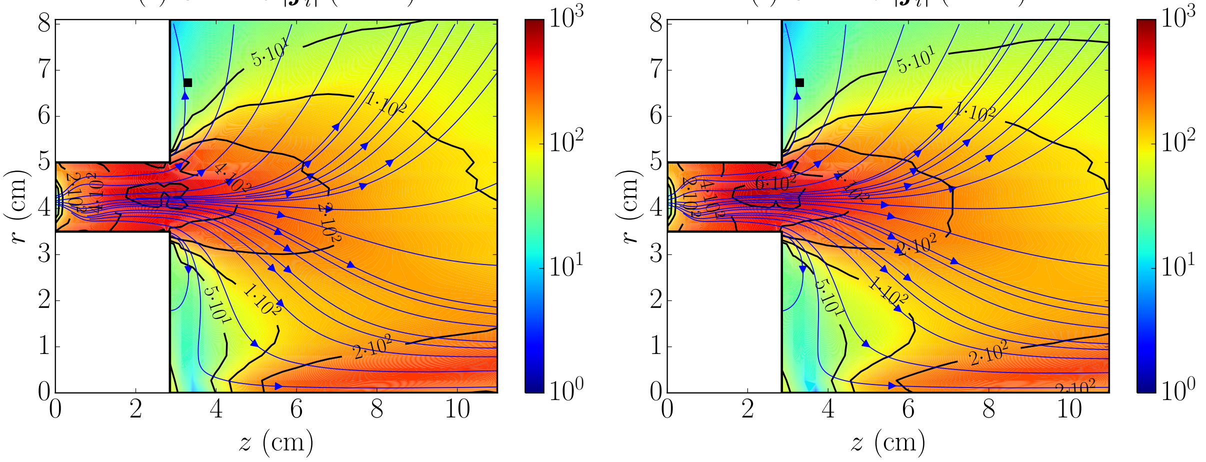

(e) Case T6 $|\tilde{\boldsymbol{j}}_i|$ (Am^{-2})

(f) Case T7 $|\tilde{\boldsymbol{j}}_i|$ (Am^{-2})

Figure B.21: 2D magnitude contour plot and streamlines of the time-averaged ion 2D (z, r) current density vector $\tilde{\boldsymbol{j}}_i$ for the simulation cases (a) T2, (b) T3, (c) T4, (d) T5, (e) T6 and (f) T7. The black square marker indicates the cathode position at C1 [see Fig. 4.6(b)].

Bibliography

[1] R. G. Jahn. *Physics of electric propulsion.* McGraw-Hill, New York, 1968. Reprinted by Dover.

[2] M. Martínez-Sánchez and J. E. Pollard. Spacecraft electric propulsion-an overview. *Journal of propulsion and power*, 14(5):688–699, 1998.

[3] D. M. Goebel and I. Katz. *Fundamentals of electric propulsion: Ion and Hall thrusters.* Willey, New York, 2008.

[4] E. Ahedo. Plasmas for space propulsion. *Plasma Physics and Controlled Fusion*, 53(12):124037, 2011.

[5] J. P. Boeuf. Tutorial: physics and modeling of Hall thrusters. *Journal of Applied Physics*, 121(1):011101, 2017.

[6] J. S. Snyder, J. R. Brophy, R. R. Hofer, D. M. Goebel, and I. Katz. Experimental investigation of a direct-drive Hall thruster and solar array system at power levels up to 10 kW. In *48th Joint Propulsion Conference and Exhibit*, paper AIAA 2012-4068, Altanta, GA, USA, July 30 - August 1, 2012. American Institute of Aeronautics and Astronautics, https://www.aiaa.org.

[7] R. R. Hofer, B. A. Jorns, J. E. Polk, I. G. Mikellides, and J. S. Snyder. Wear test of a magnetically shielded hall thruster at 3000 seconds specific impulse. In *33rd International Electric Propulsion Conference*, paper IEPC 2013-033, Washington D. C., USA, October 7-10, 2013. Electric Rocket Propulsion Society, https://erps.spacegrant.org.

[8] F. F. Chen. Plasma ionization by helicon waves. *Plasma Physics and Controlled Fusion*, 33(4):339, 1991.

[9] R. W. Boswell and F. F. Chen. Helicons-the early years. *IEEE Transactions on Plasma Science*, 25(6):1229–1244, 1997.

[10] K. Takahashi, C. Charles, R. W. Boswell, W. Cox, and R. Hatakeyama. Transport of energetic electrons in a magnetically expanding helicon double layer plasma. *Applied Physics Letters*, 94(19):191503, 2009.

[11] E. Ahedo and J. Navarro-Cavallé. Helicon thruster plasma modeling: Two-dimensional fluid-dynamics and propulsive performances. *Physics of Plasmas*, 20(4):043512, 2013.

[12] T. Lafleur. Helicon plasma thruster discharge model. *Physics of Plasmas*, 21(4):043507, 2014.

[13] J. Navarro-Cavallé. *Plasma simulation in space propulsion: the Helicon plasma thruster*. PhD thesis, Universidad Politécnica de Madrid. Escuela Técnica Superior de Ingenieros Aeronáuticos. Departamento de Matemática Aplicada a la Ingeniería Aeroespacial, Madrid, Spain, December 2016.

[14] J Navarro-Cavallé, M Wijnen, P Fajardo, and E Ahedo. Experimental characterization of a 1 kW helicon plasma thruster. *Vacuum*, 149:69–73, 2018.

[15] B. Tian, M. Merino, and E. Ahedo. Two-dimensional plasma-wave interaction in an helicon plasma thruster with magnetic nozzle. *Plasma Sources Science and Technology*, 27(11):114003, 2018.

[16] D. B. Miller and G. W. Bethke. Cyclotron resonance thruster design techniques. *AIAA Journal*, 4(5):835–840, 1966.

[17] J. C. Sercel and D. J. Fitzgerald. ECR plasma thruster research: Preliminary theory and experiments. In *25th Joint Propulsion Conference and Exhibit*, paper AIAA 1989-2379, Monterey, CA, USA, July 10-13, 1989. American Institute of Aeronautics and Astronautics, https://www.aiaa.org.

[18] M. Lampe, G. Joyce, W. M. Manheimer, and S. P. Slinker. Quasi-neutral particle simulation of magnetized plasma discharges: General formalism and application to ECR discharges. *IEEE Transactions On Plasma Science*, 26:1592–1609, 1998.

[19] H. Kuninaka and S. Satori. Development and demonstration of a cathodeless electron cyclotron resonance ion thruster. *Journal of Propulsion and Power*, 14(6):1022–1026, 1998.

[20] J. Jarrige, P. Q. Elias, F. Cannat, and D. Packan. Performance comparison of an ECR plasma thruster using argon and xenon as propellant gas. In *33rd International Electric Propulsion Conference*, paper IEPC 2013-420, Washington D. C., USA, October 7-10, 2013. Electric Rocket Propulsion Society, https://erps.spacegrant.org.

[21] T. Vialis, J. Jarrige, A. Aanesland, and D. Packan. Direct thrust measurement of an electron cyclotron resonance plasma thruster. *Journal of Propulsion and Power*, 34(5):1323–1333, 2018.

[22] R. W. Hockney and J. W. Eastwood. *Computer simulations using particles*. Adam Hilger, Bristol and New York, 1988.

[23] M. Martínez-Sánchez, J Navarro-Cavallé, and E Ahedo. Electron cooling and finite potential drop in a magnetized plasma expansion. *Physics of Plasmas*, 22(5):053501, 2015.

[24] M. Merino, P. Fajardo, and E. Ahedo. Collisionless electron cooling in unmagnetized plasma thruster plumes. In *52nd Joint Propulsion Conference and Exhibit*, paper AIAA 2016-5037, Salt Lake City, UT, USA, July 25-27, 2016. American Institute of Aeronautics and Astronautics, https://www.aiaa.org.

[25] M. Merino, J. Mauriño, and E. Ahedo. Direct-Vlasov study of electron cooling mechanisms in paraxial, unmagnetized plasma thruster plumes. In *35th International Electric Propulsion Conference*, paper IEPC 2017-104, Atlanta, GA, USA, October 8-12, 2017. Electric Rocket Propulsion Society, https://erps.spacegrant.org.

[26] M. Merino, J. Mauriño, and E. Ahedo. Kinetic electron model for plasma thruster plumes. *Plasma Sources Science and Technology*, 27(3):035013, 2018.

[27] G. Sánchez-Arriaga, J. Zhou, E. Ahedo, M. Martínez-Sánchez, and J. J. Ramos. Kinetic features and non-stationary electron trapping in paraxial magnetic nozzles. *Plasma Sources Science and Technology*, 27(3):035002, 2018.

[28] D. Sydorenko, A. Smolyakov, I. Kaganovich, and Y. Raitses. Modification of electron velocity distribution in bounded plasmas by secondary electron emission. *IEEE Transactions on Plasma Science*, 34(3):815–824, 2006.

[29] I. D. Kaganovich, Y. Raitses, D. Sydorenko, and A. Smolyakov. Kinetic effects in a hall thruster discharge. *Physics of Plasmas*, 14(5):057104, 2007.

[30] F. Taccogna, S. Longo, M. Capitelli, and R. Schneider. Particle-in-cell simulation of stationary plasma thruster. *Contributions to Plasma Physics*, 47(8-9):635–656, 2007.

[31] F. Taccogna, S. Longo, M. Capitelli, and R. Schneider. Surface-driven asymmetry and instability in the acceleration region of a Hall thruster. *Contributions to Plasma Physics*, 48(4):1–12, 2008.

[32] F. Taccogna, R. Schneider, S. Longo, and M. Capitelli. Kinetic simulations of a plasma thruster. *Plasma Sources Science and Technology*, 17(2):024003, 2008.

[33] D. Tskhakaya, K. Matyash, R. Schneider, and F. Taccogna. The particle-in-cell method. *Contributions to Plasma Physics*, 47(8-9):563–594, 2007.

[34] V. Croes, T. Lafleur, Z. Bonaventura, A. Bourdon, and P. Chabert. 2D particle-in-cell simulations of the electron drift instability and associated anomalous electron transport in Hall-effect thrusters. *Plasma Source Science and Technology*, 26(3):034001, 2017.

[35] A. Domínguez-Vázquez, F. Taccogna, and E. Ahedo. Particle modeling of radial electron dynamics in a controlled discharge on a Hall thruster. *Plasma Sources Science and Technology*, 27(6):064006, 2018.

[36] C. K. Birdsall and A. B. Langdon. *Plasma physics via computer simulation.* Adam Hilger, Bristol, Philadelphia and New York, 1991.

[37] C. K. Birdsall. Particle-in-Cell charged particle simulations, plus Monte Carlo collisions with neutral atoms, PIC-MCC. *IEEE Transactions on Plasma Science*, 19(2):65–85, 1991.

[38] G. A. Bird. *Molecular gas dynamics and the direct simulation of gas flows.* The Oxford Engineering Science Series. Oxford University Press, Great Clarendon Street, Oxford OX2 6DP, 1994.

[39] M. Merino, F. Cichocki, and E. Ahedo. Collisionless plasma thruster plume expansion model. *Plasma Sources Science and Technology*, 24(3):035006, 2015.

[40] I. G. Mikellides and I. Katz. Numerical simulations of hall-effect plasma accelerators on a magnetic-field-aligned mesh. *Physical Review E*, 86(4):046703, 2012.

[41] I. G. Mikellides, B. A. Jorns, I. Katz, and A. L. Ortega. Hall2De simulations with a first-principles electron transport model based on the Electron Cyclotron Drift Instability. In *52nd Joint Propulsion Conference and Exhibit*, paper AIAA 2016-4618, Salt Lake City, UT, USA, July 25-27, 2016. American Institute of Aeronautics and Astronautics, https://www.aiaa.org.

[42] A. L. Ortega, I. Katz, I. G. Mikellides, and D. M. Goebel. Self-consistent model of a high-power Hall thruster plume. *IEEE Transactions on Plasma Science*, 43(9):2875–2886, 2015.

[43] I. G. Mikellides and A. L. Ortega. Challenges in the development and verification of first-principles models in Hall-effect thruster simulations that are based on anomalous resistivity and generalized Ohm's law. *Plasma Sources Science and Technology*, 28(1):014003, 2019.

[44] J. M. Fife. *Hybrid-PIC modeling and electrostatic probe survey of Hall thrusters.* PhD thesis, Aeronautics and Astronautics Dept., Massachuchusetts Institute of Technology, Cambridge, Massachusetts, USA, September 1998.

[45] F. I. Parra, E. Ahedo, J. M. Fife, and M. Martínez-Sánchez. A two-dimensional hybrid model of the Hall thruster discharge. *Journal of Applied Physics*, 100(2):023304, 2006.

[46] D. Escobar and E. Ahedo. Two-dimensional electron model for a hybrid code of a two-stage Hall thruster. *IEEE Transactions on Plasma Science*, 36(0):2043–2057, 2008.

[47] G. J. M. Hagelaar, J. Bareilles, L. Garrigues, and J. P. Boeuf. Two-dimensional model of a stationary plasma thruster. *Journal of Applied Physics*, 91(9):5592–5598, 2002.

[48] M. M. Santi. Hall thruster plume simulation using a hybrid-PIC algorithm. Master's thesis, Massachusetts Institute of Technology, Cambridge, Massachusetts, USA, July 2003.

[49] M. Celik, M. Santi, S. Cheng, M. Martínez-Sánchez, and J. Peraire. Hybrid-PIC simulation of a Hall thruster plume on an unstructured grid with DSMC collisions. In *28th International Electric Propulsion Conference*, paper IEPC 2003-134, Toulouse, France, March 17-21, 2003. Electric Rocket Propulsion Society, https://erps.spacegrant.org.

[50] I. Boyd and J. Yim. Hall thruster plume simulation using a detailed hybrid model. In *40th Joint Propulsion Conference and Exhibit*, paper AIAA 2004-3952, Fort Lauderdale, FL, USA, July 11-14, 2004. American Institute of Aeronautics and Astronautics, https://www.aiaa.org.

[51] D. Kahnfeld, R. Schneider, F. Cichocki, M. Merino, E. Ahedo, J. Duras, and N. Koch. HEMPT thruster discharge and plume simulation with a 2D3v-PIC-MCC and a 3D hybrid fluid-PIC code. In *35th International Electric Propulsion Conference*, paper IEPC 2017-309, Atlanta, GA, USA, October 8-12, 2017. Electric Rocket Propulsion Society, https://erps.spacegrant.org.

[52] F. Cichocki. *Analysis of the expansion of a plasma thruster plume into vacuum.* PhD thesis, Universidad Carlos III de Madrid (UC3M), Leganés, Madrid, Spain, 2017.

[53] F. Cichocki, A. Domínguez-Vázquez, M. Merino, and E. Ahedo. Hybrid 3D model for the interaction of plasma thruster plumes with nearby objects. *Plasma Sources Science and Technology*, 26(12):125008, 2017.

[54] A. Domínguez-Vázquez, F. Cichocki, M. Merino, P. Fajardo, and E. Ahedo. Axisymmetric plasma plume characterization with 2D and 3D particle codes. *Plasma Sources Science and Technology*, 27(10):104009, 2018.

[55] L. Garrigues, S. Santhosh, L. Grimaud, and S. Mazouffre. Operation of a low-power Hall thruster: Comparison between magnetically unshielded and shielded configuration. *Plasma Sources Science and Technology*, 2019. Accepted manuscript.

[56] G. Kornfeld, N. Koch, and H. P. Harmann. Physics and evolution of hemp-thrusters. In *30th International Electric Propulsion Conference*, paper IEPC 2007-108, Florence, Italy, September 17-20, 2007. Electric Rocket Propulsion Society, https://erps.spacegrant.org.

[57] N. Koch, M. Schirra, S. Weis, A. Lazurenko, B. van Reijen, J. Haderspeck, A. Genovese, P. Holtmann, R. Schneider, K. Matyash, and O. Kalentyev. The HEMPT concept - a survey on theoretical considerations and experimental evidences. In *32nd International Electric Propulsion Conference*, paper IEPC 2011-236, Wiesbaden, Germany, September 11-15, 2011. Electric Rocket Propulsion Society, https://erps.spacegrant.org.

[58] F. Cichocki, A. Domínguez, M. Merino, and E. Ahedo. A 3D hybrid code to study electric thruster plumes. In *Space Propulsion Conference*, paper SP2016-3124968, Rome, Italy, May 2-6, 2016. 3AF, https://www.3af.fr/.

[59] D. Pérez-Grande, J. Zhou, A. Domínguez-Vázquez, P. Fajardo, and E. Ahedo. Development updates for a two-dimensional axisymmetric hybrid code for plasma thruster discharges. In *35th International Electric Propulsion Conference*, paper IEPC 2017-201, Atlanta, GA, USA, October 8-12, 2017. Electric Rocket Propulsion Society, https://erps.spacegrant.org.

[60] D. Pérez-Grande. *Fluid modeling and simulation of the electron population in Hall effect thrusters with complex magnetic topologies*. PhD thesis, Universidad Carlos III de Madrid (UC3M), Leganés, Madrid, Spain, 2018.

[61] A. Domínguez-Vázquez, D. Pérez-Grande, P. Fajardo, and E. Ahedo. NOMADS: development of a versatile plasma discharge simulation platform for electric propulsion. In *Space Propulsion Conference*, paper SP2016-3124869, Rome, Italy, May 2-6, 2016. 3AF, https://www.3af.fr/.

[62] A. Domínguez-Vázquez, F. Cichocki, M. Merino, P. Fajardo, and E. Ahedo. 2D and 3D hybrid PIC-fluid modeling of electric thruster plumes. In *35th International Electric Propulsion Conference*, paper IEPC 2017-209, Atlanta, GA, USA, October 8-12, 2017. Electric Rocket Propulsion Society, https://erps.spacegrant.org.

[63] A. Domínguez-Vázquez, F. Taccogna, P. Fajardo, and E. Ahedo. Influence of relevant parameters on the radial PIC simulation of a Hall effect thruster discharge. In *Space Propulsion Conference*, paper SP2018-288, Sevilla, Spain, May 14-18, 2018. 3AF, https://www.3af.fr/.

[64] A. Domínguez-Vázquez, F. Taccogna, P. Fajardo, and E. Ahedo. Influence of relevant parameters on the radial particle simulation of a Hall thruster discharge. Submitted to Journal of Physics D: Applied Physics.

[65] F. B. de Saavedra. Modeling and optimization of magnetic circuits for next generation Hall-effect trusters. Master's thesis, Universidad Carlos III de Madrid (UC3M). Escuela Politécnica Superior. Departamento de Bioingeniería e Ingeniería Aeroespacial, 2017.

[66] D. Pérez-Grande, O. Gonzalez-Martinez, P. Fajardo, and E. Ahedo. Analysis of the numerical diffusion in anisotropic mediums: Benchmarks for magnetic field aligned meshes in space propulsion simulations. *Applied Sciences*, 6(11):354, 2016.

[67] J. Zhou, A. Domínguez-Vázquez, D. Pérez-Grande, P. Fajardo, and E. Ahedo. An axisymmetric hybrid model for the plasma transport in a Helicon plasma thruster. In *Space Propulsion Conference*, paper SP2018-308, Sevilla, Spain, May 14-18, 2018. 3AF, https://www.3af.fr/.

[68] A. Sánchez-Villar and M. Merino. Advances in wave-plasma modelling in ECR thrusters. In *Space Propulsion Conference*, paper SP2018-346, Sevilla, Spain, May 14-18, 2018. 3AF, https://www.3af.fr/.

[69] J. P. Verboncoeur. Symmetric spline weighting for charge and current density in particle simulation. *Journal of Computational Physics*, 174:421–427, 2001.

[70] F. I. Parra. Actualización y mejora de un códio PIC-fluido bidimensional para el flujo de plasma en motores de efecto Hall. Master's thesis, Universidad Politécnica de Madrid. Escuela Técnica Superior de Ingenieros Aeronáuticos. Departamento de Fundamentos Matemáticos, Agosto 2004.

[71] D. Escobar. Motores de efecto Hall de alto impulso específico. Master's thesis, Universidad Politécnica de Madrid. Escuela Técnica Superior de Ingenieros Aeronáuticos. Departamento de Fundamentos Matemáticos, Septiembre 2005.

[72] R. Santos. *Código híbrido avanzado de motores de plasma de efecto Hall*. PhD thesis, Universidad Politécnica de Madrid. Escuela Técnica Superior de Ingenieros Aeronáuticos. Departamento de Fundamentos Matemáticos, Madrid, Spain, Junio 2012.

[73] K. Nanbu. Stochastic theory of motion and collision of charged particle in a uniform electric field. *J. Phys. Soc. Jpn.*, 63(3):979–983, 1994.

[74] S. J. Araki, R. S. Martin, D. Bilyeu, and J. W. Koo. SM/MURF: Current capabilities and verification as a replacement of AFRL plume simulation tool COLISEUM. In *52nd Joint Propulsion Conference and Exhibit*, paper AIAA 2016-4939, Salt Lake City, UT, USA, July 25-27, 2016. American Institute of Aeronautics and Astronautics, https://www.aiaa.org.

[75] R. Santos and E. Ahedo. Implementation of the kinetic Bohm condition in a Hall thruster hybrid code. In *45th Joint Propulsion Conference and Exhibit*, paper 2009-4913, Denver, CO, USA, August 2-5, 2009. American Institute of Aeronautics and Astronautics, https://www.aiaa.org.

[76] E. Ahedo, R. Santos, and F. I. Parra. Fulfillment of the kinetic Bohm criterion in a quasineutral particle-in-cell model. *Physics of Plasmas*, 17(7):073507, 2010.

[77] D. Y. Oh. *Computational modeling of expanding plasma plumes in space using a PIC-DSMC algorithm*. PhD thesis, Massachusetts Institute of Technology, Cambridge, Massachusetts, USA, February 1996.

[78] Y. Azziz. *Experimental and theoretical characterization of a Hall thruster plume*. PhD thesis, Massachusetts Institute of Technology, Cambridge, Massachusetts, USA, June 2007.

[79] J.S. Miller, S.H. Pullins, D.J. Levandier, Y. Chiu, and R.A. Dressler. Xenon charge exchange cross sections for electrostatic thruster models. *Journal of Applied Physics*, 91(3):984–991, 2002.

[80] D. Rapp and W. E. Francis. Charge exchange between gaseous ions and atoms. *Journal of Chemical Physics*, 37(11):2631–2645, 1962.

[81] M. Dalvie, S. Hamaguchi, and R. T. Farouki. Self-consistent Monte Carlo simulation of the cathode fall including treatment of negative-glow electrons. *Physical Review A*, 46(2):1066, 1992.

[82] K. Nanbu and Y. Kitatani. An ion-neutral species collision model for particle simulation of glow discharge. *Journal of Physics D: Applied Physics*, 28(2):324, 1995.

[83] M. Mitchner and C. H. Kruger Jr., editors. *Partially ionized gases*. John Wiley and Sons, Inc., New York, 1973.

[84] E. W. Bell, N. Djurić, and G. H. Dunn. Electron-impact ionization of In^+ and Xe^+. *Physical Review A*, 48(6):4286, 1993.

[85] H.B. Garrett. The charging of spacecraft surfaces. *Reviews of Geophysics*, 19(4):577–616, 1981.

[86] I. D. Boyd and A. Ketsdever. Interactions between spacecraft and thruster plumes. *Journal of Spacecraft and Rockets*, 38(3):380–380, 2001.

[87] R. J. Goldston and P. H. Rutherford. *Introduction to plasma physics*. IOP Publishing, Bristol and Philadelphia, 1995.

[88] P. M Bellan. *Fundamentals of plasma physics*. Cambridge University Press, 2008.

[89] J. A. Bittencourt. *Fundamentals of plasma physics*. Springer-Verlag New York, Inc., New York, 2013.

[90] E. R. Harrison and W. B. Thompson. The low pressure plane symmetric discharge. *Proceedings of the Physical Society*, 74(2):145, 1959.

[91] K. U. Riemann. The Bohm criterion and sheath formation. *J. Phys. D: Appl. Phys.*, 24:492–518, 1991.

[92] K. U. Riemann. The Bohm criterion and boundary conditions for a multicomponent system. *IEEE Transactions On Plasma Science*, 23:709–716, 1995.

[93] J. Zhou, D. Pérez-Grande, P. Fajardo, and E. Ahedo. Numerical treatment of a magnetized electron fluid within an electromagnetic plasma thruster code. To be submitted to PSST.

[94] I. Maqueda, D. Escobar, and E. Ahedo. Advances on a Hall thruster hybrid code. In *30th International Electric Propulsion Conference*, paper IEPC 2007-066, Florence, Italy, September 17-20, 2007. Electric Rocket Propulsion Society, https://erps.spacegrant.org.

[95] G. S. Janes and R. S. Lowder. Anomalous electron diffusion and ion acceleration in a low-density plasma. *The Physics of Fluids*, 9(6):1115–1123, 1966.

[96] A. I. Morozov, Yu V. Esipchuk, A. M. Kapulkin, V. A. Nevrovskii, and V. A. Smirnov. Effect of the magnetic field a closed-electron-drift accelerator. *Soviet Physics Technical Physics*, 17:482, 1972.

[97] A. I. Bugrova, A. I. Morozov, and V. K. Kharchevnikov. Experimental studies of near wall conductivity. *Fizika Plazmy*, 16(12):1469–1481, 1990.

[98] E. Ahedo, J. M. Gallardo, and M. Martínez-Sánchez. Effects of the radial-plasma wall interaction on the axial Hall thruster discharge. *Phys of Plasmas*, 10(8):3397–3409, 2003.

[99] E. Ahedo. Radial macroscopic model of a plasma flowing along annular dielectric walls. *Physics of Plasmas*, 9(7):3178–3186, 2002.

[100] E. Ahedo. Presheath/sheath model with secondary electron emission from two parallel walls. *Physics of plasmas*, 9(10):4340–4347, 2002.

[101] D. Escobar. *Electron transport and azimuthal oscillations in Hall thrusters.* PhD thesis, Universidad Politécnica de Madrid. Escuela Técnica Superior de Ingenieros Aeronáuticos. Departamento de Fundamentos Matemáticos, Madrid, Spain, June 2015.

[102] L. Garrigues, G. J. M. Hagelaar, C. Boniface, and J. P. Boeuf. Anomalous conductivity and secondary electron emission in hall effect thrusters. *Journal of applied physics*, 100(12):123301, 2006.

[103] R. R. Hofer, I. Katz, D. M. Goebel, K. K. Jameson, R. M. Sullivan, L. K. Johnson, and I. G. Mikellides. Efficacy of electron mobility models in hybrid-PIC Hall thruster simulations. In *44th Joint Propulsion Conference and Exhibit*, paper AIAA 2008-4924, Hartford, CT, USA, July 21-23, 2008. American Institute of Aeronautics and Astronautics, https://www.aiaa.org.

[104] E. Y. Choueiri. Plasma oscillations in Hall thrusters. *Physics of Plasmas*, 8(4):1411–1426, 2001.

[105] S. Barral, K. Makowski, Z. Peradzyński, and M. Dudeck. Transit-time instability in Hall thrusters. *Physics of Plasmas*, 12(7):073504, 2005.

[106] S. Barral and E. Ahedo. Low-frequency model of breathing oscillations in Hall discharges. *Physical Review E*, 79(4):046401, 2009.

[107] J. P. Boeuf and L. Garrigues. Low frequency oscillations in a stationary plasma thruster. *Journal of Applied Physics*, 84(7):3541–3554, 1998.

[108] E. Ahedo, J. M. Gallardo, and M. Martınez-Sánchez. Model of the plasma discharge in a Hall thruster with heat conduction. *Physics of Plasmas*, 9(9):4061–4070, 2002.

[109] E Ahedo and J Rus. Vanishing of the negative anode sheath in a Hall thruster. *Journal of Applied Physics*, 98(4):043306, 2005.

[110] A. R. Barakat and R. W. Schunk. Transport equations for multicomponent anisotropic space plasmas: a review. *Plasma Physics*, 24(4):389, 1982.

[111] R. Fernández-Feria. *Mecánica de fluidos.* Servicio de Publicaciones e Intercambio Científico de la Universidad de Málaga, 2001.

[112] T. Lafleur, S. D. Baalrud, and P. Chabert. Theory for the anomalous electron transport in Hall effect thrusters. I. insights from particle-in-cell simulations. *Physics of Plasmas*, 23(5):053502, 2016.

[113] T. Lafleur, S. D. Baalrud, and P. Chabert. Theory for the anomalous electron transport in Hall effect thrusters. II. kinetic model. *Physics of Plasmas*, 23(5):053503, 2016.

[114] T. Lafleur, S. D. Baalrud, and P. Chabert. Characteristics and transport effects of the electron drift instability in Hall-effect thrusters. *Plasma Sources Science and Technology*, 26(2):024008, 2017.

[115] T. Lafleur, R. Martorelli, P. Chabert, and A. Bourdon. Anomalous electron transport in Hall-effect thrusters: Comparison between quasi-linear kinetic theory and particle-in-cell simulations. *Physics of Plasmas*, 25(6):061202, 2018.

[116] E. Sozer, C. Brehm, and C. C. Kiris. Gradient calculation methods on arbitrary polyhedral unstructured meshes for cell-centered CFD solvers. In *52nd AIAA Aerospace Sciences Meeting*, paper AIAA 2014-1440, National Harbor, MD, USA, January 13-17, 2014. American Institute of Aeronautics and Astronautics, https://www.aiaa.org.

[117] C. G. Petra, O. Schenk, M. Lubin, and K. Gäertner. An augmented incomplete factorization approach for computing the Schur complement in stochastic optimization. *SIAM Journal on Scientific Computing*, 36(2):C139–C162, 2014.

[118] C. G. Petra, O. Schenk, and M. Anitescu. Real-time stochastic optimization of complex energy systems on high-performance computers. *Computing in Science & Engineering*, 16(5):32–42, 2014.

[119] E. Ahedo and V. de Pablo. Combined effects of electron partial thermalization and secondary emission in Hall thruster discharges. *Physics of Plasmas*, 14:083501, 2007.

[120] M. Hayashi. Determination of electron-xenon total excitation cross-sections, from threshold to 100 eV, from experimental values of Townsend's α. *Journal of Physics D: Applied Physics*, 16(4):581, 1983.

[121] M. Masselin. Development of a hybrid PIC code for the simulation of plasma spacecraft interactions. Master's thesis, University of Stockholm, Sweden, 2012.

[122] M. Wartelski, C. Theroude, C. Ardura, and E. Gengembre. Self-consistent simulations of interactions between spacecraft and plumes of electric thrusters. In *33rd International Electric Propulsion Conference*, paper IEPC 2013-73, Washington D. C., USA, October 7-10, 2013. Electric Rocket Propulsion Society, https://erps.spacegrant.org.

[123] F. Taccogna, D. Pagano, F. Scortecci, and A. Garulli. Three-dimensional plume simulation of multi-channel thruster configuration. *Plasma Sources Science and Technology*, 23(6):065034, 2014.

[124] B. Korkut and D. A. Levin. Three dimensional DSMC-PIC simulations of ion thruster plumes with SUGAR. In *50th Joint Propulsion Conference and Exhibit*, paper AIAA 2014-3447, Cleveland, OH, USA, July 28–30, 2014. American Institute of Aeronautics and Astronautics, https://www.aiaa.org.

[125] C. Cai. Numerical studies on plasma plume flows from a cluster of electric propulsion devices. *Aerospace Science and Technology*, 41:134–143, 2015.

[126] D. L. Kahnfeld. Hybrid plume modeling. Master's thesis, Mathematisch-Naturwissenschaftliche Fakultät Ernst-Moritz-Arndt-Universität Greifswald, Greifswald, Germany, 2015.

[127] B. Korkut, Z. Li, and D. A. Levin. 3-D simulation of ion thruster plumes using octree adaptive mesh refinement. *IEEE Transactions on Plasma Science*, 43(5):1706–1721, 2015.

[128] F. Cichocki, M. Merino, and E. Ahedo. Spacecraft-plasma-debris interaction in an ion beam shepherd mission. *Acta Astronautica*, 146:216–227, 2018.

[129] W. M. Ruyten. Density-conserving shape factors for particle simulations in cylindrical and spherical coordinates. *Journal of Computational Physics*, 105(2):224–232, 1993.

[130] D. J. Larson, D. W. Hewett, and A. B. Langdon. Correction factors for PIC accumulation on radial grids. *Computer Physics Communications*, 90(2-3):260–266, 1995.

[131] P. A. Vázquez and A. Castellanos. Weighting of charge in PIC codes for unstructured meshes in cylindrical coordinates: application to charged jets. In *CEIDP '05. 2005 Annual Report Conference on Electrical Insulation and Dielectric Phenomena*, pages 499–502, Nashville, TN, USA, October 16-19, 2005. Institute of Electrical and Electronics Engineers, https://www.ieee.org/.

[132] S. J. Araki and R. E. Wirz. Cell-centered particle weighting algorithm for PIC simulations in a non-uniform 2D axisymmetric mesh. *Journal of Computational Physics*, 272:218–226, 2014.

[133] G. Lapenta. Particle rezoning for multidimensional kinetic particle-in-cell simulations. *Journal of Computational Physics*, 181(1):317–337, 2002.

[134] R. S. Martin and J. L. Cambier. Octree particle management for DSMC and PIC simulations. *Journal of Computational Physics*, 327:943–966, 2016.

[135] J. E. Polk, R. Y. Kakuda, J. R. Anderson, J. R. Brophy, V. K. Rawlin, M. J. Patterson, J. Sovey, and J. Hamley. Validation of the NSTAR ion propulsion system on the Deep Space One mission: overview and initial results. In *35th Joint Propulsion Conference and Exhibit*, paper AIAA 1999-2274, Los Angeles, CA, USA, June 20-24, 1999. American Institute of Aeronautics and Astronautics, https://www.aiaa.org.

[136] J. R. Brophy. NASA's Deep Space 1 ion engine (plenary). *Review of Scientific Instruments*, 73(2):1071–1078, 2002.

[137] F. Cichocki, M. Merino, E. Ahedo, D. Feili, and M. Ruiz. Electric propulsion subsystem optimization for "Ion Beam Shepherd" missions. In *34th International Electric Propulsion Conference*, paper IEPC 2015-420, Hyogo-Kobe, Japan, July 6-10, 2015. Electric Rocket Propulsion Society, https://erps.spacegrant.org.

[138] D.E. Parks and I. Katz. A preliminary model of ion beam neutralization. In *14th International Electric Propulsion Conference*, paper IEPC 1979-2049, Princeton, NJ, USA, October 30 - November 1, 1979. Electric Rocket Propulsion Society, https://erps.spacegrant.org.

[139] F. Cichocki, M. Merino, and E. Ahedo. A 3d electron fluid model to study magnetic field effects on an expanding plasma thruster plume. In *Space Propulsion Conference*, paper SP2018-295, Sevilla, Spain, May 14-18, 2018. 3AF, https://www.3af.fr/.

[140] H. Saltsburg, J. N. Smith, Jr., and M. Rogers. *Fundamentals of gas-surface interactions*. Academic Press, New York and London, 1967.

[141] L.B. Thomas. Accommodation of molecules on controlled surfaces- experimental developments at the University of Missouri, 1940-1980. In *12th International Symposium on Rarefied Gas Dynamics*, paper 217, pp. 83–108, Charlottesville, VA, USA, July 7-11, 1980. American Institute of Aeronautics and Astronautics, https://www.aiaa.org.

[142] J.C. Gregory and P.N. Peters. A measurement of the angular distribution of 5eV atomic oxygen scattered off a solid surface in earth orbit. In *15th International Symposium on Rarefied Gas Dynamics*, paper A88-16826 04-34, vol. 2, pp. 644-654, Grado, Italy, June 16-20, 1986. Stuttgart, B. G. Teubner, 1986, Germany.

[143] K. Moe and M. M. Moe. Gas–surface interactions and satellite drag coefficients. *Planetary and Space Science*, 53(8):793–801, 2005.

[144] G. I. Font. Computational acceleration of orbital neutral sensor ionizer simulation through phenomena separation. *Journal of Computational Physics*, 316:1–9, 2016.

[145] V.J. Murray, M.D. Pilinski, E.J. Smoll Jr, M. Qian, T.K. Minton, S.M. Madzunkov, and M.R. Darrach. Gas–surface scattering dynamics applied to concentration of gases for mass spectrometry in tenuous atmospheres. *The Journal of Physical Chemistry C*, 121(14):7903–7922, 2017.

[146] J. M. Fife, M. Martínez-Sánchez, and J. Szabo. A numerical study of low-frequency discharge oscillations in Hall thrusters. In *33rd Joint Propulsion Conference and Exhibit*, paper AIAA 1997-3052, Seattle, WA, USA, July 6-9, 1997. American Institute of Aeronautics and Astronautics, https://www.aiaa.org.

[147] A. Anton and E. Ahedo. Contour algorithms for a Hall thruster hybrid code. In *42nd Joint Propulsion Conference and Exhibit*, paper AIAA 2006-4834, Sacramento, CA, USA, July 9-12, 2006. American Institute of Aeronautics and Astronautics, https://www.aiaa.org.

[148] D. Escobar, A. Antón, and E. Ahedo. Simulation of high-specific-impulse and double-stage Hall thrusters. In *29th International Electric Propulsion Conference*, paper IEPC 2005-040, Princeton, NJ, USA, October 31 - November 4, 2005. Electric Rocket Propulsion Society, https://erps.spacegrant.org.

[149] E. M. Granstedt, Y. Raitses, and N. J. Fisch. Cathode effects in cylindrical Hall thrusters. *Journal of Applied Physics*, 104(10):103302, 2008.

[150] Y. Raitses, A. Smirnov, and N. J. Fisch. Effects of enhanced cathode electron emission on Hall thruster operation. *Physics of Plasmas*, 16(5):057106, 2009.

[151] A. Smirnov, Y. Raitses, and N. J. Fisch. Controlling the plasma flow in the miniaturized cylindrical Hall thruster. *IEEE Transactions on Plasma Science*, 36(5):1998–2003, 2008.

[152] M. K. Scharfe, N. Gascon, M. A. Cappelli, and E. Fernández. Comparison of hybrid Hall thruster model to experimental measurements. *Physics of Plasmas*, 13(8):083505, 2006.

[153] N. Meezan and M. Cappelli. Electron density measurements for determining the anomalous electron mobility in a coaxial Hall discharge plasma. In *36th Joint Propulsion Conference and Exhibit*, paper AIAA 2000-3420, Las Vegas, NV, USA, July 24-28, 2000. American Institute of Aeronautics and Astronautics, https://www.aiaa.org.

[154] N. Meezan, W. A. Hargus Jr, and A. Cappelli. Anomalous electron mobility in a coaxial Hall discharge plasma. *Physical Review E*, 63(2):026410, 2001.

[155] M. Cappelli, N. Meezan, and N. Gascon. Transport physics in Hall plasma thrusters. In *40th AIAA Aerospace Sciences Meeting and Exhibit*, paper AIAA 2002-0485, Reno, NV, USA, January 14-17, 2002. American Institute of Aeronautics and Astronautics, https://www.aiaa.org.

[156] D. Bohm. *The characteristics of electrical discharges in magnetic fields.* McGraw-Hill, New York, p. 77, 1949.

[157] A. I. Morozov and V. V. Savelyev. Fundamentals of stationary plasma thruster theory. In *Reviews of plasma physics*, pages 203–391. Springer, 2000.

[158] J. J. Szabo, Jr. *Fully kinetic numerical modeling of a plasma thruster.* PhD thesis, Aeronautics and Astronautics Dept., Massachuchusetts Institute of Technology, Cambridge, Massachusetts, USA, February 2001.

[159] A. L. Ortega, I. Katz, and V. H. Chaplin. A first-principles model based on saturation of the Electron Cyclotron Drift Instability for electron transport in hydrodynamics simulations of Hall thruster plasmas. In *35th International Electric Propulsion Conference*, paper IEPC 2017–178, Atlanta, GA, USA, October 8-12, 2017. Electric Rocket Propulsion Society, https://erps.spacegrant.org.

[160] G. J. M. Hagelaar, J. Bareilles, L. Garrigues, and J. P. Boeuf. Role of anomalous electron transport in a stationary plasma thruster simulation. *Journal of Applied Physics*, 93(1):67–75, 2003.

[161] J. Fox, A. Batishcheva, O. Batishchev, and M. Martínez-Sánchez. Adaptively meshed fully-kinetic PIC-Vlasov model for near vacuum Hall thrusters. In *42nd*

Joint Propulsion Conference and Exhibit, paper AIAA 2006-4324, Sacramento, CA, USA, July 9-12, 2006. American Institute of Aeronautics and Astronautics, https://www.aiaa.org.

[162] J. W. Koo and I. D. Boyd. Modeling of anomalous electron mobility in Hall thrusters. *Physics of Plasmas*, 13(3):033501, 2006.

[163] J. R. Brophy. Stationary plasma thruster evaluation in Russia. 1992.

[164] B. A. Jorns. Data driven model for electron transport in a Hall effect thruster. In *Space Propulsion Conference*, paper SP2018-346, Sevilla, Spain, May 14-18, 2018. 3AF, https://www.3af.fr/.

[165] Ch. Wang, L. Wei, and D. Yu. A basic predator-prey type model for low frequency discharge oscilations in Hall thrusters. *Contributions to Plasma Physics*, 51(10):981–988, 2011.

[166] S. Barral and J. Miedzik. Numerical investigation of closed-loop control for Hall accelerators. *Journal of Applied Physics*, 109(1):013302, 2011.

[167] S. Barral, J. Kaczmarczyk, J. Kurzyna, and M. Dudeck. Active control and excitation of breathing oscillations in a Hall thruster with a fast digital signal processor. In *33rd International Electric Propulsion Conference*, paper IEPC 2013-339, Washington D. C., USA, October 7-10, 2013. Electric Rocket Propulsion Society, https://erps.spacegrant.org.

[168] K. Vladimir, D. Grdlichko, V. Kozlov, A. Lazourenko, G. Popov, and A. Skrylnikov. Local plasma parameter measurements by nearwall probes inside the SPT accelerating channel under thruster operation with Kr. In *38th Joint Propulsion Conference and Exhibit*, paper AIAA 2002-4108, Indianapolis, IN, USA, July 7-10, 2002. American Institute of Aeronautics and Astronautics, https://www.aiaa.org.

[169] K. Vladimir, V. Kozlov, A. Skrylnikov, L. Umnitsin, V. Svotina, A. Bouchoule, and M. Prioul. Investigation of the local plasma parameter distributions in the SPT accelerating channel under increased discharge voltages. In *29th International Electric Propulsion Conference*, paper IEPC 2005-004, Princeton, NJ, USA, October 31 - November 4, 2005. Electric Rocket Propulsion Society, https://erps.spacegrant.org.

[170] Y. Raitses, D. Staack, M. Keidar, and N. J. Fisch. Electron-wall interaction in Hall thrusters. *Physics of Plasmas*, 12(5):057104, 2005.

[171] Y. Raitses, D. Staack, A. Smirnov, and N. J. Fisch. Space charge saturated sheath regime and electron temperature saturation in Hall thrusters. *Physics of Plasmas*, 12(7):073507, 2005.

[172] R. D. Hazeltine and J. D. Meiss. *Plasma confinement.* Redwood City, CA: Addison-Wesley, 1992.

[173] S. Barral, Z. Peradzynski, K. Makowski, and M. Dudeck. An alternative theory of transit-time oscillations in Hall thrusters. In *28th International Electric Propulsion*

Conference, paper IEPC 2003-335, Toulouse, France, March 17-21, 2003. Electric Rocket Propulsion Society, https://erps.spacegrant.org.

[174] E. Ahedo and F.I. Parra. Model of radial plasma-wall interactions in a Hall thruster. In *38th Joint Propulsion Conference and Exhibit*, paper AIAA 2002-4106, Indianapolis, IN, USA, July 7-10, 2002. American Institute of Aeronautics and Astronautics, https://www.aiaa.org.

[175] E. Ahedo and F. I. Parra. Partial trapping of secondary electron emission in a Hall thruster plasma. *Physics of Plasmas*, 12(7):073503, 2005.

[176] H. Wang, M. Campanell, I. Kaganovich, and G. Cai. Effect of asymmetric secondary emission in bounded low-collisional E × B plasma on sheath and plasma properties. *Journal of Physics D: Applied Physics*, 47(40):405204, 2014.

[177] M. A. Furman and M. T. F. Pivi. Probabilistic model for the simulation of secondary electron emission. *Physical Review Special Topics-Accelerators and Beams*, 5(12):124404, 2002.

[178] K. Nanbu. Probability theory of electron-molecule, ion-molecule, molecule-molecule, and Coulomb collisions for particle modeling of materials processing plasmas and gases. *IEEE Transactions on plasma science*, 28(3):971–990, 2000.

[179] K. Nanbu. Simple method to determine collisional event in Monte Carlo simulation of electron-molecule collision. *Japanese Journal of Applied Physics*, 33(8):4752–4753, 2000.

[180] M. Surendra, D. B. Graves, and I. J. Morey. Electron heating in low-pressure rf glow discharges. *Appl. Phys. Lett.*, 56(11):1022–1024, 1990.

[181] K. Nanbu. Theory of cumulative small-angle collisions in plasmas. *Phys. Rev. E*, 55(4):4642–4652, 1997.

[182] K. Nanbu and S. Yonemura. Weighted particles in Coulomb collision simulations based on the theory of a cumulative scattering angle. *Journal of Computational Physics*, 145:639–654, 1998.

[183] A. V. Bobylev and K. Nanbu. Theory of collision algorithms for gases and plasmas based on the Boltzmann equation and the Landau-Fokker-Plack equation. *Physical Review E*, 61(4):4576–4586, 2000.

[184] C. Wang, T. Lin, R. Caflisch, B. I. Cohen, and A. M. Dimits. Particle simulation of Coulomb collisions: comparing the methods of Takizuka & Abe and Nanbu. *Journal of Computational Physics*, 227(9):4308–4329, 2008.

[185] R. Santos, E. Ahedo, and R. Santos. Implementation of the kinetic Bohm condition in a Hall thruster hybrid code. In *45th Joint Propulsion Conference and Exhibit*, paper AIAA 2009-4913, Denver, CO, USA, August 2-9, 2009. American Institute of Aeronautics and Astronautics, https://www.aiaa.org.

[186] W. H. Press, S. A. Teukolsky, W. T. Vetterling, and B. P. Flannery. *Numerical recipes in Fortran 77: the art of scientific computing*. Cambridge University Press, New York, 2001. Available online: http://numerical.recipes/.

[187] A. Domínguez-Vázquez, P. Fajardo, E. Ahedo, and F. Taccogna. Non-Maxwellian electron VDF features in a Hall thruster chamber. In *Princeton ExB Plasma Workshop*, Princeton University, Princeton, NJ, USA, November 1-2, 2018. Princeton Plasma Physics Laboratory, https://htx.pppl.gov/exb2018about.html.